Brett J. Tully

Magdalen College

Supervisor

Yiannis Ventikos

ALLOSTASIS OF CEREBRAL WATER:
Modelling the Transport of Cerebrospinal Fluid

A thesis submitted for the degree of Doctor of Philosophy

Trinity 2010

To my parents for always instilling that
"Luck is the intersection of preparation and opportunity."

To my grandfather whose many years of advice on integrity, humility and pressure would always be delivered with the perfect cricket analogy: *"keep your eye on the ball . . . keep your left elbow up . . . play through the 'V' early on . . . most of all, enjoy yourself."*

No Fear.
No Limits.
No Excuses.

A thesis submitted for the degree of Doctor of Philosophy.

Allostasis of Cerebral Water: Modelling the Transport of Cerebrospinal Fluid

By Brett J. Tully, Magdalen College.

Submitted Trinity 2010.

Societal Impact Summary

A validated model of water transport in the cerebral environment is both an ambitious and timely task; many brain diseases relate to imbalances in water regulation. From tumours to strokes, chronic or acute, transport of fluid in the brain plays a crucial role. The importance and complexity of the brain, together with the range of unmet clinical needs that are connected with this organ, make the current research a high-priority.

One of the most paradoxical cerebral conditions, hydrocephalus, serves as an excellent metric for judging the success of any model developed. In particular, normal pressure hydrocephalus (NPH) is a paradoxical condition with no known cure and existing treatments display unacceptably high failure rates. NPH is considered to be a disease of old age, and like many such diseases, it is related to a change in the transport of fluid in the cerebral environment. This complex system ranges from organ-level transport to cellular membrane channels such as aquaporins; through integrating it in a novel mathematical framework, we suggest that the underlying logic of treatment methods may be misleading.

By modelling the transport of cerebrospinal fluid (CSF) between the ventricular system, cerebral tissue and blood networks, we find that changes to the biophysical properties of the brain (rather than structural changes such as aqueduct obstruction) are capable of producing clinically relevant ventriculomegaly in the absence of any obstruction to CSF flow through the ventricular system. Specifically, the combination of increased leakiness and compliance of the capillary bed leads to the development of enlarged ventricles with a normal ventricular pressure, replicating clinical features of the presentation of NPH. These results, while needing experimental validation, imply that treatment methods like shunting, that are focussed on structural manipulation, may continue to fail at unacceptably high rates.

A thesis submitted for the degree of Doctor of Philosophy.

Allostasis of Cerebral Water: Modelling the Transport of Cerebrospinal Fluid

By Brett J. Tully, Magdalen College.

Submitted Trinity 2010.

Extended Abstract

The world is in the midst of a profound change in population demographics: by 2050, the most populous age group will no longer be those under fifteen years old, but those over sixty. People are living longer, and in most regions quality of life is also increasing. However, as the number of citizens living beyond the age of sixty grows, diseases of old age will continue to drive up demand for the already limited health services available. In order to meet these needs, medical experts and policy makers are increasingly aware that the efficacy and economy of treatment is strongly linked with the personalization of treatment.

An important common factor in many diseases of old age is that they are associated with a breakdown in the cerebral environment. The importance and complexity of the brain, together with the range of unmet clinical needs that are connected with this organ, make related research a high-priority. Biological systems can no longer be regarded as isolated modules and a multi-disciplinary, multi-scale approach is necessary to derive predictive clinical information.

A validated model of water transport in the cerebral environment is both an ambitious and timely task; many brain diseases relate to imbalances in water regulation. Tumours may lead to obstructions and problems in absorption of cerebrospinal fluid (CSF), stroke leads to oedemas, malformations result in hydrocephalus, and elevated intra-cranial pressure may lead to ischaemic dementia - of great significance to an ageing population. Common or rare - chronic or acute conditions, transport of water in the brain plays a crucial role.

Hydrocephalus is an active distension of the ventricular system of the brain resulting from inadequate passage of CSF from its point of production to its point of absorption into the systemic circulation. The condition can be either congenital (present at birth) or acquired through injury or trauma to the brain, and can be

further defined by a sub classification of: **acute hydrocephalus**, caused by intraventricular obstruction of the CSF flow pathways; or **chronic hydrocephalus**, characterized by prolonged time scales for development and the absence of radiographically identifiable flow obstruction.

One of the most paradoxical cerebral conditions, *chronic* hydrocephalus, serves as an excellent metric for judging the success of any model developed. While the clinical presentation of *acute* hydrocephalus and its relatively obvious source provides us with a useful set of parameters (those of ventricular displacement and CSF pressure) that can be used to validate mathematical models developed.

The complexity and paradoxical nature of hydrocephalus has enthralled researchers for many years. Experience and intuition alone have been largely ineffective in understanding the condition. While different approaches can be taken for modelling the dynamics of the system, each model is based on underlying assumptions about the flow of CSF. Historically, the pressure-volume relationship provided by the Monro-Kellie doctrine led many researchers to approach the cerebral environment as a series of compartments and lumped parameters. More recently, the need for spatially informed models has become more apparent to capture changes within individual systems and subsystems.

Three primary types of spatial models have been developed in the literature: a) tissue deformation studies assuming pressure boundaries without including the fluid; b) flow studies treating the tissue as a (possibly porous) rigid body; and, c) flow studies treating the tissue as a (possibly porous) deformable body. Given the right assumptions for model parameters, the first two categories produce results that are in good agreement with clinical observations, but only the final category is capable of capturing the underlying physics of the environment required for complete understanding.

The current state of knowledge about hydrocephalus, brain dynamics more generally and the constitutive requirements, suggests that poroelastic theory provides a suitable framework to garner a better understanding of the disease. This mathematical framework combines Hooke's law for elastic bodies, Darcy's law for flow through a porous medium and the Naviér-Stokes equations for fluid flow. Most recent studies using poroelastic theory are based on simplified cylindrically or spherically symmetric geometries; however, a significant drawback is the conflation of CSF and cerebral blood into a common network. While multiple-network poroelastic models have long been applied to soil mechanics, where the soil and rock contained both storage and transport porosities, poroelasticity applied to the brain has

been confined to a single fluid network.

In this research we propose a novel application of Multiple-Network Poroelastic Theory (MPET) to investigate water transport in the cerebral environment. Specifically, MPET is modified to allow a detailed investigation of spatio-temporal transport of fluid between the cerebral blood, cerebrospinal fluid (CSF) and brain parenchyma across multiple scales. This framework thus allows an exploration of hypotheses defining the initiation and progression of both acute and chronic hydrocephalus.

In acute hydrocephalus there are several possible locations for CSF flow obstruction to occur; the most common of which is the aqueduct of Sylvius, referred to from here on as the cerebral aqueduct. For this phase of the study, we simplify the MPET model to a single fluid network and couple the system to a multi-dimensional representation of the aqueduct. In doing so, it is possible to investigate the role of pulsations in CSF flow, assess the potential for small intra-cranial pressure gradients to lead to ventricular dilation and determine the impact of the magnitude of the stenosis on ventricular pressure and dilation.

The findings demonstrate clearly the importance that the fluidic-poroelastic coupling plays: ventricular enlargement is significantly smaller with local (more realistic) stenosis patterns and almost all of the observable pressure drop occurs across the stenosis.

Unlike acute hydrocephalus, chronic hydrocephalus develops with a paradoxical absence of blockage of the ventricular system; it is increasingly apparent that it cannot be considered as a simple mechanical disruption of the flow of CSF. It is distinctly possible that the ventriculomegaly observed in clinical situations is the result of biological changes within the cerebral environment. The single compartment model is incapable of capturing these biological changes.

The introduction of a four-network MPET model allows the separation of cerebral fluid into many compartments, such as the arterial, arteriole, capillary and venous blood networks, and the extra-cellular and ventricular networks containing CSF. In doing so, many more locations for biological change within the environment can be investigated.

The lack of relevant experimental data meant that an extensive parametric search of the one-dimensional MPET model was conducted to find appropriate values for the various mechanical constants. Parameters related to physiological mechanisms – including a breakdown in the blood-brain and blood-CSF barriers and a changes in the mechanical properties of the cerebral vascular networks – were

identified as potential locations for physiological mechanisms for NPH.

Results show that a breakdown in the transport mechanisms between the arterial vascular network and interstitial space within the parenchyma may be a cause of accumulation of CSF in the ventricles. Specifically, there must be an increase in the compliance of the arteriole/capillary network, which may combine with a breakdown in the blood-CSF barrier to allow an increased flow from the arteriole/capillary blood to the CSF.

In concluding, the novelty of the MPET system is both a tremendous strength and an inherent weakness. For the first time, we are able to produce clinically relevant ventriculomegaly in the absence of any visible CSF flow obstruction; however, this is completed with a notable absence of experimental validation of the material parameters.

Cerebral diseases are recognized as pivotal in healthcare; they relate to a whole host of unmet clinical needs. We are convinced that basic understanding of fluid transport is the most promising way to address these needs meaningfully, in a clinical setting. We hope that publishing this study will prove useful to guide experimental exploration in areas that warrant further investigation and validation.

Statement of Originality

I hereby declare that this submission is my own work and to the best of my knowledge it contains no materials previously published or written by another person, or substantial proportions of material which have been accepted for the award of any other degree or diploma at the University of Oxford or any other educational institution, except where due acknowledgement is made in the thesis.

Any contribution made to the research by others, with whom I have worked at the University of Oxford or elsewhere, is explicitly acknowledged in the thesis.

I also declare that the intellectual content of this thesis is the product of my own work, except to the extent that assistance from others in the project's design and conception or in style, presentation and linguistic expression is acknowledged.

Brett Tully.
September 16, 2010.

Acknowledgements

I would first of all like to thank Professor Yiannis Ventikos, without whom I would not have had the chance to enjoy such an amazing experience in Oxford. His instrumental role in securing my position at the University and his supervision will not be forgotten. Furthermore, my colleagues in the Fluidics and Biocomplexity Group made going to the lab each day all the more enjoyable.

Various people have provided intellectual support throughout this work. Thank you to: Prof. James Byrne and Dr. Jaladhar Neelavalli for providing the patient-specific data; Dr. Andy Wathen for his help with understanding FEM; Jon Krohn and John Feddersen for their useful statistics tips; Tim Bowker and Dr Vernon Bailey for their support with the computational resources; and finally Dr Eric Knight for seeing technology through a different lens.

I would like to thank two mentors from my schooling and undergraduate studies: Dr Atit Bhargava, formerly of The Southport School, and Rev Prof John Morgan, Warden of St. John's College University of Queensland.

Of course, studying on the other side of the world can be difficult at times, so I finish by thanking my family back in Australia for their incredible love and support.

This work was supported by the Oxford University Clarendon Fund and a British Overseas Research Students (ORS) Award. I kindly acknowledge: Magdalen College and the Oxford University Department of Engineering Science for their additional financial support; the ESI Group (Paris, France) and Dr. M. Megahed for making the CFD-ACE+ platform available to us; and the Engineering and Physical Sciences Research Council for providing the computational resources to conduct this study (infrastructure grant EP/F033710/1).

Dissemination

Peer-Reviewed Journal Papers

Tully, B., & Ventikos, Y. (2011). *Cerebral Water Transport Using Multiple-Network Poroelastic Theory: Application to Normal Pressure Hydrocephalus.* Journal of Fluid Mechanics, 667, pp 188-215 doi:10.1017/S0022112010004428

Tully, B., & Ventikos, Y. (2011). *Patient-Specific Normal Pressure Hydrocephalus Using Multiple-Network Poroelastic Theory.* Nature Neuroscience (in review).

Tully, B., & Ventikos, Y. (2009). *Coupling Poroelasticity and CFD for Cerebrospinal Fluid Hydrodynamics.* IEEE Transactions on Biomedical Engineering, 56(6), 1644-1651.

Peer-Reviewed Conference Proceedings

Tully, B., Byrne, J., & Ventikos, Y. (2010). *Is Normal Pressure Hydrocephalus More Than a Mechanical Disruption to CSF Flow?* Proceedings of the 32nd Annual International Conference of the IEEE Engineering in Medicine and Biology Society. September 2010.

Tully, B., & Ventikos, Y. (2010). *Modelling Normal Pressure Hydrocephalus as a 'Two-Hit' Disease Using Multiple-Network Poroelastic Theory.* Proceedings of the ASME 2010 Summer Bioengineering Conference. June 2010. (Finalist for student paper award)

Orlowski, P.$^{+}$, Tully, B.$^{+}$, & Ventikos, Y. (2010). *Porous and poroelastic methods for cerebral disease diagnosis and intervention design.* Proceedings of the 3rd International Conference on Porous Media and its Applications in Science and Engineering. ($^{+}$ equal contribution).

Tully, B., & Ventikos, Y. (2009). *Water regulation in the cerebral environment.* Proceedings of the 5th UKRI PG Conference in Biomedical Engineering and Medical Physics.

Conference Presentations and Posters

Transport of Fluid Between Blood and Brain, Bioengingeering '10, Nottingham, September 2010.

Multiple-Network Poroelasticity Applied to Cerebral Hydrodynamics, Bioengingeering '09, Oxford, September 2009.

Multiple-Network Poroelastic Theory and Cerebral Hydrodynamics, PG-BioMed '09. Oxford, July 2009. (Best poster award)

Coupling Poroelasticity and CFD for Cerebrospinal Fluid Hydrodynamics, Bioengineering '08. Imperial College, London, September 2008.

CONTENTS

LIST OF FIGURES

LIST OF TABLES

ACRONYMS

MPET	Multiple network poroelastic theory
SPET	Single network poroelastic theory
CSF	Cerebrospinal fluid
ECF	Extra-cellular fluid
ICP	Intra-cranial pressure
CBV	Cerebral blood volume
CBF	Cerebral blood flow
MRI	Magnetic resonance imaging
CT	Computerized tomography scan
WHO	World Health Organisation
AD	Alzheimer's disease
CM	Chiari malformations
PD	Parkinson's disease
TBI	Traumatic brain injury
SVS	Slit-ventricle syndrome
NPH	Normal pressure hydrocephalus
DWMI	Deep white matter ischaemia
TV	Third ventriculostomy
CFD	Computational fluid dynamics
PDE	Partial differential equation
FEM	Finite element analysis
FVM	Finite volume method
UDS	User-defined subroutine
SGE	Sun grid engine
BBB	Blood-brain barrier
BCB	Blood-CSF barrier
CGS	Conjugate gradient square method
AMG	Algebraic multigrid method
SIMPLEC	Semi-implicit method for pressure-linked equations – consistent

CHAPTER 1

MOTIVATION, PHYSIOLOGY & DISEASE

As we move into the twenty-first century and an era of ageing populations, medical experts and policy makers are increasingly aware that the efficacy and economy of treatment is strongly linked with personalization of treatment. The creation of advanced computational technology may prove to be crucial to achieving patient-specific health-care provision. This chapter will outline the motivation for this research, introduce the cerebral environment and outline what can ultimately be described as Dementia's Elusive Cure.

Across the globe, people are living longer and in most regions, quality of life is (slowly, but surely) improving. At face value, this is a positive reflection on the efforts focused on achieving these goals. However, a scan of academic journals reveals increasing concern about the correlation of population demographics and the demand on global healthcare services.

Performing a search on **Google Scholar** with the terms *ageing population* and *healthcare* retrieves over 50,000 results. Some argue that the ageing population will not increase the per capita cost-burden of healthcare; others argue that it will. However, neither side disputes that as the number of citizens living beyond the age of sixty increases, diseases of old age will continue to drive up the demand for healthcare and have a huge impact on the quality of life of millions of people world-wide.

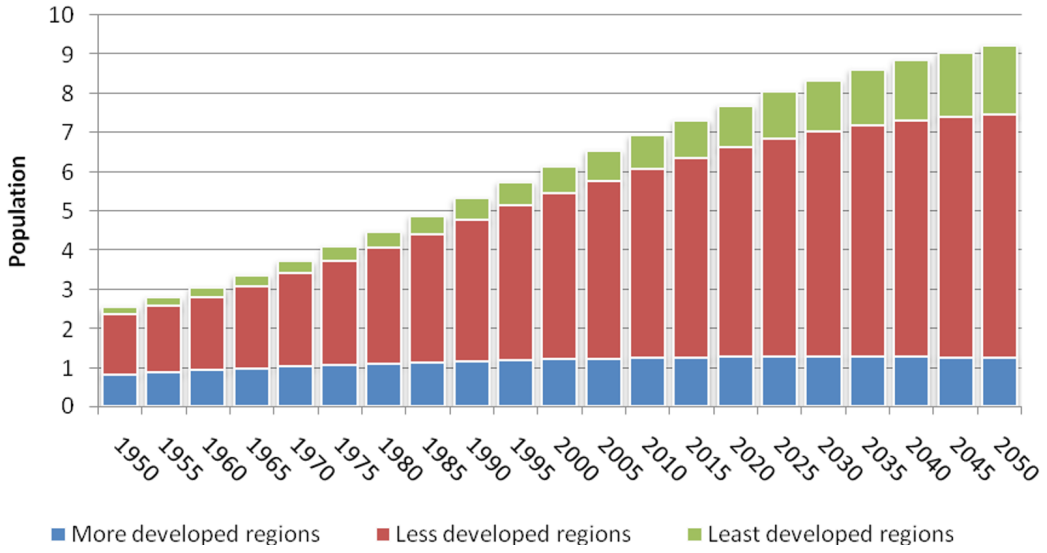

Figure 1.1: Population prediction (in billions) for the century starting from 1950. While the global population growth is due to slow significantly by 2050, the predominate growth is clearly seen in the less developed regions where poverty and unemployment are endemic. Data source: Population Division of the Department of Economic and Social Affairs of the United Nations (2005).

1.1 CHANGING GLOBAL DEMOGRAPHICS

We are in the midst of profound changes in population demographics: by 2050, the most populous age group will no longer be those under fifteen years old, but those over sixty (Raleigh, 1999). During the past two centuries, global fertility and mortality rates have continually fallen, yet the population growth rate has soared. It took until 1800 AD to reach a global population of one billion, the next four were added in just two centuries and the last billion accumulated in just twelve years. Growth rates are diminishing and it is expected that the global population will have stabilized around nine billion by 2050; with most of this new growth occurring in the less developed regions of the world (see Figure 1.1).

While vast gender and geographical inequalities will persist, all regions will experience the shift to an older population and a flattening of the population pyramid (see Figure 1.2). The number of elderly citizens (those over 60 years) will increase four-fold – meaning a doubling of their total percentage of the population (from 9% to 21%). Significantly, 38.5% of the world's elderly population will reside in India and China; and more than 7% of the Chinese population will be very elderly (aged over

Figure 1.2: The global shift in population demographics is predicted to result in a flattening of the population pyramid. While the most populous age group is currently those under 15 years of age, by 2050 this will change to those aged over 60 years. While vast gender and geographical inequalities will persist, all regions of the globe will experience an ageing of the population with the number of elderly (those aged over 60 years) increasing four-fold by 2050. Significantly, 38.5% of the elderly population will reside in India or China. Data source: Population Division of the Department of Economic and Social Affairs of the United Nations (2005).

80 years) (Population Division of the Department of Economic and Social Affairs of the United Nations, 2005).

1.1.1 The Importance of Age

According to the World Health Organization (WHO), this transition of population demographics is leading to an unprecedented epidemiological transition that carries a double burden of disease (Boutayeb, 2006; Raleigh, 1999; World Health Organization, 1999).

There is a growing affliction of non-communicable diseases in both industrialized and developing nations: cardiovascular disease, cancer, neurological condi-

tions and injury have become the leading causes of disability and premature death. The ageing Chinese population is expected to witness a tripling of cardiovascular related deaths during the period of 2000-2040 (Chatterji et al., 2008). The second burden is associated with the continuing challenge of communicable diseases that will remain a prevalent cause of morbidity and mortality in the developing world.

1.1.2 Health Economics

In addition to the population transition, the twenty-first century will also witness a reallocation of economic power. By 2050, the Gross Domestic Product (GDP) of the BRIC (Brazil, Russia, India and China) economies may exceed that of the now defunct G6 (France, Germany, Italy, Japan, the United Kingdom and the United States) in US dollar terms (Wilson and Purushothaman, 2003). At that time, the list of the world's largest economies is expected to look quite different from today – with China heading the list and India third. In an added complexity, the largest economies (in terms of GDP) may no longer be the richest (by income per capita), with China's per capita income approaching the current levels experienced in the developed world (about US$30,000) (Luard, 2004).

Combined with the shift to an older population, these economic developments give credence to the prediction that the Chinese and Indian consumer-class will increase ten-fold by 2025 (Farrell and Beinhocker, 2007). Along with changing diets influencing global food prices, disposable income driving up demand for consumer goods and infrastructure needs energising commodity markets, the consumer-class has a greater expectation of the level of healthcare provided, and importantly, its success rate. Private healthcare spending (as a percentage of consumer spending) in India is forecast to double to 13% by 2025 due to dissatisfaction with public-sector provided services and the consumer-class possessing a willingness to spend disposable income on private providers (Farrell and Beinhocker, 2007).

1.1.3 Technology and the Provision of Healthcare

The twenty-first century developments in population and economic demographics appear to have a two-fold impact on the provision of healthcare services. There may be more users (and proportionally fewer providers) of healthcare due to the popu-

lation shift; and the increase in affluence of this population may lead to a greater expectation of speed, accuracy, and ultimately success, of treatment.

In order to meet these needs, medical experts and policy makers are increasingly aware that the efficacy and economy of treatment is strongly linked with the personalization of treatment. Technology-based healthcare offers solutions that show great potential for the future, and particularly the use of patient-specific technologies that underline the need for efficacy, not just effectiveness. To continue on a service as usual trajectory will result in the sector being weighed down by increased expectations and demand.

Utilizing technological advances, such as those provided by engineering and numerical analysis, will allow the important step-change to the way we approach pathology, physiology and ultimately healthcare in general. Biological systems can no longer be regarded as isolated modules and a multi-disciplinary, multi-scale approach is necessary to achieve predictive clinical information. Within this paradigm, the importance of the brain and the impact of connected unmet clinical needs make the cerebral environment particularly worthy of investigation through modelling technologies.

1.2 Cerebral Anatomy & Physiology

The brain and spinal cord are delicate semi-solid structures that require a great deal of protection and support (Carpenter, 1991). Together, they form a remarkably complex organ that is very sensitive to changes in its environment and contains three distinct systems within the rigid skull: the brain tissue (parenchyma), blood vessels and spaces filled with CSF.

Within the skull there are layers of tissue, known as the meninges, that cover the brain and spinal cord and separate the three systems: the dura mater, the arachnoid mater and the pia mater (see Figure 1.3). The pia mater lies on the surface of the brain, the dura mater is the outermost covering of the brain and generally follows the contour of the skull and vertebral canal, and the arachnoid mater is pressed against the dura mater by the CSF pressure. Also of interest to CSF flow paths is the sub-arachnoid space - the space between the arachnoid mater and the pia mater.

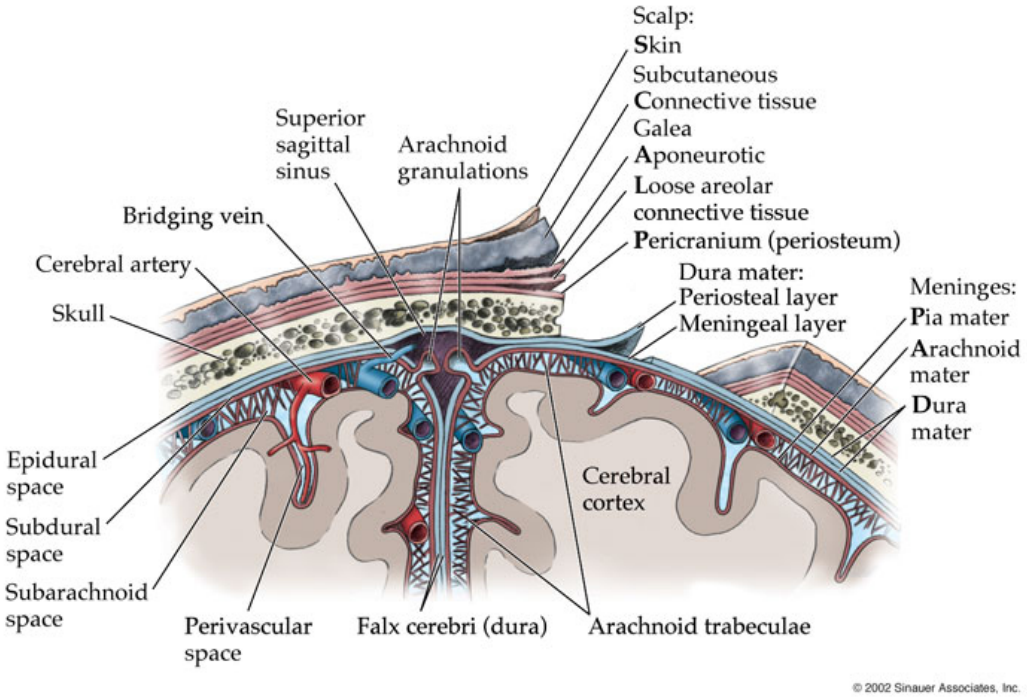

Figure 1.3: Macro-scale biological structures in the human brain (Blumenfeld, 2002)

The neonatal development of the cerebral environment leads to a distinct series of fluid pathways through the tissue; the brain "folds" over itself creating unique structures in its core, called ventricles (Brodal, 2004; Carpenter, 1991). It is within the ventricles that CSF is produced, while irregularities in ventricular size is a clear indicator of the neurological condition hydrocephalus (see §1.4).

1.2.1 Ventricular Structure

Within the brain, there are four ventricles: a pair of lateral ventricles, the third ventricle and the fourth ventricle (as seen in Figure 1.4). The lateral ventricles extend from a central part in the parietal lobe out into horns in each of the other three lobes: an anterior (frontal) horn, a posterior (occipital) horn and an inferior (temporal) horn extending downward and anteriorly into the temporal lobe. The central part of the ventricle lies just above the thalamus.

The third ventricle is a thin slit-like space between the two thalami and it communicates with the lateral ventricles through the inter-ventricular foramen (of

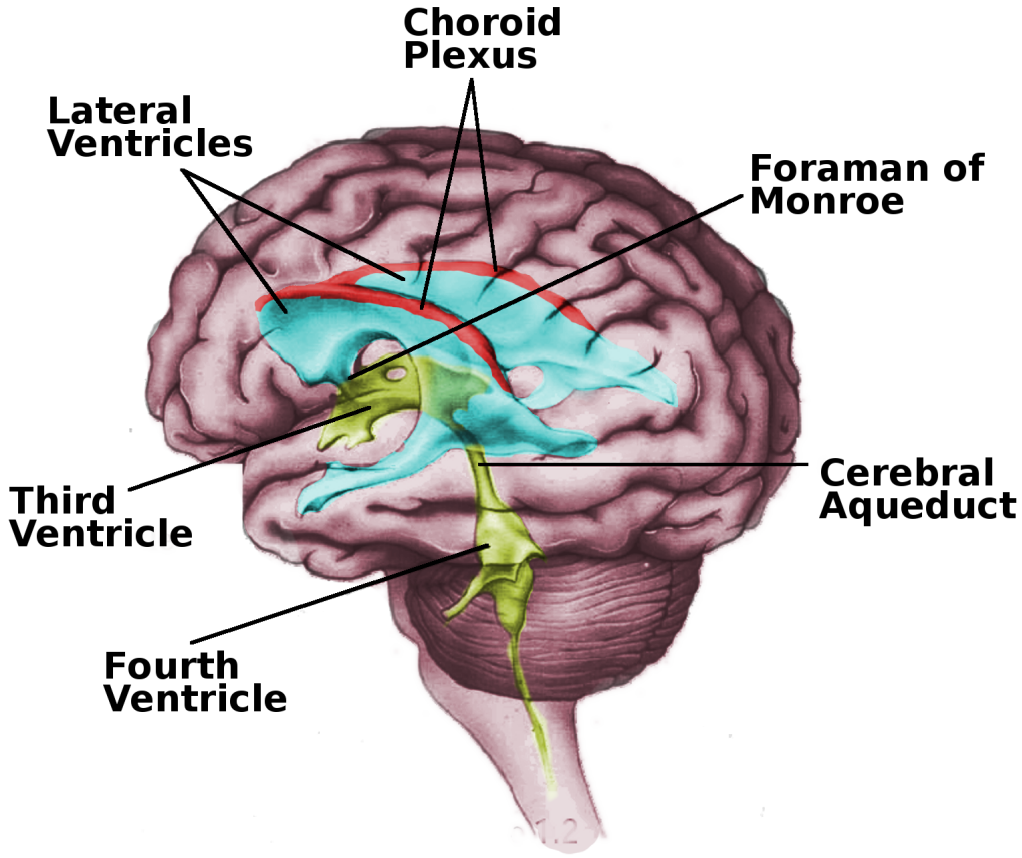

Figure 1.4: The ventricular system of the human brain showing the location of the cerebral ventricles (Cheng, 2006).

Monro). The third and fourth ventricles are connected via the narrow cerebral aqueduct with the fourth ventricle taking the form of a much smaller tent-like space with the apex projecting into the cerebellum. Finally, the fourth ventricle connects to the sub-arachnoid space through three openings in its roof: one in the mid-line posteriorly, the foramen of Magendie, and two laterally, the lateral recesses or foramina of Luschka. All of the ventricles and the sub-arachnoid space are filled with CSF; a clear, watery fluid.

1.2.2 Cerebrospinal Fluid

Cerebrospinal fluid is a clear, watery fluid of which around 70% is produced within the ventricles by the choroid plexus. The remaining 30% is likely formed through mixing with the extracellular fluid (ECF) – with which the CSF is in direct contact –

that results from the ongoing metabolic processes in the parenchyma (Brodal, 2004; Carpenter, 1991; Tisell et al., 2004). The speed of mixing and diffusion of the CSF and ECF is governed by the brain cell size, shape and arrangement (Gevertz and Torquato, 2008) and means that in practice, it is not possible to distinguish between the two (Greitz, 2004; Sato, 1994).

CSF acts as both a mechanical and chemical buffer to the brain and turnover is required to help clear toxic molecules from the interstitial-fluid space of the brain to the bloodstream (Silverberg, 2003). A brain weighing 1500g in air, weighs only 50g when immersed in CSF, meaning that the vessels and nerves of the central nervous system are under less traction (Carpenter, 1991). Furthermore, the damping properties of the fluid mean that the effect of blows to skull are lessened, protecting the all important tissue.

CSF contains small amounts of protein, glucose and potassium, and relatively large amounts of sodium chloride. There are no substances found in CSF that cannot be found in blood plasma (Carpenter, 1991) and it is possible that within the choroid plexus, the movement of ions creates an osmotic gradient that drives the secretion of H_2O (Brodal, 2004). The concentration of some ions is similar between CSF and blood, the level of glucose is reduced while the major difference is the lack of proteins in the CSF (less than 0.5% of the plasma concentration).

In the healthy brain, CSF flows freely through the open channels and, in addition, studies show evidence of fluid transport through the brain parenchyma (Hakim and Adams, 1965; Hakim, 1971; Hakim et al., 1976; Levine, 1999). Flow from the arterioles and capillaries to the extracellular space – about 20% of the total cerebral volume (Carpenter, 1991; Gevertz and Torquato, 2008) – is governed by pressure and osmotic gradients, while re-entry to the venous capillaries is thought to be driven by osmotic pressure only, as any major pressure gradient may collapse the capillaries and veins (Bradley et al., 2006). Furthermore, transmembrane water fluxes are controlled at a cellular level by specific water channels (aquaporins), showing that CSF exchange occurs across all spatial scales from organ level through to cellular level transport (Amiry-Moghaddam et al., 2003; Agre et al., 2004; Agre, 2006).

CSF produced in the lateral ventricles flows through the foramen of Monro into the third ventricle, then through the cerebral aqueduct and into the fourth ventricle. More fluid is added along the way by the choroid plexi in the third and fourth

ventricles.

Importantly, the brain and CSF environments are protected from the cerebral vascular compartment through tightly controlled barriers (see Figure 1.5). This responsibility is shared between the blood-brain barrier (BBB), blood-CSF barrier and brain-CSF interface. The BBB is a series of interfaces between arterial blood, CSF and neural tissue that regulates the transport of chemical substances. Tight junctions in the cells of the cerebral capillaries forming the BBB restrict the passage of solutes from the blood into the extra-cellular compartment.

The epithelium of the choroid plexus represents the barrier between the blood and the CSF (the blood-CSF barrier) such that many substances that can leave the capillaries of the choroid plexus cannot enter the CSF. Similarly, the brain-CSF interface consists of the ependymal lining of the the ventricles, and the membranes on the external surface of the brain. Along with the blood-brain barrier, these two barriers protect the highly sensitive neurons from any changes in composition of their environment and prevent the unwanted exchange of solutes between the CSF and the parenchyma.

Once the CSF leaves the ventricular system it enters the sub-arachnoid space (more specifically, the cisterna magna) through the foramen of Magendie and the foramina of Luschka and spreads out over the entire brain and spinal cord. Finally, it is believed that large molecular-weight substances can pass from the CSF into the venous blood via the arachnoid granulations in the venous sinuses.

The fluid pressure in the cerebral environment is governed by the Monro-Kellie doctrine that confines the total volume of tissue, blood and CSF to the (fixed in adult subjects) volume of the skull (Williams, 2008) (see Chapter 2). The pulsatile nature of CSF flow through the open channels – confirmed *in vivo* by Magnetic Resonance Imaging (MRI) (Egnor et al., 2001) – can be related to the change in cerebral blood volume through the heartbeat (Stoquart-ElSankari et al., 2009).

Within this restricted cranial volume, around 500 mL of CSF is produced each day. The total volume in the ventricles and sub-arachnoid space is 130-140 mL (approximately 25 mL is in the ventricles) and approximately 75 mL surrounds the spinal cord (Carpenter, 1991). Thus, it can be said that cranial CSF is renewed several times each day and an effective drainage system must exist.

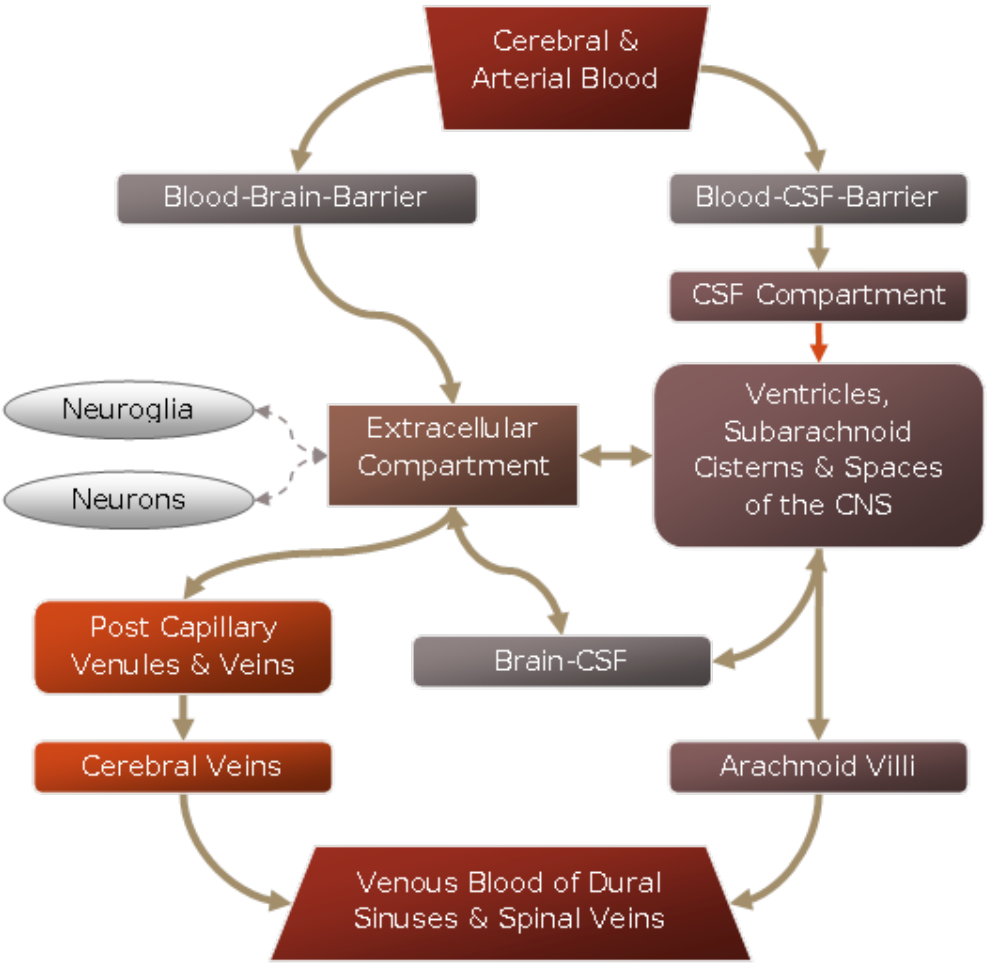

Figure 1.5: Schematic of the cerebral environment showing the potential barriers through which water must pass if it is to play a role in the CSF system. Importantly, this diagram shows that not only does water move through the traditional CSF route, but furthermore, a role is assumed in the extra-cellular compartment of the parenchyma. These two routes are in constant communication through the walls of the ventricular system and the brain-CSF interface (modified from Carpenter (1991)).

1.3 Diseases of the Cerebral Environment

Disruption to the dynamics of CSF is of importance in many structural neurological conditions: from the rare case of symptomatic flow disturbance indirectly caused by malignant prostate tumour (Winkler et al., 2007) to the far more common and often visible traumatic brain injury or the more subtle cases of dementia (Silverberg, 2003). Understanding the regulation of water and ion transport, which plays a role across all of the spatial scales from microscopic cellular levels to the macroscopic ventricles, is central to providing useful information about these diseases.

1.3.1 Traumatic Brain Injury

Traumatic brain injury (TBI) is a non-degenerative, non-congenital affliction of the brain. Its source stems from an external mechanical force and possibly leads to permanent, or temporary, impairment of cognitive, physical and psychological functions, and an associated diminished or altered state of consciousness (Steyerberg et al., 2008; Niedzwecki et al., 2008).

TBI may manifest itself by any one of the following:

- A period of loss of consciousness
- A loss of memory for events immediately before or after the incident.
- An alteration in mental state at the time of the accident
- Possibly transient, focal neurologic deficits

TBI is generally classed as severe, moderate, or mild using the Glasgow Coma Scale and can manifest clinically from concussion to coma and death (Dawodu, 2009). Injuries are often obvious when viewed using non-invasive brain imaging (for example, see Figure 1.6) and are usually divided into two sub-categories:

- primary injury, occurring at the moment of trauma, such as impact, impulsive or static/quasi-static loading resulting in focal, or diffuse injury; and,

- secondary injury, which occurs immediately after the trauma and produces effects that may continue for a long time. For example, conditions associated with increased intra-cranial pressure (ICP) such as cerebral oedema, hydrocephalus or brain herniation.

1.3.1.1 Epidemiology

Inconsistency in the definition of TBI makes it difficult to report an accurate epidemiology of the disease. For example, many patients with mild TBI may not present to the hospital for treatment, or proper records may not be collected from brief visits to the Emergency Department.

That being said the incidence of TBI is increasing globally, largely due to an increase in motor vehicle use in low- and middle-income countries (Maas 2008). In contrast, safety measures introduced in high-income countries has seen proportionally fewer cases of TBI associated with motor vehicle accidents (MVAs).

In the European Union the yearly aggregate incidence of TBI hospitalizations and fatalities is estimated at 235 per 100,000 (Maas et al., 2008), while the yearly incidence is estimated at 503.1 per 100,000 people in the United States (Bazarian et al., 2005). Of the total 500,000 hospitalized cases, 52,000 deaths result from TBI in the US (D'Ambrosio and Perucca, 2004; Dawodu, 2009); the mortality rate for severe TBI is high at 33% while falling to the much lower rate of 2.5% for moderate TBI. In total, it is estimated that between 2.5 and 6.5 million Americans live with TBI-related disabilities (Dawodu, 2009). Importantly, injury is the leading cause of death among Americans younger than 45 years, and TBI is the major cause of death related to injury.

MVAs are the leading cause of TBI in the United States accounting for more than 50% of cases, while coming third to falls and assaults in the United Kingdom (Dawodu, 2009). Falls and firearms are the next highest causes, the latter being the leading cause among individuals aged 25-34 years.

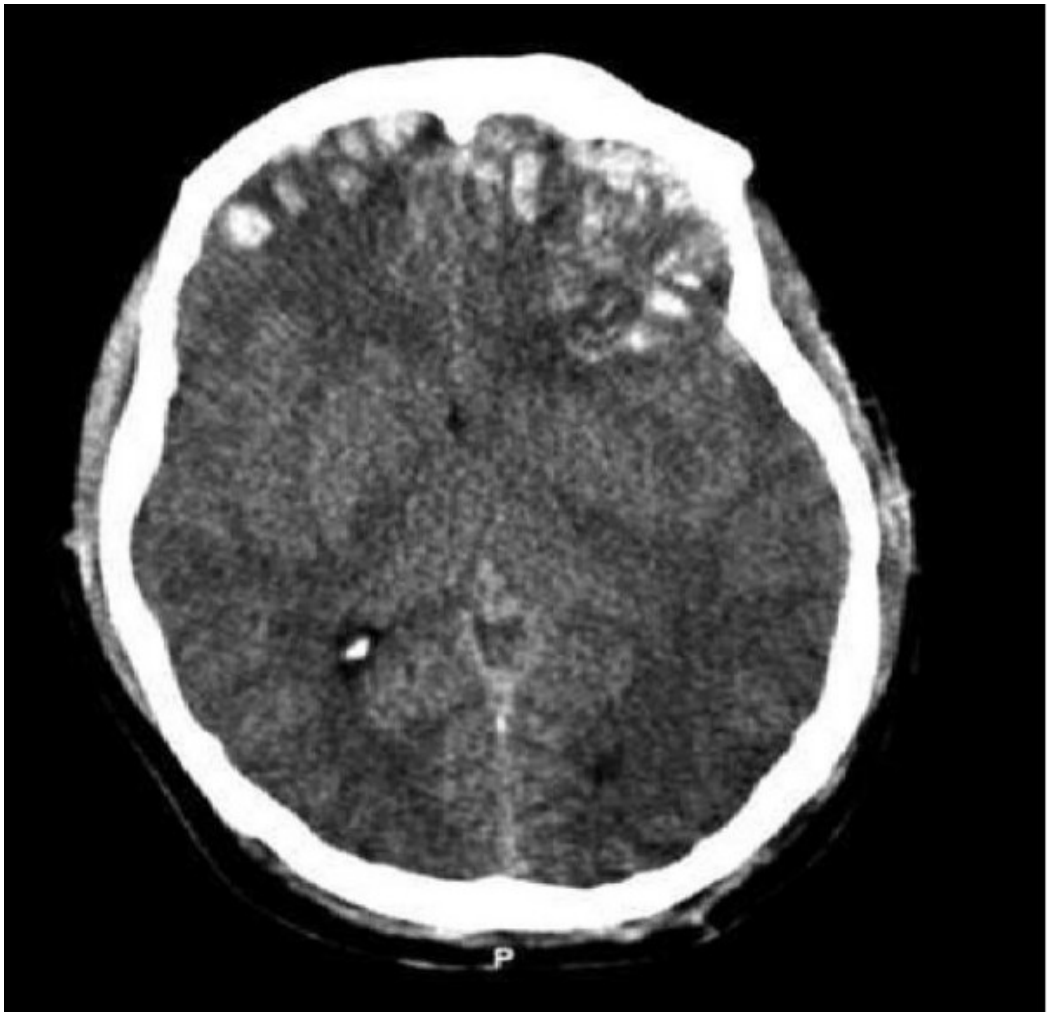

Figure 1.6: A Preoperative CT scan of a patient with a Glasgow Coma Scale of 14 (E4, M5, V1). The 35 year-old male patient suffered a traumatic brain injury after falling approximately ten feet at a construction site, reportedly striking his head on the ground. CT imaging revealed a sagittally oriented skull fracture extending from the vertex to the foramen magnum as well as a transverse parietal and temporal bone fracture. Approximately 15 hours after admission, the patient deteriorated over several minutes. His mental status declined, first losing the ability to follow commands and rapidly becoming unresponsive with fixed and dilated pupils. The repeat CT scan eight hours later revealed new infarcts in the left thalamus and right occipital lobe (Rehman et al., 2008).

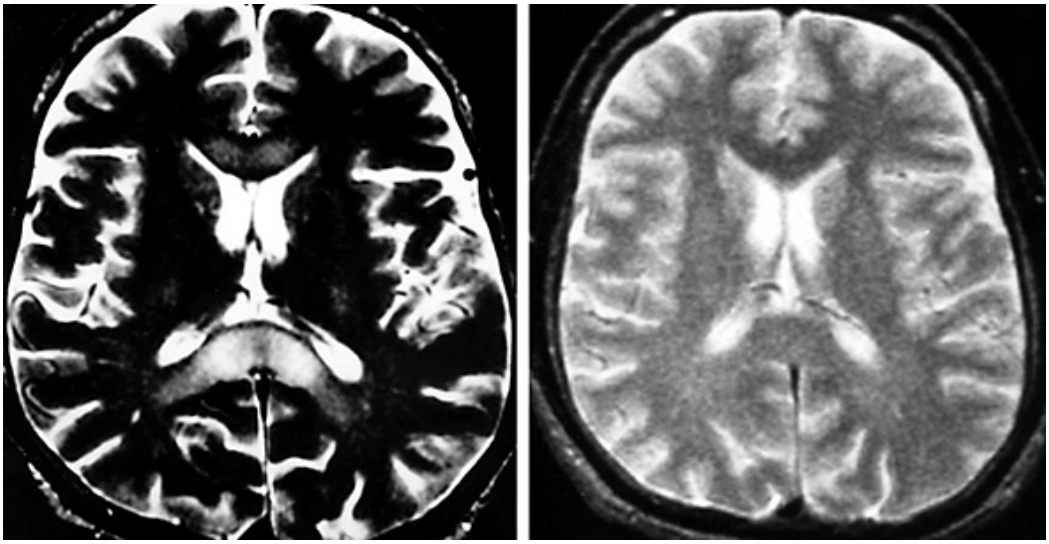

Figure 1.7: MRI scans of a patient suffering from high-altitude cerebral oedema: Left, Axial T2-weighted magnetic resonance image of patient 9 demonstrating high signal in splenium and mild increased signal in centrum semiovale. Right, Axial T2-weighted magnetic resonance image of the same patient demonstrating complete resolution of abnormal signals 11 months later (Hackett et al., 1998).

1.3.1.2 Treatment

It is important that emergency treatment be administered in the so-called 'golden hour' following the injury. In the acute phase, much of the treatment is focused on stabilization of the patient and preventing further injury as there is little to be done at this stage to reverse the initial injury. The primary treatment phase is rehabilitation in the chronic stages of the condition. Clinical guidelines have been proposed with the aim of guiding decisions on TBI treatment in this phase (Maas et al., 2008).

1.3.2 Cerebral Oedema

Cerebral oedema is the excess accumulation of water in the intra- and/or extracellular spaces of the brain (Jha, 2003). Its pathophysiology is complex at the cellular level. Damaged cells swell, injured blood vessels leak and blocked absorption pathways force fluid to enter the brain tissue (see Figure 1.7).

Cerebral oedema can be strictly classified into four categories – vasogenic, cellular (cytotoxic), osmotic and interstitial cerebral oedema (Qureshi and Suarez, 2000)

– however, in practice it is rarely possible to separate the condition into a distinct category.

- Vasogenic cerebral oedema: refers to the influx of fluid and solutes into the brain due to a breakdown of the tight junctions of the endothelial cells that make up the blood-brain barrier (BBB). This allows normally excluded intravascular proteins and fluid to penetrate into the cerebral parenchyma and extracellular space. It is the most common type of brain oedema and primarily affects the white matter.
- Cellular cerebral oedema: refers to cellular swelling with an intact BBB. It often presents in conjunction with conditions such as traumatic brain injury and hypoxia (Jha, 2003). Cytotoxic oedema is caused by swelling of glia, neurons, endothelial cells and onset is within minutes of injury.
- Osmotic cerebral oedema: occurs when the blood plasma is diluted, for example, by an excess uptake of water, haemodialysis, or a rapid reduction of blood glucose. This causes the brain osmolality to exceed the serum osmolality creating an abnormal pressure gradient down which water will flow into the parenchyma.
- Interstitial cerebral oedema: is commonly associated with obstructive hydrocephalus when the outflow of CSF is reduced, intra-ventricular pressure increases, and the CSF-brain barrier is ruptured. A resulting trans-ependymal flow is established, permitting CSF to penetrate the parenchyma and spread in the extracellular space of the white matter. The primary difference between interstitial and vasogenic oedema is that fluid in the former is almost devoid of protein.

The consequence of cerebral oedema are best explained through the Monro-Kellie doctrine, which states the volumetric sum of brain parenchyma, cerebral blood and CSF must remain confined due to the rigid container of the skull (in adulthood). Hence, any increase in one component must result in a decrease of one, or both, of the other components. Hence, if there is excessive water, as in oedema, there is a resulting compression of brain tissue and/or a decrease in cerebral blood volume. As coping mechanisms begin to fail the ICP rises, eventually reaching a

level that produces local ischaemia; until this point, cerebral oedema will not produce clinical neurological abnormalities (Jha, 2003).

1.3.2.1 Epidemiology

Cerebral oedema tends to be a resulting pathology of other injuries and as such, general epidemiological data is hard to come by. A key example is that 5-10% of stroke patients develop symptomatic cerebral oedema (Jha, 2003).

1.3.2.2 Treatment

Recent developments in understanding the mechanisms of cerebral oedema have not been reflected in a change of treatment methodology (Jha, 2003).

The most popular treatment method remains osmotherapy as it reflects a rapid and relatively effective means of decreasing water in the parenchyma. Osmotic therapy is designed to reverse the osmotic gradient between the plasma and tissue, hence drawing water out and reducing the blood viscosity. Consequently, the ICP is decreased and cerebral blood flow is increased.

Alternative therapies include the use of diuretics to prolong the osmotic effect of osmotherapy, corticosteroids and controlled hyperventilation. These treatments are used sparingly; in some instances of corticosteroid use symptoms can be worsened or, in the case of hyperventilation, new pathologies may be introduced (Jha, 2003).

1.3.3 Chronic Ischaemic Dementia

Chronic ischaemic dementia (see Figure 1.8), also known as multi-infarct dementia, and referred to here simply as vascular dementia is a common cause of dementia in the elderly. In general, it is caused by multiple major or minor strokes, or disruption of blood flow to the brain that leads to damaged brain tissue. Some of these strokes are asymptomatic and are referred to as 'silent strokes' that are often unknown to the patient. Over time, the damage accumulates, more small vessels become blocked and the patient become symptomatic (NINDS, 2010b). Individuals with vascular

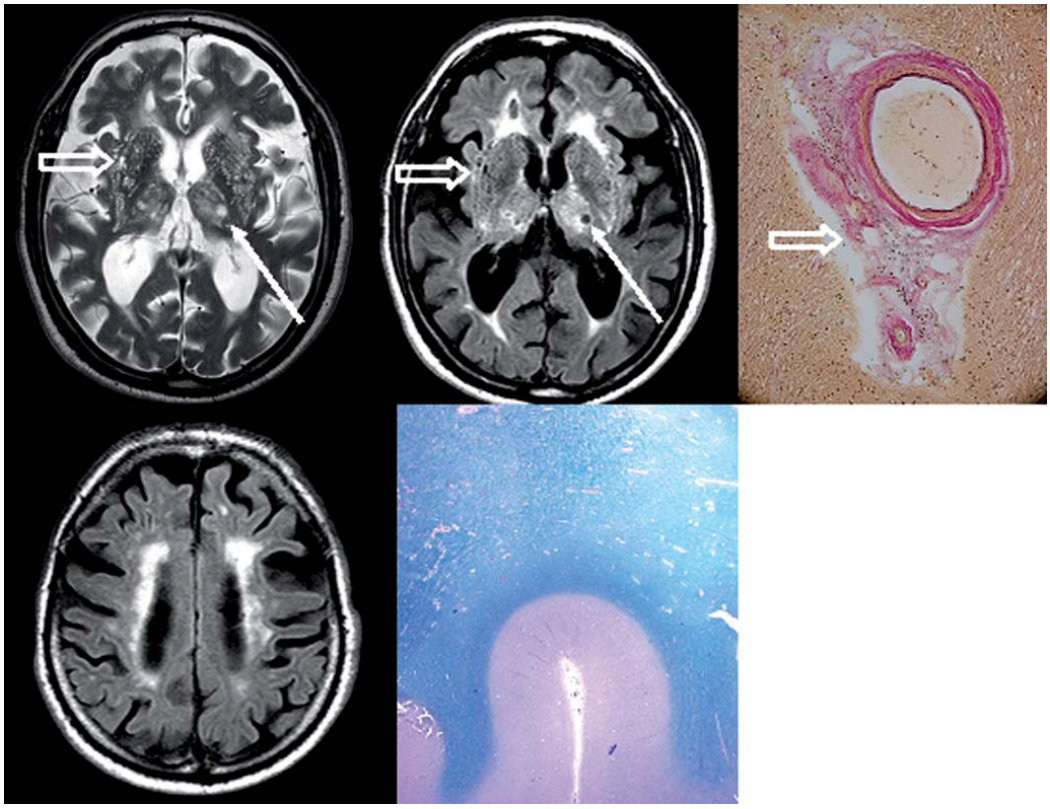

Figure 1.8: MRI of an 81-year-old mildly demented man. Small lacunar infarct (a, b: arrow), dilated perivascular (Virchow- Robin's) spaces (a: hollow arrow), both surrounded by hyperintense brain substance. Pathologically, lipoid material is found in a dilated perivascular space (c: Elastica van Gieson staining, hollow arrow). Confluent hyperintensity is found in the periventricular white matter (d), which appears pale on histological sections due to a loss and rarefication of myelin sheaths and axons (e: PASluxol fast blue staining) (Urbach et al., 2007).

dementia often manifest cognitive impairment and dementia, behavioural changes and mood disorder, and specific neurological symptoms (Pinkston et al., 2009).

Traditionally, vascular dementia has been characterized by sudden onset, stepwise progression and focal neurological deficits associated with the region of the brain affected. However, recent research reveals that an estimated 20% of cases of vascular dementia are characterised by an insidious onset and a steadily progressive course (Chapman et al., 2006).

Post-mortem examinations of individuals with dementia suggest that the coexistence of Alzheimer's disease and vascular dementia is not uncommon (Chapman et al., 2006). Differentiating between Alzheimer's disease and vascular dementia for

diagnostic purposes is not straightforward. Subtle differences can often be seen in the symptomatic progression and also in the metabolic pathways (Pinkston et al., 2009). In fact, it is reported that 60% to 77% of persons with presumed Alzheimer's disease also have vascular dementia (Chapman et al., 2006; Peters, 2006), and perhaps Alzheimer's is a vascular disorder in itself (de la Torre, 2002). However, in practice, these statements are extremely difficult to verify.

1.3.3.1 Epidemiology

Vascular dementia has been estimated to account for 15% to 30% of all dementias among older adults (Chapman et al., 2006). In the United States, this accounts for 2.1 million cases of vascular dementia at any one time (Pinkston et al., 2009). Lacunar infarcts – a characterising factor of subcortical ischemic vascular dementia – represent 20-30% of symptomatic strokes and thus form an important subtype of vascular cognitive impairment (Chui, 2007).

It is difficult to know the depth of the penetration of vascular ischaemia in the general population. Until recent advances in non-invasive imaging techniques the first evidence was provided by a symptomatic stroke; CT and MRI are continually discovering 'silent' vascular brain injury without a history of a corresponding clinical event (Chui, 2007).

1.3.3.2 Treatment

There is no treatment that is capable of reversing the damage done to the brain tissue. Generally, the aim of the treatment/management is to prevent further degradation of the vascular structures. Included in this approach is the administeration of anti-platelet drugs and controlling the major risk factors, such as hypertension and smoking. The best treatment for vascular dementia is prevention in early life (NINDS, 2010b).

1.3.4 Chiari Malformations

Chiari malformations (CMS) are a structural disorder of the cerebellum, the part of the brain that controls balance. CM results from a variety of causes, most often, it

is a congenital defect that is the result of structural defects that appear in the brain during foetal development – this is known as primary CM. Secondary, or acquired, CM is far less common and is the result of over-drainage of CSF from the lumbar or thoracic areas of the spine due to, for instance, injury or infection.

CM is classified by the severity of the disorder and the anatomical feature protruding into the spinal canal (NINDS, 2010a).

Type I : involves the extension of the cerebellar tonsils into the foramen magnum, without involving the brain stem. It is the most common CM and is generally asymptomatic during childhood, but often manifests with headaches and cerebellar symptoms (Kojima 2009). An example of a 44-year-old female patient with Chiari I malformation is shown in Figure 1.9.

Type II : also called classic CM or Arnold-Chiari malformation, involves the extension of both cerebellar and brain stem tissue into the foramen magnum. It is usually accompanied by paralysis below the spinal defect and hydrocephalus is often present.

Type III : is the most serious form of CM. The cerebellum and brain stem herniated through the foramen magnum and into the spinal cord. Part of the 4th ventricle may also protrude into the spinal cord.

Type IV : is a rare form of CM which involves an incomplete or underdeveloped cerebellum.

1.3.4.1 Epidemiology

In the past, it was estimated that the condition occurs in about one in every 1,000 births. However, the increased use of diagnostic imaging has shown that CM may be much more common. Complicating this estimation is the fact that some children who are born with the condition may not show symptoms until adolescence or adulthood, if at all. CMs occur more often in women than in men and Type II malformations are more prevalent in certain groups, including people of Celtic descent (NINDS, 2010a).

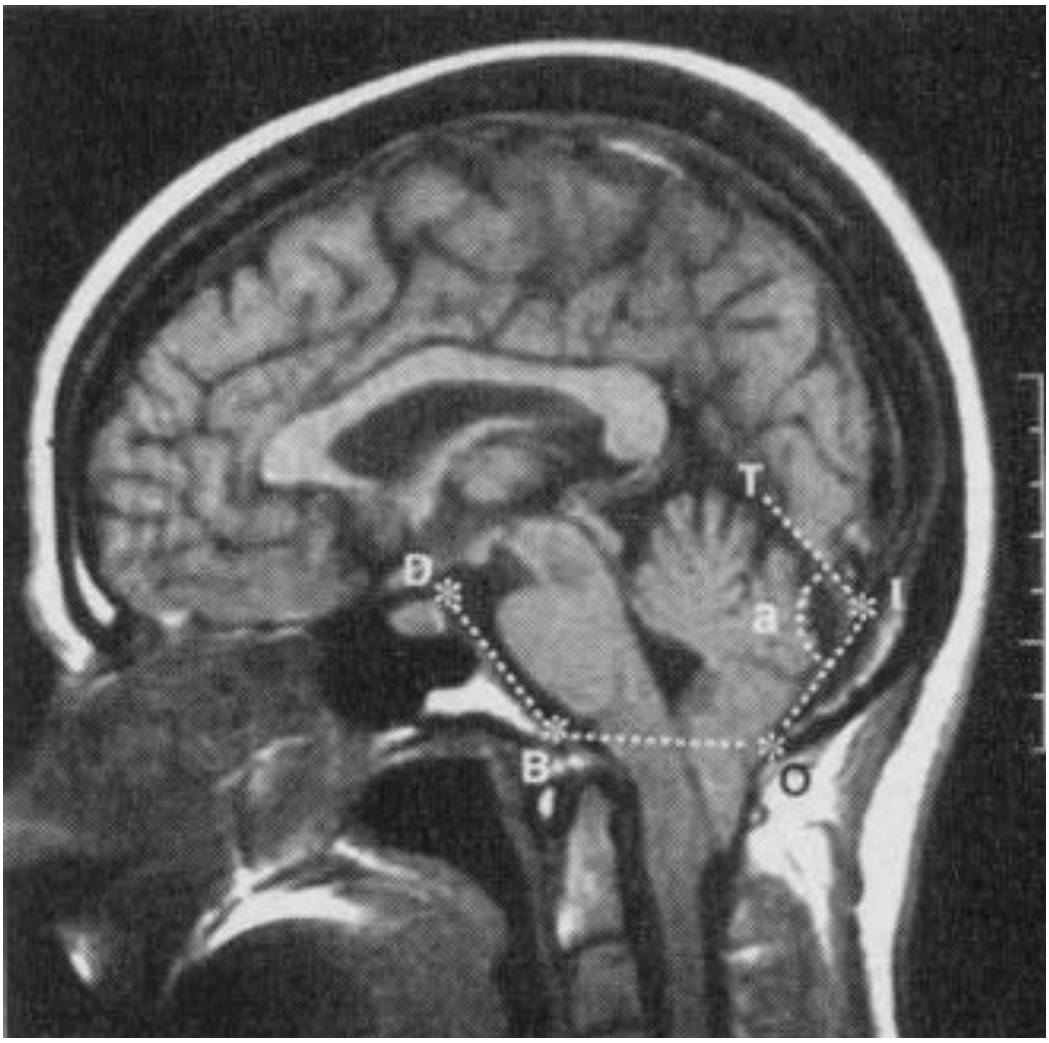

Figure 1.9: Measurements of posterior cranial fossa morphological characteristics using T1-weighted sagittal MRI scans of a 44-year-old female patient with Chiari I malformation. The length of the supraocciput (IO) was measured along a line drawn from the center of the internal occipital protuberance (I) to the opisthion (O). The length of the clivus (DB) was measured along a line drawn from the top of the dorsum sella (D) to the basion (B). The slope of the tentorium (T) was calculated by measuring the angle (a) formed by the tentorium and the supraocciput. The extent of tonsillar herniation was measured from the tips of the cerebellar tonsils to a line drawn between the basion and the opisthion. Findings in this case consisted of a short supraocciput, increased slope of the tentorium, hypoplasia of the clivus, and descent of the cerebellar tonsils 1.6 cm below the foramen magnum (Milhorat et al., 1999).

1.3.4.2 Treatment

In some cases CMs are asymptomatic while in other cases, medication may ease symptoms such as pain. However, in general, decompression surgery is the only treatment available to correct functional disturbances or halt the progression of central nervous system damage (NINDS, 2010a). Further to this surgical removal of bone from the occipital bone of the skull, a shunt may also be inserted to relieve the symptoms associated with hydrocephalus.

1.3.5 Other Cerebral Conditions

Further to the primary diseases above, Psuedotumour Cerebri, Slit Venticle Syndrom and Alzheimer's Disease may also be associated with a disturbed flow of CSF.

1.3.5.1 Psuedotumour Cerebri

Pseudotumour cerebri, also known as idiopathic intra-cranial hypertension, is a syndrome that is characterized by symptoms and signs of increased intra-cranial pressure with no increase in cerebrospinal fluid pressure and the absence of ventricular enlargement and intra-cranial mass lesion (Levine, 2000).

1.3.5.2 Slit Ventricle Syndrome

Slit Ventricle Syndrome (SVS) relates to hydrocephalus patients with small ventricles. While SVS has an unknown aetiology, it is thought to be related to over-shunting and occurs more often in children (Cheng, 2006).

Case 2 of Maroulis et al. (2008) describes a 53-year-old male patient who is diagnosed with hydrocephalus due to stenosis of the aqueduct and treated with a VP shunt; subsequently, a decade later the patient presented with neurological symptoms of no upward gaze and "diplopia consistent with a left fourth nerve palsy." MRI scans showed slit ventricles and a notable absence of other abnormalities, and depression was diagnosed. Two years later, symptoms remained and intra-cranial pressure was monitored, revealing that the shunt was over-draining. The patient's

shunt was replaced with a programmable valve shunt, yet adjustment of the pressure sensitivity resulted in either slit, or dilated ventricles (see Figure 1.10-(b) and Figure 1.10-(c), respectively); the patient fell unconscious with dilated ventricles and rapidly improved as the shunt was altered. A Third Ventriculostomy was performed and the shunt set to the highest setting (200 mm H_2O) that resulted in a normalization of the ventricles and the neurological symptoms resolving (Figure 1.10-(d)).

1.3.5.3 Alzheimer's Disease

Alzheimer's disease (AD) is the most common form of dementia and is incurable, degenerative and terminal. It presents with shrinkage of the cerebral cortex and hippocampus and enlarged ventricles, yet the cause and progression are not well understood. It is hypothesized that a lower production of CSF, and hence a lower turnover of CSF, may lead to a decrease in the clearance of toxic molecules such as amyloid-β peptide from the interstitial-fluid space of the brain (Silverberg, 2003). Furthermore, it is possible that advanced AD may be connected to lower CSF pressure (De Deyn et al., 2009).

1.4 HYDROCEPHALUS

Of all cerebral conditions, hydrocephalus presents us with an opportunity for clinically observable symptoms presenting with relatively difficult aetiology. Hydrocephalus is an active distension of the ventricular system of the brain resulting from inadequate passage of CSF from its point of production to its point of absorption into the systemic circulation (Rekate, 2008; Tully and Ventikos, 2009). While radiographic observation of enlarged ventricles (cf. Figure 1.11 and Figure 1.12) is not conclusive evidence for hydrocephalus, an absence of enlarged ventricles precludes the condition.

Hydrocephalus can be either congenital (present at birth) or acquired through injury or trauma to the brain and can be further defined by a sub classification of:

Acute hydrocephalus caused by obstruction of the CSF flow pathways, as per the conventional view.

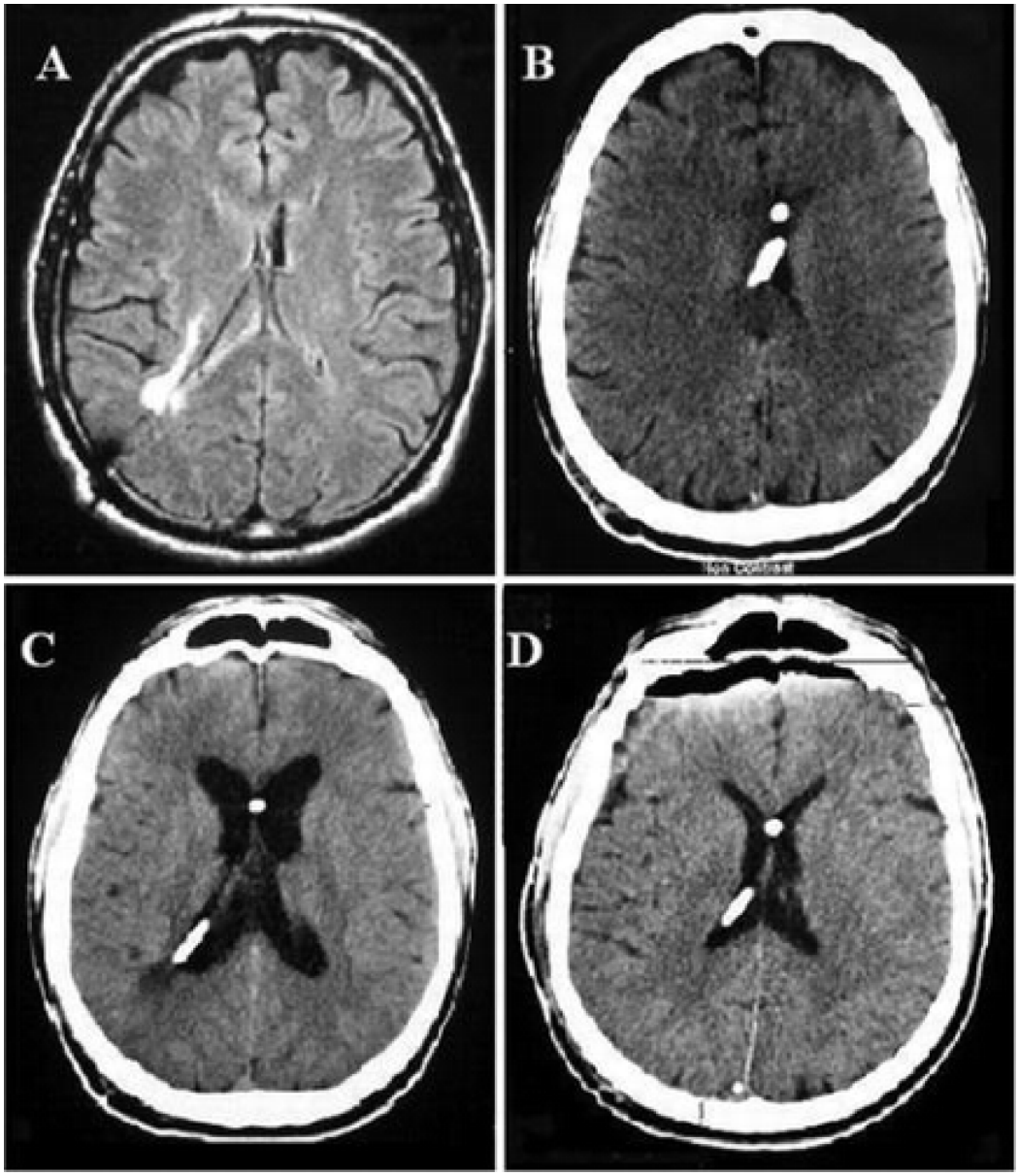

Figure 1.10: MRI scans of a 53-year-old male patient with alternating slit and dilated ventricles: **(a)** showing slit ventricles on presentation that did not change on CT **(b)** after the shunt was reset to 150 mm H_2O, but showed dilation on CT **(c)** with only a 10 mm H_2O increase in opening pressure to 160 mm H_2O. The slit ventricles returned to normal size on CT **(d)** after the third ventriculostomy procedure (Maroulis et al., 2008).

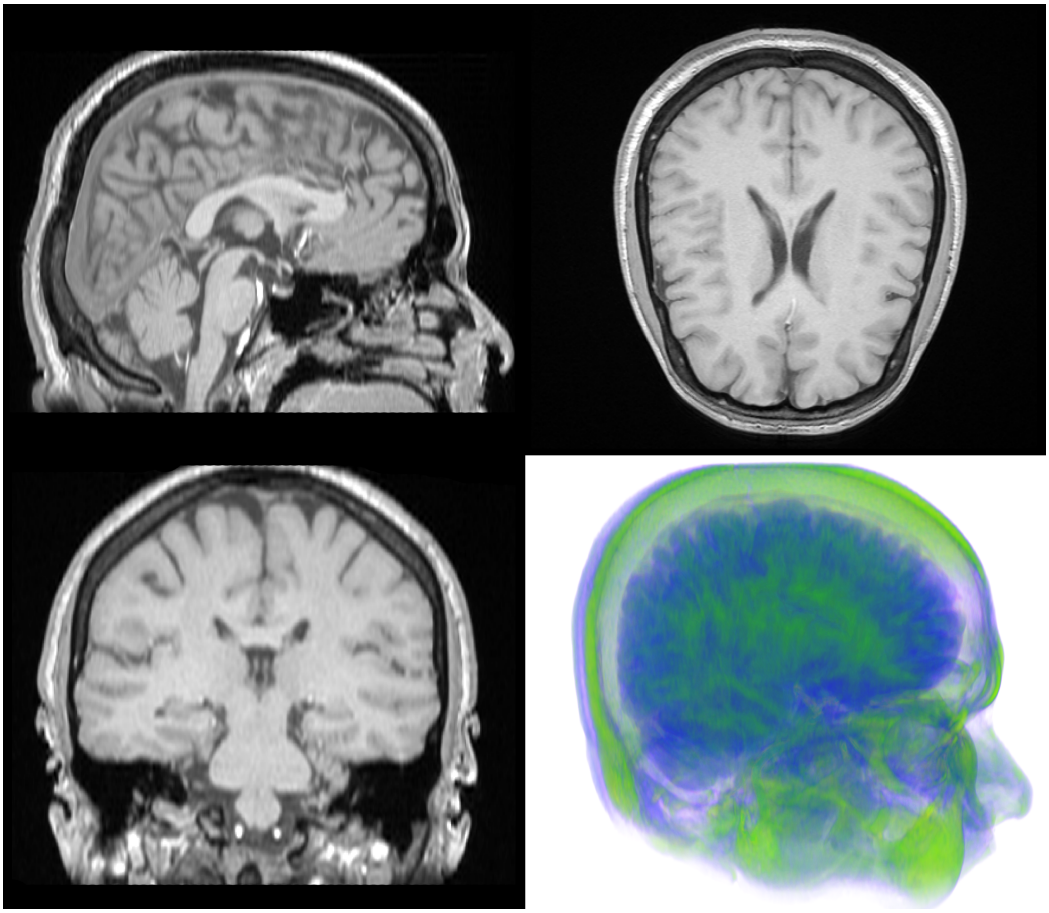

Figure 1.11: Sagittal and Coronal MRI slices of a healthy brain from the patient described in §4.2.1.1.2.

Chronic hydrocephalus characterized by prolonged time scales for development and the absence of radiographically identifiable flow obstruction (Greitz, 2004, 2007a). A seemingly counter-intuitive argument, there is contention as to the underlying mechanisms of this class of hydrocephalus; it is possible that altered compliance of the parenchyma and/or increased CSF viscosity may play a role (Greitz, 2004; Sato, 1994; Sobey and Wirth, 2006).

However, it has been shown that there is no significant difference in the clinical biomarkers of ventricular CSF in patients with acute or chronic hydrocephalus, indicating that similar pathophysiologies and turnover rates must exist despite the altered CSF dynamics (Tisell et al., 2004).

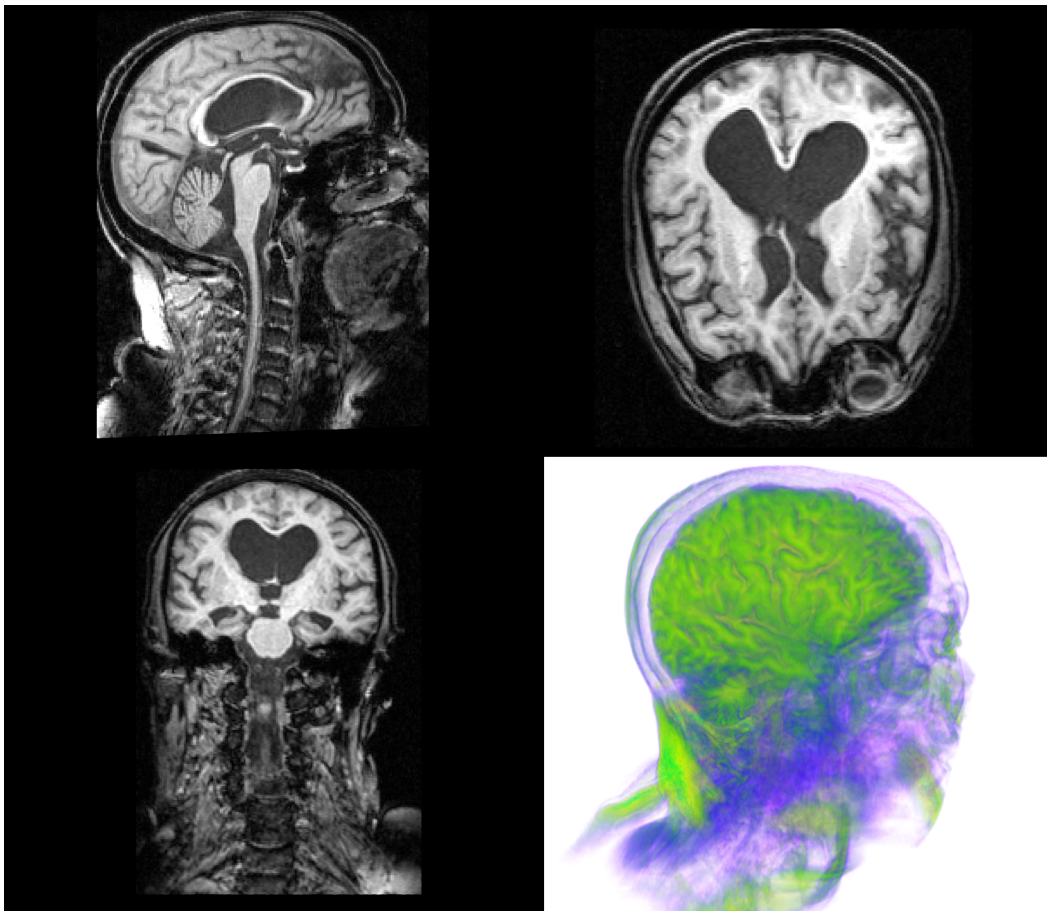

Figure 1.12: Sagittal and Coronal MRI slices of a hydrocephalic brain from the patient described in Case 2 of §5.2.1.1. This patient suffered from chronic hydrocephalus with no observable blockage to the CSF flow path; the enlarged lateral ventricles are easily observed, yet it is important to notice the enlarged CSF flow path (aqueduct, third and fourth ventricles) that would be absent if a flow obstruction was present in the cerebral aqueduct. It is also possible to see compression and distortion of other areas of the brain such as the cerebellum and white matter.

1.4.0.4 Acute Hydrocephalus

Acute hydrocephalus is caused by a radiographically identifiable obstruction of the CSF flow pathways, as per the conventional view. There are several possible locations for obstruction to occur, and each results in a different enlargement pattern of the ventricular system:

- Foramen of Monro: obstruction may lead to dilatation of one (or if the obstruction is large enough, both) of the lateral ventricles.
- The aqueduct of sylvius: normally narrow already, this may be obstructed by a number of genetic, or acquired, lesions and leads to dilatation of both lateral ventricles and the third ventricle.
- Fourth Ventricle: obstruction will lead to dilatation of the aqueduct and the lateral and third ventricles.
- The foramina of Luschka and the foramen of Magendie: may be obstructed due to a congenital failure of opening (Dandy-Walker malformation).
- The sub-arachnoid space surrounding the brain stem: may also be obstructed due to inflammatory or haemorrhagic fibrosing meningitis, leading to widespread dilatation, including the fourth ventricle.

1.4.0.4.1 Epidemiology The prevalence of congenital acute hydrocephalus does not appear to be related to geographic factors; including race, diet, region or development. According to the European Surveillance of Congenital Anomalies (EUROCAT) the incidence of hydrocephalus throughout Europe over the past 20 years has hovered between 2 and 10 cases per 10,000 live births. The general trend is relatively level, with a slight upward tilt over the last decade, and average values around 4 or 5 in every 10,000 (EUROCAT, 2007). In Sweden between 1999 and 2002, 6.6 in every 10,000 births displayed hydrocephalus (Persson et al., 2007), while in Japan during 1987 the incidence is estimated at 6 in 10,000 live births (Tamakoshi et al., 1991). The incidence rate in the United States is estimated at 20 in 10,000 (NINDS, 2008) with an associated cost of health care in excess of US$1 billion per annum (Patwardhan and Nanda, 2005).

1.4.0.4.2 Physiological mechanisms The disruption to the flow of CSF in acute hydrocephalus may be from obvious causes, such as a clear blockage, or from less obvious causes such as infection or congenital defects. It is often very difficult to establish the exact cause of congenital hydrocephalus as there are generally a number of contributing factors. This is particularly the case in premature babies where swings in blood pressure risk rupture of the undeveloped blood vessels leading to a haemorrhage and blockage of the cerebral aqueduct. Furthermore, most infants born with Spina Bifida also suffer hydrocephalus (Laurence, 1960). The associated developmental abnormalities in the brain restrict CSF movement, causing hydrocephalus, which compounds the compression in damaged parts of the brain.

Infection related acute hydrocephalus is not necessarily restricted to infants. Meningitis (an infection of the meninges) causes inflammation and debris which can block the CSF drainage. Similarly, Dandy-Walker Cysts and tumours can cause swelling and compression of the CSF pathways resulting in poor CSF drainage. The treatment of brain tumours generally involves measures to control hydrocephalus, which may be either temporary or permanent. In some very rare cases, the cause of hydrocephalus may also be attributed to hereditary factors (Zhang et al., 2006).

1.4.0.4.3 Clinical observations Dandy and Blackfan (1913, 1914) created the first animal model of hydrocephalus by blocking the aqueduct with cotton swabs. They went on to conclude that animals subjected to such occlusions would not develop enlarged ventricles following a choroid plexectomy. This work gained the attention of Bering (1962), who found that, in experiments with dogs injected with kaolin[1] following a choroid plexectomy, only ventricles with intact choroid plexus expanded. If the choroid plexus had been removed, the ventricle did not enlarge. Furthermore, it was seen that pulse pressure was higher in lateral ventricles with choroid plexus (dilated) than in those without (normal size) even though the static pressures were the same. Thus, he concluded that the choroid plexus is necessary for ventricular expansion in communicating hydrocephalus.

Linninger et al. (2005) continued with kaolin induced hydrocephalus in animals and of the six dog experiments carried out, one case showed a drastic increase in Intra-cranial Pressure (ICP) occasioning death. Autopsy revealed that the sub-

[1] *Kaolin* is a native hydrated aluminium silicate that is used as a demulcent and adsorbent in many different products from paint, to paper, to pharmaceuticals. Throughout the twentieth century, kaolin was used to induce hydrocephalus in animals by injecting it into the CSF.

arachnoid spaces were clogged with kaolin and the ventricles were expanded, consistent with acute hydrocephalus. The conclusion was that the ventricular expansion appeared to be the result of an accumulation of CSF. The duration of the experiment was consistent with CSF accumulation at constant production, with minimal resorption. In this study, no transmural pressure differences were seen, however, it is possible they were below the sensitivity (133-266 Pa) of the equipment.

The advent of Magnetic Resonance Imaging (MRI) studies has allowed investigators to observe CSF flow *in vivo*. Flow sensitive MRI allow us to recreate the dynamics in the cerebral environment and give, for example, accurate values for CSF velocity through the aqueduct of sylvius (Linninger et al., 2007). In this study, they were able to conclude that hydrocephalic patients display an average CSF velocity 2.7 times higher than healthy subjects in the foramina and aqueduct of sylvius. MRI studies also reveal that almost all motion of the blood and CSF is pulsatile (Egnor et al., 2001) and we can use data from MRI to give physical parameters to computational models (Kurtcuoglu et al., 2005; Kurtcuoglu, 2006; Loth et al., 2001; Lundervold et al., 2000).

1.4.0.5 Chronic Hydrocephalus

Normal Pressure Hydrocephalus, a form of chronic hydrocephalus, is a paradoxical condition that cannot be explained by the current assumed knowledge of CSF flow dynamics. Until the 1980's many questioned the existence of NPH, however, its counter-intuitive symptoms have recently driven a reconsideration of the dynamics of the CSF system as a whole (Bradley, 2008).

1.4.0.5.1 Epidemiology The clinical presentation of NPH is characterized by dementia's well known triad of gait disturbance, cognitive decline and urinary incontinence. It is associated with ventriculomegaly – a distension of the cerebral ventricles – in the absence of elevated CSF pressure and a notable absence of motor weakness (Gallia et al., 2006; Hebb and Cusimano, 2001; Byrd, 2006). However, the patient-to-patient variance of symptoms is significant, posing a diagnostic challenge and it is estimated that as many as 6% of nursing home residents in the United States may suffer from undiagnosed NPH (Byrd, 2006).

An increase in the occurrence of dementia correlates with age and most symptoms manifest themselves in the sixth or seventh decade. AD is associated with most

(60-70%) cases of dementia whereas NPH represents a much rarer form of cognitive defect occurring in about 5% of cases. However, importantly, NPH may be the only known curable form of dementia (Hebb and Cusimano, 2001; Stoquart-ElSankari et al., 2007; Gallia et al., 2006).

1.4.0.5.2 Clinical observations The mechanisms of hydrocephalus are often disputed and it is now believed that a mechanical imbalance between formation and resorption of CSF is not the sole mechanism involved (Greitz, 2004, 2007a,b; Hebb and Cusimano, 2001; Levine, 1999, 2000, 2008; Malm and Eklund, 2006; Sato, 1994). The traditional assumption is the existence of a breakdown in resorptive capacity of the arachnoid granulations (Bradley et al., 2006). However, intuition would suggest that if resistance was at the arachnoid villi only, the pressure increase would cause a dilation of the sub-arachnoid space – not in the ventricles (Greitz, 2004). A disturbance of the CSF dynamics alone cannot explain the clinical features of NPH (see Table 2 Malm and Eklund, 2006, page 17) and increasingly more attention is being paid to the role of a compromised blood-CSF barrier, and changes in brain parenchyma, vascular resistance and CSF circulation that result in altered compliance and diminished cerebral blood flow (Bradley et al., 2006; Dombrowski et al., 2009; Greitz, 2004; Hebb and Cusimano, 2001; Johanson et al., 2004; Silverberg et al., 2001; Stoquart-ElSankari et al., 2009; Williams, 2008).

The diagnosis of NPH is a non-trivial challenge as the condition is easily confused with PD, while also being associated with cerebrovascular disease or AD (Gallia et al., 2006; Jellinger, 1976). In a study by Silverberg et al. (2006), 4% of a selected group of AD patients had NPH and these patients were significantly younger and less demented than the remainder of the group.

Neuroimaging is an essential tool to assess ventricle size in diagnosing NPH; enlarged ventricles are not sufficient to make the diagnosis, however, absence of ventriculomegaly precludes NPH. Other important radiographic findings in NPH include: periventricular hyper-intensities, increased CSF flow velocity in the aqueduct, thinning and elevation of the corpus collosum on sagittal images, and absence of a visible obstruction to CSF flow (Gallia et al., 2006; Balédent et al., 2004).

The time scales of chronic hydrocephalus imply that the physiological changes occur slowly. It may be that the patient has suffered from the condition for many years, with various coping mechanisms that maintain allostasis; in the ageing body,

these coping mechanisms breakdown and the patient becomes symptomatic. For example, a patient with decreased absorption at the arachnoid villi may be more reliant on resorption through the parenchyma; a change in the capacity of any part of the system – such as altered compliance of the tissue, vascular network or spinal region, or an imbalance in the mechanical coupling between arterial, venous, CSF and brain tissue – could upset the equilibrium (Bradley et al., 2006; Greitz, 2004, 2007a; Hamlat et al., 2006; Stoquart-ElSankari et al., 2007, 2009).

There are many fundamental questions about chronic hydrocephalus that remain unanswered – such as why the ventricles dilate in the absence of a visible flow obstruction – and the future success of diagnosis and treatment hinges on gaining a better understanding (Bergsneider et al., 2006). Many theories and hypotheses attempt to explain the pathophysiology of chronic hydrocephalus; the primary ideas are the disruption of the intra-cranial pressure, changes in the capacity of the vascular network, and changes in the mechanical properties of the tissue.

Disruption of the intra-cranial pressure A transmantle pressure gradient is often offered as a plausible cause of ventriculomegaly. Greitz (2004) suggests that the initiation of hydrocephalus may be traced to increased arterial and capillary pulse pressure due to a breakdown of the dampening capacity of the arterial tree. However, studies of communicating hydrocephalus have provided little evidence to support an increased pressure gradient (Penn et al., 2005; Stephensen et al., 2002) and additional mechanisms may explain why CSF is preferentially absorbed through the walls of the ventricles into the deep brain parenchyma and not into the much larger capillary bed afforded by the cortex (Bateman, 2005).

Only very small pressure gradients (5-10 Pa) are required for CSF circulation to be maintained and it is possible that the increase in this gradient is smaller than the sensitivity of the pressure sensors used in experimentation (133-267 Pa) (Penn et al., 2005). Theories that rely on larger pressure gradients should be reconsidered and Linninger et al. (2007) predicts that the average transmantle gradient is indeed within the range of error of the measurements (reaching 30 Pa in hydrocephalic geometries), with a peak to peak value of pressure four times higher than the healthy case.

Disruption of the vascular network Studies allude to the importance of age-related changes in compliance and resorptive capacity of the cerebral vascular network that lead to the development of NPH (Rubenstein, 1998; Silverberg et al., 2001). Experimental and clinical data clearly show changes in the cerebral blood flow and associated dynamics with phase contrast MRI allowing clinical quantification in a non-invasive manner (Byrd, 2006; Corkill et al., 2003; da Silva et al., 1995; Owler and Pickard, 2001). Through this method it is shown that the total cerebral blood flow decreases with age with a preserved intra-cranial compliance; where vascular compliance relates the ability of a vessel to expand its volume as the transmural pressure increases and intra-cranial compliance depends primarily on CSF oscillations and vascular compliance (Balédent et al., 2004; Stoquart-ElSankari et al., 2007).

Williams (2008) suggests that hydrocephalus is a self-perpetuating condition caused by a loss of compliance, while at the same time causing a loss of compliance through the over-accumulation of extracellular fluid; both of which can be traced to inadequate venous drainage. Experimental results show that the peak flow in the jugular vein occurs consistently earlier in patients with chronic hydrocephalus, and hence, agree that NPH may cause a decrease in vascular compliance or venous compromise (Balédent et al., 2004; Bateman, 2001; Dombrowski et al., 2009).

NPH symptoms may be caused by a complex interaction between a disturbance of the CSF dynamics and cerebrovascular disease in the periventricular deep white matter (Malm and Eklund, 2006). This is quantified by cerebral biopsies, which indicate an increase in transcapillary filtration through an enlarged extracellular space with otherwise normal neuropil (Jellinger, 1976) and is a good clinical indicator for a negative response to shunt treatment (Woodworth et al., 2009).

Bateman (2008) argues that Deep White Matter Ischaemia (DWMI) is not a prerequisite for NPH, however, Bradley and colleagues are convinced that it plays at least a contributing role by suggesting that NPH is actually a dormant congenital disease that becomes active later in life (Bradley, 2000; Bradley et al., 2006; Bradley, 2008). These authors assert that NPH starts as a kind of benign hydrocephalus in infancy that lays dormant until the onset of DWMI in old age. This theory is supported by evidence that NPH patients have statistically larger cranial volumes, implying that the condition began before the sutures closed.

Change in the tissue properties One of the many paradoxes associated with hydrocephalus is that ventricular enlargement can occur with an absence of a large pressure gradient across the cerebral mantle (Bergsneider et al., 2006; Levine, 2008). It is possible that an obstruction to the CSF flow produces a mini-gradient of pressure (~ 133 Pa) that is sufficient to overcome the added resistance to the flow. Depending on the efficiency with which ventricular pressure is transmitted through the parenchyma to the outer surface of the brain, this mini-gradient can coexist with high, or with normal intra-cranial pressure. This transmission efficiency depends primarily on the elastic – or more specifically, the poroelastic (see Chapter 2) – properties of the brain (Levine, 2008).

If the brain is relatively incompressible, then transmission is efficient and the ICP must rise to maintain the mini-gradient, resulting in high pressure chronic hydrocephalus. Conversely, if the brain is more compressible, then the parenchyma attenuates the increase in ICP reducing transmission to the outer surface. Hence, ICP need not rise above normal levels to maintain the mini-gradient, leading to normal pressure chronic hydrocephalus.

The size of this mini-gradient is determined by the severity of the obstruction and the availability of alternate pathways for CSF absorption. These alternate pathways - such as through the capillary wall, or a change in porous properties - are likely to require time to develop, hence, a sudden severe obstruction favours acute (high pressure) hydrocephalus. While a more gradually developing obstruction favours chronic hydrocephalus with normal pressure throughout its course.

1.4.0.6 Approaches to treatment

It is important to consider that no known cure exists for hydrocephalus. Hence, the current treatment methods do not address the underlying conditions, rather they attempt to alleviate the symptoms through mechanical means. More than eighty years ago, Davidoff (1929) remarked “in hardly a single other condition have cures been so elusive or so often wrecked on purely mechanical obstacles.” Furthermore, controversy surrounds the decision of which is the optimal treatment method – largely due to the unacceptably high failure rates across the board (Patwardhan and Nanda, 2005).

Ventricular shunt procedures remain one of the most common neurosurgical

procedures performed. In America in the year 2000, almost as many shunt replacements (42.8%) were performed as new shunt implants (43.4%) (Patwardhan and Nanda, 2005). Endoscopic Third Ventriculostomy (TV) is an alternative procedure to treat non-communicating hydrocephalus and avoid inherent shunt related complications (Kim et al., 2004), however, failure from TV is not unlike that of CSF shunts when analysed by survival methods. In fact, there is no statistically significant difference between the two in the efficacy for treating pediatric tumor or aqueductal stenosis (Drake et al., 2009; Tuli et al., 1999).

While there is arguable little difference in the treatment methods, most patients undergo a shunt implant. The purpose of a shunt is to provide an alternative route for drainage of the CSF through the insertion of a catheter into the ventricular system. The catheter is then connected, via a one-way valve with varying degrees of sophistication, to a drainage location in the body (see Figure 1.13). The most common location is the peritoneum due to its ability to accommodate a patient's growth (especially in young children) while alternatives include the right cardiac atrium or the pleural (chest) cavity.

Causes of shunt malfunction may include obstruction, mechanical disconnection or breakage, infection and over-drainage (Wu et al., 2007), however, the most common factor causing shunt failures is misplacement (Aschoff et al., 1999). Multiple shunt failures and infections are common and revisions account for 48% of all shunt related procedures in the United States. In pediatric surgical series, shunt failures occur in 14% of patients in just the first month after shunt placement, and 40-50% fail within the first year. In adults, this figure is still relatively high at 29% (Wu et al., 2007). The overall incidence of over-drainage in long-term shunt patients is from 10-12% and represents less than 10% of shunt failures in pediatric series, and about 30% in adult series (Kim et al., 2004).

1.4.0.6.1 Treatment of chronic hydrocephalus While the pathophysiology of NPH remains unknown, some patients respond dramatically to treatment; it gains importance as one of the few reversible forms of dementia (Stein et al., 2006; Owler and Pickard, 2001). It has been said that NPH is more than simply a disorder of CSF production and resorption, and treatment methods that manipulate the flow dynamics are merely enabling the marginal brain to function at a higher level (see Hebb and Cusimano, 2001, comments). Furthermore, cognitive impairment is the least likely

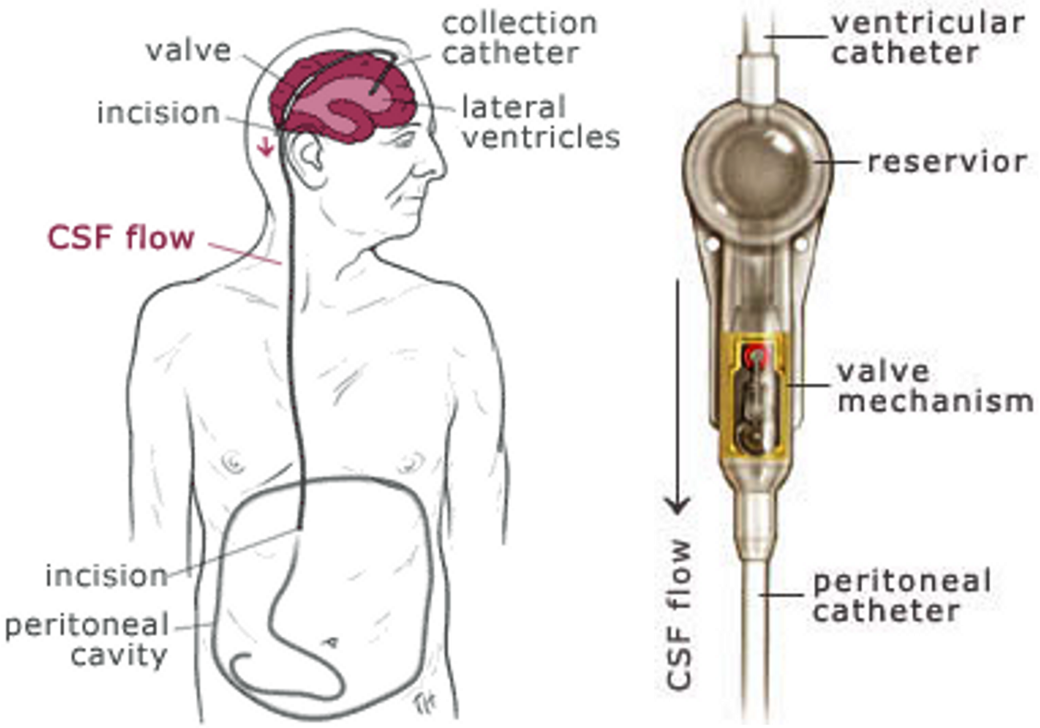

Figure 1.13: An example of a Codman & Shurtleff (Raynham, MA, United States) ventriculoperitoneal shunt design inserted into the lateral ventricles of an adult subject.

of the triad of symptoms to improve following treatment (Gallia et al., 2006).

The current technique for treatment involves a surgical diversion of CSF by altering the existing flow channels (i.e. TV), or adding a new flow path (i.e. inserting a cerebral shunt) (Gallia et al., 2006; Gangemi et al., 2004). The response of patients to CSF shunting remains highly variable, perhaps due to the difficulty in distinguishing NPH from other non CSF-related neurodegenerative conditions (Hebb and Cusimano, 2001; Woodworth et al., 2009). At the same time, patients who present with a short duration of symptoms, a prevalence of gait disturbance and slight mental impairment respond equally well to TV as they do to shunting (Gangemi et al., 2004). In cases of successful shunt treatment, the shunt may provide a necessary additional resorption route, however, successful treatment through TV in selected patients suggest that natural CSF resorption is at least sufficient in these cases (Bradley, 2000; Gangemi et al., 2004).

Herein lies the difficulty for clinical decision-making and intervention. Stein et al. (2006) argue that more patients with suspected NPH should undergo shunt in-

sertion and attribute the low success rate to inappropriate case selection – through statistical methods these authors conclude that if 50% of patients experience shunt complications, the shunt response rate would need to be lower than 5% for shunt insertion to do more harm than good.

Many of the patients treated for NPH showed subjective improvement (72%), gait improvement (57%) and incontinence improvement (58%), yet none improved in psychometric testing. It is possible that the former are caused by enlarged ventricles and removed through shunting, while the latter is the result of the breakdown in the ability of the CSF to clear the neuro-toxins from the cerebral environment (Silverberg, 2003).

Biochemical markers in the ventricular CSF and experimental data have been shown to aid the treatment decision. Specifically, a high ratio of albumin and sulfatide concentrations have negative implications for surgical intervention (Tisell et al., 2004), while a positive response to CSF drainage is a reliable indicator for positive shunt responsiveness (Woodworth et al., 2009). However, while the shunting procedure is relatively straight forward, shunt complications seriously reduce the effectiveness of the treatment method and can be categorized into three main groups (Malm et al., 1995; Malm and Eklund, 2006; Gallia et al., 2006):

(a) those related to the surgical procedure (i.e. infection);

(b) those related to the shunt system (i.e. valve malfunction); and,

(c) those related to the flow characteristics of the shunt (i.e. over-drainage).

Finally, it is possible that the variable success of CSF shunting may be due to a competing cause of disturbed CSF flow, such as a breakdown in the transport of fluid between the cerebral blood network and extracellular spaces.

1.5 Dementia's Elusive Cure

The brain is the most important and complex of all the human organs, yet our ability to effectively treat a host of neurological conditions may be hindered by our lack of

understanding of the basic mechanics of this environment. Normal Pressure Hydrocephalus (NPH) may be the only curable form of dementia, yet the pathophysiology is paradoxical and a cure remains elusive.

Through well-developed processes, the brain is able to function under a variety of conditions and respond to, sometimes drastic, changes in its environment. Central to this capacity are a set of delicate yet extremely efficient and sophisticated mechanisms that control the regulation of water and ion flow, playing a pivotal role across all the spatial scales.

In common with NPH, the evolution of many cerebral diseases such as Alzheimer's Disease (AD) and Parkinson's Disease (PD), Cerebral Oedema, Stroke, and Tumour are strongly correlated to a change in the transport properties of fluid in the brain. The study of cerebrospinal fluid (CSF) flow characteristics may teach us useful information about cerebral dynamics and allow a better understanding of the mechanisms involved in maintaining allostasis in the brain.

Ageing brings about two noticeable changes in CSF flow properties (Silverberg, 2003):

(a) there is a trend towards lower production and hence a lower turnover; and,

(b) a greater overall resistance to CSF resorption.

These changes highlight the relative importance of CSF in neurological diseases such as AD and NPH. It has been suggested that the underlying pathophysiology of dementia in both these diseases may be traced, at least partly, to a breakdown in the ability of the CSF to cleanse neurotoxins from the cerebral environment – hypothesizing that AD may be the result in the failure in production of CSF, while NPH develops if the failure is in the resorption of the fluid (Silverberg, 2003; Silverberg et al., 2006; Wostyn, 2004; Johanson et al., 2004; Jellinger, 1976). Furthermore, the rate of production is normal in patients with PD – a disease whose symptoms are often confused with those of NPH – while it is markedly reduced in patients with AD (Silverberg et al., 2001).

Cerebral diseases are recognized as pivotal in healthcare; they relate to a whole host of unmet clinical needs. We are convinced that basic understanding of fluid transport is the most promising way to address these needs meaningfully, in a clin-

ical setting. The goal of this research is to investigate this basic understanding through the use of mathematical and computational models of water transfer in the brain. The levels of interrogative representation and multi-scalarity in these models will be progressed beyond the state-of-the-art to more physically representative levels.

CHAPTER 2

MODELLING: HISTORY AND OBSERVATIONS

This chapter aims to define the role of mathematical modelling in the study of cerebral dynamics, with a specific focus on hydrocephalus. The complexity and paradoxical nature of hydrocephalus has enthralled researchers for many years. Experience and intuition alone have been largely ineffective in understanding the condition. Mathematical and computer modelling provides a hypothesis test-bed in many disciplines and efforts in modelling hydrocephalus have increased the understanding of the disease (Clarke and Meyer, 2007).

More than two centuries ago, Alexander Monro applied the concepts of physics to intra-cranial dynamics for the first time (Monro et al., 1783). After several revisions, what became known as the Monro-Kellie doctrine suggests that the sum of the volumes of brain tissue, CSF and cerebral blood remains constant. An increase in one, will lead to a decrease in one or both of the remaining two. Disruption of the harmony between each volume in the cranium causes serious ailment and their interactions have long been observed.

While different approaches can be taken for modelling the dynamics of the system, each model is based on underlying assumptions about the flow of CSF. Production and absorption of CSF is complex and the middle of the twentieth-century witnessed a formation of two theories to explain the underlying mechanisms: bulk-flow theory resulting from the work of Pappenheimer (Pappenheimer and Heisey, 1961); and pulsatile flow as proposed by Bering (Bering, 1962) and further investi-

gated by others (Wilson and Bertan, 1967).

Bulk-flow theory can formally be traced back to Cushing (1925) who described a 'Third Circulation' (the first two being blood and lymphatic circulation) which outlined the flow of water in the cerebral fluid space. Pappenheimer's work, while not discrediting the role of pulsatility, described how to measure bulk-production and -absorption in a seductive and easily observable way. As a result, for the next several decades CSF was considered to flow in a steady manner according to bulk theory (Madsen et al., 2006).

Using bulk-flow as the base assumption, Ransohoff et al. (1960) suggest that all hydrocephalus is indeed obstructive and can thus be explained by bulk-flow models. Rekate (2007) investigates this statement through an exploration of possible sites to CSF obstruction. He proposes that all hydrocephalus is obstructive, however, the role of pulsations should not be ruled out and both models should be included in ongoing research.

Clinically, the presumption that all hydrocephalus is obstructive (specifically caused by obstructed arachnoid granulations) may be directly tested – Emam, Abashiya, Chareunsack, Skordos, Oh, Choi, Kralick, and Noh (2008) have designed a micro-array of needles with one-way valves to at as prosthetic arachnoid granulations. If the presumption is incorrect then the device is likely to be ineffective in treating hydrocephalus; conversely, if it is true, then we may be seeing a truly novel treatment method. Initial flow tests have demonstrated the low cracking pressure of the micro-valves, however, the devices are yet to be tested *in situ*.

Regardless of the outcome of the micro-array experiments, Rekate's observation of the importance of pulsatility in models of hydrocephalus is indeed wise. The advent of flow-sensitive MRI has meant that *in vivo* observations of CSF show conclusively that the flow is dominated by the pulsatile nature of the cardiovascular system (Kurtcuoglu et al., 2005; Kurtcuoglu, 2006; Linninger et al., 2005). This reconsideration of pulsatile CSF flow has been largely driven by a desire to explain the paradoxical nature of NPH. Patients with NPH have a higher peak velocity of CSF flow through the aqueduct (Gideon et al., 1994) and it follows then, that the peak driving force (or transmantle pressure gradient) must also be higher.

Interestingly, both arterial and venous blood flows are pulsatile. However, intuition (and observation elsewhere) tells us that capillary flow is relatively smooth, or

free from pulsation, and the pulsatile component of the arterial blood flow is attenuated by dissipation to the surrounding fluids and tissue (Egnor et al., 2001). Most likely though, it is through these same media that the pulsations are transferred to the venous flow via compression of the cortical veins by sub-arachnoid CSF. Egnor et al. (2001) summarize the idea with the following postulate: arterial pulsations are dissipated through the CSF to the cerebral veins, bypassing capillary circulation. It has been suggested that the hyper-dynamic pulsation of the choroid plexi leads to ventricular enlargement (Wilson and Bertan, 1967; Egnor et al., 2002), however, this pulsation is more likely to be driven by the expansion and contraction of the arterial vessels than it is by pulsatile flow in the local capillaries.

Levine (2008) proposes several challenges for the role of pulsatility in hydrocephalus. Firstly, many conditions that give a rise in pulsatility are not associated with the condition, for instance, aortic insufficiency[1] and hypercapnia[2]. The theory also attributes ventricular enlargement to irreversible tissue damage and, as such, struggles to account for the rapid reduction in ventricular volume occasionally seen after shunting or TV. Finally, it fails to explain why periventricular tissue is more affected by hydrocephalus than the cerebral cortex, as both sites are adjacent to pulsatile CSF. These challenges must be taken up if a theory of NPH progression is to place a greater importance on pulsatility.

2.1 MODELLING TECHNIQUES

Modern studies use a variety of techniques to achieve the hydrodynamic coupling of fluid and tissue. Historically, the pressure-volume relationship provided by the Monro-Kellie doctrine led many researchers to approach the cerebral environment as a series of compartments and lumped parameters. More recently, the need for spatially informed models has become more apparent to capture changes within individual systems and subsystems.

[1] *aortic insufficiency* describes a malfunction of the aortic valve causing pumped-out blood to return into the left ventricle.

[2] *hypercapnia* is a condition related to an abnormally high concentration of CO_2 in the blood stream.

2.1.1 Compartmental Analysis

Compartmental analysis has long been employed as a tool to investigate intracranial dynamics. Lumped parameter, pressure-volume models satisfy various modelling goals, such as surgery simulation, investigating cardiac driven pulsations and large-scale arterial modelling. These models are used to study the interaction between the different systems and compartments in the brain, the interplay between CSF and blood pressure, as well as the mechanisms of auto-regulation and control and thereby their stability in different physiological and pathological situations.

Often, these sophisticated compartmental models capture the cerebral fluidic system based on an electrical analogue representation of the dynamics. Mathematical relationships are formed between ICP, cerebral blood volume (CBV), CSF dynamics and the action of cerebral blood flow (CBF) regulatory mechanisms. Recent publications are based around the work completed by Ursino and Di Giammarco (1991) whose model placed particular emphasis on reproducing the mechanical properties of arteries and arterioles, and their response to changes in perfusion pressure and CBF. The same model was extended to explore the relationship between cerebral auto-regulation, arteriolar blood volume changes and ICP. This was achieved through the inclusion of hemodynamics of the arterial-arteriolar cerebrovascular bed, CSF production and re-absorption processes, the non-linear pressure-volume relationship of the craniospinal compartment, and a Starling resistor[3] mechanism for the cerebral veins (Ursino and Lodi, 1997).

The work of Ursino and colleagues contributed to the well accepted practice that treatment of patients with TBI cannot neglect the role of CBV changes and the possible detrimental effect on ICP and CBF. The clinical importance of cerebral auto-regulation means that there has been substantial impetus to develop extensions of such compartmental models. Often referred to as 'physiologically-based models' (as opposed to, for example, transfer function analysis), these systems are built upon to include many variants of bio-chemical, electro-chemical and/or chemo-mechanical subsystems.

An attempt to understand the many feedback pathways of CBF control lead to

[3] A *Starling resistor* refers to the variable resistance of a fluid-filled tube as its cross-sectional area changes in response to the pressure gradient across its walls.

a model that combines the biophysics of the circulatory system with a basic model of the brain metabolic biochemistry and a model of the vascular smooth muscle (Banaji et al., 2005). Others are focussed on the arterial blood pressure as clinically viable validation data (Payne, 2006; Payne and Tarassenko, 2006). These models predict the response of the cerebral vasculature to changes in arterial blood pressure, arterial CO_2 concentration and neural stimulation; something that is critical to improving our understanding of brain activation seen through the lens of fMRI.

Compartmental models have also proven to be useful in experimental and clinical settings. With the heavy reliance on animal studies in the workflow of medical researchers and biologists, compartmental models allow assessments to be made on the extent to which animal studies can be extrapolated to humans. For example, based on the work of Ursino, Daun and Tjardes (2007) produce a model of cerebral hydrodynamics in both rats and humans that particularly focuses on the comparison of experimental and clinical data in the case of traumatic brain injury.

Animal compartmental models also serve a role in basic science whereby results provide considerable utility alongside laboratory research and experimental design. A combination of electro-chemical and chemo-mechanical subsystem models of the smooth muscle cell is an example of an integrative modelling approach to the characterization of the electrical, chemical, and mechanical behaviour of the single cerebrovascular smooth muscle cell in rats (Yang, 2003).

In hydrocephalus, compartmental models have been used both for basic understanding, and investigation of surgical intervention techniques. In a review paper, a group of scientists and clinicians in Cambridge, UK, present the basics of modelling CSF dynamics with a lumped parameter approach (Czosnyka et al., 2004). This approach offers the ability to investigate alternative theories – for instance, that the lymphatic pathway around the olfactory nerve plays a large role in the drainage of CSF (Fard et al., 2007) – however, a significant benefit to the electrical analogue is computational efficiency provided for such a complex environment.

The stark difference in computational requirements is shown by comparing the resources needed to produce a patient-specific, fully three-dimensional simulation of the human arterial tree. It is estimated that a single multi-scale run of the brain vascular network requires almost 28 wall clock hours per cardiac cycle, when run on *110,000 processors*, yet the agreement in results between the fully three-dimensional

simulation and a compartmental model (where eight cardiac cycles took only 20 minutes) are remarkable (Anor et al., 2009; Grinberg et al., 2009b,a). The efficiency of compartment models allows for realistic investigation of short time-scale variations such as the effect of cardiac-driven CBV pulsations. For example, a six compartment lumped-parameter model of the craniospinal system is used to describe its basic dynamic response to these pulsations with a good correlation between model results and flow-sensitive MRI data of the movement of CSF (Otahal et al., 2007).

A particular focus of these cardiac-driven pulsation models is the application and variance of the Windkessel[4] effect. The Windkessel effect aids the dampening of cardiac-pulsations in blood vessels, witnessed by the pulsatile flow of blood in arteries becoming relatively smooth by the time it reaches the capillary bed. However, venous outflow is also pulsatile and it is logical to assume that these pulsations are thus transmitted by either the CSF or the parenchyma – it is suggested that CSF acts as a pulsation absorber and forms the basis of the Windkessel effect in the brain (Egnor et al., 2001). Furthermore, Egnor et al. (2002) developed a model of intra-cranial pulsations based on the electrical circuit analogy, where increased impedance to CSF pulsation in the sub-arachnoid space results in a redistribution of pulsations through the cranium (primarily to ventricular CSF and venous blood) and clinical features of chronic hydrocephalus are recovered.

An inherent weakness of compartmental models is that, by definition, they treat systems or subsystems as an entity and thus cannot account for changes within each individual system. In particular, a compartmental approach is unable to capture spatial variations in the mechanical properties of the brain, which may dictate the severity and permanency of hydrocephalic changes (Clarke and Meyer, 2007).

Recent work has attempted to allay this weakness by coupling the compartment model with multi-dimensional representations of other aspects of the system. Clatz et al. (2007) couple a three-dimensional representation of the parenchyma with a scalar description of CSF circulation. In the model, the cerebral aqueduct is unobstructed and thus flow of CSF through the ventricular wall (and hence the parenchyma) is neglected, and it is assumed that interstitial fluid and CSF are not in communication and maintain different pressures. The gradient between the two

[4] Literally translated from German, *Windkessel* means 'air chamber' although in this context, it is referring instead to an elastic reservoir.

pressures drives tissue displacement and fluid exchange between the interstitial fluid and cerebral blood is accounted for in the parenchyma. In a similar approach, Linninger et al. (2009) link a compartmental methodology of the CSF system with a fluid-structure solution of tissue displacement in the parenchyma.

Increasingly, however, it is believed that knowledge of the spatial distribution of changes within the cerebral environment are of importance to both understanding cerebral dynamics and optimizing clinical intervention.

2.1.2 Spatially Distributed Models

An alternative approach was provided by Hakim and colleagues, who described the brain as a sponge-like material and gave rise to modelling the cerebral environment with spatially distributed methods (Hakim and Adams, 1965; Hakim, 1971; Hakim et al., 1976). Spatial techniques are advantageous as models account for hydrodynamic coupling between ventricles (geometry and wall motion) and allow quantitative statements to be made on the flow and pressure in the ventricular space (Kurtcuoglu et al., 2005). These fall into three primary categories:

(a) tissue deformation studies assuming pressure boundaries without including the fluid (Miller et al., 2006);

(b) flow studies treating the tissue as a (possibly porous) rigid body (Linninger et al., 2007); and,

(c) flow studies treating the tissue as a (possibly porous) deformable body (Levine, 1999; Smillie et al., 2005).

Given the right assumptions for model parameters, the first two categories produce results that are in good agreement with clinical observations, but only the final category is capable of capturing the underlying physics of the environment required for complete understanding. In this final category, the most common models are formed using viscoelastic or poroelastic theory in the constitutive relationship.

2.1.2.1 Deformable Multi-Phase Models

In the published literature, deformable models are usually presented as either viscoelastic or poroelastic. The intrinsic viscoelastic properties of the solid matrix (parenchyma) influence the short term response of the system to force; however, this response dissipates over time (Cheng, 2006). Through a series of mechanical tests of the elastic and viscoelastic properties of excised tissue, it is found that: under cyclic uniaxial stress, the tissue properties are qualitatively similar to filled elastomers (viscoelastic); while under volumetric stress (as in hydrocephalus), the tissue is similar to fine soils obeying consolidation theory (Franceschini, 2006).

These tests further showed that the drained and undrained (cf. §3.1.3) elastic moduli of the tissue are practically identical, shedding light on the different approaches to modelling the parenchyma. Consolidation theory is appropriate for problems that involve high values of mean applied stress for a considerable period of time (as in hydrocephalus) when the ratio of volumetric strain to applied stress is small under drained conditions. While it plays a role as a 'correction' to single phase non-linear theory when the problem involves large deviatoric deformations. These results do not exclude, and even support, a viscous behaviour of the solid phase; however, it is clearly shown that the leading mechanism for delayed volumetric deformation is consolidation.

The ability of a model to predict the optimal shunt placement is used to make a direct comparison of poroelastic and viscoelastic theory (Sivaloganathan, 2005; Sivaloganathan et al., 2005). In these studies, the poroelastic model includes a permeability that varies with deformation of the ventricular wall, while the viscoelastic model assumes the parenchyma is an impermeable, viscoelastic solid. It is shown that there are both advantages and disadvantages to each model and that the spatial and temporal structure of the solution remains qualitatively unchanged by allowing the permeability to change with deformation. The comparison suggests that interaction between CSF and tissue is best modelled with a poroelastic approach, whereas the response of tissue to applied loads is best modelled with a viscoelastic approach. Lee (2006) is clear that the time-scale of current viscoelastic models may be suitable for brain traumatic injury, but it is insignificant in modelling hydrocephalus. These viscoelastic models are challenged by a requirement to know the full strain history and state of stress of the tissue (very difficult in practice) (Drake et al., 2009; Lee, 2006), however, the final decision on which theory is most appro-

priate must be made in light of experimental data (Sivaloganathan, 2005; Sivaloganathan et al., 2005; Drapaca et al., 2006).

Finally, the assumption of linear elasticity in most poroelastic models is likely to be an over-simplification for the study of hydrocephalus (Kaczmarek et al., 1997; Sobey and Wirth, 2006). However, given the current state of knowledge about hydrocephalus, brain dynamics more generally and the constitutive requirements, we believe that poroelastic theory provides the framework most likely to garner a better understanding of hydrocephalus.

2.1.2.1.1 Cerebral Poroelastic Models In the late 1980's Hakim's concept of the 'brain-as-a-sponge' was extended mathematically using the theory of consolidation (Nagashima et al., 1987). This mathematical framework – applied from geomechanics and known as poroelastic theory or Biot's theory – combines Hooke's law for elastic bodies, Darcy's law for flow through a porous medium and the Navier-Stokes equations for fluid flow (Biot, 1941; Biot and Willis, 1957). Included in Nagashima's reworked system is the Terzaghi effective stress principle (discussed in Chapter 3) to give the four principles of the biomechanical poroelastic model (Clarke and Meyer, 2007).

Most recent studies using poroelastic theory are based on simplified geometries where the brain is assumed to be either cylindrically, or spherically, symmetric while expanding the model in other areas. The cylindrical, two-phase, small-strain poroelastic model is solved analytically and used to investigate obstructive hydrocephalus (Kaczmarek et al., 1997). Large deformation is catered for by the superposition of the responses obtained from incrementally increasing the loading. However, the spherical model provides a more realistic representation of the system and many models of the last decade follow this approach.

Early work with a three-dimensional poroelastic model was conducted to explore the role of CSF absorption in the parenchyma in the development of NPH, and the relationship between ventricular size and impaired CSF absorption in psuedotumor cerebri (Levine, 1999, 2000). In the latter, an analytic spherical poroelastic representation of the parenchyma is investigated by varying the Biot parameter (see Chapter 3) as a measure of the relative roles of blood and interstitial fluid in changing the parenchymal volume when a mechanical stress is applied (assuming a constant fluid pressure). The results obtained show that the change in volume of the

ventricular and sub-arachnoid space depends both on how compressible the vessels are and on the degree to which the outer surface of the brain is tethered to the dura.

Smillie et al. (2005) pioneered a new approach with a two-phase, spherical, poroelastic model that includes the flow dynamics through the previously obstructed aqueduct. Their model provides a new set of boundary conditions with a more realistic representation of the physical system and quasi-steady time-dependence. The later works use small-strain poroelastic theory, with a non-linear, strain-dependant permeability and non-spherical geometry included for increased complexity (Sobey and Wirth, 2006; Wirth and Sobey, 2006). It is shown that the developed theories resulting from poroelastic studies remain consistent when the model is implemented in more complex geometries.

In these studies by Sobey and colleagues, the Biot parameter is varied over time (to display a change in compliance of the tissue) and to show that the ventricle can dilate without any abnormal transmantle pressure gradient and an open aqueduct. The study concludes that: (a) for accuracy to be enhanced, the linear elastic model must be replaced by non-linear, or even viscoelastic equations; and, (b) assuming that poroelastic properties remain constant is likely to be incorrect.

However, a potential weakness of the state-of-the-art hydrocephalus models is the lumping of CSF and cerebral blood into a common network. Two cases have been published as exceptions where the traditional cerebral poroelastic model (see Equation (3.19), Chapter 3) is modified by including an additional fluid network encapsulating the capillaries and veins: Wirth and Sobey (2009) investigate the CSF dynamics of the brain during an infusion test using a spherically symmetric model that captures the pressure in the blood network, without allowing water exchange between it and the extracellular space. Levine (1999) allows slow communication between the interstitial fluid and blood networks using Starling's law – relating the role of hydrostatic and oncotic forces in the movement of fluid across capillary membranes (Starling, 1896) – for absorption of interstitial fluid into the capillaries. The parenchyma is modelled as a spherical three-phase linear poroelastic structure consisting a solid deformable matrix permeated by a incompressible interstitial fluid and a network of compressible capillary and venous channels.

The model is used to test three theories of CSF physiology:

(a) the ventricular wall is impermeable to CSF;

(b) ventricular CSF seeps into the parenchyma, from which it is efficiently absorbed; and,

(c) ventricular CSF seeps into the parenchyma but is absorbed inefficiently.

Concluding that only the second theory can account for the clinical observations of NPH. Further analysis of this model a decade later reconciles the view that hydrocephalus is the result of obstruction to the flow of CSF with clinical and theoretical observations that the transmantle pressure gradient is often too small to be detected (Levine, 2008). It does so by varying the mechanical/poroelastic properties of the tissue that correlate to an altered state in the brain whereby the transmission of ventricular pressure to radial stress in the periphery is less efficient.

In each of these cases, the additional fluid network is included by introducing a source/sink term to the fluid continuity equation (3.3); however, both of these models ignore this new fluid network in the stress equation and CSF and blood remain coupled through a common pressure.

2.2 Assessment of A Cerebral Transport Model

A validated model of water transport in the cerebral environment is both an ambitious and timely task; many brain diseases relate to imbalances in water regulation (as we saw in §1.3 and §1.4). Tumours may lead to obstructions and problems in absorption of CSF, strokes and injuries lead to oedemas, malformations of the ventricles and passages result in hydrocephalus or Chiari disease, and elevated intracranial pressure may lead to ischaemic dementia - of great significance to an ageing population. Common or rare - chronic or acute conditions, transport of water in the brain plays a crucial role.

The importance and complexity of the brain, together with the range of unmet clinical needs that are connected with this organ, make the current research a high-priority. One of the most paradoxical cerebral conditions, hydrocephalus, serves as an excellent metric for judging the success of any model developed. The clinical presentation of acute hydrocephalus and its relatively obvious source provide

us with a useful set of parameters (those of ventricular displacement and CSF pressure) that can be extracted to validate the mathematical model. Furthermore, there are many fundamental questions about chronic hydrocephalus that remain unanswered – such as why the ventricles dilate in the absence of a visible flow obstruction – and the future success of diagnosis and treatment hinges on gaining a better understanding (Bergsneider et al., 2006).

Importantly, any model capable of producing clinically relevant data for acute hydrocephalus must also be capable of reproducing chronic hydrocephalus – despite the significant differences in the pathophysiology of each form of hydrocephalus. The underlying pathophysiology of chronic hydrocephalus most likely involves changes in brain parenchyma, vascular resistance and CSF circulation, resulting in an altered intra-cranial compliance and diminished cerebral blood flow (Dombrowski et al., 2009).

Through a substantial review of clinical observations, Egnor et al. (2002) recommend several features that must be present in a comprehensive mathematical model of hydrocephalus. The list is extensive, although perhaps not exhaustive, and supplies a useful metric with which to judge the flexibility of the framework presented in this research; including:

- Deformation of the ventricles and the sub-arachnoid spaces;
- Elevated ICP and intra-cranial pressure waves;
- The temporal horns and third ventricle dilate first;
- Hyper-dynamic CSF pulsations in the aqueduct;
- Intra-cranial venous hypertension;
- Diminished cerebral blood flow;
- Diminished pressure gradient between sub-arachnoid spaces and venous sinuses;
- Mal-absorption of CSF;
- Hyper-dynamic arterial pulsations in the sub-arachnoid arteries; and,
- Selective compression of white matter and relative sparing of grey matter.

The search for improved understanding of NPH is imperative if we are to enable better diagnostic and treatment capabilities.

CHAPTER 3

MODELLING A POROUS, ELASTIC MEDIUM

This chapter outlines the mathematical methodology and numerical techniques used to develop a spatio-temporal model of water regulation and tissue displacement in the cerebral environment. Computational fluid dynamics will be coupled with other numerical discretization techniques thus enabling quantitative and qualitative clinical observations of acute and chronic hydrocephalus to be used for validation.

The relationship between the pressure of a fluid permeating a solid matrix and its displacement was first described by Biot (1941). In this instance, the model was developed to describe the settlement of soil under load and is now referred to (interchangeably) as consolidation theory, Biot theory, or poroelastic theory. The mechanism for consolidation is identical to the process of squeezing a fluid from an elastic porous medium such as a sponge; however, it was soon apparent that soil and rock contained both storage and transport porosities. Poroelastic theory was thus extended to multiple-network poroelastic theory (MPET) to model naturally fractured reservoirs (Aifantis, 1979, 1980; Aifantis and Hill, 1980; Bai et al., 1993; Berryman, 2002).

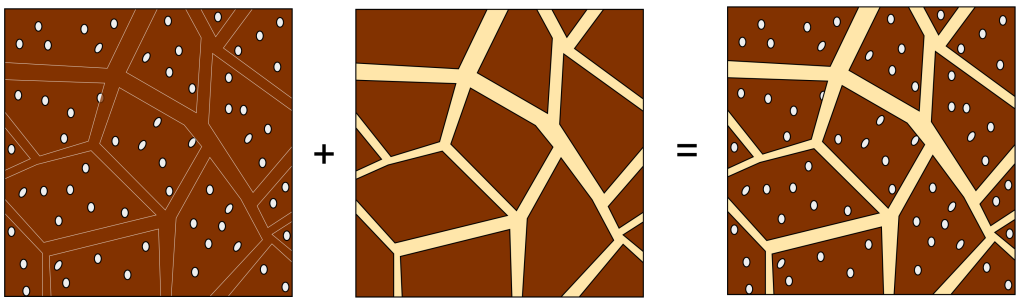

Figure 3.1: Description of a typical double MPET system used in geotechnical engineering. In this instance, the material is considered to be comprised of a solid matrix permeated by a network of low porosity pores and a network of high porosity fissures. Water transport can occur between the two fluid domains, each with a unique pressure and set of mechanical properties

3.1 MULTIPLE-NETWORK POROELASTIC THEORY

In geomechanics, the MPET medium is comprised of a solid matrix permeated by low porosity pores and high porosity fissures that are in communication and fluid can transfer between them (see Figure 3.1). MPET combines conservation of mass and momentum principles, porous flow laws, stress-strain relationships, and the Terzaghi effective stress principle (see (3.5)). Within the system, a solid matrix (superscript s) is permeated by $a = 1, \ldots, A$ different fluid networks each containing a unique porosity (n^a), density (ρ^a), permeability (k^a), pressure (p^a) and fluid velocity relative to the solid matrix (w_i^a / n^a).

3.1.1 System Equations

The equation of motion of the entire system is described with the fluid acceleration defined relative to the solid matrix (Bai et al., 1993; Beskos and Aifantis, 1986; Wilson and Aifantis, 1982; Zienkiewicz, 1982; Zienkiewicz and Shiomi, 1984; Zienkiewicz et al., 1990).

$$\sigma_{ij,j} + \rho\left(b_i - \frac{\partial^2 u_i}{\partial t^2}\right) = \sum_{a=1}^{A} \rho^a \left(\frac{\partial w_i^a}{\partial t} + w_j^a w_{i,j}^a\right) \tag{3.1}$$

where σ_{ij} is the stress in the solid matrix, b_i are the local body forces (eg. gravity), u_i is the displacement of the solid matrix, $\rho = \sum_{a=1}^{A} n^a \rho^a + (1-n)\rho_s$ is the total density

of the system, ρ_s is the density of the solid and $n = \sum_{a=1}^{A} n^a$ is the total porosity of the combined fluid networks.

The momentum of each fluid network (a) is described by the sum of divergence of the pore pressure field (p^a), external forces and viscous drag force (F^a) and is equal to the acceleration of the fluid relative to the solid matrix,

$$\rho^a \left(b_i - \frac{\partial^2 u_i}{\partial t^2} \right) - p^a_{,i} - F^a_i = \frac{\rho^a}{n^a} \left(\frac{\partial w^a_i}{\partial t} + w^a_j w^a_{i,j} \right). \tag{3.2}$$

Finally, the rate of change of fluid content for each network is a function of the compressibility of the system for a given strain rate, the flux of the fluid through the matrix, any source or sink terms, and the compressibility of the fluid.

$$\frac{1}{Q^a} \frac{\partial p^a}{\partial t} + \alpha^a \frac{\partial \epsilon_{ii}}{\partial t} + w^a_{i,i} - \sum_{b=1, b\neq a}^{A} \dot{s}_{b\rightarrow a} = -\frac{1}{\rho} \frac{\partial \rho^a}{\partial t} \tag{3.3}$$

where ϵ_{ij} is the strain in the solid matrix, α^a is the Biot parameter of the network a and $\dot{s}_{b\rightarrow a}$ is the rate of fluid exchange from network b to network a. The significance of the Biot parameter is discussed in more detail in §3.1.3 and Q^a indicates the combined compressibility of the solid and fluid phase and it is suggested in geomechanics to be related to the bulk moduli of each component (Biot and Willis, 1957; Zienkiewicz, 1982; Zienkiewicz et al., 1990) such that,

$$\frac{1}{Q^a} = \frac{n^a}{K^a} + \frac{\alpha^a - n^a}{K_s} \tag{3.4}$$

where K^a and K_s are the bulk moduli of the relevant fluid and solid phase, respectively (Liggett and Liu, 1983).

3.1.2 Ancillary Equations

The system of equations described in §3.1.1 can be combined with a set of ancillary constitutive equations that relate stress and strain. It is observable from experiments that when a porous medium is subjected to a uniform increase in fluid pressure, there is a relatively small deformation of the elastic matrix. This lead to Terzaghi's concept of effective stress(Terzaghi, 1943),

$$\sigma'_{ij} = \sigma_{ij} + \delta_{ij} p, \tag{3.5}$$

an extension, of which combined with Biot's theory (Biot, 1941; Biot and Willis, 1957; Zienkiewicz, 1982), to multiple fluid networks gives,

$$\sigma_{ij} = \sigma'_{ij} - \sum_{a=1}^{A} \alpha^a \delta_{ij} p^a \tag{3.6}$$

where σ_{ij} and σ'_{ij} are the total and effective stress in the solid matrix, respectively.

Stress and strain are related through constitutive and rotation matrices in the normal manner

$$\mathrm{d}\sigma'_{ij} = D_{ijkl}\left(\mathrm{d}\epsilon_{kl} - \mathrm{d}\epsilon^0_{kl}\right) + \sigma'_{ik}\mathrm{d}\omega_{kj} + \sigma'_{jk}\mathrm{d}\omega_{ki} \tag{3.7}$$

where ϵ^0_{ij} defines the initial strain state and the constitutive matrix is given by D_{ijkl}. Finally,

$$\mathrm{d}\epsilon_{ij} = \frac{1}{2}\left(\mathrm{d}u_{i,j} + \mathrm{d}u_{j,i}\right) \tag{3.8a}$$

$$\mathrm{d}\omega_{ij} = \frac{1}{2}\left(\mathrm{d}u_{j,i} - \mathrm{d}u_{i,j}\right) \tag{3.8b}$$

3.1.3 Poroelastic Constants

The physical meaning of the poroelastic constants (α^a and Q^a) introduced in (3.3) are not immediately obvious, nor intuitive. For understanding, it is useful to take the approach of Wang (2000) in its preview of the constitutive relations.

A single fluid network porous medium is represented by two linear constitutive equations for the case of an isotropic stress field, σ. Other quantaties are the volumetric strain, $\epsilon \equiv \frac{\delta V}{V}$, fluid content, ζ, and fluid pressure, p. Thus, the linear system can be given as,

$$\epsilon = \frac{1}{K}\sigma + \frac{1}{H}p, \tag{3.9a}$$

$$\zeta = \frac{1}{H}\sigma + \frac{1}{\Gamma}p. \tag{3.9b}$$

The equations are a statement of the observation that changes in applied stress and/or pore pressure: produce a fractional change in the volumetric strain; and, require fluid to be added of removed from storage in the pores, respectively. The poroelastic constants ($\frac{1}{K}$, $\frac{1}{H}$, and $\frac{1}{\Gamma}$) are defined as ratios of field variables while maintaining various constraints on the elementary control volume.

The coefficient $\frac{1}{K}$ measures the ratio of volumetric strain to applied stress while maintaining a constant pore pressure, referred to as the *drained condition*. As such, $\frac{1}{K}$ can be defined as the compressibility of the material measured under drained conditions, and K is the bulk modulus. The coefficient $\frac{1}{H}$ measures the ratio of volumetric strain to changes in the pore pressure under a constant applied stress and is analogous to the thermal expansion coefficient in thermoelasticity. Finally, $\frac{1}{\Gamma}$ is the unconstrained specific storage constant measured under conditions of constant applied stress and defines the rate of change in water content with respect to changes in the pore pressure.

These three constants, along with an independent constant such as the Poisson's ratio or shear modulus, completely define the linear single-network poroelastic model. However, to maintain the equations in their most general form it is more useful to define the system as a function of strain rather than stress, as shown in (3.16). Thus, (3.9) becomes more similar to the formulation by Biot (1941),

$$\sigma = K\epsilon - \frac{K}{H}p, \tag{3.10a}$$

$$\zeta = \frac{K}{H}\epsilon + \left(\frac{1}{\Gamma} - \frac{K}{H^2}\right)p, \tag{3.10b}$$

and allows us to relate the Biot parameter, $\alpha = \frac{K}{H}$, and constrained specific storage, $\frac{1}{Q} = \left(\frac{1}{\Gamma} - \frac{K}{H^2}\right)$, to those parameters already defined.

The constrained specific storage parameter has already be defined in terms of the porosity and relative moduli of the fluid and solid phases in (3.4). If we look at it in terms of (3.10), we can see that it defines the rate of change in water content with respect to changes in the pore pressure under conditions of constant volumetric strain.

Symmetry in the coupling of the linear system means that the Biot parameter can be defined by relating stress and pressure, (3.10a), or strain and water content, (3.10b). Using the latter, α is the rate of change of water content with respect to changes in the bulk volume under the assumption that pore pressure remains unchanged. Alternatively, α specifies the ratio of change in stress on the matrix divided by the change in pore pressure in the matrix in the absence of a change in bulk volume. In other words, in what proportions is an applied stress distributed through the fluid network; a value smaller than one indicates that the fluid is no longer able to bear all of the load and a proportion must be taken up by the matrix.

In a single network poroelastic model, decreasing the Biot parameter corresponds to an increase in compliance of the fluid network (defined as $C = \frac{\partial V}{\partial p}$) (Sobey and Wirth, 2006). In the cerebral poroelastic model it is postulated that the source of altered compliance of the parenchyma may be related to volumetric changes in the vascular networks (Bateman, 2000).

3.2 MODIFICATIONS FOR THE CEREBRAL ENVIRONMENT

Section 3.1 describes the interaction of many fluid networks permeating a deformable solid matrix. In this research, we propose that MPET may be used to describe the transport of water through biological tissue, effectively capturing the transfer between blood networks and the extracellular spaces. In doing so, we make several simplifications regarding relevant time scales, the solution geometry and material properties.

3.2.1 Simplified Governing Equations: the $u-p$ formulation

Equations (3.1), (3.2) and (3.3) with the ancillary equations (3.12), (3.6)-(3.8) present a well defined problem and solutions have been shown in the literature (Zienkiewicz, 1982; Zienkiewicz and Shiomi, 1984; Zienkiewicz et al., 1990). Albeit, the system is highly non-linear and hence computationally expensive. In a simplifying assumption, we take the flow of fluid in the individual networks to be slow, viscous flow (Reynold's number less than one), such that the right-hand side of equations (3.1), (3.2) and (3.3) can be neglected (Zienkiewicz and Bettess, 1982), giving,

$$\sigma_{ij,j} + \rho\left(b_i - \ddot{u}_i\right) = 0, \tag{3.11a}$$

$$\rho^a\left(b_i - \ddot{u}_i\right) - p^a_{,i} - F^a_i = 0, \tag{3.11b}$$

$$\frac{1}{Q^a}\dot{p^a} + \alpha^a \dot{\epsilon}_{ii} + w^a_{i,i} - \sum_{b=1, b\neq a}^{A} \dot{s}_{b\rightarrow a} = 0. \tag{3.11c}$$

Furthermore, the viscous drag force can be described by Darcy's law,

$$k^a_{ij} F^a_j = w^a_i, \tag{3.12}$$

where the permeability k_{ij} may be isotropic ($k_{ij} = k\delta_{ij}$) or, more likely, a function of fluid velocity or strain: $k_{ij} = k(w_i, n)_{ij}$ or $k_{ij} = k(w_i, u_{i,i})_{ij}$. This assumption is valid for flow through the low permeability networks such as the parenchyma and slow networks such as the capillary bed where the fluid's viscosity can be adjusted to capture the Fåhræus-Lindqvist effect.[1] However, Darcy's law is likely to be an over-simplification for the arterial network with large pipe diameters and higher peak velocities. For this initial study, we are prepared to accept this over-simplification and future work will move to resolve the arterial network with a higher spatial dimension or a more complex porous flow law.

The omission of fluid accelerations and the assumption of Darcy's law allows w_i^a to be eliminated from the system, retaining u and p^a as primary variables, by combining (3.12) and (3.11b),

$$w_i^a = k_{ij}^a \rho^a \left(b_j - \ddot{u}_j\right) - k_{ij}^a p_{,j}^a, \tag{3.13}$$

and substituting (3.13) into (3.11c),

$$\frac{1}{Q^a}\dot{p}^a + \alpha^a \dot{\epsilon}_{ii} + \left[k_{ij}^a \rho^a \left(b_j - \ddot{u}_j\right) - k_{ij}^a p_{,j}^a\right]_{,i} - \sum_{b=1, b\neq a}^{A} \dot{s}_{b\to a} = 0. \tag{3.14}$$

The primary equation of motion, (3.11a), is combined with the effective stress, (3.6),

$$\sigma'_{ij,j} - \sum_{a=1}^{A} \alpha^a \delta_{ij} p_{,j}^a + \rho\left(b_i - \ddot{u}_i\right) = 0, \tag{3.15}$$

and the final system, Equations (3.14) and (3.15), is thus written in vector notation as:

$$\nabla \cdot \boldsymbol{\sigma}' - \sum_{a=1}^{A} \alpha^a \nabla p^a + \rho\left(\mathrm{b} - \frac{\partial^2 \mathrm{u}}{\partial t^2}\right) = 0, \tag{3.16a}$$

$$\frac{1}{Q^a}\frac{\partial p^a}{\partial t} + \alpha^a \frac{\partial(\nabla \cdot \mathrm{u})}{\partial t} + \nabla \cdot \left[\mathrm{k}^a \cdot \rho^a \left(\mathrm{b} - \frac{\partial^2 \mathrm{u}}{\partial t^2}\right) - \mathrm{k}^a \cdot \nabla p^a\right] - \sum_{b=1, b\neq a}^{A} \dot{s}_{b\to a} = 0. \tag{3.16b}$$

3.2.2 General Assumptions

As the research progresses, applications of the MPET framework will take on specific assumptions. However, assumptions about the system geometry and material properties of the parenchyma and CSF network will remain largely consistent.

[1] The Fåhræus-Lindqvist effect explains the decrease in apparent viscosity of a suspension fluid, such as blood, as the diameter of the tube decreases below 0.3 mm.

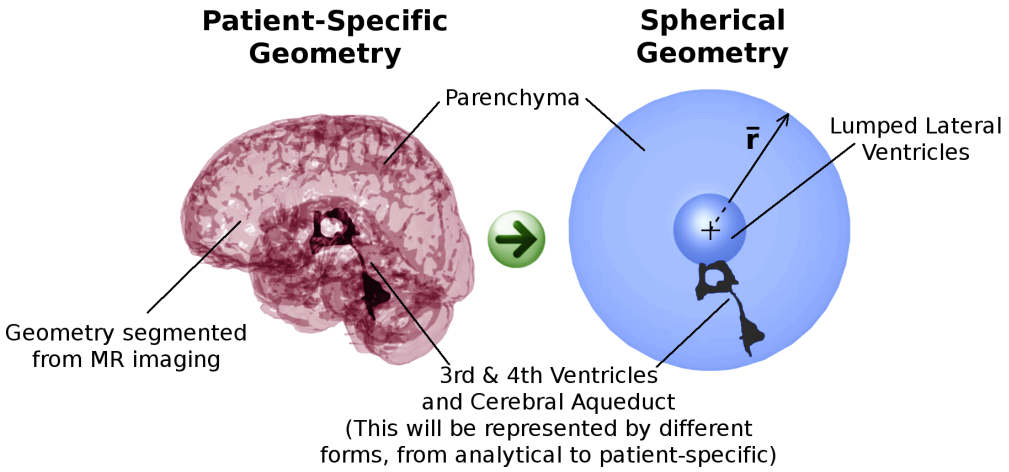

Figure 3.2: Computational domain of the brain with a 3-D representation of the cerebral aqueduct. The parenchyma of the brain is simplified to a spherical shell with physically relevant values for the ventricle and tissue radii of a healthy adult male. The ventricles are connected to the sub-arachnoid space via a representation of the cerebral aqueduct, third and fourth ventricles; depending on the case under investigation, this channel may be specified as a one-dimensional analytical pipe, or an axi-symmetric, three-dimensional or patient specific volume.

Thus far, the MPET framework has been described independently of coordinate system. For this report, however, we use a spherical representation of the geometry of the brain (see Figure 3.2). While this is a significant simplification, it maintains the mechanical properties that we are concerned with. The parenchyma of the brain is simplified to a spherical shell with physically relevant values for the ventricle and tissue radii of a healthy adult male. The shell is assigned an outer radius $r_M = 100$ mm and the lateral ventricles lumped together as a spherical cavity of radius $r_1 = 30$ mm (Kaczmarek et al., 1997). We assume that we are modelling an adult human so the skull can be treated as a rigid wall (Smillie et al., 2005), as a result, the sub-arachnoid space, dura mater, skull and scalp are ignored without a loss of generality in the model.

Within the lumped ventricles, we assume that CSF is produced at a constant production rate of Q_p and the ventricles are connected to the sub-arachnoid space via a representation of the cerebral aqueduct, third and fourth ventricles. Depending on the model under investigation, this channel may be specified as a one-dimensional, analytical pipe (with diameter $d = 4$ mm in the healthy configuration) obeying Poiseuille flow law; or alternatively, it may be defined as an axi-symmetric, three-

Parameter	Value	Parameter	Value
r_1	30×10^{-3} m	E	584 Pa
r_M	100×10^{-3} m	ν	0.35
d	4×10^{-3} m	μ^e	8.9×10^{-4} Nsm^{-2}
ρ^e	997 kgm^{-3}	Q_p	5.8×10^{-9} m^{3}s^{-1}
α^e	1.0	R	8.5×10^{13} m^{-3}
κ^e	1.4×10^{-14} m^2	p_{bp}	650 Pa

Table 3.1: Physical values used in the single network poroelastic equations (Smillie et al., 2005; Tully and Ventikos, 2009).

dimensional or patient specific volume.

The success of computational models of hydrocephalus is heavily reliant on experimental data to provide accurate values for the physical factors in the model (Tully and Ventikos, 2009). The general properties of the CSF (viscosity, μ^e, and density, ρ^e) are well known; while the permeability, κ^e, and Biot parameter, α^e, of the interstitial fluid network are approximated in the literature and we adopt the same values as published in Smillie et al. (2005). However, such data are scarce for parenchyma tissue and there are inherent difficulties in applying traditional mechanical tests to tissue. This is particularly true when the tissue is likely to have 'active' transport mechanisms that will not be functional in excised tissue.

Clinical studies show that there is an observable difference in the properties of the white and grey matter. However, there is a lack of appropriate experimental data to quantify these differences. Hence, many current models treat the parenchyma as a homogeneous tissue (Levine, 1999, 2000; Sobey and Wirth, 2006; Tully and Ventikos, 2009; Wirth and Sobey, 2006). Promising studies using magnetic resonance elastography (MRE) calculate the shear stiffness of cerebral tissue *in vivo*, however, they are yet to establish a consistent and agreeable value with the reported numbers differing by orders of magnitude (Sack et al., 2008; Kruse et al., 2008). For this study, we continue to use the data selected by the current state-of-the-art as summarized in Table 3.1.

3.2.3 Single-Network Poroelastic Theory

Both the historical first, and the simplest form of the MPET framework is a solid matrix permeated by exactly one fluid network (Biot, 1941). In the absence of external forces, all multiple-network poroelastic models must reduce to single-network poroelastic theory (SPET) (Berryman, 2002). The model is a simplification of (3.16) made by setting $A = 1$ the parenchyma is considered to be a solid, deformable matrix permeated by a single network of interstitial pores filled with CSF (superscript e):

$$\nabla \cdot \boldsymbol{\sigma}' - \alpha^e \nabla p^e + \rho^e \left(\mathrm{b} - \frac{\partial^2 \mathrm{u}}{\partial t^2} \right) = 0, \tag{3.17a}$$

$$\frac{1}{Q^e} \frac{\partial p^e}{\partial t} + \alpha^e \frac{\partial (\nabla \cdot \mathrm{u})}{\partial t} + \nabla \cdot \left[\mathrm{k}^e \cdot \rho^e \left(\mathrm{b} - \frac{\partial^2 \mathrm{u}}{\partial t^2} \right) - \mathrm{k}^e \cdot \nabla p^e \right] - \dot{s}_0 = 0, \tag{3.17b}$$

where $\dot{s}_0$ describes any additional sink or source of fluid in the parenchyma.

The SPET equations have been used successfully in the modelling of a host of biomechanical processes. For instance, studies on the relationship of water and tissue in cartilage (Ateshian and Wang, 1995; Tanck et al., 1999) while poroelastic representations of the brain have been utilized to demonstrate qualitative information about the pathophysiology of acute and chronic hydrocephalus (Kaczmarek et al., 1997; Levine, 1999, 2000, 2008; Smillie et al., 2005; Sobey and Wirth, 2006; Wirth and Sobey, 2006). For reasons of simplicity, these published models assume a linear stress-strain relationship in the parenchyma such that the effective stress is given by (the generalized Hooke's law (B.3) inverted for stress according to §B.2.1),

$$\boldsymbol{\sigma}' = 2G \left[\boldsymbol{\epsilon} + \frac{\nu}{1-2\nu} \mathrm{Tr}(\boldsymbol{\epsilon}) \mathrm{I} \right], \tag{3.18}$$

where $G = \frac{E}{2(1+\nu)}$ is the shear modulus of the tissue, $\varepsilon = \mathrm{Tr}(\boldsymbol{\epsilon})$ is the volumetric strain and ν is the Poisson's ratio.

Substituting (3.18) (through the conversion in §B.2.2) and an isotropic permeability (i.e. $k_{ij} = k\delta_{ij} = \frac{\kappa}{\mu}\delta_{ij}$) into (3.17), the well known SPET equations are recovered:

$$G\nabla^2 \mathrm{u} + \frac{G}{1-2\nu} \nabla (\nabla \cdot \mathrm{u}) - \alpha^e \nabla p^e + \rho^e \left(\mathrm{b} - \frac{\partial^2 \mathrm{u}}{\partial t^2} \right) = 0, \tag{3.19a}$$

$$\frac{1}{c} Q \frac{\partial p^e}{\partial t} + \alpha^e \frac{\partial (\nabla \cdot \mathrm{u})}{\partial t} - k^e \nabla^2 p^e + k^e \nabla \cdot \left[\rho^e \left(\mathrm{b} - \frac{\partial^2 \mathrm{u}}{\partial t^2} \right) \right] - \dot{s}_0 = 0. \tag{3.19b}$$

Finally, this vectorial system can be simplified to the spherically symmetric geometry outlined in the previous section using the transformations in Appendix B.1, giving the ultimate SPET system as:

$$G\left(\frac{\partial^2 u}{\partial r^2}+\frac{2}{r}\frac{\partial u}{\partial r}-\frac{2}{r^2}u\right)+\frac{G}{1-2\nu}\left(\frac{\partial^2 u}{\partial r^2}+\frac{2}{r}\frac{\partial u}{\partial r}-\frac{2}{r^2}u\right)-\alpha\frac{\partial p}{\partial r}+\rho\left(b_r-\frac{\partial^2 u}{\partial t^2}\right)=0$$

$$\frac{\partial^2 u}{\partial r^2}+\frac{2}{r}\frac{\partial u}{\partial r}-\frac{2}{r^2}u-\frac{1-2\nu}{2G(1-\nu)}\left[\alpha\frac{\partial p}{\partial r}-\rho\left(b_r-\frac{\partial^2 u}{\partial t^2}\right)\right]=0 \tag{3.20a}$$

$$\frac{1}{Q}\frac{\partial p}{\partial t}+\alpha\frac{\partial}{\partial t}\left(\frac{\partial u}{\partial r}+\frac{2}{r}u\right)-k\left(\frac{\partial^2 p}{\partial r^2}+\frac{2}{r}\frac{\partial p}{\partial r}\right)+k\left[\frac{\partial\rho^a\left(b_r-\ddot{u}\right)}{\partial r}+\frac{2}{r}\rho^a\left(b_r-\frac{\partial^2 u}{\partial t^2}\right)\right]-\dot{s}_0=0 \tag{3.20b}$$

3.2.4 Multiple-Network Poroelastic Theory

While the SPET model produces ventricular dilation that correlate with clinical data, it has been shown that the single network poroelastic model may underestimate the ventricular displacement when physically relevant aqueductal stenosis patterns are used to model acute hydrocephalus (Tully and Ventikos, 2009) (cf. Chapter 4). This discrepancy might be explained by the conflation of the blood and CSF into one fluid network.

In order to fully capture the dynamics of fluid transfer in the brain, the MPET framework is extended to include independent networks for the cerebral blood and CSF. The interstitial fluid can be considered as a slow moving flow through a low porosity, low permeability network, while the network of blood vessels have a higher porosity and permeability.

The elegant transfer of fluid between networks in the MPET framework is both a strength and a weakness. In soil, the transfer of fluid between fluid networks is described using a scaled hydrostatic pressure gradient (Bai et al., 1993); in the biological context, it is likely that this transfer will be driven by more complex processes that require empirical relationships to be developed. However, active and/or biological transfer mechanisms (for instance cellular-level water-flux through aquaporins (Agre et al., 2004; Agre, 2006)) are not adequately well-quantified yet for inclusion in the model.

A double fluid-network approach with a blood network and a CSF network advances the model beyond the state-of-the-art. By setting $A = 2$ in equations (3.16a)

and (3.16b) (where b represents the blood network and e is the CSF network) we achieve the pragmatic equivalent to the Equations (1)–(3) in Bai et al. (1999).

$$\nabla \cdot \boldsymbol{\sigma}' - \alpha^b \nabla p^b - \alpha^e \nabla p^e + \rho \left(\mathrm{b} - \frac{\partial^2 \mathrm{u}}{\partial t^2} \right) = 0, \tag{3.21a}$$

$$\frac{1}{Q^b} \frac{\partial p^b}{\partial t} + \alpha^b \frac{\partial (\nabla \cdot \mathrm{u})}{\partial t} + \nabla \cdot \left[\mathrm{k}^b \cdot \rho^b \left(\mathrm{b} - \frac{\partial^2 \mathrm{u}}{\partial t^2} \right) - \mathrm{k}^b \cdot \nabla p^b \right] - \dot{s}_{e \to b} = 0, \tag{3.21b}$$

$$\frac{1}{Q^e} \frac{\partial p^e}{\partial t} + \alpha^e \frac{\partial (\nabla \cdot \mathrm{u})}{\partial t} + \nabla \cdot \left[\mathrm{k}^e \cdot \rho^e \left(\mathrm{b} - \frac{\partial^2 \mathrm{u}}{\partial t^2} \right) - \mathrm{k}^e \cdot \nabla p^e \right] - \dot{s}_{b \to e} = 0. \tag{3.21c}$$

However, the two-network system is limited by the necessary implementation issues of applying physically relevant boundary conditions and transfer coefficients. This problem is overcome by extending the model to $A = 3$ in equations (3.16a) and (3.16b) (where a represents the arterial blood network, v the venous blood network and e is the CSF network) giving a three compartment model of the cerebral environment:

$$\nabla \cdot \boldsymbol{\sigma}' - \alpha^a \nabla p^a - \alpha^e \nabla p^e - \alpha^v \nabla p^v + \rho \left(\mathrm{b} - \frac{\partial^2 \mathrm{u}}{\partial t^2} \right) = 0, \tag{3.22a}$$

$$\frac{1}{Q^a} \frac{\partial p^a}{\partial t} + \alpha^a \frac{\partial (\nabla \cdot \mathrm{u})}{\partial t} + \nabla \cdot \left[\mathrm{k}^a \cdot \rho^a \left(\mathrm{b} - \frac{\partial^2 \mathrm{u}}{\partial t^2} \right) - \mathrm{k}^a \cdot \nabla p^a \right] - \dot{s}_{e \to a} - \dot{s}_{v \to a} = 0, \tag{3.22b}$$

$$\frac{1}{Q^e} \frac{\partial p^e}{\partial t} + \alpha^e \frac{\partial (\nabla \cdot \mathrm{u})}{\partial t} + \nabla \cdot \left[\mathrm{k}^e \cdot \rho^e \left(\mathrm{b} - \frac{\partial^2 \mathrm{u}}{\partial t^2} \right) - \mathrm{k}^e \cdot \nabla p^e \right] - \dot{s}_{a \to e} - \dot{s}_{v \to e} = 0, \tag{3.22c}$$

$$\frac{1}{Q^v} \frac{\partial p^v}{\partial t} + \alpha^v \frac{\partial (\nabla \cdot \mathrm{u})}{\partial t} + \nabla \cdot \left[\mathrm{k}^v \cdot \rho^v \left(\mathrm{b} - \frac{\partial^2 \mathrm{u}}{\partial t^2} \right) - \mathrm{k}^v \cdot \nabla p^v \right] - \dot{s}_{a \to v} - \dot{s}_{e \to v} = 0. \tag{3.22d}$$

This added complexity allows a better implementation of the physical system by extending the model to include a high pressure arterial network and a low pressure venous network. Specifically, this allows the model to capture the source and drainage of fluid from the CSF network. However, in the physical system when blood passes from the arteries, through the arterioles and into the capillaries there is a significant pressure drop that is not captured sufficiently by the three-network model.

Finally, it appears that the most appropriate MPET model is a quadruple fluid-network system where the arterial blood compartment is further segmented into the high pressure arterial network and the lower pressure arteriole/capillary network (Figure 3.3). Setting $A = 4$ in equations (3.16a) and (3.16b) (where a represents the arterial blood network, c the arteriole/capillary network, e is the extracellular/CSF

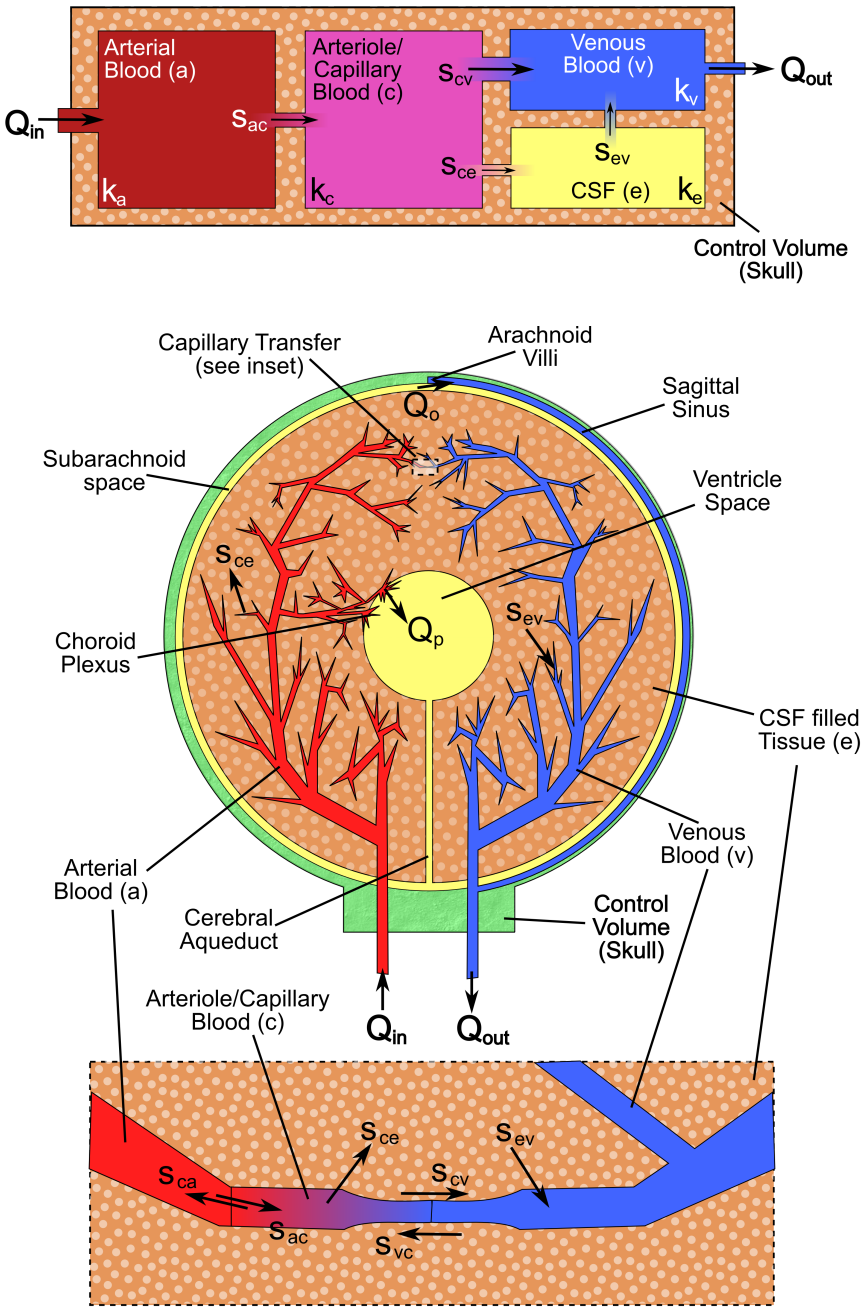

Figure 3.3: A four-network MPET description of the brain. Based on arguments about the wall thickness and 'leakiness' of blood vessels in this system, assumptions are made about transfer between the fluid networks. Directional transfer can occur from the arteriole/capillary network to the CSF and venous networks and from the CSF to the venous network. Flow is prohibited between the CSF and arterial network, or directionally from the venous network to the CSF or arteriole/capillary networks (more detail is given in §5.1).

network and v is the venous blood network) gives a four-compartment model:

$$\nabla\cdot\boldsymbol{\sigma}' - \alpha^a\nabla p^a - \alpha^c\nabla p^c - \alpha^e\nabla p^e - \alpha^v\nabla p^v + \rho\left(\mathrm{b} - \frac{\partial^2\mathrm{u}}{\partial t^2}\right) = 0, \tag{3.23a}$$

$$\frac{1}{Q^a}\frac{\partial p^a}{\partial t} + \alpha^a\frac{\partial(\nabla\cdot\mathrm{u})}{\partial t} + \nabla\cdot\left[\mathrm{k}^a\cdot\rho^a\left(\mathrm{b} - \frac{\partial^2\mathrm{u}}{\partial t^2}\right) - \mathrm{k}^a\cdot\nabla p^a\right] - \dot{s}_{c\to a} - \dot{s}_{e\to a} - \dot{s}_{v\to a} = 0, \tag{3.23b}$$

$$\frac{1}{Q^c}\frac{\partial p^c}{\partial t} + \alpha^c\frac{\partial(\nabla\cdot\mathrm{u})}{\partial t} + \nabla\cdot\left[\mathrm{k}^c\cdot\rho^c\left(\mathrm{b} - \frac{\partial^2\mathrm{u}}{\partial t^2}\right) - \mathrm{k}^c\cdot\nabla p^c\right] - \dot{s}_{a\to c} - \dot{s}_{e\to c} - \dot{s}_{v\to c} = 0, \tag{3.23c}$$

$$\frac{1}{Q^e}\frac{\partial p^e}{\partial t} + \alpha^e\frac{\partial(\nabla\cdot\mathrm{u})}{\partial t} + \nabla\cdot\left[\mathrm{k}^e\cdot\rho^e\left(\mathrm{b} - \frac{\partial^2\mathrm{u}}{\partial t^2}\right) - \mathrm{k}^e\cdot\nabla p^e\right] - \dot{s}_{a\to e} - \dot{s}_{c\to e} - \dot{s}_{v\to e} = 0, \tag{3.23d}$$

$$\frac{1}{Q^v}\frac{\partial p^v}{\partial t} + \alpha^v\frac{\partial(\nabla\cdot\mathrm{u})}{\partial t} + \nabla\cdot\left[\mathrm{k}^v\cdot\rho^v\left(\mathrm{b} - \frac{\partial^2\mathrm{u}}{\partial t^2}\right) - \mathrm{k}^v\cdot\nabla p^v\right] - \dot{s}_{a\to v} - \dot{s}_{c\to v} - \dot{s}_{e\to v} = 0. \tag{3.23e}$$

Further generalizations are made by assuming the stress-strain relationship is linear, as in (3.18), and the permeabilities are isotropic:

$$G\nabla^2\mathrm{u} + \frac{G}{1-2\nu}\nabla(\nabla\cdot\mathrm{u}) - \alpha^a\nabla p^a - \alpha^c\nabla p^c - \alpha^e\nabla p^e - \alpha^v\nabla p^v + \rho\left(\mathrm{b} - \frac{\partial^2\mathrm{u}}{\partial t^2}\right) = 0, \tag{3.24a}$$

$$\frac{1}{Q}\frac{\partial p^a}{\partial t} + \alpha^a\frac{\partial(\nabla\cdot\mathrm{u})}{\partial t} - k^a\nabla^2 p^a + k^a\nabla\cdot\left[\rho^a\left(\mathrm{b} - \frac{\partial^2\mathrm{u}}{\partial t^2}\right)\right] - \dot{s}_{c\to a} - \dot{s}_{e\to a} - \dot{s}_{v\to a} = 0, \tag{3.24b}$$

$$\frac{1}{Q}\frac{\partial p^c}{\partial t} + \alpha^c\frac{\partial(\nabla\cdot\mathrm{u})}{\partial t} - k^c\nabla^2 p^c + k^c\nabla\cdot\left[\rho^c\left(\mathrm{b} - \frac{\partial^2\mathrm{u}}{\partial t^2}\right)\right] - \dot{s}_{a\to c} - \dot{s}_{e\to c} - \dot{s}_{v\to c} = 0, \tag{3.24c}$$

$$\frac{1}{Q}\frac{\partial p^e}{\partial t} + \alpha^e\frac{\partial(\nabla\cdot\mathrm{u})}{\partial t} - k^e\nabla^2 p^e + k^e\nabla\cdot\left[\rho^e\left(\mathrm{b} - \frac{\partial^2\mathrm{u}}{\partial t^2}\right)\right] - \dot{s}_{a\to e} - \dot{s}_{c\to e} - \dot{s}_{v\to e} = 0, \tag{3.24d}$$

$$\frac{1}{Q}\frac{\partial p^v}{\partial t} + \alpha^v\frac{\partial(\nabla\cdot\mathrm{u})}{\partial t} - k^v\nabla^2 p^v + k^v\nabla\cdot\left[\rho^v\left(\mathrm{b} - \frac{\partial^2\mathrm{u}}{\partial t^2}\right)\right] - \dot{s}_{a\to v} - \dot{s}_{c\to v} - \dot{s}_{e\to v} = 0, \tag{3.24e}$$

Using standard transformations for the spherical geometry (Appendix B.1), we can shift (3.24) to the spherically symmetric (one-dimensional) geometry giving the final system equations of the cerebral environment as:

$$\frac{\partial^2 u}{\partial r^2} + \frac{2}{r}\frac{\partial u}{\partial r} - \frac{2}{r^2}u = \frac{1-2\nu}{2G(1-\nu)}\left[\alpha^a\frac{\partial p^a}{\partial r} + \alpha^c\frac{\partial p^c}{\partial r} + \alpha^e\frac{\partial p^e}{\partial r} + \alpha^v\frac{\partial p^v}{\partial r} - \rho\left(b_r - \frac{\partial^2 u}{\partial t^2}\right)\right] \tag{3.25a}$$

$$\frac{1}{Q^a}\frac{\partial p^a}{\partial t} + \alpha^a\frac{\partial}{\partial t}\left(\frac{\partial u}{\partial r} + \frac{2}{r}u\right) - k^a\left(\frac{\partial^2 p^a}{\partial r^2} + \frac{2}{r}\frac{\partial p^a}{\partial r}\right) + k^a\left[\frac{\partial\rho^a(b_r - \ddot{u})}{\partial r} + \frac{2}{r}\rho^a\left(b_r - \frac{\partial^2 u}{\partial t^2}\right)\right] - \dot{s}_{c\to a} - \dot{s}_{e\to a} - \dot{s}_{v\to a} = 0 \tag{3.25b}$$

$$\frac{1}{Q^c}\frac{\partial p^c}{\partial t} + \alpha^c\frac{\partial}{\partial t}\left(\frac{\partial u}{\partial r} + \frac{2}{r}u\right) - k^c\left(\frac{\partial^2 p^c}{\partial r^2} + \frac{2}{r}\frac{\partial p^c}{\partial r}\right) + k^c\left[\frac{\partial\rho^c(b_r - \ddot{u})}{\partial r} + \frac{2}{r}\rho^c\left(b_r - \frac{\partial^2 u}{\partial t^2}\right)\right] - \dot{s}_{a\to c} - \dot{s}_{e\to c} - \dot{s}_{v\to c} = 0 \tag{3.25c}$$

$$\frac{1}{Q^e}\frac{\partial p^e}{\partial t} + \alpha^e \frac{\partial}{\partial t}\left(\frac{\partial u}{\partial r} + \frac{2}{r}u\right) - k^e\left(\frac{\partial^2 p^e}{\partial r^2} + \frac{2}{r}\frac{\partial p^e}{\partial r}\right) + k^e\left[\frac{\partial \rho^e (b_r - \ddot{u})}{\partial r} + \frac{2}{r}\rho^e\left(b_r - \frac{\partial^2 u}{\partial t^2}\right)\right] - \dot{s}_{a\to e} - \dot{s}_{c\to e} - \dot{s}_{v\to e} = 0 \quad (3.25d)$$

$$\frac{1}{Q^v}\frac{\partial p^v}{\partial t} + \alpha^v \frac{\partial}{\partial t}\left(\frac{\partial u}{\partial r} + \frac{2}{r}u\right) - k^v\left(\frac{\partial^2 p^v}{\partial r^2} + \frac{2}{r}\frac{\partial p^v}{\partial r}\right) + k^v\left[\frac{\partial \rho^v (b_r - \ddot{u})}{\partial r} + \frac{2}{r}\rho^v\left(b_r - \frac{\partial^2 u}{\partial t^2}\right)\right] - \dot{s}_{a\to v} - \dot{s}_{c\to v} - \dot{s}_{e\to v} = 0. \quad (3.25e)$$

Obviously, it is possible to continue the breakdown of cerebral blood networks into smaller compartments, however, there is a fine balance between gaining enough flexibility to represent the physical system, and being overloaded by model constants (such as Biot parameters) for which there are no experimental data.

CHAPTER 4

ACUTE HYDROCEPHALUS

Acute hydrocephalus is dominated by a radiographically identifiable blockage of the cerebral aqueduct. The current state-of-the-art uses Single-Network Poroelastic (SPET) models to investigate the cerebral environment in a simplified geometry. In this chapter we use the reduced system, SPET, to replicate the state-of-the-art and extend it to patient-specific geometries.
This chapter has been published in an alternative form in Tully and Ventikos (2009).

In acute hydrocephalus there are several possible locations for CSF flow obstruction to occur: the foramen of Monro, the aqueduct of sylvius, the fourth ventricle, the foramina of Luschka and the foramen of Magendie, and the sub-arachnoid space surrounding the brain stem. The most common location of obstruction is the aqueduct of sylvius, referred to from here on as the cerebral aqueduct or simply the aqueduct. The aqueduct, joining the third and fourth ventricles, is normally narrow already and may be obstructed by a number of congenital, genetic, or acquired lesions and generally leads to dilatation of both lateral ventricles and the third ventricle.

It has been shown in the current state-of-the-art that the SPET model described in §4.1 is useful for investigating acute hydrocephalus (Smillie et al., 2005; Sobey and Wirth, 2006; Wirth and Sobey, 2006). In this chapter, the mathematical model is converted to a discrete numerical system and implemented in a stand-alone numerical solver. In the first instance, the solver is used to replicate the results of the

literature and subsequent investigations delve into understanding more about the dynamics of the system as a whole; such as including the effect of changing the aqueduct diameter and introducing pulsatility to the system.

Finally, we will then investigate the capability of the model to represent acute hydrocephalus caused by obstruction of the cerebral aqueduct. This will done by comparing the differences between one-dimensional analytic and multi-dimensional numerical representations for the flow of CSF through the stenosed aqueduct

4.1 SPET: MODELLING IN ONE-DIMENSION

The first stage of the investigation is to reproduce the results that are published in Smillie et al. (2005). In this study, the authors use a spherical representation of the SPET system with physical and material constants introduced based on various literature. Importantly, the flow of CSF through the cerebral aqueduct is considered to obey Poiseuille flow through a pipe. This obvious and distinct simplification allows the model to be computed in a purely one-dimensional fashion. In doing so, the computations are quick and certain system dynamics can be interrogated efficiently; however, it also restricts the level of quantitative information that can be gathered from the final result.

An important finding that can be garnered from the implementation of SPET in studying acute hydrocephalus is the extent to which the aqueduct must be obstructed before the ventricles enlarge. One of the goals here is to assess the charge that stenosis of the aqueduct cannot be regarded as the cause of hydrocephalus unless the cross-sectional area of the most severely constricted area is less than 0.031mm^2 (or an equivalent circular diameter of 0.2mm) (Woollam and Millen, 1953). Furthermore, by altering the time profile of the aqueduct diameter a more complete investigation into the nature of the poroelastic equations is possible. In essence, this value determines the amount of CSF that is able to flow through the analytic aqueduct (cf. (4.3)).

One of the many hypotheses for hydrocephalus relates to an alteration of the pulsatile properties of the cerebral environment. Until now, this has been largely ignored in the poroelastic modelling of hydrocephalus. In an effort to increase the

clinical applicability of this study, we investigate the potential transient nature of the system and, in particular, the effect from the pulsatile blood pressure.

Several authors believe that the pulsatile motion of the CSF cannot be ignored as a factor in hydrocephalus (Egnor et al., 2001, 2002; Greitz, 2004; Linninger et al., 2005, 2007; Madsen et al., 2006). MRI studies clearly show that CSF flows in and out of the cerebral aqueduct in a pulsatile manner, with a peak velocity much greater than that assumed in the bulk flow hypothesis; however, it is unclear as to the source of these oscillations.

To investigate the role of pulsations, this study considers three different locations for the driving force. The first location involves linking the cerebrovenous pressure – which is intuitively pulsatile like most major vessels in the body – to pulsations within the heart. Secondly, the production of CSF is specified in a pulsatile manner in order to model the potential blood pulse travelling through the capillaries in the choroid plexus. Finally, it is hypothesized that a decreased compliance of the brain tissue leads to a decrease in its ability to dissipate the pulsations of the arterial vessels resulting in an abnormally high displacement of tissue during the cardiac cycle (Egnor et al., 2001). Thus, we indirectly investigate this in the third case by manually adjusting the boundary conditions to invoke a pulsatile volume change in the cerebral tissue/blood network, mimicking the difference in blood volume through systole and diastole.

4.1.1 Methodology

The approach taken to the study of acute hydrocephalus is to simplify the most general form of the SPET model to a spherically symmetric representation of the system. This model is then implemented in a C++ solver which can be modified to investigate the disease, or coupled in a novel manner to the multi-physics simulation of CSF flow through the aqueduct.

4.1.1.1 Final Model Assumptions

Simplifications are made to the model to enable a thorough investigation of the parameters of specific interest. We assume the time scale for development of hydrocephalus is in the order of days and weeks (possibly even years) and so it is reason-

able to assume that the system is quasi-steady ($\frac{\partial^2}{\partial t^2}, \frac{\partial}{\partial t} \to 0$). There are no external forces on, or sources in, the system ($b_r = 0$ and $\dot{s}_0 = 0$); gravity is neglected; and, the reference frame is stationary. Hence, the system equations, (3.20), reduce to:

$$\frac{\partial^2 u}{\partial r^2} + \frac{2}{r}\frac{\partial u}{\partial r} - \frac{2}{r^2}u - \frac{1-2\nu}{2G(1-\nu)}\alpha\frac{\partial p}{\partial r} = 0 \tag{4.1a}$$

$$\frac{\partial^2 p}{\partial r^2} + \frac{2}{r}\frac{\partial p}{\partial r} = 0, \tag{4.1b}$$

with a requirement of four boundary conditions to be satisfied for closure. Two are applied at the wall of the ventricles ($r = r_1$) and two at the sub-arachnoid space / skull ($r = r_M$) (Smillie et al., 2005).

4.1.1.1.1 Boundary Conditions at the Ventricular Wall

The first boundary condition is given by the pressure and stress equilibrium on the ventricle wall as derived from Equation (3.17). The implies conservation of mass and introduces a quasi-steady time dependence for the system,

$$\frac{2G}{1-2\nu}\left[(1-\nu)\left.\frac{\partial u}{\partial r}\right|_{r_1} + 2\nu\frac{u(r_1,t)}{r_1}\right] = (\alpha-1)\,p(r_1,t). \tag{4.2}$$

Within the ventricles, it is assumed that any CSF that is produced (Q_p) and does not flow through the cerebral aqueduct or the parenchyma (obeying Darcy's Law) must accumulate within the ventricles and cause the volume to increase,

$$\begin{aligned} Q_p = {} & \frac{\pi d^4}{128\mu L}\left[p(r_1,t) - p(r_M,t)\right] \\ & - \frac{4\pi\kappa\left[r_1 + u(r_1,t)\right]^2}{\mu}\left.\frac{\partial p}{\partial r}\right|_{r_1} \\ & + 4\pi\left[r_1 + u(r_1,t)\right]^2\left.\frac{\partial u}{\partial t}\right|_{r_1}. \end{aligned} \tag{4.3}$$

In the first instance, the flow through the aqueduct is modelled using Poiseuille's Law[1]; however, when the poroelastic model is coupled to a multi-dimensional simulation of the aqueduct (see §4.2), this term in the RHS of (4.3) is computed from the numerical flow simulation. Furthermore, this boundary condition can also be modified to include time-varying parameters that investigate the effect of pulsatility (as in §4.1.2.3).

[1] Poiseuille's Law: $Q_{Poiseuille} = \frac{\pi d^4}{128\mu L}\left[p(r_1,t) - p(r_M,t)\right]$

4.1.1.1.2 Boundary Conditions at the Skull We assume zero deformation of a purely rigid skull (valid exclusively for the investigation of hydrocephalus where the skull has fused),

$$u(r_M, t) = 0, \tag{4.4}$$

and that CSF absorption at the skull causes a pressure rise dependent on the resistance to absorption at the arachnoid granulation, R, and the rate of absorption, Q_o, such that,

$$p(r_M, t) = p_{bp} + \mu R Q_o. \tag{4.5}$$

Here p_{bp} is the blood pressure in the sagittal sinus, μ is the dynamic viscosity of the CSF and in the quasi-steady approach adopted in this research the rate of absorption, Q_o, is assumed to be the same as the production rate, Q_p.

4.1.1.1.3 Pulsatile Boundary Conditions The first major extension of the state-of-the-art comes from introducing dynamic specifications in the boundary conditions of the model. In order to investigate the role of pulsations in the cerebral environment, we impose a dynamic oscillation to three different variables in the boundary conditions of the poroelastic solver. Starting from the idealized equation representing the cardiac cycle (Linninger et al., 2007),

$$\phi(t) = \phi_0 + \alpha \left[\sin\left(\omega t - \frac{\pi}{2}\right) - \frac{1}{2}\cos\left(\omega t - \frac{\pi}{2}\right) \right], \tag{4.6}$$

we modify ϕ_0 and α as appropriate to each case below, while ω is chosen so that the oscillations pulse with a frequency of 1 Hz.

Case 1: Pulsation is applied to the blood pressure, $\phi = p_{bp}$, in (4.5), synonymous to a pulsation of the pressure in the venous sinus that causes a dynamic pressure in the sub-arachnoid space.

Case 2: Pulsation is applied to the production of CSF, $\phi = Q_p$, in (4.3), testing the theory that pulsations in the choroid plexus give a dynamic production of CSF and hence impact the ventricular dynamics.

Case 3: Pulsation is applied by modifying (4.3) to artificially oscillate the ventricular volume by adding or subtracting from the displacement at the ventricular wall, $\phi = \Delta u$.

4.1.1.2 Solution Method and Implementation

The model equations described in (3.20) form a coupled linear system that can be discretized into the form of $\mathbf{Ax} = \mathbf{b}$. The necessary multi-scalarity of both the spatial and temporal domains requires the model to be discretized in an implicit manner to overcome the stiffness of the system.

Once in discrete form, the system is implemented in a `C++` framework utilizing the Template Numerical Toolkit (TNT) (Mathematical and Computational Sciences Division, National Institute of Standards and Technology, United States, `http://math.nist.gov/tnt/`) and the associated translation of the Java Matrix Library (JAMA). This poroelastic `C++` solver is lightweight and relatively simple, and makes use of the *LU-decomposition* built into JAMA to solve the linear system directly.

4.1.1.2.1 Discretization of the System The system in §3.2.3 is specified as a boundary value problem and a finite differences approach is used to discretize the model equations. If we start from the definition of the derivative given by difference quotients,

$$\frac{\partial \phi(x)}{\partial x} = \lim_{h \to 0} \frac{\phi(x+h) - \phi(x)}{h},$$

then this forms the basis of the well known explicit **forward difference**,

$$\frac{\partial \phi(x)}{\partial x} \approx \frac{\phi(x+h) - \phi(x)}{h},$$

implicit **backward difference**,

$$\frac{\partial \phi(x)}{\partial x} \approx \frac{\phi(x) - \phi(x-h)}{h},$$

and **central difference**,

$$\frac{\partial \phi(x)}{\partial x} \approx \frac{\phi(x+\frac{1}{2}h) - \phi(x-\frac{1}{2}h)}{h},$$

schemes. Analysing these with Taylor's theorem shows that truncation error in both the forward and backward difference schemes is proportional to the order of the grid spacing, $O(h)$, whereas the error for central differences is proportional to the square of the grid spacing, $O(h^2)$. While more numerically intensive (it requires a solving a linear system at each iteration) the implicit method is unconditionally stable for all values of h.

For this study, we use the central difference scheme for spatial discretization for the equations of motion, forward or backward difference schemes as appropriate for estimating spatial derivatives in the boundary conditions and the forward difference scheme for temporal discretization,

$$\begin{aligned}
\frac{\partial^2\phi}{\partial r^2} &= \frac{\phi_{i+1}^{n+1} - 2\phi_i^{n+1} + \phi_{i-1}^{n+1}}{\Delta r^2} & r_i &= r_A + i\Delta r & i &= 0,\dots,M \\
\frac{\partial\phi}{\partial r} &= \frac{\phi_{i+1}^{n+1} - \phi_{i-1}^{n+1}}{2\Delta r} & t^n &= n\Delta t & n &= 0,\dots,N \\
\frac{\partial\phi}{\partial t} &= \frac{\phi_i^{n+1} - \phi_i^n}{\Delta t} & \phi_i^n &= \phi\left(r_i, t^n\right) & & \\
\frac{\partial}{\partial t}\left(\frac{\partial\phi}{\partial r}\right) &= \frac{\phi_{i+1}^{n+1} + \phi_{i-1}^n - \phi_{i-1}^{n+1} - \phi_{i+1}^n}{2\Delta r\Delta t}. & & & &
\end{aligned}$$

Applying this discretization template to the system gives:

Displacement Equation (4.1a) becomes,

$$\frac{u_{i+1}^{n+1} - 2u_i^{n+1} + u_{i-1}^{n+1}}{\Delta r^2} + \frac{2}{r_i}\frac{u_{i+1}^{n+1} - u_{i-1}^{n+1}}{2\Delta r} - \frac{2}{r_i^2}u_i^{n+1} - \frac{\alpha(1-2\nu)}{2G(1-\nu)}\frac{p_{i+1}^{n+1} - p_{i-1}^{n+1}}{2\Delta r} = 0,$$

rearranging for the nodal values,

$$\begin{aligned}
\left(\frac{1}{\Delta r^2} - \frac{1}{r_i\Delta r}\right)u_{i-1}^{n+1} + \left(\frac{-2}{\Delta r^2} + \frac{-2}{r_i^2}\right)u_i^{n+1} + \left(\frac{1}{\Delta r^2} + \frac{1}{r_i\Delta r}\right)u_{i+1}^{n+1} \\
+ \frac{\alpha(1-2\nu)}{4G(1-\nu)\Delta r}p_{i-1}^{n+1} - \frac{\alpha(1-2\nu)}{4G(1-\nu)\Delta r}p_{i+1}^{n+1} = 0, \quad (4.7)
\end{aligned}$$

or simply,

$$a_i u_{i-1}^{n+1} + b_i u_i^{n+1} + c_i u_{i+1}^{n+1} + d_i p_{i-1}^{n+1} + e_i p_{i+1}^{n+1} = 0.$$

Pressure Equation (4.1b) becomes,

$$\frac{p_{i+1}^{n+1} - 2p_i^{n+1} + p_{i-1}^{n+1}}{\Delta r^2} + \frac{2}{r_i}\frac{p_{i+1}^{n+1} - p_{i-1}^{n+1}}{2\Delta r} = 0,$$

rearranging for the nodal values,

$$\left(\frac{1}{\Delta r^2} - \frac{1}{r_i\Delta r}\right)p_{i-1}^{n+1} + \left(\frac{-2}{\Delta r^2}\right)p_i^{n+1} + \left(\frac{1}{\Delta r^2} + \frac{1}{r_i\Delta r}\right)p_{i+1}^{n+1} = 0, \quad (4.8)$$

or simply,

$$f_i p_{i-1}^{n+1} + g_i p_i^{n+1} + h_i p_{i+1}^{n+1} = 0.$$

Boundary Conditions

Stress equilibrium in the ventricle wall, (4.2), becomes

$$(1-\nu)\frac{u_2^{n+1}-u_1^{n+1}}{\Delta r}+2\nu\frac{u_1^{n+1}}{r_1}-\frac{(\alpha-1)(1-2\nu)}{2G}p_1^{n+1}=0, \tag{4.9}$$

simplified as,

$$\left[\frac{2\nu}{r_1}-\frac{1-\nu}{\Delta r}\right]u_1^{n+1}+\frac{1-\nu}{\Delta r}u_2^{n+1}-\frac{(\alpha-1)(1-2\nu)}{2G}p_1^{n+1}=0$$
$$Au_2^{n+1}+Bu_1^{n+1}+Cp_1^{n+1}=0.$$

Conservation of mass in the ventricle, (4.3), becomes

$$Q_p=\frac{\pi d^4}{128\mu L}\left(p_1^{n+1}-p_M^{n+1}\right)-4\pi\kappa(r_1+u_1^n)^2\frac{p_2^{n+1}-p_1^{n+1}}{\Delta r}+4\pi(r_1+u_1^n)^2\frac{u_1^{n+1}-u_1^n}{\Delta t}, \tag{4.10}$$

simplified as,

$$Q_p+4\pi(r_1+u_1^n)^2\frac{u_1^n}{\Delta t}=\frac{4\pi(r_1+u_1^n)^2}{\Delta t}u_1^{n+1}+\left[\frac{\pi d^4}{128\mu L}+\frac{4\pi\kappa(r_1+u_1^n)^2}{\Delta r}\right]p_1^{n+1}$$
$$-\frac{4\pi\kappa(r_1+u_1^n)^2}{\Delta r}p_2^{n+1}-\frac{\pi d^4}{128\mu L}p_M^{n+1}$$
$$H=Du_1^{n+1}+Ep_1^{n+1}+Fp_2^{n+1}+Gp_M^{n+1}.$$

Displacement at the skull, (4.4), becomes

$$u_M^{n+1}=0, \tag{4.11}$$

and pressure rise at the skull, (4.5), becomes

$$p_M^{n+1}=p_{bp}+\mu RQ_0. \tag{4.12}$$

4.1.1.2.2 Numerical Template Collecting these discrete representations of the system into the form $\mathbf{Ax}=\mathbf{b}$, then the following gives the numerical template for a sys-

tem where $M = 6$:

$$\left[\begin{array}{cccccc|cccccc}
A & B & & & & & C & & & & & \\
a_2 & b_2 & c_2 & & & & d_2 & & e_2 & & & \\
 & a_3 & b_3 & c_3 & & & & d_3 & & e_3 & & \\
 & & a_4 & b_4 & c_4 & & & & d_4 & & e_4 & \\
 & & & a_5 & b_5 & c_5 & & & & d_5 & & e_5 \\
 & & & & & 1 & & & & & & \\
\hline
D & & & & & & E & F & & & & G \\
 & & & & & & f_2 & g_2 & h_2 & & & \\
 & & & & & & & f_3 & g_3 & h_3 & & \\
 & & & & & & & & f_4 & g_4 & h_4 & \\
 & & & & & & & & & f_5 & g_5 & h_5 \\
 & & & & & & & & & & & 1
\end{array}\right]
\left[\begin{array}{c} u_1 \\ u_2 \\ u_3 \\ u_4 \\ u_5 \\ u_6 \\ \hline p_1 \\ p_2 \\ p_3 \\ p_4 \\ p_5 \\ p_6 \end{array}\right]
=
\left[\begin{array}{c} \\ \\ \\ \\ \\ \\ \hline H \\ \\ \\ \\ \\ I \end{array}\right].$$

and,

$$\begin{aligned}
a_i &= \tfrac{1}{\Delta r^2} - \tfrac{1}{r_i \Delta r} & A &= \tfrac{2\nu}{r_1} - \tfrac{1-\nu}{\Delta r} \\
b_i &= \tfrac{-2}{\Delta r^2} + \tfrac{-2}{r_i^2} & B &= \tfrac{1-\nu}{\Delta r} \\
c_i &= \tfrac{1}{\Delta r^2} + \tfrac{1}{r_i \Delta r} & C &= \tfrac{(1-\alpha)(1-2\nu)}{2G} \\
d_i &= \tfrac{\alpha(1-2\nu)}{4G(1-\nu)\Delta r} & D &= \tfrac{4\pi(r_1+u_1^n)^2}{\Delta t} \\
e_i &= \tfrac{\alpha(2\nu-1)}{4G(1-\nu)\Delta r} & E &= \tfrac{\pi d^4}{128\mu L} + \tfrac{4\pi\kappa(r_1+u_1^n)^2}{\Delta r} \\
f_i &= \tfrac{1}{\Delta r^2} - \tfrac{1}{r_i \Delta r} & F &= \tfrac{-4\pi\kappa(r_1+u_1^n)^2}{\Delta r} \\
g_i &= \tfrac{-2}{\Delta r^2} & G &= \tfrac{-\pi d^4}{128\mu L} \\
h_i &= \tfrac{1}{\Delta r^2} + \tfrac{1}{r_i \Delta r} & H &= Q_p + 4\pi(r_1+u_1^n)^2 \tfrac{u_1^n}{\Delta t} \\
 & & I &= p_{bp} + \mu R Q_0
\end{aligned} \quad , \tag{4.13}$$

4.1.1.2.3 Implementation Throughout the course of this study, various implementations of the system were executed, ranging from rapid prototypes written in `python`, to `C++` object orientated implementations and simplified single-function routines. Ultimately, it was found in the latter stages of this work, that the simple one-function routine written in `C++` was most useful, particularly when wrapped with `FORTRAN` for compatibility with **CFD-ACE+** (cf. §4.2).

The Template Numerical Toolkit (TNT) is a collection of interfaces and reference implementations of numerical objects useful for scientific computing in `C++`. It defines interfaces for basic data structures, such as multidimensional arrays and sparse matrices, commonly used in numerical applications; of particular importance to the poroelastic `C++` solver are the C-style numerical arrays, `TNT::Array1D`

and TNT::Array2D. These arrays can be sized at run time, utilize the familiar $\mathbf{A}[i][j]$ notation and are used to house the discretization template, grid domain, and the boundary condition and solution vectors.

The JAMA *LU-decomposition* implemented within TNT is utilized to solve the linear system. Whereby, given the system, $\mathbf{Ax} = \mathbf{LUx} = \mathbf{b}$, solving for $\mathbf{x}$ is completed in two logical steps: (i) first the system $\mathbf{Ly} = \mathbf{b}$ is solved; and then the system $\mathbf{Ux} = \mathbf{y}$ is solved.

4.1.2 Results

Typically, poroelastic models in the literature represent the brain in either spherical or cylindrical coordinates. The current state-of-the-art model, as proposed by Smillie et al. (2005), has proven useful in the modelling of acute hydrocephalus and forms the starting point for this research. As we progress, this model shall be extended through an investigation of the pulsatile properties of the system, and of the impact of cerebral aqueduct geometry on overall ventricular displacement. In the first instance, however, we develop a numerical solver capable of producing results similar to those in the literature.

4.1.2.1 Reproducing the Results of Smillie et al. (2005)

As it has been outlined in previous sections of this chapter, a poroelastic C++ solver has been created to solve the SPET model developed by Smillie et al. (2005). In this paper, graphs are produced for both the steady-state and transient response of the system and these are used for comparison with the finite differences solver produced here.

For the first compartive investigation, each of the several different implementations of the numerical solver returned virtually identical results in an ultimately grid and time-step independent manner. The quantitative agreement between these implementations was encouraging, however, there was not a direct corroboration of the complete aqueduct occlusion data presented in Smillie et al. (2005) (see Figure 4.1).

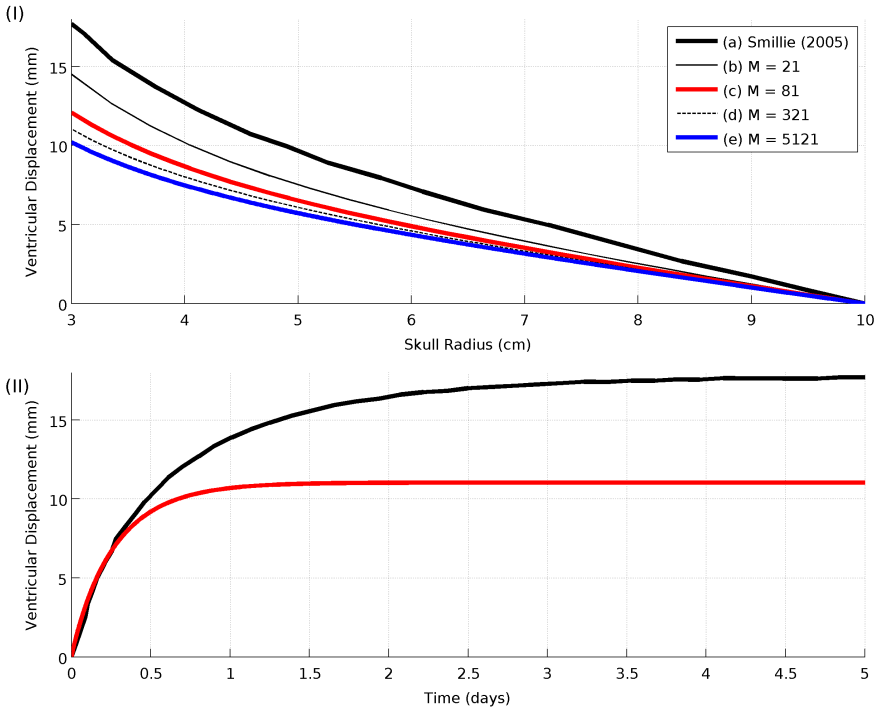

Figure 4.1: There is a qualitative agreement between the **(I)** steady-state displacement of the tissue through the skull, and **(II)** the transient development of the displacement at the ventricular wall for a completely occluded cerebral aqueduct in: **(a)** the data reported in Smillie et al. (2005); and **(b)**–**(e)** the data produced by the poroelastic C++ solver. Cases **(b)**–**(e)** further represent the results of a grid independence study of the current poroelastic C++ solver with M = 21, 81, 321 & 5121, respectively. Case **(e)** gives the grid independent response of the system, while Case **(c)** shows the response of the system used in the remainder of the study.

While the results are qualitatively similar to the literature, the magnitude of the ventricular enlargement is smaller than the results garnered from the poroelastic C++ solver. A possible explanation for this may be found in the grid independence study where the truncation error of the poroelastic C++ solver contribute to a narrowing of the gap between the data provided in the literature, and that gathered in this study.

It can be seen that the grid independent implementation (M = 5121, Figure 4.1-(e)) results in a steady-state ventricular enlargement of about 10 mm; however, this comes at significant computational cost and it is not feasible to conduct the remainder of the study with such a fine mesh. In a compromise, the remainder of the study shall be conducted with an increased grid size, without suffering too much of an

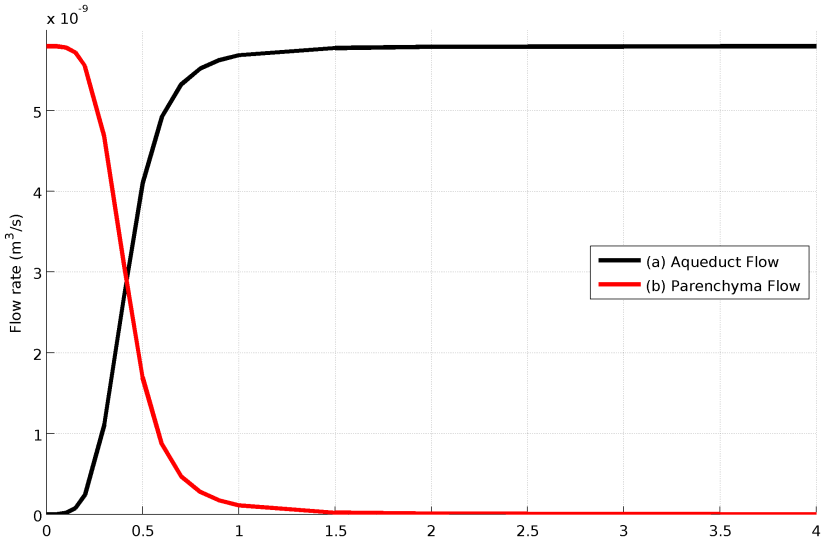

Figure 4.2: The effect of closing the aqueduct diameter on the major terms in ventricular mass conservation boundary condition.

increase in truncation error ($M = 81$, Figure 4.1-(c), error $\approx 2\%$).

4.1.2.2 Investigating the Analytical Cerebral Aqueduct

In order to gain a greater understanding of the nature of the equations, the diameter of the aqueduct is specified as a function of time in the conservation of mass boundary condition, Equation (4.3). The extent to which the aqueduct can be restricted is important both in understanding the tight coupling of the dynamics of the system, but also more generally as a goal for diagnostic capabilities in the clinic.

It is suggested in the literature that for aqueductal stenosis to be the cause of acute hydrocephalus, the cross-sectional area of the most severely constricted area is less than 0.031 mm^2 (or an equivalent circular diameter of 0.2 mm) (Woollam and Millen, 1953). When generally accepted values for the physical constants and material properties are adopted, the relationship between the Darcy flow through the parenchyma and the Poiseuille flow through the aqueduct is such that the Poiseuille term dominates until the aqueduct diameter decreases below 1.0 mm (see Figure 4.2).

Furthermore, we speculated that inducing a time-dependent diameter for the aqueduct might offer some useful insight into the coupling characteristics of the

boundary conditions and the system as a whole. The hypothesis being that initially, the pressure would rise as resistance through the aqueduct is increased; once it assumes a constant value, the system relaxes and the pressure normalizes at a slightly lower steady-state value.

The results of this study show that the quasi-steady assumption prevents such a dynamic response, provided that the changes in the diameter are made sufficiently slowly as to not violate the inherent assumption (see Figure 4.3). A closer investigation revealed the following observational patterns:

Initial/Minor decrease in the diameter

- increase in $p(r_1,t)$ is negligible but enough to drive fluid through the aqueduct.
- $\frac{\partial p}{\partial r}\Big|_{r_1}$ remains negligible and no flow is seen through the parenchyma.
- $\frac{\partial u}{\partial t}\Big|_{r_1}$ remains negligible and there is no change in the ventricle volume.

Major decrease in the diameter

- increase in $p(r_1,t)$ but less flow is observed through the aqueduct.
- $\frac{\partial p}{\partial r}\Big|_{r_1}$ increases and flow begins through the parenchyma.
- $\frac{\partial u}{\partial t}\Big|_{r_1}$ increases, and thus, a larger ventricular volume is observed.

Diameter remains constant at smaller value

- $p(r_1,t)$ and $\frac{\partial p}{\partial r}\Big|_{r_1}$ continue to increase and $\frac{\partial u}{\partial t}\Big|_{r_1} \rightarrow 0$ until an equilibrium is found as which point the system is in steady-state and there is no longer a time dependence.
- Once this has occurred, there are no further changes made to the boundary conditions and hence, there are no observed changes in the pressure of the system regardless of which the final aqueduct diameter is set to.

Assuming this new information both on the dynamic properties of the aqueduct, and of the relationship between the diameter of the aqueduct and amount of flow through the parenchyma, we can make a compromise on the assertion that the stenosis must be less than 0.2 mm to be considered as the cause of acute hydrocephalus. For the remainder of this study and unless otherwise mentioned, we

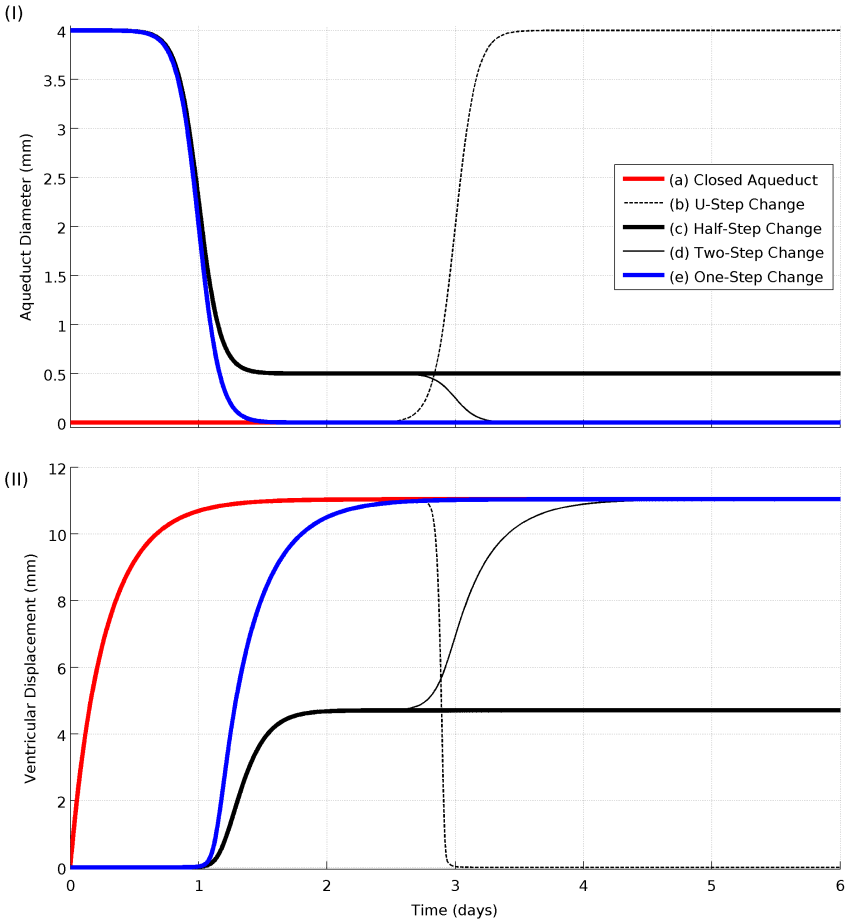

Figure 4.3: Investigation of aqueduct diameter profiles: The left column shows the aqueduct diameter profiles, the middle column are the displacement responses and the right-hand column shows the pressure responses.

assume an obstructed diameter of 0.25 mm for the stenosed aqueduct. It is important to notice that this is well below the current resolution of clinically applied imaging techniques – in this sense, obstructions that result in the aqueduct falling below about 0.5 mm will appear on the radiographic imaging as a fully occluded channel.

4.1.2.3 Pulsatile Boundary Conditions

Until now, the pulsatility of the cerebral environment has been largely ignored in the poroelastic modelling of hydrocephalus. Here, we consider three different locations for the driving force. Case 1 involves linking the cerebrovenous pressure to pulsa-

tions within the heart; Case 2 specifies the production of CSF in a pulsatile manner; and Case 3 induces a manual oscillation on the displacement of the tissue at the ventricular wall.

The pulsation of Case 1 is applied to the blood pressure, p_{bp}, in (4.5); this is synonymous to a pulsation of the pressure in the venous sinus which causes a dynamic pressure in the sub-arachnoid space. In doing so, we found that the oscillation of the blood pressure is transmitted entirely through the system networks such that the pressure gradient across the aqueduct is constant though the cycle. It follows then, that the flow rate through the aqueduct is also constant, and consequently, there is no impact on the displacement of the ventricle walls (see Figure 4.4-(b))[2].

The second variable to be made time-dependent, or Case 2, was the production of CSF, Q_p, in (4.3); testing the theory that pulsations in the choroid plexus give a dynamic production of CSF and hence impact the ventricular dynamics. Here, the pressure remains constant at the skull, and hence, the absorption of CSF does also; furthermore, there is a fluctuation in the amount of CSF in the system at any one time. Consequently, there are pulsations in the displacement of the ventricle walls. However, the amplitude of the oscillations is small enough such that the changes in ventricle wall displacement are in the order of microns, and hence, negligible in comparison to the overall steady-state displacement (see Figure 4.4-(c)).

Finally, it has been suggested that the decreased intra-cranial compliance of the brain tissue leads to a decrease in its ability to dissipate the pulsations of the arterial vessels (Egnor et al., 2001). The result of this, is that there is an abnormally high displacement of tissue during the cardiac cycle. To model this in Case 3, we explicitly increase or decrease the ventricle wall deformation, $u(r_1)$, using (4.6) before each time step is computed (Kurtcuoglu et al., 2005). These pulsations in the ventricle wall lead to an oscillation in the ventricular pressure that is not present at the skull. Hence, there is a dynamic pressure gradient across the aqueduct and thus, a pulsatile flow of CSF through the aqueduct. However, it can be seen in Figure 4.4-(d)–(f) that this does not result in an increase to the average ventricular enlargement, nor to the rate of dilation. The difference in thickness of oscillation for each plot is due

[2] We must note that the use of a Poiseuille law in such a pulsatile system, although an approximation, is not a detrimental one: the Womersley number of the unobstructed aqueduct is low enough ($\alpha = 0.33$) to assume that the departure from a Poiseuille velocity distribution is small. We used a Womersley number definition of $\alpha = R\left(\frac{\rho\omega}{\mu}\right)^{\frac{1}{2}}$

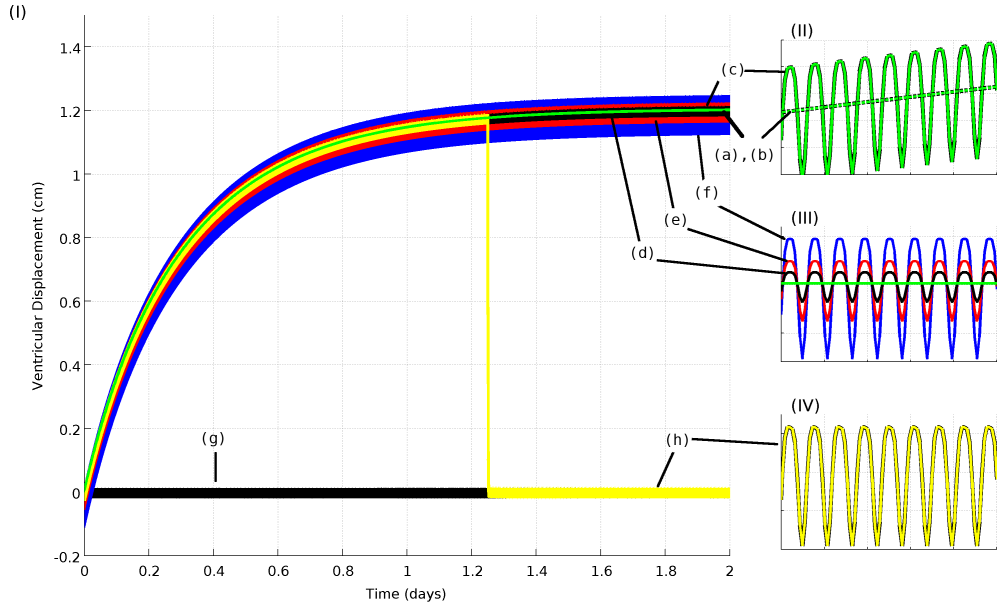

Figure 4.4: A three case investigation of the role of pulsatility as introduced to the boundary conditions of the SPET model. **(I)** shows the difference between each dynamic boundary condition: **(a)** no pulsatile input; **(b)** Case 1; **(c)** Case 2; **(d)**–**(f)** Case 3 with different wall motion amplitudes - corresponding to 0.25 mm, 0.5 mm and 1 mm respectively; **(g)** shows Case 3 with a 0.25 mm wall amplitude and no flow obstruction (i.e. open aqueduct); and, **(h)** shows Case 3 with a 0.25 mm wall amplitude with the aqueduct flow obstruction removed at $t = 1.25$ days. **(II)**–**(IV)** show close zooms of the final nine heart beats of the simulations to exemplify that the solid lines of **(I)** are actually oscillating.

only to the change in amplitude of the imposed wall motion. We should also note that the imposed dynamic wall motion does not change the need for a significant obstruction to the flow for ventricles to dilate (see Figure 4.4-(g)).

Finally, one of the paradoxes of chronic hydrocephalus is that there does not appear to be any observed obstruction to the flow of CSF. It is theorized that a temporary obstruction may form and the resulting ventricular dilation remains after the blockage has cleared. However, Figure 4.4-(h) shows that without any change in material properties, it is unlikely, in the quasi-steady model, that this is due to pulsations alone. It follows then, that for this theory to show promise, there must be associated changes to the mechanical properties of the parenchyma (cf. Chapter 5).

From these Cases, there does not seem to be a change in the ventricular displacement as a response to the pulsatile loading of the boundary conditions. It may

be that pulsations do not play a role at all, however, it is more likely that the absence of findings here are due to the assumption of a quasi-steady model. It was decided that for the remainder of this research, the quasi-steady assumption will remain, however, the idea of pulsatility should not be ignored in future work.

4.2 SPET: 1D-3D Coupled Model

It has been shown in the previous section (§4.1), a particular drawback of the current poroelastic models is the assumption that Poiseuille flow through a pipe can model the dynamic effects of a stenosed aqueduct. To model the obstructed aqueduct, it is assumed that the diameter decreases along the full length of the pipe. In this form of acute hydrocephalus, we hypothesize that the geometric properties of the obstruction cannot be sufficiently captured by this analytic assumption.

4.2.1 Methodology

In order to more accurately investigate the physics of the system, we extend current capabilities by coupling the one-dimensional poroelastic solver with multi-dimensional representations of the cerebral aqueduct (a 1D-3D coupled model). Through this coupling we are able to investigate, for the first time, the impact of physically relevant stenosis patterns on ventricular enlargement. Within this context, we extend current capabilities by linking the one-dimensional poroelastic C++ solver from the previous section with axi-symmetric, fully three-dimensional, and patient-specific aqueduct geometries.

CFD-ACE+, a multi-physics solver, is used to simulate the CSF flow dynamics through the cerebral aqueduct. From this, the flux of CSF through the aqueduct is calculated and then used to replace the Poiseuille assumption in the boundary condition given by (4.3). The remainder of this sub-section will explore the details of this novel coupling method which can be roughly grouped into three categories: model set-up; simulation set-up; and, running the simulation (see Figure 4.5).

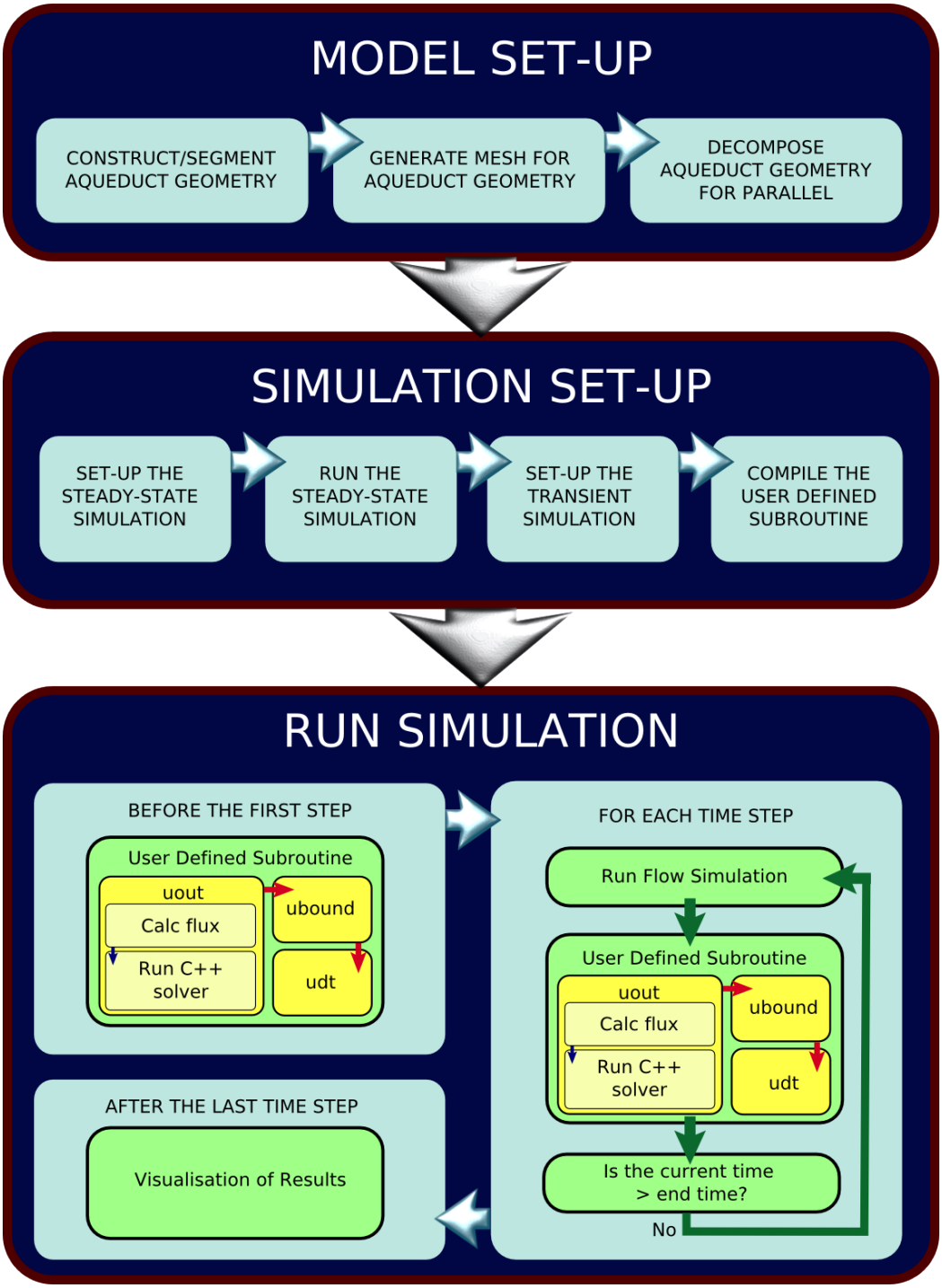

Figure 4.5: The state-of-the-art is extended through a novel coupling of the poroelastic C++ solver and the multi-physics software, **CFD-ACE+**. The coupling method which can be roughly grouped into three categories: model set-up; simulation set-up; and, running the simulation.

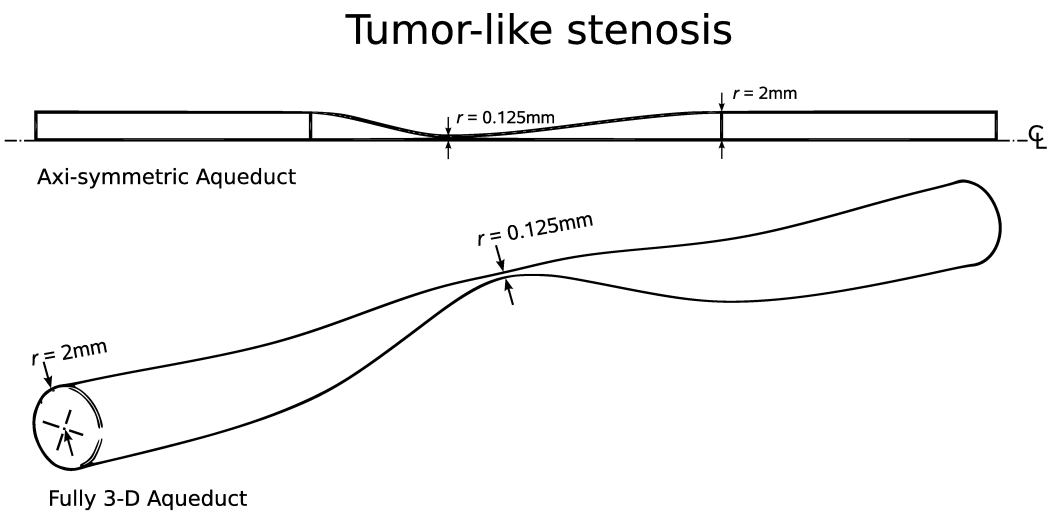

Figure 4.6: Pseudo-anatomic representations of the cerebral aqueduct geometries used in the **CFD-ACE+** solver. For reproducibility, each geometry is constructed using cubic Bézier curves to define important features; such as the contraction and expansion curves of the stenosis.

4.2.1.1 Model Set-up

During the model set-up phase, the multi-dimensional aqueduct geometry is created, converted to a computational mesh and prepared for parallel simulation with **CFD-ACE+**. In this study, there are three different classes of aqueduct geometry: pseudo-anatomic axi-symmetric, pseudo-anatomic three-dimensional, and patient-specific cerebral aqueducts.

4.2.1.1.1 Pseudo-Anatomic Aqueduct Geometry Construction The pseudo-anatomic aqueduct geometries are constructed using various cubic Bézier curves to denote the contraction and expansion of the walls of the geometry. The ultimate goal in creating these geometries is to closely match the idea of the cerebral aqueduct being represented by a pipe (as in the analytic case), yet, with locally defined stenosed areas. For this reason, the geometries created are much more closely related to a cylindrical representation than they are to the anatomical description of the ventricular system (see Figure 4.6 and compare to Figure 1.4).

For computational speed, simple geometry creation, and easy mesh generation the first stage of the investigation makes use of an axi-symmetric model of the aqueduct. The two cubic Bézier curves define the stenosis reflecting a more physical ap-

proach to modelling the aqueduct and visually observed stenoses (see Figure 4.6).

The x-y control points (in mm) for the contraction and expansion curves are:

Cubic Bézier curve: $\mathbf{B}(t) = (1-t)^3\mathbf{p}_0 + 3t(1-t)^2\mathbf{p}_1 + 3t^2(1-t)\mathbf{p}_2 + t^3\mathbf{p}_3, \quad t \in [0,1]$

$\mathbf{p}_{\text{contraction}}$		$\mathbf{p}_{\text{expansion}}$	
x	y	x	y
20.0	2.000	30.0	0.125
30.0	2.000	50.0	0.125
20.0	0.125	30.0	2.000
30.0	0.125	50.0	2.000

The next step towards incorporating an anatomically accurate simulation is a fully three-dimensional aqueduct. This geometry is important to the overall investigation for two reasons. Firstly, it introduces flow features that are not seen in the simulations to this point, such as an off-axis stenosis and an elliptical cross-section with a twisted orientation of the major and minor axes. Secondly, this is a relatively computationally inexpensive simulation that shows the potential for coupling the fully three-dimensional flow simulations to the one-dimensional poroelastic `C++` solver. Again, this geometry is more closely related to a pipe than to the patient-specific geometry that will be considered later in this chapter.

For reproducibility, the geometry construction is well defined; the centre-line for the aqueduct cross-section is given by (in mm),

$$x(z) = 3.94 \times 10^{-25} z^8 (z - 70.0)^8$$
$$y(z) = 2.95 \times 10^{-25} z^8 (z - 70.0)^8,$$

and the rotation is linear with a maximum value of $\frac{\pi}{2}$. The radii of the major and minor axes of the elliptical cross-section are governed by two fifth-order Bézier curves defined, respectively, by the a-z and b-z control point pairs (see below and Figure 4.7-(II)).

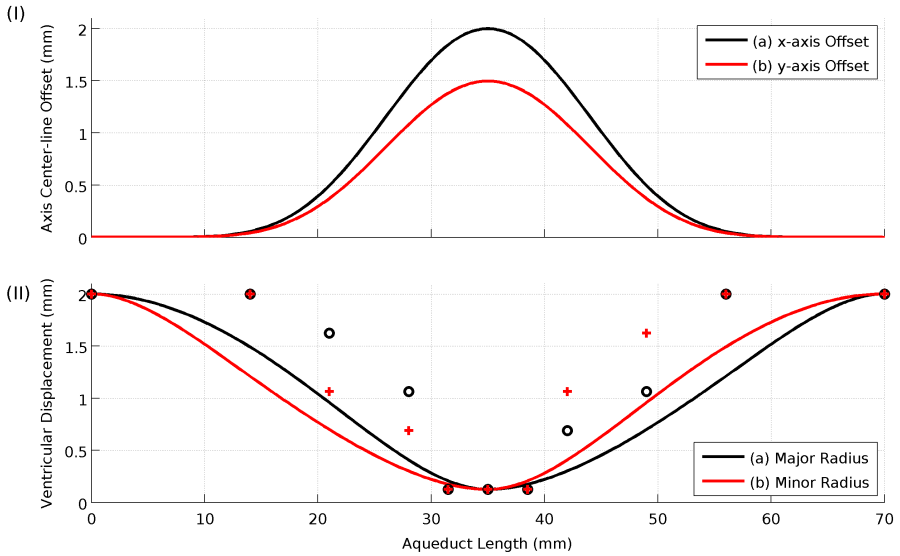

Figure 4.7: Geometric properties of the three-dimensional pseudo-anatomic representation of the cerebral aqueduct. **(I)** shows the x- and y-axis offset for the centreline of the elliptical cross-sections; and, **(II)** shows the profile of the major and minor radii of the elliptical cross-sections and their associated control points.

$$n\text{-th order Bézier curve: } \mathbf{B}(t) = \sum_{i=0}^{n} \binom{n}{i} (1-t)^{n-i} t^i \mathbf{p}_i, \, t \in [0,1]$$

$\mathbf{p}_{\text{contraction}}$				$\mathbf{p}_{\text{expansion}}$			
a	z	b	z	a	z	b	z
2.0000	00.0	2.0000	00.0	0.1250	35.0	0.1250	35.0
2.0000	14.0	2.0000	14.0	0.1250	38.5	0.1250	38.5
1.6250	21.0	1.0625	21.0	0.6875	42.0	1.0625	42.0
1.0625	28.0	0.6875	28.0	1.0625	49.0	1.6250	49.0
0.1250	31.5	0.1250	31.5	2.0000	56.0	2.0000	56.0
0.1250	35.0	0.1250	35.0	2.0000	70.0	2.0000	70.0

In order to create the geometry, scripting features of the **Gambit** (formerly FLUENT Inc.; now ANSYS Inc., Canonsburg, Pennsylvania) software package were used. **Gambit** is generally considered as a pre-processor for CFD analysis; it has many features in common with a typical CAD package, such as the creation of complex lines, surfaces and volumes according to the ACIS standard. It is primarily used as the pre-processor to the **FLUENT** CFD solver, however, in this instance the geometry/mesh file is saved in a format that can be read by **CFD-ACE+**.

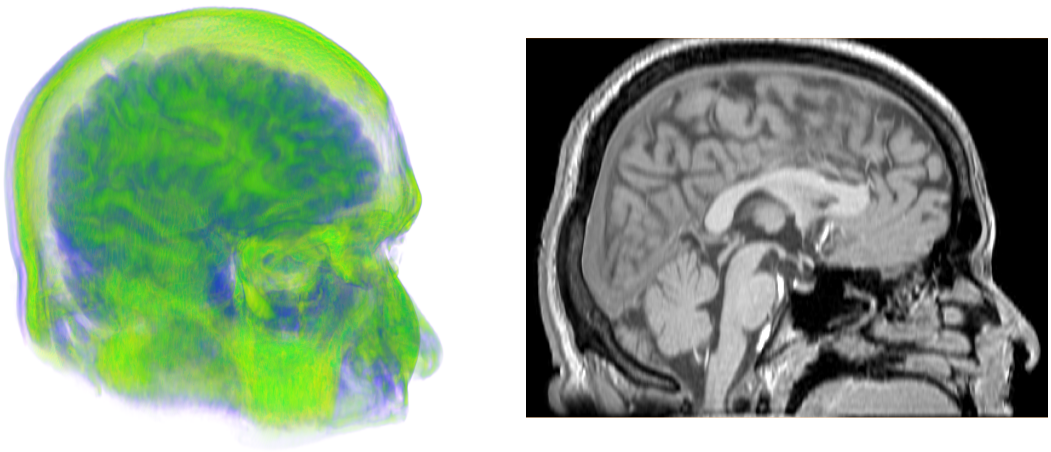

(a) (b)

Figure 4.8: Patient-specific MRI scans of Case 1, a healthy volunteer with an open cerebral aqueduct. **(a)** shows the scan in three dimensions, while **(b)** is a single slice showing the ventricular system.

The first step to create the three-dimensional geometry was to generate a text file of the centre point (and the quadrant points that fall on the perimeter) of each of the elliptical cross-sections using a `python` script. These points were subsequently read by a **Gambit** journal file (a method for automated text user interface interaction, see Appendix D.1) that then utilized the points to create the ellipses at the appropriate places and split these curves into quadrants. A series of axial `NURBS` curves were constructed through the quadrant points of the ellipses and then split at each ellipse. Finally, volumes were created for each pair of adjoining elliptical cross-sections (for reasons that will be explained in the meshing section, §4.2.1.1.3) using the `wire-frame` method.

4.2.1.1.2 Patient-Specific Aqueduct Geometry Creation

In this study, we consider the aqueduct geometry extracted from the MRI scan of a healthy volunteer. The subject, Case 1, is male, aged in his sixties and for all intents and purposes, completely healthy (see Figure 4.8).

To extract the ventricular system from the series of `DICOM` files produced by the MRI scan, we utilize the software package **Amira** (Visage Imaging GmbH, Berlin, Germany). The methodology used to segment data in **Amira** is dependent on a mixture of the task at hand and personal preference (an example of tissue and fluid

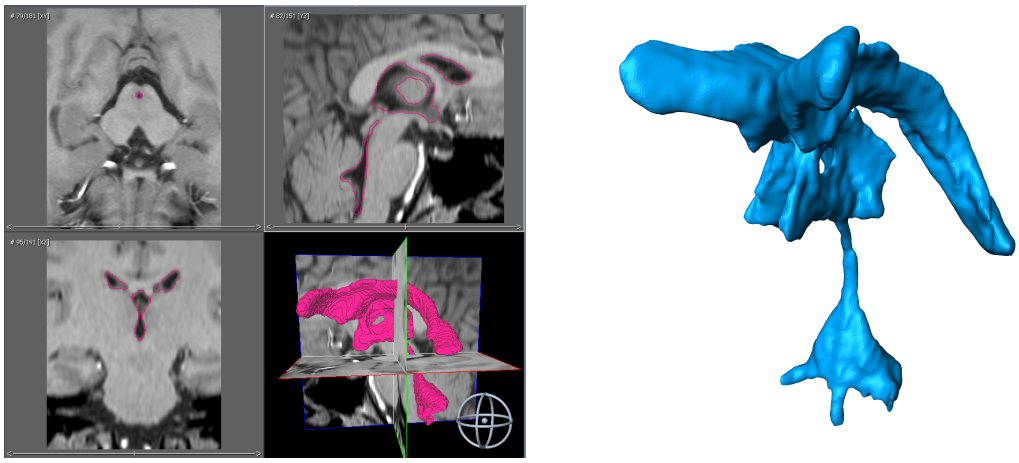

(a) (b)

Figure 4.9: The MRI segmentation process in **Amira** is completed by **(a)** importing the raw data and creating 'labels' for the features of interest – in this case the ventricular system. This can be completed automatically, or for more detail, the feature can be highlighted in each slice, slowly building up a three-dimensional volume. **(b)** For this labelled volume, a surface is created and optional smoothing algorithms can be executed to create the final surface of the ventricular system.

segmentation can be seen in Figure C.1).

Obtaining the aqueduct geometry is a non-trivial task. A significant challenge of the segmentation process is the relative size of the diameter of the aqueduct compared to the voxel size of the scan – see Kurtcuoglu (2006) for an investigation of the associated challenges. In practice this means that the automated features of segmentation in **Amira** cannot be utilized and instead, the process must be completed manually in a slice-by-slice fashion. The approach taken for these geometries was to:

1. Create and **Amira** network and import the MRI data.
2. (optional) If the voxel size was small (giving a large data file) then crop the data to include only the region of interest to speed-up computational performance.
3. Create a set of "labels" that define the CSF flow region of interest. In other words, define the ventricles, the cerebral aqueduct and the outlet foramina (see Figure 4.9-(a)) by:

- Create a new label for the CSF region.
- Proceed slice-by-slice highlighting the CSF region with the paint brush tool.
- Add the current selection to the appropriate label.
- (optional) Depending on the voxel size, this segmentation is likely to be discontinuous between the slices. To increase the continuity of what will be the computational domain, various "Segmentation" and "Selection" menu tools can be used to *fill holes*, *remove islands* or *smooth the selection* on either the current slice, all slices, or the three-dimensional volume.
- Highlighting in a slice-by-slice manner is iterative, and surface continuity is increased through many iterations, in addition to a change in slice orientation (for instance, sagittal to coronal).

4. From these labels, a surface is generated on the CSF domain. Notably, this should be done without the use of any smoothing algorithm.

5. (optional) The coarse surface of the previous step can be improved through the addition of a "Smooth Surface" filter. This gives far more control over the amount of smoothing done and is important to maintain the anatomic features of the domain.

6. The generated surface is exported as a Stereo Lithography (STL) file for use in the next stage of the work flow (see Figure 4.9-(b)).

Final Preparation of the Geometry While some smoothing is completed in the last stages of surface creation in **Amira** it was found that the smoothing algorithms were too aggressive and anatomical features were being lost. To overcome this, an intermediate step was introduced using the open-source three-dimensional modelling software, **Blender** (The Blender Foundation, `www.blender.org`).

Blender is a community developed package with extremely powerful wireframe, node-by-node, editing capabilities. Originally an in-house tool for the commercial animation company NeoGeo, **Blender** was released under the GNU General Public License and has since been used in large scale professional projects, such as *Spider-Man 2* (2004). The result is that the algorithms are well developed, and the

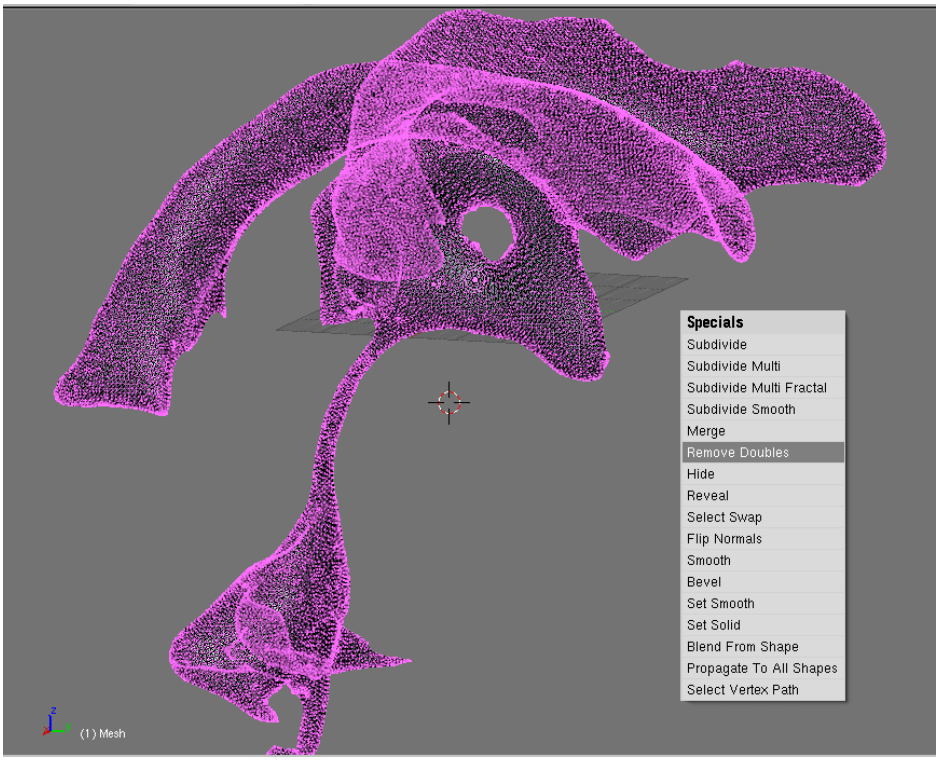

Figure 4.10: The advanced three-dimensional modelling capabilities of **Blender** are used to perform smoothing operations on the STL surface prior to its import to meshing software. Furthermore, **Blender** is used to artificially impart the two degrees of stenosis to the cerebral aqueduct of the healthy volunteer.

smoothing employed in **Blender** does an exceptional job at improving the continuity of the aqueduct domain, without destroying the anatomical features that are interesting to this study.

In order to complete the smoothing, the STL file (created by **Amira**) is imported into **Blender**. An important caveat is that **Blender** imports the STL file explicitly and the result is a bunch of disconnected triangles. However, if you enter the edit mode (see Figure 4.10), select all nodes and *Remove Doubles*, the software will merge all vertices within a specified tolerance. In doing so, the duplicate vertices of adjoining triangles are removed, and the connectivity of the surface is restored. Once this has been achieved, and whilst still in edit mode, clicking the *Smooth* button on the *Mesh* panel will perform the smoothing operation. Again this is an iterative process, and judgement was required to ensure that the surface was sufficiently smooth for the final CFD computation, while maintaining all of the anatomical features. Optionally, the smoothing process may be improved by sub-dividing the triangular faces.

Further to the smoothing operations, **Blender** is also very useful for introducing local stenosis to the patient-specific geometries. From within the edit mode, a cross-section of vertices in the aqueduct can be selected, and expanded or contracted as appropriate. Again, the power of **Blender** allows this process to be conducted through simple nodal manipulations. This is first achieved by turning the Proportional Editing Mode to "On" and then selecting several points around the circumference of the aqueduct and scaling them inward (to stenose the aqueduct). Having the proportional editing mode on will mean that vertices within a specified radius will also scale inward according to the specified fall-off type (which was selected to be "smooth" for this work).

The geometry of the healthy volunteer was chosen to be the case explored for the obstructed aqueduct investigation. Before any stenosis was applied, the cross-section area of the aqueduct was 2.236×10^{-6} m^2, giving an equivalent circular diameter of 1.687 mm (Figure 4.11-(a)). The aqueduct was then given stenoses of differing severity: a mild stenosis with a cross-sectional area of 3.625×10^{-8} m^2, or an equivalent diameter of 0.215 mm (Figure 4.11-(b)); and, a severe stenosis with a cross-sectional area of 3.882×10^{-9} m^2, or an equivalent diameter of 0.070 mm (Figure 4.11-(c)). A reminder for comparison that the diameters used in the analytic cases were 4 mm and 0.25 mm for the open (Figure 4.11-(d)) and stenosed (Figure 4.11-(e)) cases respectively.

The final stage of the `STL` preparation – the creation of the inlet and outlet boundaries – can be performed in many different ways, such as using **Blender** (which is very slow) or the lightweight Tool Command Language script, `tcut.tcl`[3]. This script is a simple `STL` cutting tool that utilizes `vtk` for its geometric manipulations (Figure C.2). The premise is to create intersections between the computational domain and the cylinder whose parameters can be controlled through the GUI of the script. It is run from the command-line,

```
vtk tcut.tcl inputFile.stl outputFile.stl ascii o
```

where `ascii` specifies the encoding of the `outputFile.stl` and `o` stipulates that any cuts remain open in the `outputFile.stl`.

Finally, it is important to note that the diameters of both stenosed aqueducts are well below the current standard voxel size for clinical imaging. This suggests, in

[3] `tcut.tcl` is a script originally written by Dr Keri Moyle.

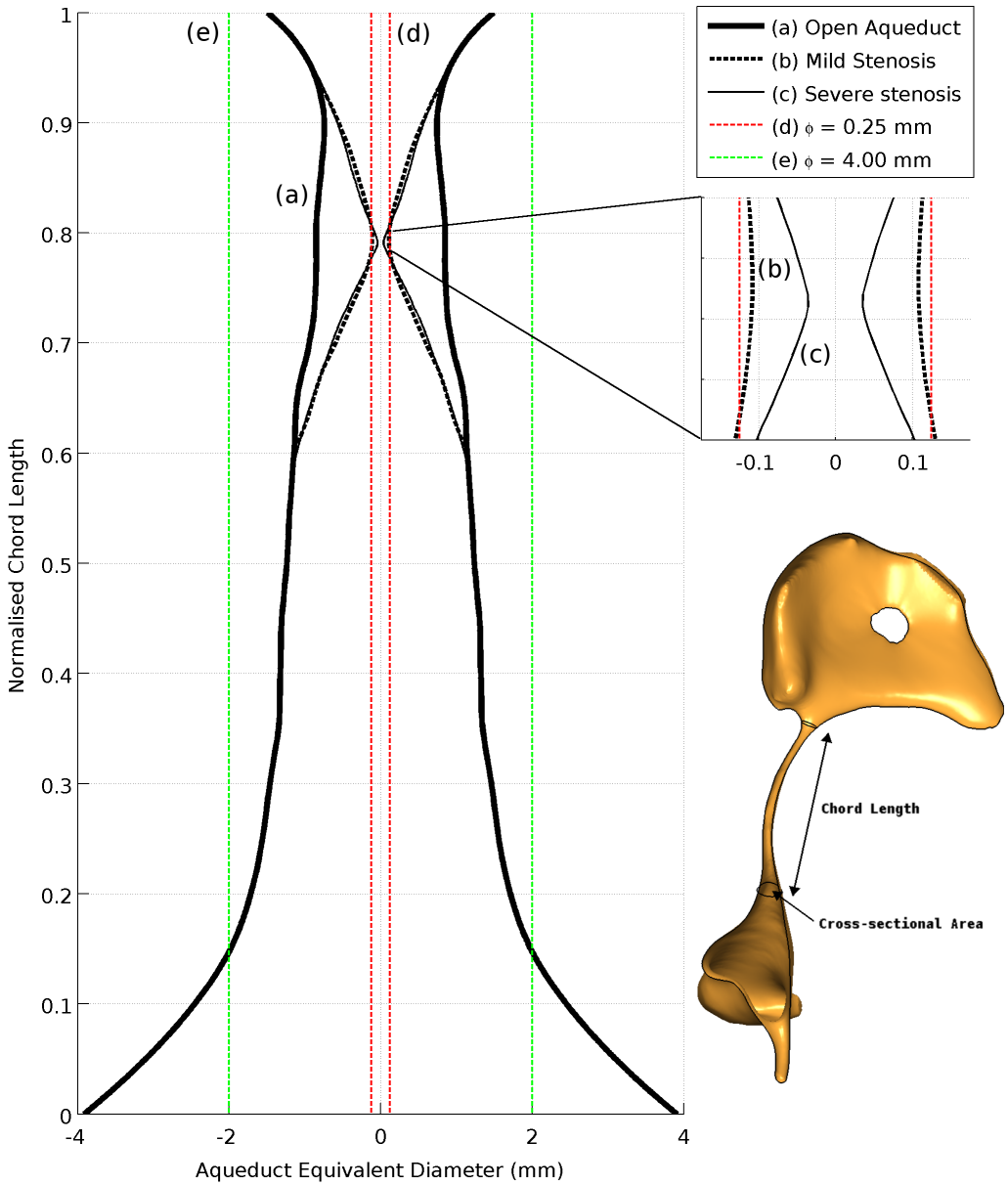

Figure 4.11: Equivalent diameters of the stenosed aqueduct geometry along the specified chord-length. Two degrees of stenosis are introduced to investigate the response of the models to acute hydrocephalus. The equivalent diameters at the most stenosed section of the aqueduct are: **(a)** the healthy geometry, $\phi = 1.687$ mm; **(b)** mild stenosis, $\phi = 0.215$ mm; **(c)** severe stenosis, $\phi = 0.070$ mm; **(d)** analytic stenosis, $\phi = 0.25$ mm; and, **(e)** analytic healthy, $\phi = 4.0$ mm.

practice, that to the radiologist, it is highly likely that the aqueduct would be considered to be fully occluded.

4.2.1.1.3 Mesh Generation

The fundamental concept of CFD is that the continuous flow domain is discretized into a finite domain of grid cells. There are many software packages available for this purpose, both open-source and commercial; however, for this research two packages, **Gambit** and **CFD-VisCart**, were utilized based on the task at hand. For the pseudo-anatomic aqueducts, **Gambit** was used to good effect, both due to the scripting abilities described previously, and its excellent unstructured meshing algorithm.

Meshing the patient-specific domains were more tricky due to the potential irregularities in the domain surface. In the first instance, **Gambit** was used due to both familiarity and the strength of its unstructured meshing capabilities, although problems arose with the way it handled imperfections in the STL file. Instead, the strength of the Cartesian surface cutting approach of **CFD-VisCart** was utilized to build a polygonal hybrid mesh in the domain.

Pseudo-Anatomic Aqueduct Mesh Generation To mesh the pseudo-anatomic aqueducts, the script written for **Gambit** was extended to include a mesh generation phase. The relative size difference between the typical aqueduct diameter and the diameter of the stenosis poses a challenge to meshing.

At any point in the flow domain, one would like the minimal grid size to be at least an order of magnitude smaller than the cross-sectional diameter. While it is straight-forward to specify a maximum cell size for the entire domain that satisfies this criterion, the result would be an unreasonably large and computationally expensive mesh.

For this reason the axial length of the aqueduct was segmented into several volumes in the geometry creation phase. These volumes become useful in meshing as they can provide source volumes for "sizing functions" – by progressing axially outwards from the volume containing the most severely stenosed cross-section, the maximum grid size is specified to increase with a geometric growth rate from one volume to the next. With these sizing functions defined, a simple call to the mesh-

ing algorithm generates the computational domain that can then be exported as a `fluent5` mesh for easy import into **CFD-ACE+**.

Patient-Specific Aqueduct Mesh Generation A significant challenge in meshing the patient-specific geometry was **Gambit**'s the requirement for the STL file to be completely free of artefacts and/or discontinuities. This requirement was nigh impossible to satisfy for imperfect geometries created from patient-specific data, and an alternative solution was sought – and found in **CFD-VisCart**.

CFD-VisCart is an unstructured adaptive Cartesian grid generation system associated with the **CFD-ACE+** suite. It handles imperfect surfaces with holes, overlaps and cracks, and is ideally suited to extremely complex geometries – in comparison, the ventricular system is relatively simple. In this study we use the Projected Single-Domain method in which Cartesian cells are generated in the majority of the domain, while grids near the geometry interface are projected to the surface to obtain a body-fit grid.

Unlike many meshing algorithms that ask for a minimum cell size, **CFD-VisCart** asks the user to specify the maximum number of times, or levels, a cell may be divided. The first cell is considered to be the bounding box of the domain, and the level selected represents how many times this cell and its subsequent children, may be divided. The resulting minimum cell size is calculated by:

$$\mathbf{X}_{\text{cell}} = \mathbf{x}_{\text{bounding box}}/2^n.$$

where n is the maximum division level. For example, Level 4 in the X direction, will cut the bounding box in X in 16 pieces.

CFD-VisCart offers both Octree and Omnitree methods for subdividing cells. With Octree (Mitchell and Vavasis, 1992), a cell is subdivided into eight sub-cells along the X, Y and Z dimensions while Omnitree can split the cell along one, two, or all three dimensions meaning that few cells numbers are required for the same minimum cell requirement. If the cell size along one dimension is specified much larger than the other two, after many levels of splitting Octree may result in badly proportioned (skinny) cells.

Cells that intersect with the edge of the flow domain are further refined through two methods. The first – *Refine with normal and tangential size* – refines the cell

based on how it is intersecting with the geometry. The second – *Refine with specific cell sizes* – allows the user to specify a consistent cell size for all intersecting cells. Within each level of refinement, the user has control over the minimum number of layers at each refinement level. The default value is one, meaning that each level of refinement only contains one layer of cells, meaning there is a relatively sharp transition from maximum to minimum cell size. This is not ideal, but a balance must be struck between this, and allowing too many layers in each level as this will significantly increase the cell count (and hence, the computational expense) of the mesh.

Finally, the relative size of the stenosed cross-section and the overall domain means that a finer mesh must be produced in that specific region. **CFD-VisCart** allows the user to define several types of refinement sources, including: point, line, surface and volume sources. In general, the mesh control is specified in the same way as the grid refinement for the domain as a whole and in this study, placing one, or several, volume source(s) around the cerebral aqueduct allows a fine mesh to be generated in this area (see Figure 4.12).

Parallel Decomposition of the Geometry Within the **CFD-ACE+** suite, there are several methods for parallelizing the computational domain. Essentially, the process can be done during mesh generation, at run time when the job is submitted, or in between. In this study, mesh decomposition was always completed, using the `dtf_decompose` utility, after the simulation was set-up, yet before the job was submitted. In doing so, more control was gained over the decomposition process, a post decomposition check ensured that the inlet was contained within one zone, and by specifying the `outFile.DTF` independently of the `inFile.DTF` the overall file size is reduced in transient simulations.

```
dtf_decompose [-metis, -x, -y, -z] -combined -file_out outFile.DTF inFile.DTF
    »simNumber numProcesses
```

The `[...]` options specify the method of decomposition. All of the options used in this study are work-load balanced – meaning that each zone should have roughly equal number of cells. The default and most commonly used method is `-metis` (multi-level graph partitioning scheme), however, the patient-specific geometries have two inlet surfaces that must be contained within the same zone (as explained in §4.2.1.2.1) and this is not always the case with the METIS method. Depending

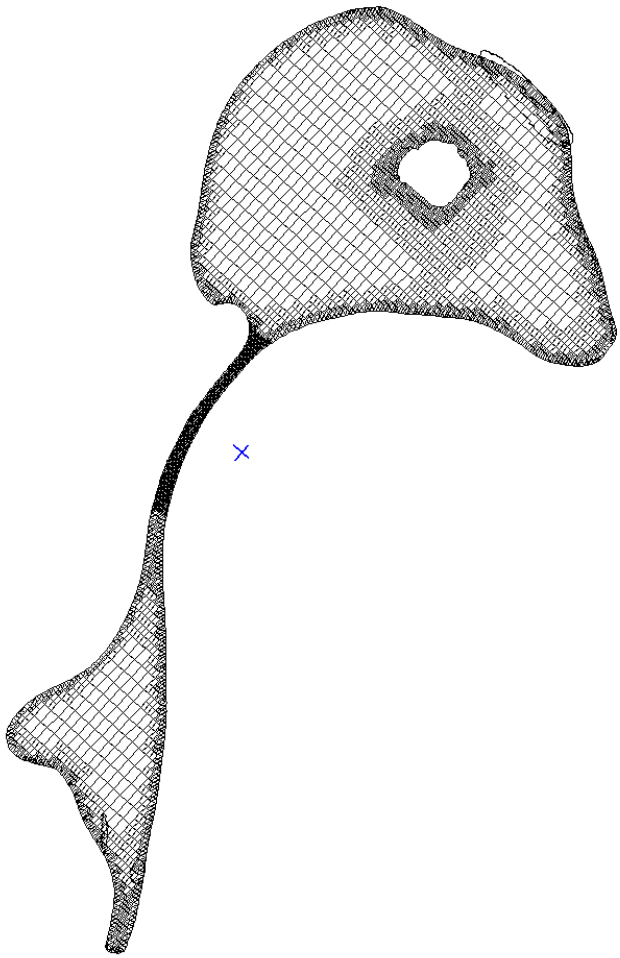

Figure 4.12: A cross section of the patient specific geometry as generated by **CFD-VisCart**. Clearly visible are the mesh refinements made at the surface of the volume, in addition to specific regions within the aqueduct. Grid independence studies were conducted by increasing the resolution within these specific regions, in addition to decreasing the speed of transition from one region's minimum cell size to the next.

on the axial orientation of the geometry, more control can be gained by a simple Cartesian decomposition; the inclusion of `-combined` strengthens the chances of common boundary labels being kept in the same zone. Finally, `simNumber` and `numProcesses` specify which simulation in the `inFile.DTF` is to be decomposed and into how many zones, respectively.

4.2.1.2 Simulation Setup

The iterative coupling between the poroelastic solver and **CFD-ACE+** results in a highly stiff system. The result is that the convergence of the transient **CFD-ACE+** solution is highly dependent on the initial conditions supplied to the model. For this reason, a steady-state solution is computed based on a set of boundary conditions ascertained from the model in §4.1. This steady-state model is then used as the initial conditions for the transient model, and the steady-state CSF flux is used in the first call to the poroelastic C++ solver.

The steady-state solver is defined using the steady flow solver module[4] with a single fluid ($\rho = 997$ kg/m^2, $\mu = 8.9 \times 10^{-4}$ kg/m/s). The outlet pressure is specified as 1088.77 Pa and the inlet pressure (taken from the one-dimensional SPET model) is 1088.825 Pa, the flow domain is initialized to the outlet pressure, and all velocities are set as zero. Central differences are used for the spatial differencing method, with a blending of 0.3, both the velocity and pressure correction solvers use the AMG method, and the maximum number of iterations is 3000 with a convergence criterion of 10^{-18}. Finally, limits are placed on the pressure solver such that $p \in [-10^5, 10^5]$.

Once the steady-state simulation has completed, a copy of the file can be transformed into the transient model. To make this change, the transient flow module is used with a user defined time step size, and the inlet pressure is specified by a user defined function (see the next section). The steady-state solution is used as the initial condition for the solver, the maximum number of iterations is decreased to 250 and the convergence criteria increased to 10^{-6} – numbers chosen such that convergence was ensured. Finally, the **CFD-ACE+** simulation is linked with the poroelastic C++ solver through an invocation of the `uout` user defined subroutine.

[4] For more details of the CFD solution method, see §A.

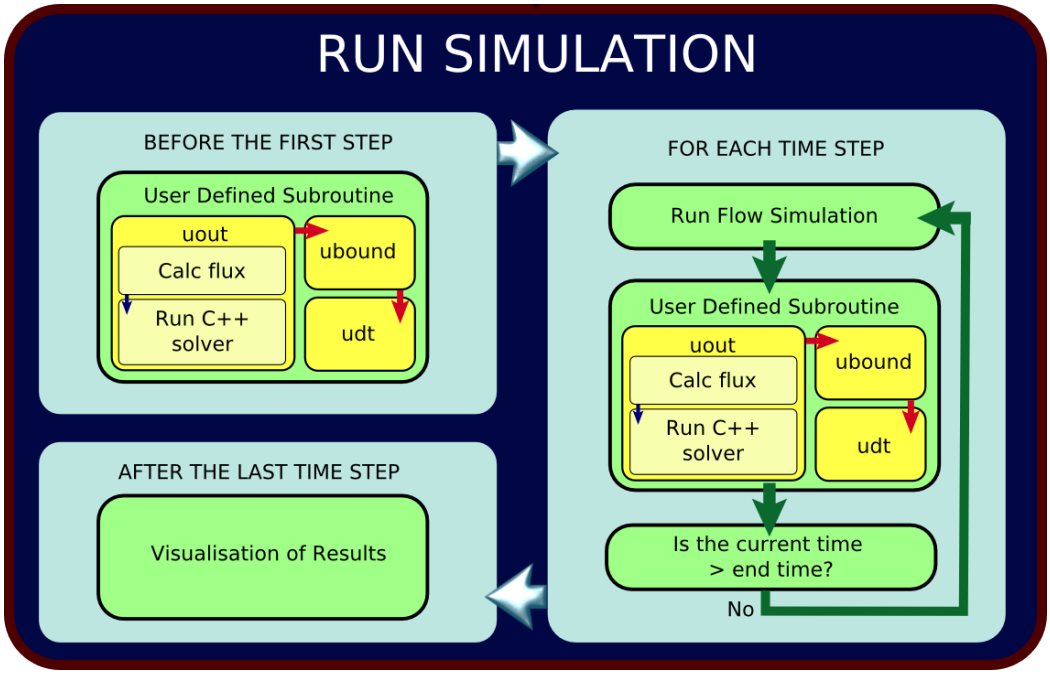

Figure 4.13: A close up of the run element of the flow diagram in Figure 4.5. The transient section of the overall simulation work flow involves a tight coupling between the poroelastic C++ solver of §4.1 and the multi-physics software **CFD-ACE+**.

4.2.1.2.1 CFD-ACE+ User Defined Subroutines

A key strength of the **CFD-ACE+** platform is the ability to implement coding routines that are specific to the problem at hand. Through the User Defined Subroutine (UDS) interface, users are able to write FORTRAN code that manipulates, or makes use of, simulation data at run time. The novel coupling approach used in this study links the poroelastic C++ solver already developed to **CFD-ACE+** at each time step (see Figure 4.13).

In the first instance, the UDS is run to initialize the system. The primary change to the poroelastic C++ solver comes about from an inability for the C++ code to hold the current solution to the linear poroelastic system in memory; each time the UDS calls the poroelastic C++ solver it creates a new instance in memory and the data is not 'remembered' from the previous time step. There are two methods to overcome this: the first is to pass the entire solution data from the C++ code to the FORTRAN code and store it in memory there. The second option is the write the solution data to a text file at the end of the time step (from within the poroelastic C++ solver) and then to read from the text file at the start of the next time step. In this study, the latter option was chosen, primarily for the reasons of debugging and data redundancy. It was assumed that the I/O time of this operation was insignificant in comparison to

other computing tasks in the overall simulation, and that it may be useful to have the solution data for every time step in the transient run.

Within the UDS calls to `uout` and `ubound` allow the pressure at the ventricle wall to be calculated in the poroelastic C++ solver based on the flux of fluid through the cerebral aqueduct. After each time step, the pressure at the ventricle wall is used as boundary condition to a numerical simulation of the CSF flow dynamics within the cerebral aqueduct. In turn, the flux of this fluid through the aqueduct is calculated and this information is used in the next iteration of the poroelastic C++ solver.

A key limitation to the **CFD-ACE+** UDS comes when running in parallel. For some unknown design reason, each thread of the parallel solver calls the UDS independently of any other. As a result, any thread calling `get_bc_index`, for example, will return an error if the requisite token is not present within its solution domain. We can navigate this flaw by ensuring that the `inlet` is completely contained within one solution zone (as described in §4.2.1.1.3) and that only the thread controlling this zone computes the coupling with the poroelastic C++ solver.

Enabling the `uout` requirement in `CFD-ACE-GUI` enables certain code to be executed a different times during the simulation according to the value of `iflag` (lines 69–172, Appendix D.2). In this study, we utilize two of these calling locations: `iflag = 1` to execute code to initialize the poroelastic C++ solver (lines 113–141, Appendix D.2); and `iflag = 4` to calculate the flux through the inlet and then pass its value to the poroelastic C++ solver for that time step (lines 143–167, Appendix D.2).

The `ubound` routine (lines 24–67, Appendix D.2) loops over all boundary faces; if the face is a member of the correct boundary zone, then it is possible to set a new value for that face. In the call to `ubound` we again check that only the thread controlling the `inlet` computational zone is able to set the pressure at the inlet using the value obtained from the poroelastic C++ solver in the call to `uout` (see lines 58–63, Appendix D.2).

The need for a dynamic time step is again due to the stiffness of the overall system. The `udt` subroutine (lines 174–217, Appendix D.2) allows control of the time step size and in this instance, we use it to slowly increase the time step from small values to more reasonable ones as the simulation settles down with increasing iterations.

Again, we use the check that only the thread that contains the `inlet` (i.e. the thread where `IN_index` is greater than zero) is allowed to modify the time step. In the code shown (lines 203–214, Appendix D.2), the time step is increased from 0.1 seconds to 10.0 seconds over 100 time steps; however, this criterion can be altered depending on the individual simulation being run.

Changes to the Poroelastic C++ Solver The high-level methodology for linking the UDS and the poroelastic C++ solver is quite clear from the previous section. However, two important structural changes were required in the poroelastic C++ solver for the code to be effective. Firstly, it was decided that added data redundancy would be achieved for a marginal increase in computational and storage expense if the result vector of displacement and pressure was written to the hard-disk at the end of each step; and the last time-step's data is read at the start of the current time-step. This implies the second structural change whereby the first time-step of the simulation must be treated differently as there is no previous data to read in. Otherwise, the poroelastic C++ solver remains the same as completed in §4.1.

Linking & Compiling the FORTRAN UDS with the Poroelastic C++ Solver The initial decision to write the poroelastic solver in C++ was made due to existing knowledge of the language and no expectations as to the steps that would be made in subsequent research. At that point, it was unknown that the UDS system of **CFD-ACE+** was written in FORTRAN. There were two options for including the poroelastic model into the UDS: it could be rewritten in FORTRAN, or a method could be found to link the existing solver to the UDS. Fortunately, linking C++ and FORTRAN code is a relatively trivial task, so that latter option was taken.

There are several intricacies with the linking process, which was ultimately completed using Intel's FORTRAN compiler `ifort`.

- Firstly, the C++ function must appear to the FORTRAN compiler as a C function. This is achieved through the use of the `extern "C" {}` declaration that allows the specification of the C++ function as an external C linkage function. The individual C++ and FORTRAN files are compiled with their respective compilers and then linked by appending `-lstdc++` to the linking options of `ifort`.

- Secondly, in the intel fortran compiler, an underscore ("_") is appended to the end of externally visible symbols such as subroutines and functions. Thus the function name of the `extern "C"` definition must include an underscore in the C++ file, yet ignore it in the FORTRAN code.
- Thirdly, it is important to note that FORTRAN passes variables by reference, while C++ passes them by value. Thus the C++ function should utilize the pointers to variables, rather than the variables themselves. However, this can be used to an advantage by passing the address of the pressure variables, PA and PC, in order to have their values modified within the C++ function, without needing to return values explicitly.
- Finally, FORTRAN strings are passed by descriptor, whereas the C++ `char` defines simply a byte. Thus in order to deal with strings being sent from FORTRAN to C++ the variable `int ll` is appended to the `extern "C"` definition right after the `char* name` variable; in practice, this integer variable is not explicitly assigned a value.

The relevant part of the C++ file shows this process most effectively.

```
extern "C"
{
    // to use this function in fortran: CALL btsolver(...)
    void bt_solver_( int* m, double* Qd, double* currentTime, int* currentStep
        », double* DT, double* PA, double* PC, char* name, int ll )
    {
        // call the C++ solver
        Solver(*m,*Qd, *currentTime, *currentStep, *DT, name, PA, PC);
    }
}
```

4.2.1.3 Running the Simulation

The modelling environment consists of a 184 core distributed memory cluster, `fbg-cluster`. Each node consists of a single motherboard with two quad-core 2.66 GHz CPU chips, each with 4 gigabytes of physical memory. The nodes are linked through high-speed Gigabit Ethernet and Infiniband connections to allow communication and hence, jobs to span more than one node. There is a controlling head

node and a high memory (32 gigabytes) node for application specific problems such as visualization.

The `fbg-cluster` runs the SuSE Linux distribution (`www.opensuse.org`) and job submission is controlled using the Sun Gird Engine (SGE) (Sun Microsystems, `http://wikis.sun.com/display/gridengine62u2/Home`). In order to submit a parallel **CFD-ACE+** job, a script must be written to set-up the run with the user explicitly stating how many nodes are required, model names and number of simulation zones; the script must also interrogate the SGE host file at runtime to create an alternative host file for use with **CFD-ACE+**. Finally, the job is run with a call to `cfd-ace-mpi` with the appropriate options as described in the user manual. The job script in Appendix D.3 is an example of submitting a run that will utilize eight CPUs (one CPU for each computational zone) on a model that has been previously decomposed and is submitted to the queue with the call: `qsub job-1.4.9.1.1.sge`.

4.2.2 Results

As we have explained, the novel coupling of the poroelastic `C++` solver with two- or three-dimensional representations of the aqueduct allows an investigation of the importance of the Poiseuille flow assumption. However, before the coupled model can be used to draw these conclusions, it is important that we are sure the coupling methodology provides accurate results.

In order to do so, two cases are run: the first with an aqueduct diameter of 0.25 mm comparing the analytic model to a coupled axi-symmetric representation of a straight-pipe aqueduct (Figure 4.14-(a)–(b)); the second compares the analytic model to a fully three-dimensional straight-pipe aqueduct each with an aqueductal diameter of 0.5 mm (Figure 4.14-(c)–(d)).

As expected, the results of these cases were in direct agreement. As such, the methodology used to execute the coupling of the different solvers is proven to be robust and the study can proceed knowing that direct comparisons can be made between local and analytic stenosis of the aqueduct. Firstly, the pseudo-anatomic geometries are used to draw a direct comparison between local and analytic stenosis pattern. Then, the pseudo-anatomic aqueducts are compared to the results gained from a patient-specific aqueduct geometry in open, mildly stenosed, and severely

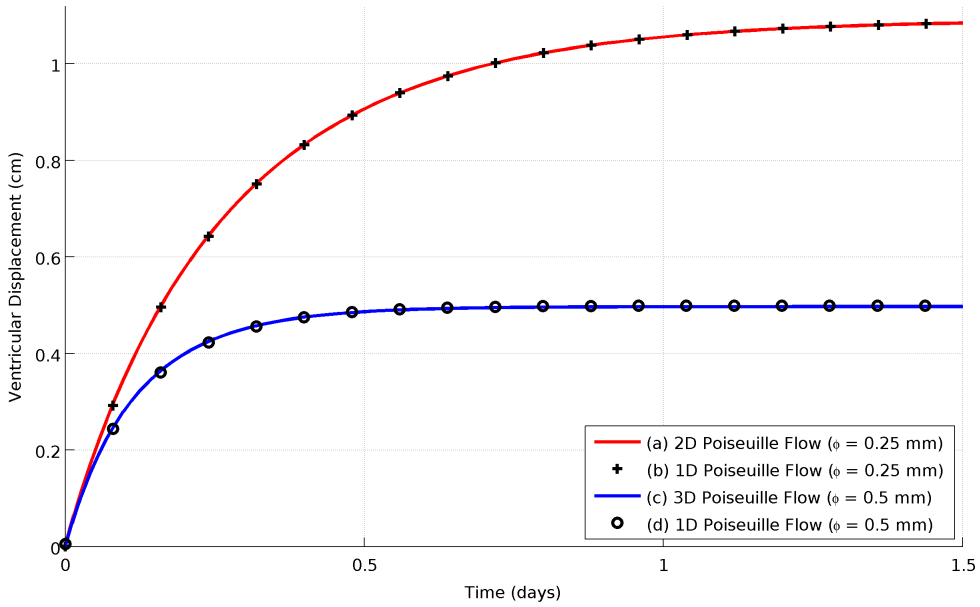

Figure 4.14: As expected, the coupled model replicates the results of the analytic model when computed with a straight pipe (i.e. replicating the analytic assumption of contracting the full length of the aqueduct). **(a)** and **(b)** show the results of the analytic and axi-symmetric coupled SPET model, respectively, for an aqueduct diameter of 0.25 mm. **(c)** compares the analytic solver with **(d)**, the fully three-dimensional coupled model, with an aqueduct diameter of 0.5 mm.

stenosed configurations.

4.2.2.1 Pseudo-Anatomic Cerebral Aqueduct

The comparison of pseudo-anatomic stenosed aqueducts with the historical collapsed pipe tells us that it is not correct to assume Poiseuille flow over the full length of the aqueduct. The impact of the local stenosis (Figure 4.15-(c)–(d)) on ventricular dilation is significantly smaller than that of simulations with the Poiseuille flow assumption (Figure 4.15-(a)–(b)).

The local stenosis gives a ten-fold increase in the peak velocity of the CSF in comparison with Poiseuille flow for the same pressure difference. However, this does not transfer into a increased ventricular dilation, as it can be explained by noticing that all of the pressure drop in the aqueduct occurs across the stenosed section (Figure 4.16-(a)). Furthermore, the flow through the aqueduct remained smooth at a Reynold's number of 21 ($\mathrm{Re} = \frac{\rho U D}{\mu}$, aqueduct diameter $D = 0.25$ mm, average veloc-

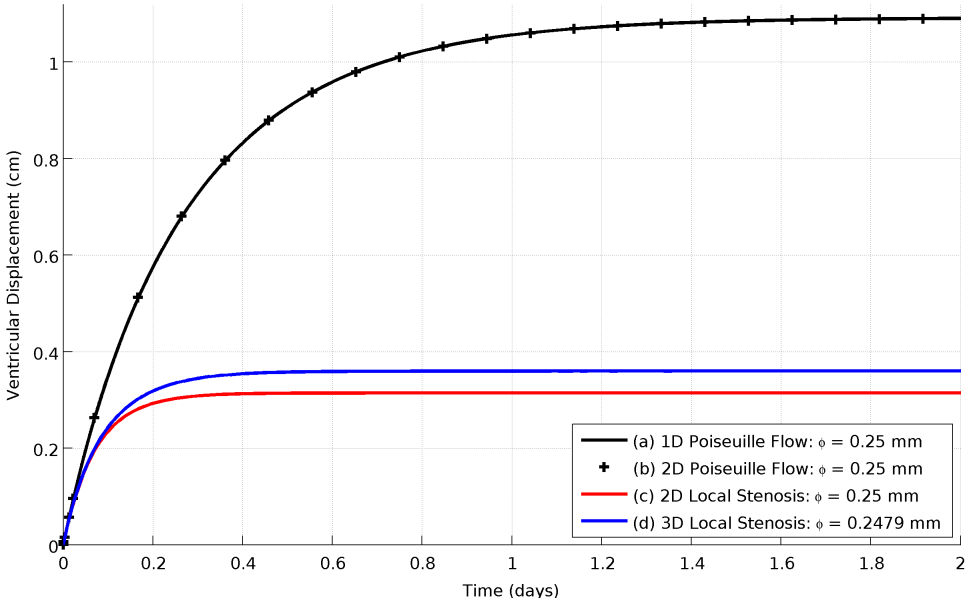

Figure 4.15: A novel coupling of the poroelastic solver with CFD allows the investigation of the Poiseuille-law assumption. The 2-D coupled model, **(a)**, agrees with the 1-D analytic model, **(b)**, when the entire length of the aqueduct is constricted (Poiseuille approach). However, when the stenosis is modelled in a physically relevant manner – as an axi-symmetric, **(c)**, and fully three-dimensional, **(d)**, local stenosis – there is a significantly smaller enlargement of the ventricles.

ity $U = 0.075$ m/s) with no observable secondary flow patterns. Finally, the acquired CFD simulations were ensured to be grid-independent (results not shown).

4.2.2.2 Patient-Specific Cerebral Aqueduct

It is obvious from the previous section that the Poiseuille flow assumption overestimates the pressure drop through the aqueduct. The results of the patient-specific investigation agree with this statement and further suggest that it is the geometry of the stenosis itself, rather than the entire flow domain, that governs the size of the ventriculomegaly.

For this part of the study, three variants of the geometry from Case 1 we used. As expected, when the SPET solver was coupled to flow dynamics through an open cerebral aqueduct there was no displacement of the ventricle wall (Figure 4.17-(a)), the flow remained smooth with a peak velocity of 0.7 cm/s (Figure 4.16-(b)).

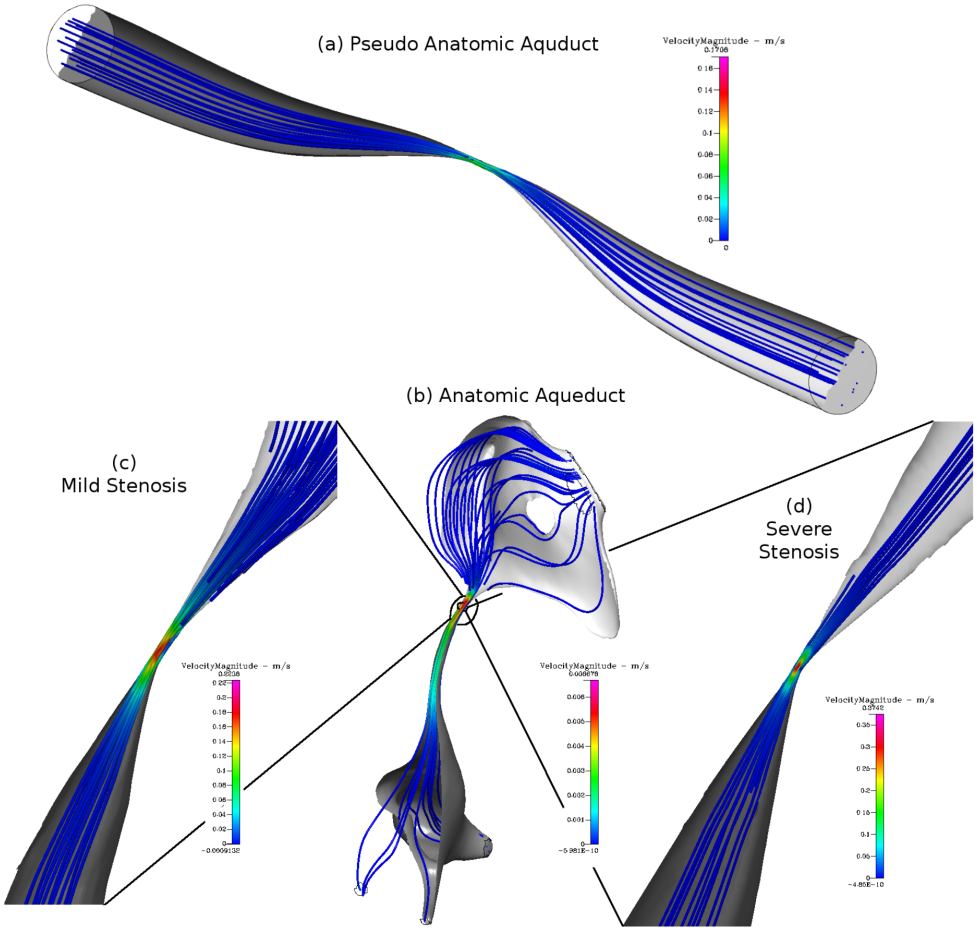

Figure 4.16: Streamlines for flow through the three-dimensional flow domains representing the cerebral aqueduct. Comparisons can be made between ventriculomegaly resulting from the pseudo- and patient-specific domains. Starting from the top, we have: **(a)** the pseudo-anatomic geometry; **(b)** the healthy geometry extracted from the MRI scan of Patient 1; **(c)** a close zoom of the mild stenosis; and **(d)**, a closer zoom of the severe stenosis.

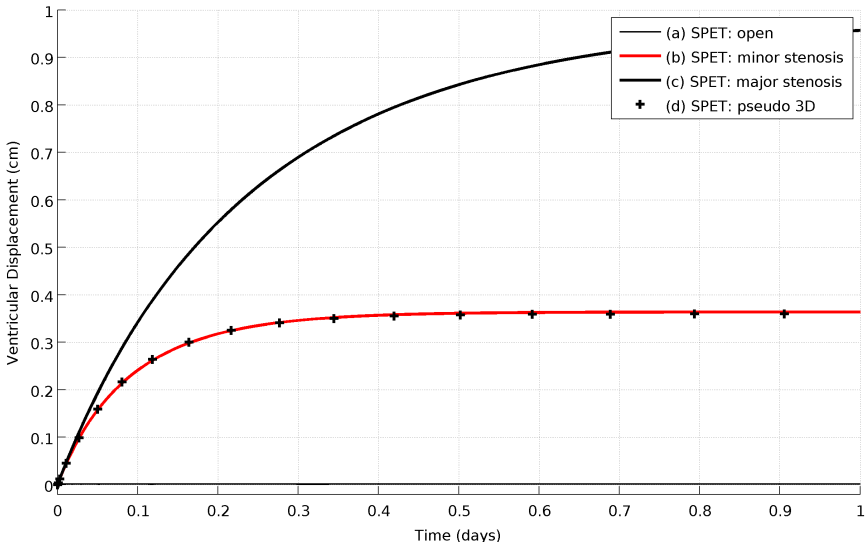

Figure 4.17: A comparison of the ventricular displacement evolution given by the single-network model with: **(a)** a patient-specific geometry with a healthy aqueduct (equivalent diameter, $d = 1.68720$ mm); **(b)** a patient-specific geometry with an imposed minor stenosis (equivalent diameter, $d = 0.21485$ mm); **(c)** a patient-specific geometry with an imposed major stenosis (equivalent diameter, $d = 0.07031$ mm); and **(d)** the pseudo three-dimensional geometry from Tully and Ventikos (2009) (equivalent diameter, $d = 0.24794$ mm.

The Case 1 aqueduct geometry with a minor stenosis produced virtually identical ventricular displacement to the pseudo-anatomic aqueduct geometry (Figure 4.17-(b) and Figure 4.17-(d) respectively). While not expected, this is not unreasonable given their cross-sectional diameters are also similar (5.4% and 6.3% of the open aqueduct respectively). In the patient-specific minor stenosis, the peak velocity of CSF through the aqueduct was 22.3 cm/s at a Reynold's number of 27 (aqueduct diameter $D = 0.22$ mm, average velocity $U = 0.11$ m/s) (Figure 4.16-(c)). The displacement of the ventricular wall increased further when a severe stenosis was imposed on the geometry of Case 1 (Figure 4.17-(c)). However, this value remained significantly smaller than would be, had the Poiseuille analytic assumption remained present in the model. Furthermore, the ventricular displacement is still well below what is encountered in the clinical presentation of hydrocephalus. The peak velocity of the CSF was 37.2 cm/s through the most stenosed part of the aqueduct, and the flow remained smooth at a Reynold's number of 15 (aqueduct diameter $D = 0.07$ mm, average velocity $U = 0.19$ m/s) (Figure 4.16-(d)).

Finally, it is important to note a few thing about the simulations run. Firstly,

the smoothness of the flow conditions are probably unique to this simplification for the system for numerical purposes. In reality, one should expect the blood-pressure boundary conditions, and the CSF as a consequence, to be pulsatile. Furthermore, in both cases of stenosis here, the cross-sectional diameter of the aqueduct is well below the scanning resolution of MRI machines. This means that in most cases, both of these stenosed aqueducts are likely to be classified by a radiographer as fully occluded.

4.3 DISCUSSION

We show in this chapter a novel extension of the state of the art in modelling hydrocephalus with poroelasticity through the inclusion of a multi-dimensional representation of the cerebral aqueduct. In doing so, it is possible to investigate the role of pulsations in CSF flow, assess the potential for small intra-cranial pressure gradients to lead to ventricular dilation and determine the impact of the magnitude of the stenosis on ventricular pressure and dilation.

Initially, the one-dimensional SPET model is used to investigate the role of the analytic cerebral aqueduct. From this, we determine that once the relative diameter of the aqueduct decreases below 0.25 mm it can be considered obstructed for the purposes of acute hydrocephalus. However, when the SPET model is combined with a multi-dimensional representation of the aqueduct, it is shown that the current analytic models may overestimate ventricular enlargement and a far greater obstruction must be present to cause ventricular enlargement on the scale seen in clinical data. Notably, severe obstruction of a patient-specific aqueduct ($d = 0.07$ mm) results in a smaller ventricular displacement than the analytic model with a diameter of 0.25 mm. To keep perspective, we should state that both of these obstructions are likely to fall below the resolution threshold of the MRI technology currently in clinical use and the aqueduct will appear to be fully occluded.

Clinical data exist that allow for some quantitative comparisons with the results found through this study. Howden et al. (2008) give a review of the velocity through the aqueduct in two different types of studies: flow found through MRI and flow found using computational models. They found that the range of velocities given by seven different studies using MRI was between 1.0 cm/s and 3.6 cm/s for the healthy

brain. This study found a reasonable correlation to this range, with the peak velocity in the pulsatile flow case (Figure 4.4-(g)) equal to 3.6 cm/s. We note however, that in the locally stenosed aqueduct, the peak velocity is ~ 16.0 cm/s.

Levine (2008) suggests that a "mini-gradient" of around 133 Pa, combined with an irregular tissue compliance may lead to hydrocephalus. Figure 4.15 shows that with a tumour-like obstruction in the cerebral aqueduct, and no pulsatility, a pressure gradient of ~ 100 Pa develops over the period of around half a day. This pressure rise causes a ~ 0.3 cm dilation of the ventricle wall. While the resulting dilation is relatively small, it may trigger a biological change in the tissue resulting in the required change in compliance (note also that the tissue permeability is not strain-dependant in this model). However, for this pressure gradient to occur, there must still be a significant obstruction of the aqueduct.

Furthermore, we have used small-strain, quasi-steady approximations in our constitutive relationship. If the characteristic time of hydrocephalus remains in the order of days, then the visco-elastic effect is likely to dissipate and can be considered negligible. However, the role of pulsations in CSF dynamics and hydrocephalus is not well understood, yet, it is known that cardiac oscillation of the cerebral blood results in pulsation of the CSF through the aqueduct.

In this study, it is shown that pulsatile CSF is present if there is a dynamic ventricular wall motion without changing the pattern of ventricular dilation for acute hydrocephalus. For future work, if pulsatile motion is considered to be important, the time-scale reduces and hyper- or visco-elastic effects may need to be considered. Ultimately, the final decision must be made in light of more confident experimental data (Sivaloganathan, 2005; Sivaloganathan et al., 2005).

Finally, Levine suggests that a challenge to the pulsation theory of hydrocephalus and altered compliance is that many conditions that lead to a rise in pulsatility are not associated with hydrocephalus (Levine, 2008). This study shows that pulsations in the ventricular wall will only result in ventricular enlargement in the presence of simultaneous flow obstruction. Furthermore, if this obstruction is removed, the ventricular dilation disappears (Figure 4.4-(h)), which suggests that the irreversible damage of some forms of hydrocephalus must also be accompanied by a biological change in the properties of the tissue.

CHAPTER 5

CHRONIC HYDROCEPHALUS

The paradoxical nature of chronic hydrocephalus cannot be explained by conflating the CSF and blood networks. In this chapter, MPET models are used to show how these networks can be separated and fluid transport between them investigated. This study is the first application of an MPET model to the interrogation of water transfer between several fluid networks in the cerebral environment.
The one-dimensional investigation in this chapter has been published in an alternative form in Tully and Ventikos (2010a) and the 1D-3D coupled model is under review (Tully and Ventikos, 2010b).

Unlike the acute, or obstructive, form of hydrocephalus investigated in the previous chapter, chronic hydrocephalus develops with a paradoxical absence of blockage in the ventricular system. Where we have used the reduced system (SPET) to study acute hydrocephalus, the full MPET model is utilized for chronic hydrocephalus as it is increasingly apparent that this form of hydrocephalus cannot be considered as a simple mechanical disruption of the flow of CSF. It is distinctly possible that the ventriculomegaly observed in clinical situations is the result of biological changes within the cerebral tissue.

The conflation of CSF and blood into a single fluid compartment, as apparent in the current state-of-the-art spatially resolved models of CSF dynamics, is challenged to capture these biological changes. The introduction of an MPET model allows the separation of cerebral fluid into many compartments, such as the arterial, arteriole, capillary and venous blood networks, and the extra-cellular and ventricu-

lar networks containing CSF. In doing so, many more locations for biological change within the environment can be investigated.

To the author's knowledge, this is the first time an MPET model has been applied to explicitly interrogate the transfer of water between several fluid networks in the cerebral environment. As a result, the availability of experimental data for validation is limited. In order to move forward, an extensive series of parametric searches are conducted to investigate the dynamics of the model. Using these investigations, the parameters for the MPET model are found such that the results of the SPET model are replicated; certain parameters are selected for closer investigation; and ultimately, two parameters are singled out as possible locations for biological change worthy of further investigation and experimental validation. These tests are initially carried out using the analytical assumptions present in in the one-dimensional SPET model, however in concluding, comparisons are drawn between results given by the analytical and patient-specific aqueduct geometries.

5.1 MPET: MODELLING IN ONE-DIMENSION

Use of an MPET model to interrogate the transfer of water between several fluid networks in the cerebral environment is a novel concept. The model developed in §3.1 requires an additional ten material constants to other reported poroelastic models, none of which can be found in the literature and are difficult to estimate through intuition. Hence, to gain an appreciation of the dynamics of the system a large-scale parametric study was conducted.

5.1.1 Methodology

From earlier discussions it is apparent that the most appropriate form of MPET is to create four compartments within the model: the arterial, arteriole/capillary, and venous blood networks and the extracellular/CSF network. Once again, this mathematical framework is implemented in a C++ solver that can be used to investigate the influence of model parameters on the outcome of the solver, or coupled to a three-dimensional simulation of CSF flow through the cerebral aqueduct. During

the parametric investigations, the steady-state ventricular displacement and network pressures are used to assess the validity of each permutation of parameters.

5.1.1.1 Final Model Assumptions

Some simplifications are made to the model that enable a thorough investigation of the parameters of specific interest. We assume a spherically symmetric geometry (as explained in §3.2.2) and that there are no external forces on the system, gravity is neglected and the reference frame is stationary. The time scale for development of hydrocephalus is in the order of days and weeks (possibly even years) and so it is reasonable to assume that the system is quasi-steady ($\frac{\partial^2}{\partial t^2}, \frac{\partial}{\partial t} \rightarrow 0$) although this is not the case if one was to consider the impact of systolic pulsation.

5.1.1.1.1 Continuity and Directional Water Transfer It is important that the transfer of water between fluid networks does not breach the law of continuity for the system as a whole. The amount of fluid in the system can be investigated by following the network transfer properties described in Figure 3.3.

$$Q_{\text{in}} = Q_{\text{out}} + Q_{\text{accumulation}} \tag{5.1a}$$

$$Q_{\text{accumulation}} = Q_a + Q_c + Q_e + Q_v \tag{5.1b}$$

$$Q_a = Q_{\text{in}} - \dot{s}_{a\rightarrow c} \tag{5.1c}$$

$$Q_c = \dot{s}_{a\rightarrow c} - \dot{s}_{c\rightarrow e} - \dot{s}_{c\rightarrow v} \tag{5.1d}$$

$$Q_e = \dot{s}_{c\rightarrow e} - \dot{s}_{e\rightarrow v} \tag{5.1e}$$

$$Q_v = \dot{s}_{c\rightarrow v} + \dot{s}_{e\rightarrow v} - Q_{\text{out}} \tag{5.1f}$$

where Q_{in} and Q_{out} are the flux of fluid in and out of the control volume, respectively; $Q_{\text{accumulation}}$ is the fluid accumulated in the control volume as a whole; Q_a, Q_c, Q_e and Q_v are the fluid accumulation in each of the arterial, arteriole/capillary, CSF and venous networks; and $\dot{s}_{y\rightarrow x}$ represents the flux of fluid from network y to network x and can be either positive or negative.

In a healthy brain, $Q_{\text{accumulation}}$ should equal zero when averaged over time. Conversely, in the symptomatic brain, water can accumulate in the CSF space (including the interstitial space) or in the blood networks.

Furthermore, based on arguments about the wall thickness and leakiness of blood vessels, and physiological observations of the system, assumptions are made on the direction of water transport between the fluid networks. Specifically, we assume that:

- directional transport will always occur from the arterial network to the arteriole/capillary network ($\dot{s}_{a\to c} = |\dot{s}_{a\to c}| = -\dot{s}_{c\to a} \geq 0$);
- transport from the arteriole/capillary network will be to either the CSF network ($\dot{s}_{c\to e} = |\dot{s}_{c\to e}| = -\dot{s}_{e\to c} \geq 0$), or the venous network ($\dot{s}_{c\to v} = |\dot{s}_{c\to v}| = -\dot{s}_{v\to c} \geq 0$); and,
- fluid in the CSF must expel into the venous network ($\dot{s}_{e\to v} = |\dot{s}_{e\to v}| = -\dot{s}_{e\to v} \geq 0$).

Moreover, the physical properties of the arterial vessels implies that there is no direct transfer of fluid from the arterial network to either the CSF or venous networks ($\dot{s}_{a\to e}, \dot{s}_{a\to v} = 0$).

Hence, the system reduces from (3.25) to,

$$\frac{\partial^2 u}{\partial r^2} + \frac{2}{r}\frac{\partial u}{\partial r} - \frac{2}{r^2}u - \frac{1-2\nu}{2G(1-\nu)}\left(\alpha^a \frac{\partial p^a}{\partial r} + \alpha^c \frac{\partial p^c}{\partial r} + \alpha^e \frac{\partial p^e}{\partial r} + \alpha^v \frac{\partial p^v}{\partial r}\right) = 0 \tag{5.2a}$$

$$-k^a\left(\frac{\partial^2 p^a}{\partial r^2} + \frac{2}{r}\frac{\partial p^a}{\partial r}\right) + |\dot{s}_{a\to c}| = 0 \tag{5.2b}$$

$$-k^c\left(\frac{\partial^2 p^c}{\partial r^2} + \frac{2}{r}\frac{\partial p^c}{\partial r}\right) - |\dot{s}_{a\to c}| + |\dot{s}_{c\to e}| + |\dot{s}_{c\to v}| = 0 \tag{5.2c}$$

$$-k^e\left(\frac{\partial^2 p^e}{\partial r^2} + \frac{2}{r}\frac{\partial p^e}{\partial r}\right) - |\dot{s}_{c\to e}| + |\dot{s}_{e\to v}| = 0 \tag{5.2d}$$

$$-k^v\left(\frac{\partial^2 p^v}{\partial r^2} + \frac{2}{r}\frac{\partial p^v}{\partial r}\right) - |\dot{s}_{c\to v}| - |\dot{s}_{e\to v}| = 0, \tag{5.2e}$$

where a positive value for $|\dot{s}|$ represents a loss of fluid from the network and a negative value indicates that fluid is added to the network.

Note that describing the transfer between networks in this manner is only relevant if the transfer is considered to be driven by a hydrostatic pressure gradient (i.e. $\dot{s}_{y\to x} = -\gamma_{yx}\left[p^x - p^y\right]$ where γ_{yx} is the transfer coefficient scaling the flow from network y to network x). Active and/or biological transfer mechanisms (for instance cellular-level water-flux through aquaporins (Agre et al., 2004; Agre, 2006)) are not adequately well-quantified yet for inclusion in the model.

5.1.1.1.2 Boundary Conditions at the Ventricular Wall The first of the boundary conditions at the ventricle wall ($r = r_1$) specifies that the stress must be continuous across the wall,

$$(1-\nu)\frac{\partial u(r_1,t)}{\partial r} + 2\nu\frac{u(r_1\,t)}{r_1} - \sum_{i=a,c,e,v}\frac{(\alpha^i-1)(1-2\nu)}{2G}p^i(r_1,t) = 0. \tag{5.3}$$

The production of CSF from the blood results in a pressure drop in the arteriole/-capillary blood network,

$$-\kappa_{c\rightarrow\text{ventricle}}\frac{\partial p^c(r_1,t)}{\partial r} = -Q_p, \tag{5.4}$$

where $\kappa_{c\rightarrow\text{ventricle}}$ is the resistance of the flow from the capillary network to the ventricles (through the choroid plexus) (its value, $\kappa_{c\rightarrow\text{ventricle}} = 6.0\times10^{-4}$ m^{5}skg^{-1}, is discussed in Figure C.3). Furthermore, based on vascular wall-thickness arguments, there is no flow into or out of the arterial and venous blood networks,

$$\frac{\partial p^a(r_1,t)}{\partial r} = \frac{\partial p^v(r_1,t)}{\partial r} = 0. \tag{5.5}$$

The mass of fluid in the ventricles is conserved (with d being the diameter of the cerebral aqueduct),

$$Q_p = \frac{\pi d^4}{128\mu^e L}\left[p^e(r_1,t) - p^e(r_M,t)\right] - 4\pi k^e(r_1+u_1^n)^2\frac{\partial p^e(r_1,t)}{\partial r} + 4\pi(r_1+u_1^n)^2\frac{\partial u(r_1,t)}{\partial t}. \tag{5.6}$$

5.1.1.1.3 Boundary Conditions at the Skull At the skull ($r = r_M$), the displacement is zero,

$$u(r_M,t) = 0. \tag{5.7}$$

The blood pressures are given by physically relevant arterial and venous blood pressures,

$$p^a(r_M,t) = p_{bpa}, \quad p^v(r_M,t) = p_{bp}. \tag{5.8}$$

There is no flow into or out of the arteriole/capillary blood network at the skull,

$$\frac{\partial p^c(r_M,t)}{\partial r} = 0, \tag{5.9}$$

and the absorption of CSF into the venous network results in a pressure rise,

$$p^e(r_M,t) = p^v(r_M,t) + \mu^e R Q_0, \tag{5.10}$$

where μ^e is the viscosity of the CSF, R is the resistance to outflow through the arachnoid granulations (as found from reported experimental data) and Q_0 is the out-flux of CSF at the skull.

5.1.1.1.4 Tissue Properties In this study we continue to use the material values for the tissue and CSF network as reported in Smillie et al. (2005) and Tully and Ventikos (2009) summarized in Table 3.1. This will allow a quantitative comparison of the results of the single and quadruple MPET models. However, the quadruple MPET model introduces an additional ten parameters that are unknown; these are the Biot parameters and permeabilities of the new blood networks, and the transfer coefficients between the fluid networks. As far as the author is aware, no suitable experimental data exist and approximations are made through an extensive parametric search detailed in §5.1.2.

5.1.1.2 Solution Method and Implementation

For the cerebral MPET model to be considered successful, it needed to: possess a healthy-state where an open aqueduct gave no change in displacement or pressure gradient; show clinically relevant results for acute hydrocephalus; and describe the paradoxical nature of NPH.

Given the lack of appropriate experimental data, the first two conditions were satisfied by tuning the parameters to replicate the results of the single network model described in Tully and Ventikos (2009). Each of the ten constants were varied four times, through several orders of magnitude, in an initial parametric study of 4^{10} permutations.

5.1.1.2.1 Discretization of the System Like SPET, the MPET model is defined as a boundary value problem and finite differences are used to discretize the system equations. The central difference scheme is used for spatial discretization for the equations of motion, forward or backward difference schemes are implemented as appropriate for estimating spatial derivatives in the boundary conditions and the forward difference scheme is utilized for temporal discretization.

Applying the same discretization template as the previous Chapter gives:

Displacement Equation Equation (5.2a) becomes,

$$\frac{u_{i+1}^{n+1}-2u_i^{n+1}+u_{i-1}^{n+1}}{\Delta r^2}+\frac{2}{r_i}\frac{u_{i+1}^{n+1}-u_{i-1}^{n+1}}{2\Delta r}-\frac{2}{r_i^2}u_i^{n+1}-\frac{(1-2\nu)}{2G(1-\nu)}\left[\alpha^b\frac{p_{i+1}^{a,n+1}-p_{i-1}^{a,n+1}}{2\Delta r}\right.$$
$$\left.+\alpha^c\frac{c,p_{i+1}^{n+1}-p_{i-1}^{c,n+1}}{2\Delta r}+\alpha^e\frac{p_{i+1}^{e,n+1}-p_{i-1}^{e,n+1}}{2\Delta r}+\alpha^v\frac{p_{i+1}^{v,n+1}-p_{i-1}^{v,n+1}}{2\Delta r}\right]=0$$

rearranging for the nodal values,

$$\left(\frac{1}{\Delta r^2}-\frac{1}{r_i\Delta r}\right)u_{i-1}^{n+1}+\left(\frac{-2}{\Delta r^2}+\frac{-2}{r_i^2}\right)u_i^{n+1}+\left(\frac{1}{\Delta r^2}+\frac{1}{r_i\Delta r}\right)u_{i+1}^{n+1}+\frac{(1-2\nu)\alpha^a}{4G(1-\nu)\Delta r}p_{i-1}^{a,n+1}$$
$$-\frac{(1-2\nu)\alpha^a}{4G(1-\nu)\Delta r}p_{i+1}^{a,n+1}+\frac{(1-2\nu)\alpha^c}{4G(1-\nu)\Delta r}p_{i-1}^{c,n+1}-\frac{(1-2\nu)\alpha^c}{4G(1-\nu)\Delta r}p_{i+1}^{c,n+1}+\frac{(1-2\nu)\alpha^e}{4G(1-\nu)\Delta r}p_{i-1}^{e,n+1}$$
$$-\frac{(1-2\nu)\alpha^e}{4G(1-\nu)\Delta r}p_{i+1}^{e,n+1}+\frac{(1-2\nu)\alpha^v}{4G(1-\nu)\Delta r}p_{i-1}^{v,n+1}-\frac{(1-2\nu)\alpha^v}{4G(1-\nu)\Delta r}p_{i+1}^{v,n+1}=0, \quad (5.11)$$

or simply,

$$a_i u_{i-1}^{n+1}+b_i u_i^{n+1}+c_i u_{i+1}^{n+1}+d_i p_{i-1}^{a,n+1}-d_i p_{i+1}^{a,n+1}+e_i p_{i-1}^{c,n+1}-e_i p_{i+1}^{c,n+1}$$
$$+f_i p_{i-1}^{e,n+1}-f_i p_{i+1}^{e,n+1}+g_i p_{i-1}^{v,n+1}-g_i p_{i+1}^{v,n+1}=0.$$

Arterial Pressure Equation (5.2b) becomes,

$$\frac{p_{i+1}^{a,n+1}-2p_i^{a,n+1}+p_{i-1}^{a,n+1}}{\Delta r^2}+\frac{2}{r_i}\frac{p_{i+1}^{a,n+1}-p_{i-1}^{a,n+1}}{2\Delta r}=\frac{1}{k^a}|\dot{s}_{a\to c}|,$$

rearranging for the nodal values,

$$\left(\frac{1}{\Delta r^2}-\frac{1}{r_i\Delta r}\right)p_{i-1}^{a,n+1}+\left(\frac{-2}{\Delta r^2}\right)p_i^{a,n+1}+\left(\frac{1}{\Delta r^2}+\frac{1}{r_i\Delta r}\right)p_{i+1}^{a,n+1}=\frac{1}{k^a}|\dot{s}_{a\to c}|, \quad (5.12)$$

or simply,

$$a_i p_{i-1}^{a,n+1}+h_i p_i^{a,n+1}+c_i p_{i+1}^{a,n+1}=S_A.$$

Arteriole/Capillary Pressure Equation (5.2c) becomes,

$$\frac{p_{i+1}^{c,n+1}-2p_i^{c,n+1}+p_{i-1}^{c,n+1}}{\Delta r^2}+\frac{2}{r_i}\frac{p_{i+1}^{c,n+1}-p_{i-1}^{c,n+1}}{2\Delta r}=-\frac{1}{k^c}|\dot{s}_{a\to c}|+\frac{1}{k^c}|\dot{s}_{c\to e}|+\frac{1}{k^c}|\dot{s}_{c\to v}|,$$

rearranging for the nodal values,

$$\left(\frac{1}{\Delta r^2}-\frac{1}{r_i\Delta r}\right)p_{i-1}^{c,n+1}+\left(\frac{-2}{\Delta r^2}\right)p_i^{c,n+1}+\left(\frac{1}{\Delta r^2}+\frac{1}{r_i\Delta r}\right)p_{i+1}^{c,n+1}=-\frac{1}{k^c}|\dot{s}_{a\to c}|+\frac{1}{k^c}|\dot{s}_{c\to e}|+\frac{1}{k^c}|\dot{s}_{c\to v}|, \quad (5.13)$$

or simply,

$$a_i p_{i-1}^{c,n+1}+h_i p_i^{c,n+1}+c_i p_{i+1}^{c,n+1}=S_C.$$

CSF *Pressure* Equation (5.2d) becomes,

$$\frac{p_{i+1}^{e,n+1}-2p_i^{e,n+1}+p_{i-1}^{e,n+1}}{\Delta r^2}+\frac{2}{r_i}\frac{p_{i+1}^{e,n+1}-p_{i-1}^{e,n+1}}{2\Delta r}=-\frac{1}{k^e}|\dot{s}_{c\rightarrow e}|+\frac{1}{k^e}|\dot{s}_{e\rightarrow v}|,$$

rearranging for the nodal values,

$$\left(\frac{1}{\Delta r^2}-\frac{1}{r_i\Delta r}\right)p_{i-1}^{e,n+1}+\left(\frac{-2}{\Delta r^2}\right)p_i^{e,n+1}+\left(\frac{1}{\Delta r^2}+\frac{1}{r_i\Delta r}\right)p_{i+1}^{e,n+1}=-\frac{1}{k^e}|\dot{s}_{c\rightarrow e}|+\frac{1}{k^e}|\dot{s}_{e\rightarrow v}|, \tag{5.14}$$

or simply,

$$a_i p_{i-1}^{e,n+1}+h_i p_i^{e,n+1}+c_i p_{i+1}^{e,n+1}=S_E.$$

Venous Pressure Equation (5.2e) becomes,

$$\frac{p_{i+1}^{v,n+1}-2p_i^{v,n+1}+p_{i-1}^{v,n+1}}{\Delta r^2}+\frac{2}{r_i}\frac{p_{i+1}^{v,n+1}-p_{i-1}^{v,n+1}}{2\Delta r}=-\frac{1}{k^v}|\dot{s}_{c\rightarrow v}|-\frac{1}{k^v}|\dot{s}_{e\rightarrow v}|,$$

rearranging for the nodal values,

$$\left(\frac{1}{\Delta r^2}-\frac{1}{r_i\Delta r}\right)p_{i-1}^{v,n+1}+\left(\frac{-2}{\Delta r^2}\right)p_i^{v,n+1}+\left(\frac{1}{\Delta r^2}+\frac{1}{r_i\Delta r}\right)p_{i+1}^{v,n+1}=-\frac{1}{k^v}|\dot{s}_{c\rightarrow v}|-\frac{1}{k^v}|\dot{s}_{e\rightarrow v}|, \tag{5.15}$$

or simply,

$$a_i p_{i-1}^{v,n+1}+h_i p_i^{v,n+1}+c_i p_{i+1}^{v,n+1}=S_V.$$

Boundary Conditions

Equation (5.3) becomes,

$$\begin{aligned}(1-\nu)\frac{u_2^{n+1}-u_1^{n+1}}{\Delta r}+2\nu\frac{u_1^{n+1}}{r_1}-\frac{(\alpha^a-1)(1-2\nu)}{2G}p_1^{a,n+1}\\ -\frac{(\alpha^c-1)(1-2\nu)}{2G}p_1^{c,n+1}-\frac{(\alpha^e-1)(1-2\nu)}{2G}p_1^{e,n+1}-\frac{(\alpha^v-1)(1-2\nu)}{2G}p_1^{v,n+1}=0,\end{aligned}$$

simplified as,

$$\begin{aligned}\left[\frac{2\nu}{r_1}-\frac{1-\nu}{\Delta r}\right]u_1^{n+1}+\frac{1-\nu}{\Delta r}u_2^{n+1}-\frac{(\alpha^a-1)(1-2\nu)}{2G}p_1^{a,n+1}\\ -\frac{(\alpha^c-1)(1-2\nu)}{2G}p_1^{c,n+1}-\frac{(\alpha^e-1)(1-2\nu)}{2G}p_1^{e,n+1}-\frac{(\alpha^v-1)(1-2\nu)}{2G}p_1^{v,n+1}=0,\end{aligned} \tag{5.16}$$

$$Au_1^{n+1}+Bu_2^{n+1}+C_A p_1^{a,n+1}+C_C p_1^{c,n+1}+C_E p_1^{e,n+1}+C_V p_1^{v,n+1}=0.$$

Equation (5.4) becomes,

$$-\kappa_{c\rightarrow\text{ventricle}}\frac{p_2^{c,n+1}-p_1^{c,n+1}}{\Delta r}=-Q_p,$$

simplified as,

$$p_2^{c,n+1}-p_1^{c,n+1}=\frac{Q_p\Delta r}{\kappa_{c\rightarrow\text{ventricle}}}, \tag{5.17}$$
$$p_1^{c,n+1}-p_2^{c,n+1}=D.$$

Equation (5.5) becomes,

$$\frac{p_2^{a,n+1}-p_1^{a,n+1}}{\Delta r}=0 \quad\rightarrow\quad p_1^{a,n+1}=p_2^{a,n+1}, \tag{5.18}$$
$$\frac{p_2^{v,n+1}-p_1^{v,n+1}}{\Delta r}=0 \quad\rightarrow\quad p_1^{v,n+1}=p_2^{v,n+1}. \tag{5.19}$$

Equation (5.6) becomes,

$$\frac{\pi d^4}{128\mu^e L}\left(p_1^{e,n+1}-p_M^{e,n+1}\right)-4\pi k^e(r_1+u_1^n)^2\frac{p_2^{e,n+1}-p_1^{e,n+1}}{\Delta r}+4\pi(r_1+u_1^n)^2\frac{u_1^{n+1}-u_1^n}{\Delta t}=Q_p,$$

simplified as,

$$\begin{aligned}\frac{4\pi(r_1+u_1^n)^2}{\Delta t}u_1^{n+1}+\left[\frac{\pi d^4}{128\mu^e L}+\frac{4\pi k^e(r_1+u_1^n)^2}{\Delta r}\right]p_1^{e,n+1}\\ -\frac{4\pi k^e(r_1+u_1^n)^2}{\Delta r}p_2^{e,n+1}-\frac{\pi d^4}{128\mu^e L}p_M^{e,n+1}=Q_p+4\pi(r_1+u_1^n)^2\frac{u_1^n}{\Delta t},\end{aligned} \tag{5.20}$$
$$Hu_1^{n+1}+Jp_1^{e,n+1}+Lp_2^{e,n+1}+Np_M^{e,n+1}=F.$$

Equations (5.7) and (5.8) become,

$$u_M^{n+1}=0, \tag{5.21}$$
$$p_M^{a,n+1}=p_{bpa}, \tag{5.22}$$
$$p_M^{v,n+1}=p_{bp}. \tag{5.23}$$

Equation (5.9) become,

$$\frac{p_M^{c,n+1}-p_{M-1}^{c,n+1}}{\Delta r}=0 \quad\rightarrow\quad p_M^{c,n+1}=p_{M-1}^{c,n+1}, \tag{5.24}$$

and finally, Equation (5.10) becomes,

$$p_M^{e,n+1}=p_M^{v,n+1}+\mu^e RQ_0 \quad\rightarrow\quad p_M^{e,n+1}-p_M^{v,n+1}=P. \tag{5.25}$$

Collecting these discrete representations of the system into the form $\mathbf{Ax}=\mathbf{b}$ gives a numerical template for the multiple-network poroelastic `C++` solver (Figure 5.1 shows the template for a system where $M=5$).

$$
\begin{array}{|cccccccccccccccccccc|c|c|}
\hline
 & A & B & & & & C_A & & & & C_C & & & & C_E & & & & C_V & & & & u_1 & \\
 & a_2 & b_2 & c_2 & & & d_2 & & -d_2 & & e_2 & & -e_2 & & f_2 & & -f_2 & & g_2 & & -g_2 & & u_2 & \\
 & & a_3 & b_3 & c_3 & & & d_3 & & -d_3 & & e_3 & & -e_3 & & f_3 & & -f_3 & & g_3 & & -g_3 & u_3 & \\
 & & & a_4 & b_4 & c_4 & & & d_4 & & -d_4 & & e_4 & & -e_4 & & f_4 & & -f_4 & & g_4 & & -g_4 & u_4 & \\
 & & & & & 1 & & & & & & & & & & & & & & & & & u_5 & \\
\hline
 & & & & & & 1 & -1 & & & & & & & & & & & & & & & p_{a,1} & \\
 & & & & & & a_2 & h_2 & c_2 & & & & & & & & & & & & & & p_{a,2} & \\
 & & & & & & & a_3 & h_3 & c_3 & & & & & & & & & & & & & p_{a,3} & \\
 & & & & & & & & a_4 & h_4 & c_4 & & & & & & & & & & & & p_{a,4} & \\
 & & & & & & & & & & 1 & & & & & & & & & & & & p_{a,5} & \\
\hline
 & & & & & & & & & & 1 & -1 & & & & & & & & & & & p_{c,1} & \\
 & & & & & & & & & & a_2 & h_2 & c_2 & & & & & & & & & & p_{c,2} & \\
 & & & & & & & & & & & a_3 & h_3 & c_3 & & & & & & & & & p_{c,3} & \\
 & & & & & & & & & & & & a_4 & h_4 & c_4 & & & & & & & & p_{c,4} & \\
 & & & & & & & & & & & & & -1 & 1 & & & & & & & & p_{c,5} & \\
\hline
 & H & & & & & & & & & & & & & & J & L & & & N & & & p_{e,1} & \\
 & & & & & & & & & & & & & & & a_2 & h_2 & c_2 & & & & & p_{e,2} & \\
 & & & & & & & & & & & & & & & & a_3 & h_3 & c_3 & & & & p_{e,3} & \\
 & & & & & & & & & & & & & & & & & a_4 & h_4 & c_4 & & & p_{e,4} & \\
 & & & & & & & & & & & & & & & & & & & 1 & & 1 & p_{e,5} & \\
\hline
 & & & & & & & & & & & & & & & 1 & -1 & & & & & & p_{v,1} & \\
 & & & & & & & & & & & & & & & a_2 & h_2 & c_2 & & & & & p_{v,2} & \\
 & & & & & & & & & & & & & & & & a_3 & h_3 & c_3 & & c_4 & & p_{v,3} & \\
 & & & & & & & & & & & & & & & & & a_4 & h_4 & & 1 & & p_{v,4} & \\
\hline
\end{array}
=
\begin{array}{|c|c|}
\hline
 & \\
\hline
 & S_A \\
 & S_A \\
 & S_A \\
\hline
 & D \\
 & S_C \\
 & S_C \\
 & S_C \\
 & p_{bpa} \\
\hline
 & F \\
 & S_E \\
 & S_E \\
 & S_E \\
 & P \\
\hline
 & S_V \\
 & S_V \\
 & S_V \\
 & p_{bp} \\
\hline
\end{array}
$$

where,

$$
\begin{aligned}
a_i &= \frac{1}{\Delta r^2} - \frac{1}{r_i \Delta r} & g_i &= \frac{\alpha^v(1-2\nu)}{4G(1-\nu)\Delta r} \\
b_i &= \frac{-2}{\Delta r^2} + \frac{1}{r_i^2} & h_i &= \frac{-2}{\Delta r^2} \\
c_i &= \frac{1}{\Delta r^2} + \frac{1}{r_i \Delta r} & S_A &= \frac{1}{k^a}\left|\dot{s}_{a\to c}\right| \\
d_i &= \frac{\alpha^a(1-2\nu)}{4G(1-\nu)\Delta r} & S_C &= -\frac{1}{k^c}\left|\dot{s}_{a\to c}\right| + \frac{1}{k^c}\left|\dot{s}_{c\to e}\right| + \frac{1}{k^c}\left|\dot{s}_{c\to v}\right| \\
e_i &= \frac{\alpha^c(1-2\nu)}{4G(1-\nu)\Delta r} & S_E &= -\frac{1}{k^e}\left|\dot{s}_{c\to e}\right| + \frac{1}{k^e}\left|\dot{s}_{e\to v}\right| \\
f_i &= \frac{\alpha^e(1-2\nu)}{4G(1-\nu)\Delta r} & S_V &= -\frac{1}{k^v}\left|\dot{s}_{c\to v}\right| - \frac{1}{k^v}\left|\dot{s}_{e\to v}\right|
\end{aligned}
$$

$$
\begin{aligned}
A &= \frac{2\nu}{r_1} - \frac{1-\nu}{\Delta r} \\
B &= \frac{1-\nu}{\frac{\Delta r}{r_1}} \\
C_A &= \frac{(1-\alpha^a)(1-2\nu)}{2G} \\
C_C &= \frac{(1-\alpha^c)(1-2\nu)}{2G} \\
C_E &= \frac{(1-\alpha^e)(1-2\nu)}{2G} \\
C_V &= \frac{(1-\alpha^v)(1-2\nu)}{2G}
\end{aligned}
$$

$$
\begin{aligned}
D &= \frac{Q_p \Delta r}{\kappa_{c-\text{ventricle}}} \\
F &= Q_p + 4\pi(r_1 + u_1^n)^2 \frac{u_1^n}{\Delta t} \\
H &= \frac{4\pi(r_1+u_1^n)^2}{\Delta t} \\
J &= \frac{\pi d^4}{128\mu^e L} + \frac{4\pi k^e (r_1+u_1^n)^2}{\Delta r} \\
L &= \frac{-4\pi k^e (r_1+u_1^n)^2}{\Delta r} \\
N &= \frac{-\pi d^4}{128\mu^e L} \\
P &= \mu^e R Q_0
\end{aligned}
$$

Figure 5.1: The MPET numerical template for $M = 5$.

5.1.1.2.2 Implementation Following from the lessons learnt in the previous chapter, the MPET model is written as a single-function C++ routine. The TNT and JAMA libraries are used again to solve the linear system through *LU-decomposition*. The primary difference in execution between the SPET solver and this solver is that a list of system properties – such as the permeabilities, transfer coefficients and Biot parameters for each fluid network – must now be passed to the solver as command line arguments. This change in methodology makes possible a large-scale parametric search, and allows it to be conducted in serial arrays on the high performance computing facility.

Conducting an extensive parametric search The MPET model requires an additional ten material constants to other reported poroelastic models. Experimental data are not available in the literature and these parameters are difficult to estimate through intuition. Hence, a large-scale parametric study is the next best approach to gain an understanding of the dynamics of the system and the level of influence for each parameter on the steady-state clinical markers of the simulation. As this is the first study of its kind, selecting appropriate ranges through which the parameters should be investigated was uncharted. The basis for selection was grounded in the accepted values used in the SPET model, and indeed it was decided to keep the values for the CSF network consistent between SPET and MPET models.

In the initial investigation, each of the ten parameters – the Biot parameters of each blood network: α^a, α^c and α^v; the network transfer coefficients: γ_{ac}, γ_{ce}, γ_{cv} and γ_{ev}; and the network permeabilities: κ^a, κ^c and κ^v – are assigned one of four values distributed linearly over their given range (see Table 5.1). For each individual value of a given parameter, a simulation was run with every possible combination of the remaining parameters resulting in a parametric run of $4^{10} = 2^{20} = 1,048,576$ permutations.

This initial investigation proved to be problematic for discerning useful information about the dynamics of the model. Almost two thirds of the permutations produced errors within the solver; assigning values linearly across exponential ranges meant that the the smaller magnitudes were not evaluated effectively; and finally, patterns and trends linking the displacement and pressure to parameters were difficult to discern with only four values for each parameter (see Figure 5.2).

To improve the parametric study, two changes were made: for each simulation

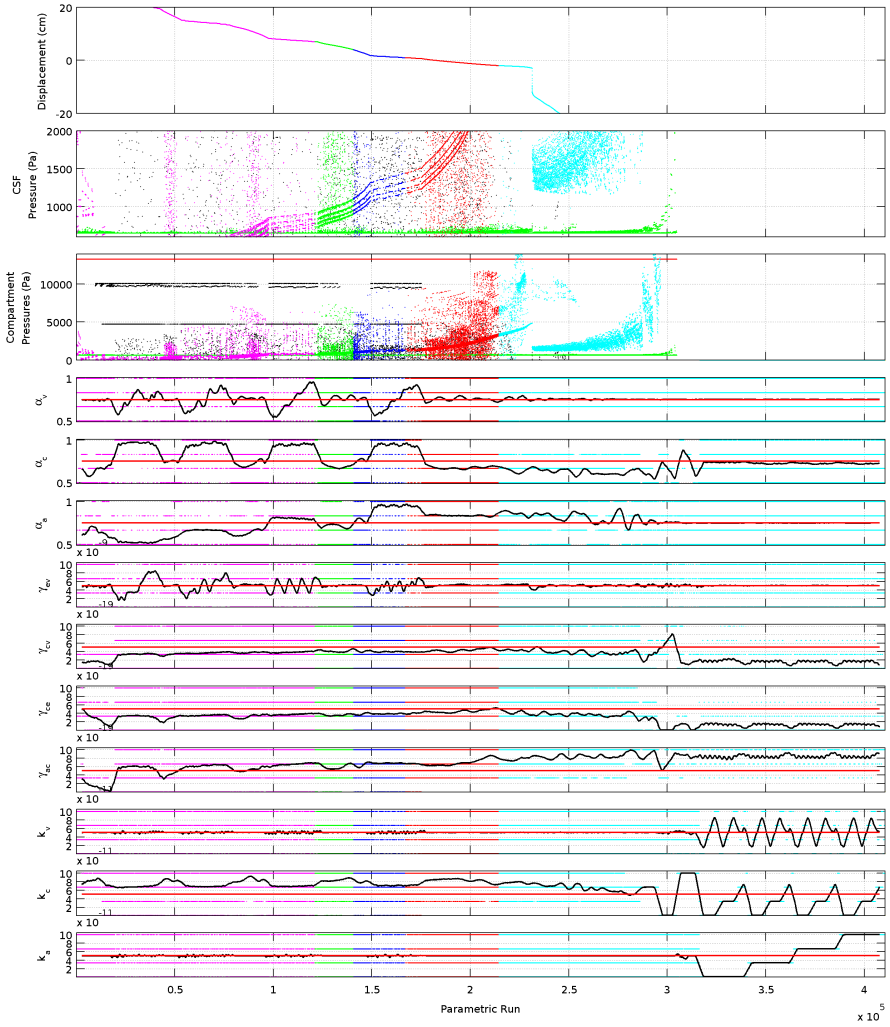

Figure 5.2: The first attempt at a parametric search was hampered by design flaws in the study. In this search each of the ten parameters was assigned four values distributed linearly across its designated range. Almost two thirds of the resulting 2^{20} permutations returned errors from the model and are omitted from this figure. The runs that returned results are organized in this image according to the method set out in the following chapter and while some useful information can be seen, patterns and trends that would move the project forward are not discernible.

Parameter	Lower Value	Upper Value	Units
$\alpha^{a,c,v}$	0.5	1.0	
$\gamma_{ac,ce,cv}$	1.0×10^{-22}	1.0×10^{-18}	$m^2N^{-1}s^{-1}$
γ_{ev}	1.0×10^{-13}	1.0×10^{-8}	$m^2N^{-1}s^{-1}$
$\kappa^{a,c,v}$	1.0×10^{-12}	1.0×10^{-10}	m^2

Table 5.1: The initial search ranges for tissue and transport properties of the MPET model. The viscosity of the blood networks, $\mu^{a,c,v}$, is assumed to be three times greater than water.

within the parametric study, Biot parameters were determined from a uniform distribution across its given range using the `python` random number generator,

$$X \sim \textbf{UNIFORM}(a, b);$$

and the values for γ and k were assigned on a log-normal (base 10) distribution,

$$X = 10^{\theta}, \qquad \text{where } \theta \sim \textbf{UNIFORM}(a, b);$$

in effect, the study was converted into a Monte-Carlo sampling of the phase space.

The difference in this approach is obvious when a comparison is drawn between the histogram of parameters from the discrete, linear run (Figure 5.3-(a)) and the continuous, log-normal run (Figure 5.3-(b)). In the discrete set, it is possible to see the domination of the simulations with errors (the yellow area) and while some trends can been seen (such as those in γ_{ac} and γ_{ce}) a great deal more information can be drawn from the continuous run and will be discussed in §5.1.2.

Analysing the parametric search As with any extensive parametric search, interpreting the results is a real challenge. Initially, statistical regressions were run with little success – while these results showed extremely good p-values for certain parameters, they were not particularly helpful for the kind of analysis needed in this study. Instead, a more graphical approach was adopted.

The key performance indicators used to judge the model are the displacement and pressures at the ventricular wall. Of these, the most clinically relevant (and easily observable) value is the displacement of the lateral ventricles. To assess the results of the parametric study and the influence of each permutation of parameters, the simulations are sorted in order of ventricular displacement and plotted

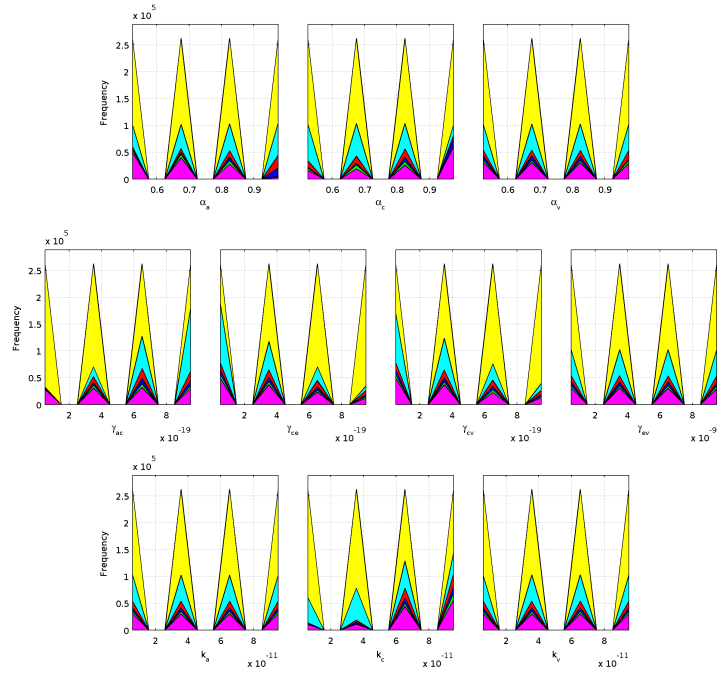

(a)

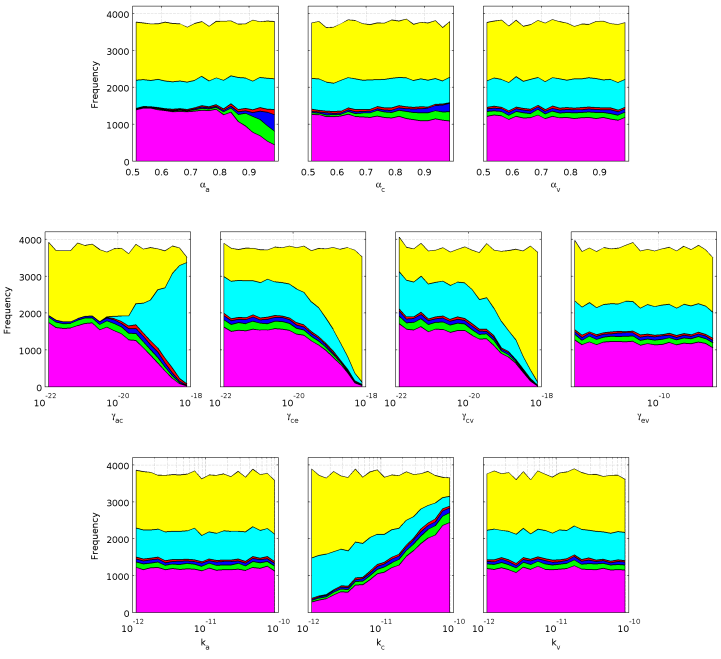

(b)

Figure 5.3: Histogram of the ten model parameters of the initial parametric searches: **(a)** shows a discrete, linear choice of parameters; and **(b)** shows a continuous, log-normal choice.

on a graph such as Figure 5.2. There are distinct levels to which the ventricles may enlarge or contract and each group is assigned a colour in the plot:

(a) Ventricular enlargement greater than the thickness of the parenchyma shell (70 mm) (and hence a non-physical result) is coloured magenta.

(b) Ventricular enlargement between the outer limit and a clinically relevant upper limit (40 mm) is coloured green.

(c) Ventricular enlargement within the clinically relevant upper limit and the displacement determined by the SPET model (9.64 mm for an obstructed aqueduct with $\phi = 0.25$ mm) is coloured blue.

(d) Ventricular enlargement that is lower than the result given by SPET, or contraction not greater than 20 mm, is coloured red.

(e) Ventricular contraction greater than 20 mm, yet not returning `NaN` (indicating a divergent solution) or an error is coloured cyan.

(f) Permutations that return no result, or a divergent result (`NaN`), are coloured yellow.

Ideally, the initial parametric search is looking to find the combination of parameters that result in ventricular displacements in the second and third categories, while also identifying a set of parameters that defines the border between the third and fourth categories.

At the same time, trends and patterns can be sought to identify which parameters bear most influence over the clinically important results of the model. While non-trivial, a useful tool in this pattern searching compares a moving average of the ranked simulations' parameters with the overall mean of that parameter. Graphically, this can be represented by the solid black and red lines, respectively, in the plots. To calculate the black line, a many-point moving average is calculated recursively five times in a manner similar to the following pseudo-code,

```
ave_ctr = 20
for i = 1:5
    for j = (ave_ctr+1):(length(f_old)-ave_ctr)
        f_new(j) = mean( f_old(j-ave_ctr), f_old(j+1-ave_ctr), ..., f_old(j),
            »..., f_old(j+ave_ctr) )
```

```
    f_old = f_new
plot f_new
```

where the number of points used in each moving average is determined by the size of the parametric search being analysed.

With this moving average constructed, its deviation from the true mean of the parameters indicates the relative influence of that parameter on the displacement of the ventricles. If black line is almost coincident, or quickly oscillating about the red line, one can assume that it is equally likely for any of the values in the parameter's range to result in the displacement at that given point. Conversely, If the black line shows a consistent trend away from the solid red line, or displays distinct directional changes, it is possible to assume that this change in the parameter is influential on the outcome of the model as a whole.

While this may seem somewhat confusing, it will become clearer as the analysis is applied to the results in §5.1.2.

Running A Parametric Search on `fbg-cluster` The distributed memory machine, `fbg-cluster`, and SGE queueing system described in §4.2.1.3 create a flexible environment in which to run a large-scale parametric search. In addition to simple serial jobs and multi-core parallel jobs, SGE is capable of controlling arrays of serial jobs. While not explicitly necessary, submitting a parametric search as an array job allows for two managerial improvements: the `TASK ID` of the job task allows a unique identifier to the particular permutation of parameters for that task; and limiting the number of tasks in each level of the job array allows the user to control how many of the available resources are consumed by the job.

The commands for controlling SGE array jobs are well documented elsewhere, however, it is advantageous to work through the specific use in the current context. Like the parallel jobs described previously, `qsub` is again used to submit the scripts to the queue; the addition of the `-t` flag allows the user to specify an array of jobs controlled using intuitive numerical loop control. For example, the following command replicates the job `myjob.sh` 50 times.

```
qsub -t 1-100:2 myjob.sh
```

Each instance of the job will have its own task identifier. In this example, the task identifiers range from 1 to 100 in steps of 2 (1, 3, 5, ... 99).

The task identifier is available to the job through the environment variable `SGE_TASK_ID` and can be used within the job script to differentiate input and output control arguments for each task. For example, the following script (created by Appendix D.4) uses the task number to read the `$SGE_TASK_ID`-th line from the file containing the parameter permutations and in turn, pass this as the argument list to the multiple-network poroelastic C++ solver, `quadMPETsolver.exe`.

```
#!/bin/sh

## The following lines are not comments, they control the SGE queue.
#$ -cwd -V
#$ -e logFiles/
#$ -o logFiles/

## Read the $SGE_TASK_ID-th line of the input file
INP=`sed ${SGE_TASK_ID}q "SIM_LIST.txt" | tail -1`

## Run the solver for SGE_TASK_ID
./quadMPETSolver.exe $INP
```

Other controlling features, `-cwd` , `-V` , `-e` , `-o`, in this script manage the working directory and location of log files.

Besides supplying the `-t` option and using the task identifier, the input script is written and submitted to the queue in the same way as a regular serial job. However, large parametric studies with thousands of serial jobs may unacceptably tie-up resources for a extended period of time. Using the facilities of the SGE submission procedure, the array can be split into more manageable chunks. To accomplish this, the option `-hold_jid` controls the submission of jobs to the queue such that the second chunk will not begin until the first has completed. For example, given 128 simulations to run in chunks of 32 cores, the submission script may look like this:

```
qsub -N job1 -t 1-32:1 myjob.sh
qsub -N job2 -hold_jid job1 -t 33-64:1 myjob.sh
qsub -N job3 -hold_jid job2 -t 65-96:1 myjob.sh
qsub -N job4 -hold_jid job3 -t 97-128:1 myjob.sh
```

where the `-N` option gives each job a name and `-N job2 -hold_jid job1` means that `job2` will not start until `job1` has finished.

The dependency of submission and job scripts on the individual parametric search being completed implies a benefit to be gained by generating these automatically. Appendix D.4 gives an example script that generates the control scripts (`myjob.sh` and `submit.sh`) and input file (`SIM_LIST.txt`) for the parametric run shown in Figure 5.4.

5.1.2 Results

The study of chronic hydrocephalus by a four network MPET model was undertaken by first completing a large-scale parametric search of the newly introduced mechanical properties. The model was tuned to reflect the results of the SPET model used in Chapter 4 for an obstructed cerebral aqueduct. With these parameters assuming the role of a 'healthy' configuration, a series of investigations were conducted with a completely open cerebral aqueduct. These investigations reveal particular parameters that offer interesting explanations on the development of chronic hydrocephalus; through these parameters, several clinical hypotheses were examined.

5.1.2.1 Tuning the MPET model

As previously mentioned, the initial parametric search – with linear, discrete changes in the material parameters – proved to be of little use in discerning useful information about the dynamics of the model (see Figure 5.2). The primary problems with the method were the discrete groupings of the parameters and logarithmic ranges being discretized with linear spacing. Hence, we begin the analysis of the results from the subsequent methodology using a uniform and log-normal selection of material parameters.

The first simulation after making the change from linear-discrete to log-continuous methodology was a run of 75,000 random permutations of the ten material parameters. In this run, there were three features that were immediately obvious: the percentage of the parametric combinations that gave results in the physical bound is low (the green, blue and red regions); almost half of the combina-

tions resulted in a system that was unbounded and the simulations returned `NaN` or an error (the yellow region); and, the Biot parameter of the arterial compartment (α^a) had the strongest trend influence on the ventricular displacement. Within the 75,000 simulations conducted in this search, there were six distinct observations to be made from the results (Figure 5.4 and Figure 5.3-(b)).

(a) Many more simulations returned an error or `NaN` when κ^c was below average (simulations 32,000–75,000 in Figure 5.4); or conversely, the likelihood of a result being obtained was increased if κ^c was closer to 1×10^{-10} m^2 (simulations (0–32,000).

(b) The largest displacements were observed when α^a and α^c were below average combined with γ_{ce} and γ_{cv} being above average (simulations 0–2,000). This also corresponded with a noticeable increase in the pressure in the arteriole/capillary network.

(c) When $\alpha^a = 0.5$ stabilized (simulations 2,000–6,000), the increasing displacement was driven by decreasing α^c.

(d) Decreasing α^a from 1.0 to 0.5 (simulations 6,000–25,000) drove a corresponding increase in ventricular displacement and values of α^a smaller than 0.8 gave displacement outside of the physical range.

(e) Once $\alpha^a = 1.0$ had stabilized (simulations 25,000–28,000), decreasing α^c drove an increased displacement.

(f) There seemed to be a distinct tipping point whereby values of γ_{ac} above $\sim 1.5 \times 10^{-19}$ m^{2}N^{-1}s^{-1}resulted in largely negative values for displacement (simulations 28,000–42,000), while below that, the displacement was positive (simulations 0–28,000).

According to the first observation, it made sense to set the permeability of the arteriole/capillary network to a constant value. At the same time, it appeared that the permeabilities for the other blood networks were relatively benign to the ventricular displacement. From these two observations, the set of parameters in the next parametric search were chosen with constant values set for the permeability of the blood networks ($\kappa^{a,c,v} = 1 \times 10^{-10}$ m^2). Furthermore, the range of selection for the Biot parameter of the blood networks (α) was narrowed from 0.5 to 0.8.

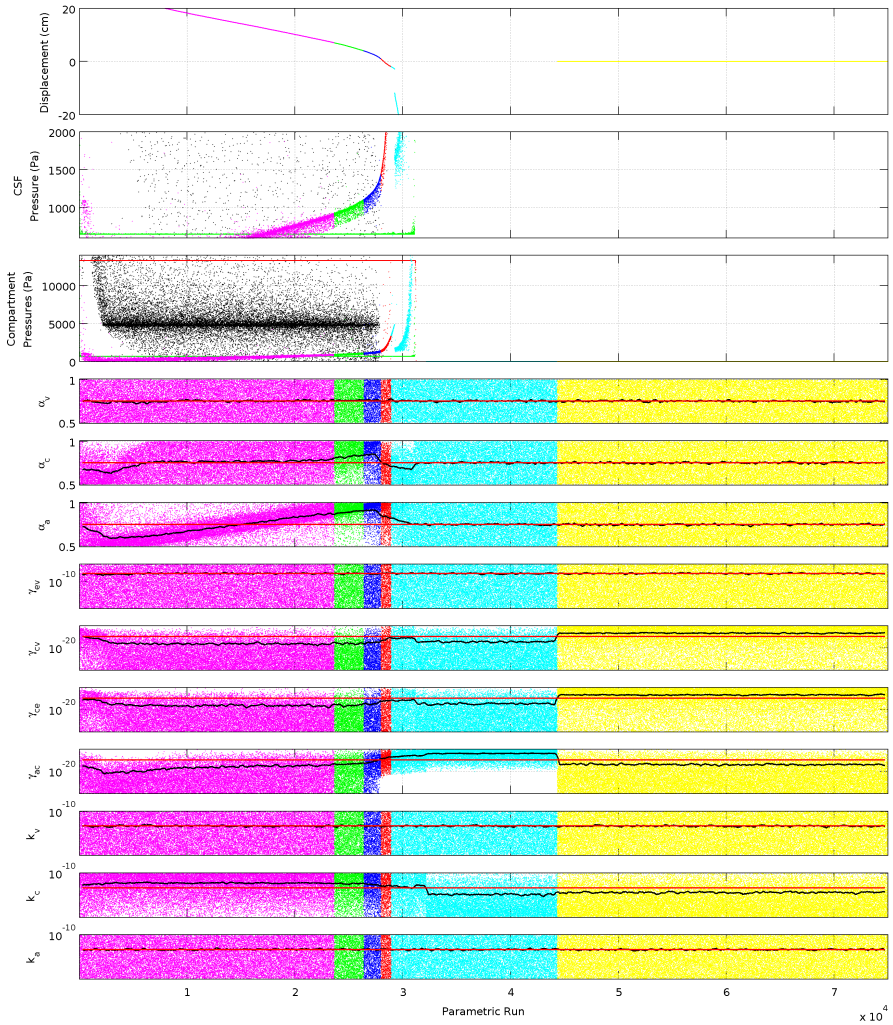

Figure 5.4: The first large-scale continuous, log-normal parametric investigation. Each of the ten tissue or transport properties is assigned a random value from the respective range in Table 5.1 in a search consisting of 75,000 permutations; the α values are determined by a uniform distribution while the γ and k values are assigned using a log-normal distribution. Almost one half of the permutations return an error (yellow), one third produce ventricular displacement exceeding the physical bounds (magenta), another one quarter give negative displacements (cyan), leaving a relative small number of parameter sets that are within the physical bounds of the simulation (green, blue and red).

This new search showed a significant decrease in the fraction of simulations that returned an error (see Figure 5.5). As you would expect, the trends and patterns were similar to those from the previous parametric study with changes being promoted by a higher density of simulations at the boundaries of change.

(a) The largest displacements corresponded to a distinct grouping of γ_{ce} and γ_{cv} above $\sim 1.0 \times 10^{-19}$ $m^2N^{-1}s^{-1}$ in the first 3,000 or so simulations of Figure 5.5-(a). This period also showed a marked increase in pressure of the arteriole/capillary network to levels beyond the arterial network (and obviously non-physical result).

(b) When $\alpha^a = 0.8$ stabilized (simulations 3,000–13,000), the increasing displacement was driven by decreasing α^c.

(c) Decreasing α^a from 1.0 to 0.8 (simulations 13,000–52,000) drove a corresponding increase in ventricular displacement and values of α^a smaller than 0.9 gave displacement outside of the clinical range.

(d) Once $\alpha^a = 1.0$ had stabilized (simulations 52,000–61,000), decreasing α^c from 1.0 to 0.8 drove an increased displacement.

(e) There seemed to be a distinct tipping point whereby values of γ_{ac} above $\sim 1.5 \times 10^{-19}$ $m^2N^{-1}s^{-1}$ resulted in largely negative values for displacement (simulations 61,000–75,000), while below that, the displacement was positive (simulations 0–61,000).

Observations would suggest once again that the ventricular displacement was largely driven by the compliance of the arterial network (through a varying Biot parameter). However, there are two reasons that this should be discounted: firstly, there is no obvious physiological explanation that accounts for a decrease in the capacity of the arteries to cope with a change in pressure; and secondly, the region of most interest for chronic hydrocephalus (labelled blue on the plot) occurs when $\alpha^a \sim 1.0$.

The latter reason was most compelling, and as a result, the third parametric search was conducted with $\alpha^a = 1.0$. The decision was justified by the significant percentage of the new run that fell within the area of clinically reasonable ventricular enlargement (the blue zone of Figure 5.6). Furthermore, it is interesting to observe the influence of the Biot parameter of the arteriole/capillary network and the

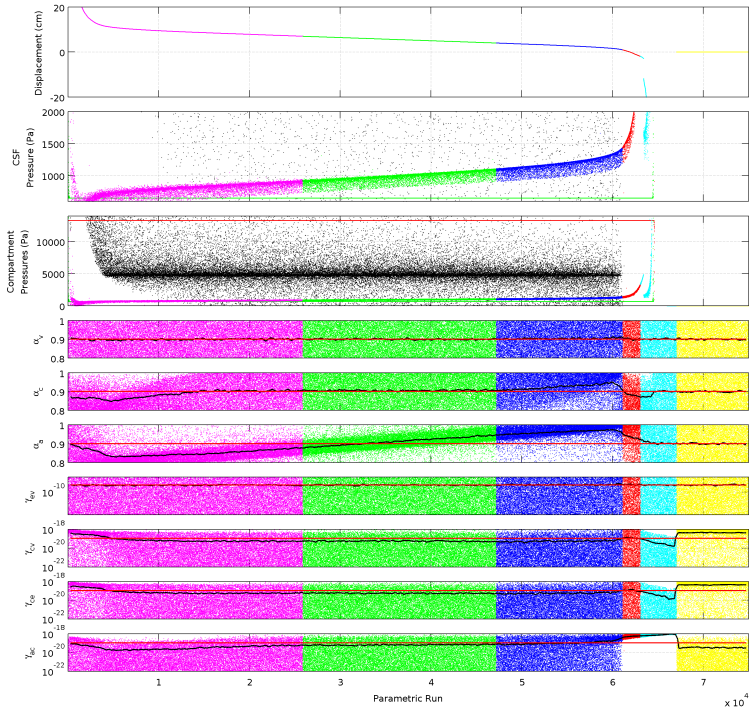

(a)

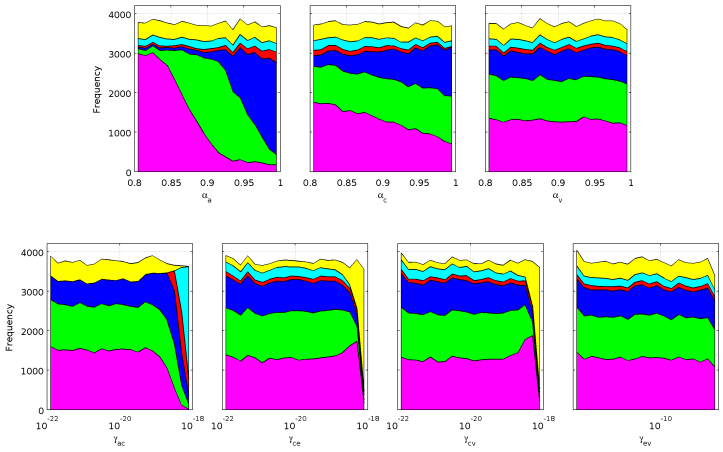

(b)

Figure 5.5: The second log-normal parametric investigation of 75,000 permutations. In this search the permeabilities of the blood networks are set to a constant ($\kappa^{a,c,v} = 1 \times 10^{-10}$ m^2) and the remaining seven tissue or transport properties are assigned randomly selected values as before. **(a)** shows the search results arranged by ventricular displacement and **(b)** shows the histogram of each material parameter coloured by the resulting displacement.

competing trend lines of the pressure in the arteriole/capillary network. More generally:

(a) The largest displacements corresponded to a distinct grouping of γ_{ce} and γ_{cv} above $\sim 1.0 \times 10^{-19}$ in the first 11,000 or so simulations of Figure 5.6-(a). This period also showed a marked increase in pressure of the arteriole/capillary network to levels beyond the arterial network (an obviously non-physical result).

(b) Decreasing α^c from 1.0 to 0.8 (simulations 11,000–52,000) drove a corresponding increase in ventricular displacement which spanned the clinically acceptable range.

(c) Once $\alpha^c = 1.0$ had stabilized (simulations 52,000–56,000), decreasing α^v from 1.0 to 0.8 drove a small increase in ventricular displacement.

(d) A combination of α^c values greater than about 0.85 and values of γ_{ac} above roughly 1.5×10^{-19} $m^2N^{-1}s^{-1}$ resulted in a secondary trend line in the pressure of the arteriole/capillary blood network. This trend line quickly proceeded to cross through the CSF pressure thus rendering these permutations outside the physically acceptable bounds (simulations 15,000–67,000).

Again, compliance was the influential property for determining the ventricular displacement; although here it was the Biot parameter of the arteriole/capillary network. Furthermore, observation of this parametric search suggests that selecting an appropriate value for the transfer coefficient between the arterial and arteriole/-capillary networks ($\gamma_{ac} = 1.5 \times 10^{-19}$ $m^2N^{-1}s^{-1}$) will allow a set of parameters to be computed for which all results are within the clinically acceptable range. Intuitively, it is possible to argue that the transfer resistance across vessel scale in the blood network should be roughly constant, hence, the transfer from arteriole/capillary to venous networks was scaled the same amount as the transfer from arterial to arteriole/capillary networks ($\gamma_{cv} = \gamma_{ac}$).

Thus, the final parametric search was defined by the random selection of the four remaining parameters (Figure 5.7-(a)): the arteriole/capillary and venous network Biot parameters; and transfer coefficients from the arteriole/capillary network to the CSF network and CSF network to the venous network. Analysis of this search revealed the two properties that we began looking for: a set of parameter ranges

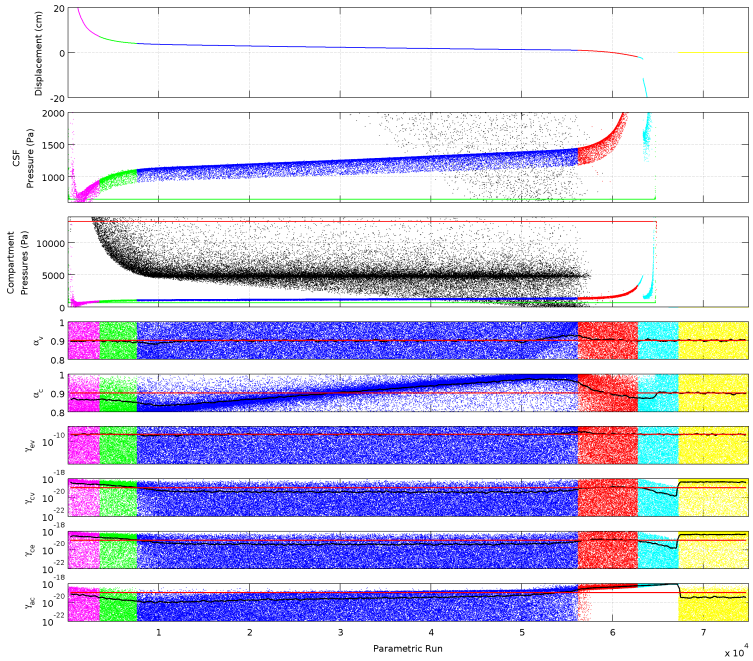

(a)

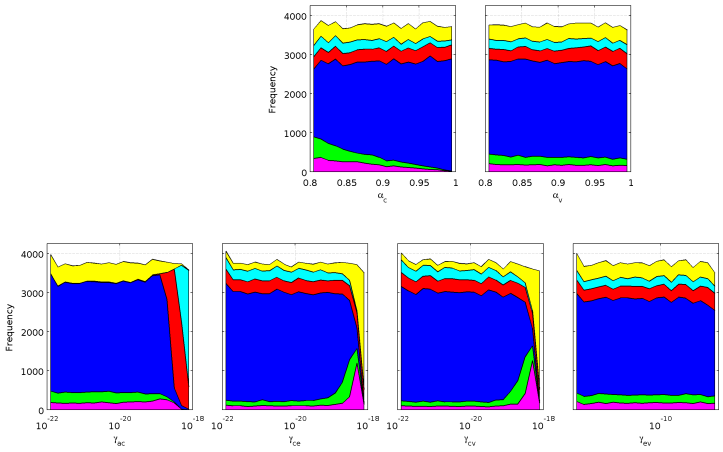

(b)

Figure 5.6: The third log-normal parametric investigation of 75,000 permutations. In this search the permeabilities of the blood networks are set to a constant ($\kappa^{a,c,v} = 1 \times 10^{-10}$ m^2), the arterial Biot parameter is constant ($\alpha^a = 1.0$ and the remaining six tissue or transport properties are assigned randomly selected values as before. **(a)** and **(b)** are the sorted results and histogram.

Parameter	Lower Value	Upper Value	Units
$\alpha^{c,v}$	0.8	1.0	
γ_{ce}	1.0×10^{-22}	1.5×10^{-19}	$m^2N^{-1}s^{-1}$
γ_{ev}	1.0×10^{-13}	1.0×10^{-8}	$m^2N^{-1}s^{-1}$

Table 5.2: A set of parameter ranges that when passed to the MPET model, return ventricular displacement within the bounds of clinical acceptability.

Parameter	Value	Parameter	Value
$\kappa^{a,c,v}$	1.0×10^{-10} m^2	$\gamma_{ac,cv}$	1.5×10^{-19} m^{2}N^{-1}s^{-1}
$\mu^{a,c,v}$	2.67×10^{-3} Nsm^{-2}	γ_{ce}	1.0×10^{-20} m^{2}N^{-1}s^{-1}
$\alpha^{a,c,v}$	1.0	γ_{ev}	1.0×10^{-13} m^{2}N^{-1}s^{-1}

Table 5.3: Healthy-state values for the MPET model as found through extensive parametric testing. The viscosity of the blood networks, $\mu^{a,c,v}$, is assumed to be three times greater than water.

that return ventricular displacement within the bounds of clinical acceptability (Table 5.2); and a set of parameters that define the 'healthy' state of the MPET model whereby the results match those from the SPET model (Table 5.3).

There is remarkable agreement between the quadruple MPET model and single network model when the aqueduct is obstructed ($\phi = 0.25$ mm) and there is a zero displacement for a fully open aqueduct (see Figure 5.7 and Figure 5.8). The MPET model is capable of capturing the dynamics of the single network model, while still displaying substantial fluid exchange between the different blood and CSF networks (as seen by the compartmental pressures in Figure 5.7).

5.1.2.2 Pursuing the Parameters of Interest

It was found through the parametric analysis that perturbations in four model constants showed potential to mimic the clinical manifestation of NPH. Biot parameters of the arteriole/capillary network and the venous network (α^c and α^v respectively), may relate to a change in compliance of the vascular networks, while transfer coefficients between the arteriole/capillary and CSF networks, and the CSF and venous networks (γ_{ce} and γ_{ev} respectively), may represent a breakdown in the blood-CSF barrier either through over- or under-absorption of water between the networks.

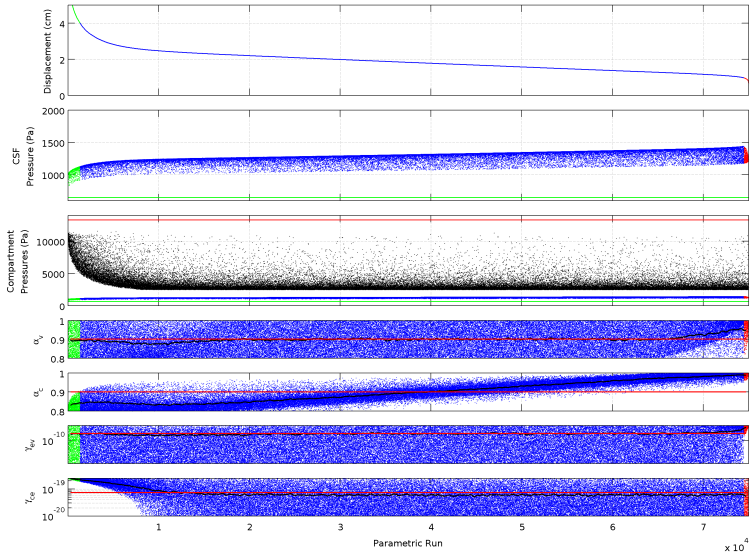

(a)

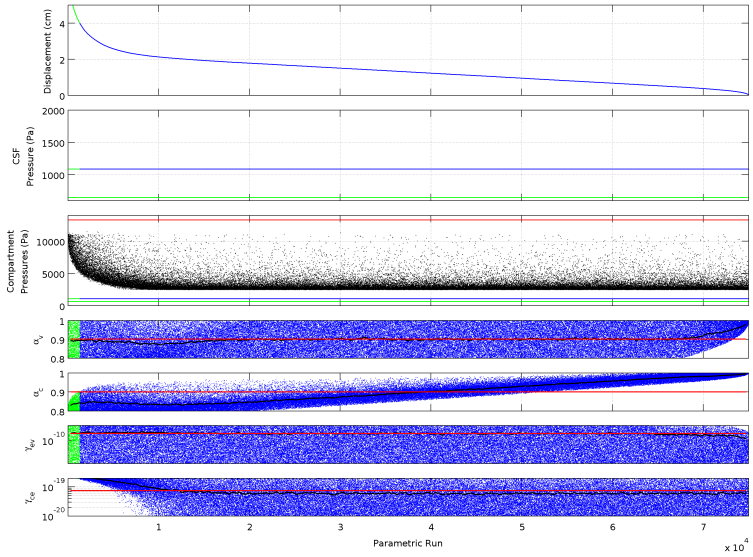

(b)

Figure 5.7: The final log-normal parametric investigations of 75,000 permutations each: **(a)** is computed with an obstructed cerebral aqueduct while the aqueduct in **(b)** is free from obstruction. In this search the arteriole/capillary and venous network Biot parameters, and transfer coefficients from the arteriole/capillary network to the CSF network and CSF network to the venous network are set to the values in Table 5.2 and the remaining parameters assume their healthy values, as given in Table 5.3.

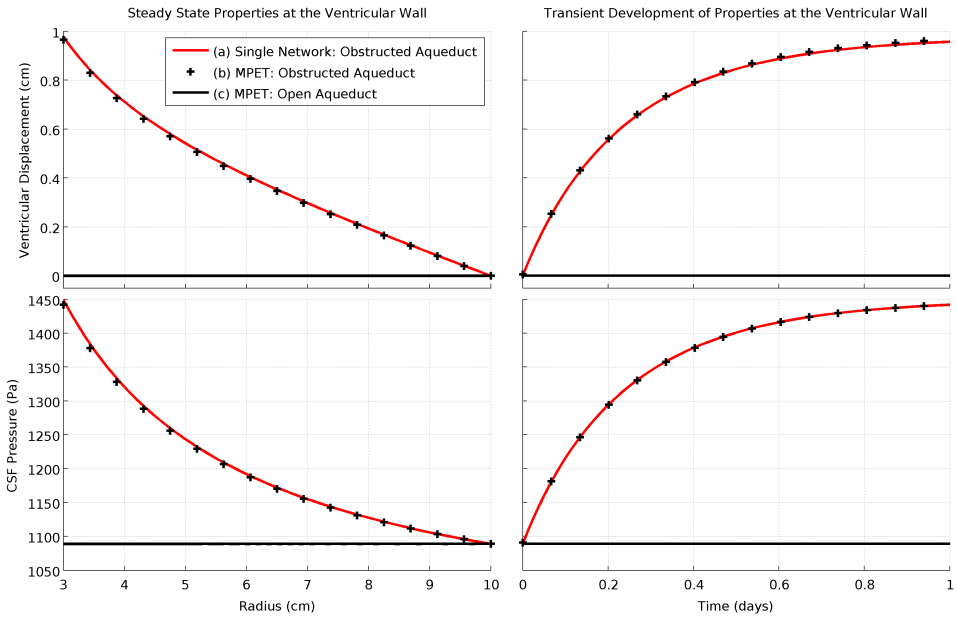

Figure 5.8: After a thorough parametric search, we were able to select a set of parameters that we can describe as the healthy-state condition. In this figure, the MPET model is shown with a fully open aqueduct ($d = 4.00$ mm) as well as a partially obstructed aqueduct ($d = 0.25$ mm). The results of the obstructed MPET model compare very favourably to those of the single network model with an obstructed aqueduct as described in (Tully and Ventikos, 2009).

Running the MPET model with these parameters varied through the range was valid for both obstructed and open cerebral aqueducts (Figure 5.7-(a) and Figure 5.7-(b) respectively); for the remainder of this chapter, the investigations were conducted with an open aqueduct to mimic the clinical presentation of NPH.

In a more detailed investigation of the parameters of interest, each of the four parameters were given one of two values: its healthy value and the value at the other end of the range in the parametric study. This study showed the potential for the system to describe the clinical presentation of NPH (Figure 5.9). Altering these parameters had a negligible impact on the venous pressure and a marginal impact on the capillary pressure. While the pressure gradient through the cerebral aqueduct did not change, the pressure distribution through the parenchyma was influenced by changing the value of γ_{ev}. Displacement was increased when both values of α were decreased, with α^c having the greater impact. Furthermore, when $\alpha^c = 1.0$, changing γ_{ce} did not influence displacement, yet had a large impact when $\alpha^c = 0.8$. This suggested that it was possible for the parameters to combine such that small

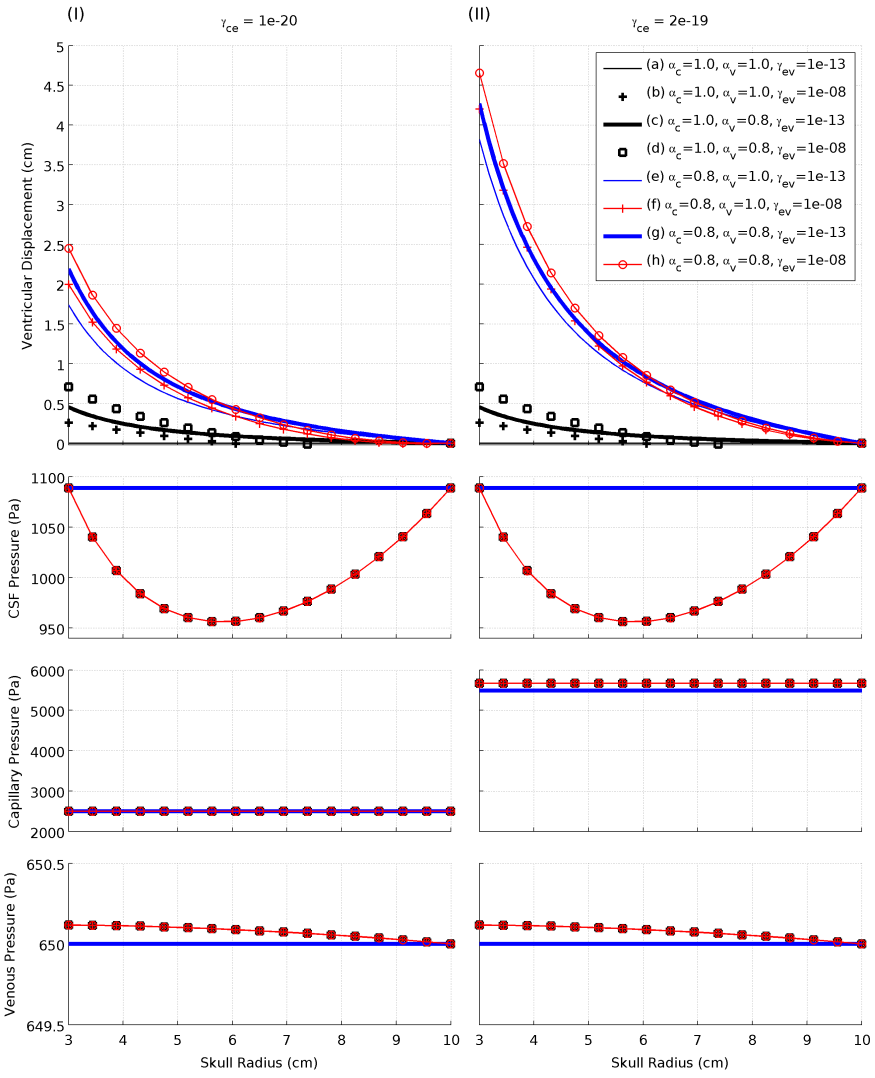

Figure 5.9: A comparison of changing the four major parameters in the MPET model to the case of a healthy brain. It can been seen that negligible change is effected on the arteriole/capillary or venous pressures, while the CSF pressure distribution is influenced by a change in γ_{ev}. Importantly though, it can be seen that all parameters impact on the displacement of the tissue to differing degrees. Decreasing either α value results in an increase in the displacement, with α^c having a larger impact. Changing γ_{ce} does not influence the displacement when $\alpha^c = 1.0$, yet it has a strong impact when $\alpha^c = 0.8$, suggesting that the interaction of these two parameters is worthy of further investigation.

changes in each gave rise to a large displacement of the ventricles.

To investigate these findings more rigorously we considered mechanical changes that mimic a change in the compliance of the vascular network, and the transfer of fluid between networks that model a breakdown in the blood-CSF barrier.

5.1.2.2.1 Investigating a change in the mechanical properties of the vascular network

Bateman (2000) measures an increase in the compliance of the vascular networks of patients with NPH, and poroelastic studies can mimic these changes by altering the Biot parameter of the vascular networks (Levine, 1999, 2000; Sobey and Wirth, 2006). The four-network MPET model encompasses adequate flexibility to investigate changes in the compliance of any of the fluid networks by modifying the relevant Biot parameter. Following from the parametric study, the Biot parameters of the arteriole/capillary and venous fluid networks were investigated more deeply.

Each α value was continuously varied between 0.8 and 1.0, while the other was assigned discrete values of 0.8, 0.9 and 1.0. Relative to the venous Biot parameter, α^v, the arteriole/capillary Biot parameter, α^c, had a much greater impact on the displacement of the ventricles when all other parameters were kept at healthy levels (Figure 5.10). The rate-of-change in displacement with respect to decreasing the venous network Biot parameter is six times slower than for the arteriole/capillary network, implying that a significantly larger change is required to have the same impact on ventriculomegaly. Notably, all changes in displacement were observed in the absence of any change in network pressures.

5.1.2.2.2 Investigating a breakdown of the blood-CSF barrier

Compromised blood-brain and blood-CSF barrier function is suggested as a potential explanation of the clinical features of NPH. Electron microscopy studies of cerebral oedema show a breakdown of the blood-brain barrier through enhanced vacuolar and vesicular transport (Castejón, 2009). Several studies (albeit congenital and infant) suggest that similar brain barrier dysfunction is present in hydrocephalus (Del Bigio, 2004; McAllister and Chovan, 1998; Seyfert and Faulstich, 2003; Seyfert et al., 2004), while others show that endothelial tight junctions are unchanged (Sada et al., 1994). In the MPET model, increasing a γ value corresponds to enhanced transport from one fluid network to the other. Blood-brain barrier breakdown was investigated by inde-

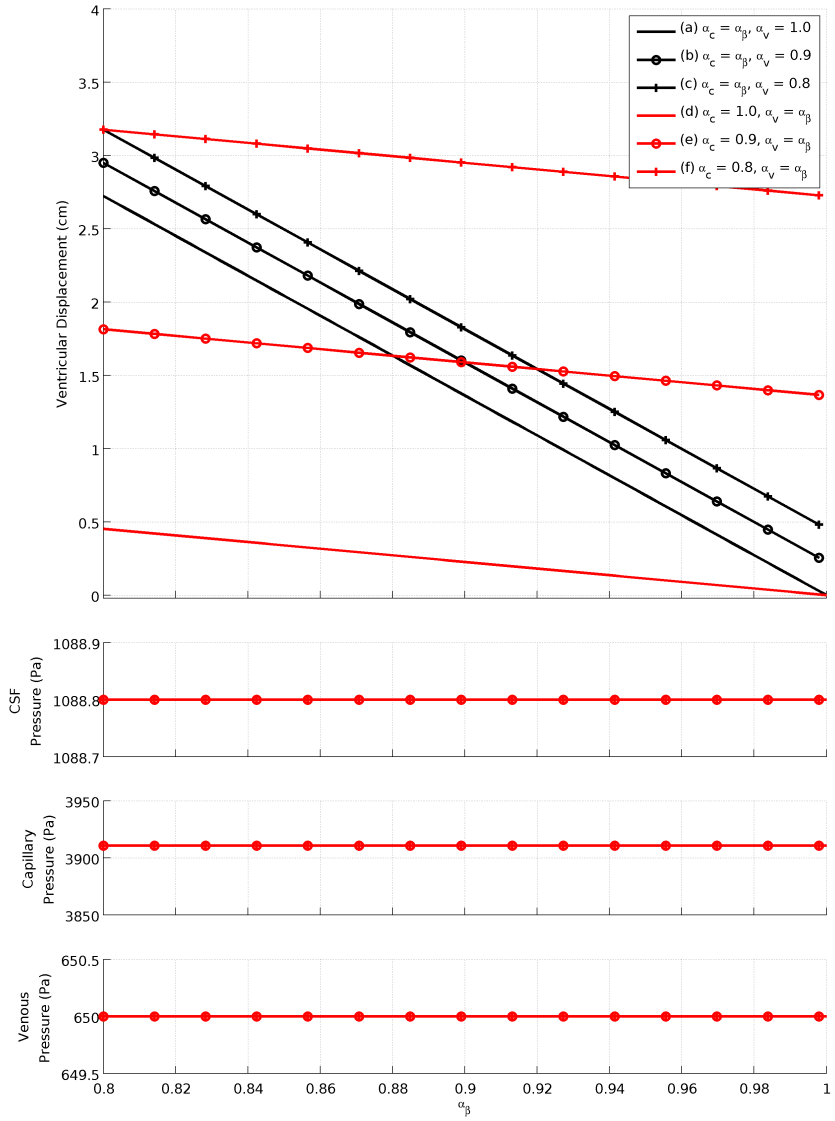

Figure 5.10: Decreasing the Biot parameters of the arteriole/capillary and venous networks shows potential to explain the clinical manifestation of NPH. Each α value is continuously varied between 0.8 and 1.0 (α^β), while the other is assigned discrete values of 0.8, 0.9 and 1.0. The black lines show the response to the model when the Biot parameter of the arteriole/capillary network is continuously varied (α^c) while the red lines show the response of continuously varying the Biot parameter of the venous network (α^v).

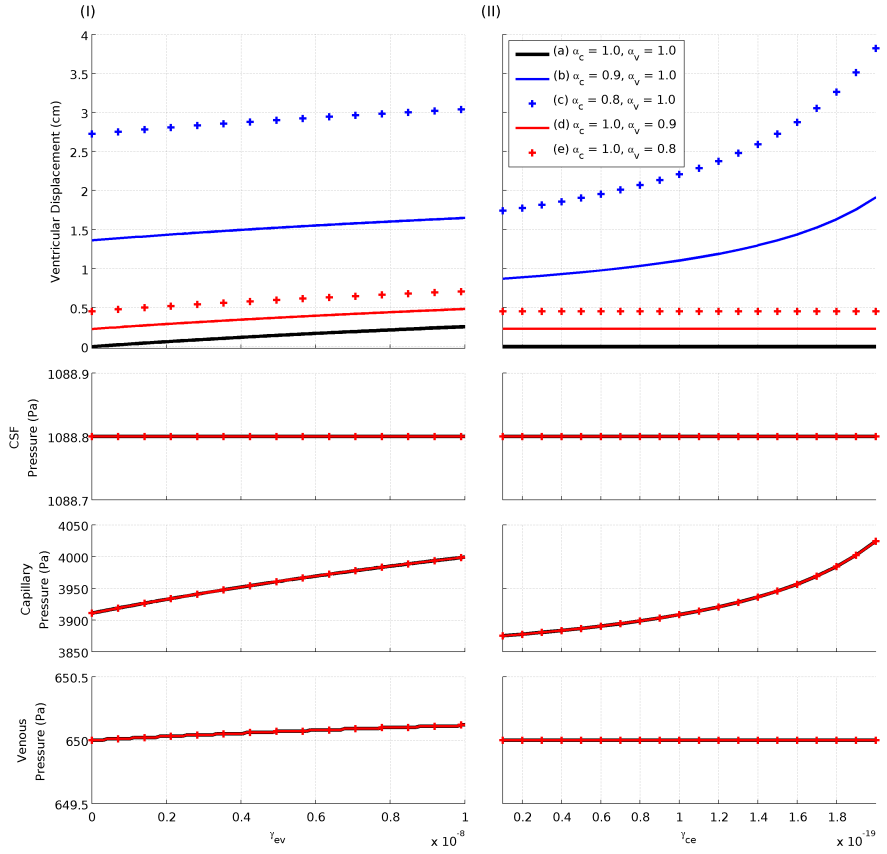

Figure 5.11: **(I)** shows an imposed breakdown in the blood-CSF barrier that lessens the resistance of flow from the CSF network to the venous network (larger values of γ_{ev}). Counter intuitively, the resulting drainage of fluid from the CSF network *increases* the displacement of the ventricles; the cause of which can be traced to an increase in the arteriole/capillary pressure that drives additional fluid from the arteriole/capillary network into the CSF network. Furthermore, altering the compliance of the blood networks (by changing the Biot parameters, α^c and α^v) does not impact on the rate-of-change of the displacement with respect to γ_{ev}. **(II)** shows an imposed breakdown in the blood-CSF barrier resulting in an increase in the flow of water from the arteriole/capillary network to the CSF network (larger values of γ_{ce}). Significantly, displacement is a function of γ_{ce} if and only if there is an associated change in the Biot parameter of the arteriole/capillary network (α^c). Again, there is a strong relationship between the arteriole/capillary pressure and the transfer coefficient and an absence of any change in the CSF or venous pressures.

pendently varying γ_{ce} and γ_{ev} while maintaining all other constants at their healthy value.

Counter-intuitively, increasing the flow of water from the CSF network to the

venous network gave an increase in the displacement of the ventricles, however, further interrogation revealed an increased arteriole/capillary pressure that drove more water into the CSF space (Figure 5.11-(I)). Ventricular displacement increased almost linearly with γ_{ev} for healthy values, and decreasing the α values for the arteriole/capillary and venous networks did not impact on the rate of change in displacement. This rate of change suggested that while displacement occurred with an easier flow path into the venous network, it was unlikely to cause enough change to result in NPH.

It was also found that the increasing ease with which fluid flowed from the arteriole/capillary network to the CSF network only influenced the displacement of the ventricles if there was an associated increase in the compliance of the arteriole/-capillary network (smaller values of α^c, Figure 5.11-(II)). However, once a relatively small decrease (~10%) in α^c was made, increasing γ_{ce} by 40% markedly increased the displacement (by more than 52%) and demonstrated clinically correlated values; this relationship can be further seen in Figure 5.12. Notably, these changes in tissue and transport properties did not influence the pressure in the fluid compartments.

5.1.2.3 NPH as a 'Two-Hit' Disease

For the past decade, Bradley and colleagues have argued that NPH may be a 'two-hit' disease; the patient may suffer from a form of benign infant hydrocephalus that becomes symptomatic in old age (Bradley, 2000; Bradley et al., 2004, 2006; Bradley, 2008). This theory is supported by data that suggests NPH patients have statistically-significant enlarged cranial volumes compared to aged matched controls (Bradley et al., 2004) – it is well known that hydrocephalic infants suffer from enlarged cranial volumes as the cranial sutures have not yet fused allowing for expansion. The theory is that the benign childhood hydrocephalus is symptom free (with slightly larger ventricles and cranium) where the patients' brain have developed coping mechanisms that adapt to the initial change; a vascular change in old age disrupts this balance and NPH results.

In an analysis of Bradley and colleagues' 2004 paper, McComb et al. (2004) makes an astute observation that it is unlikely that this theory will ever be clinically proved. In order to do so, extensive radiographic screening of infants and mid-century follow-up studies would need to be completed to assess both the prevalence

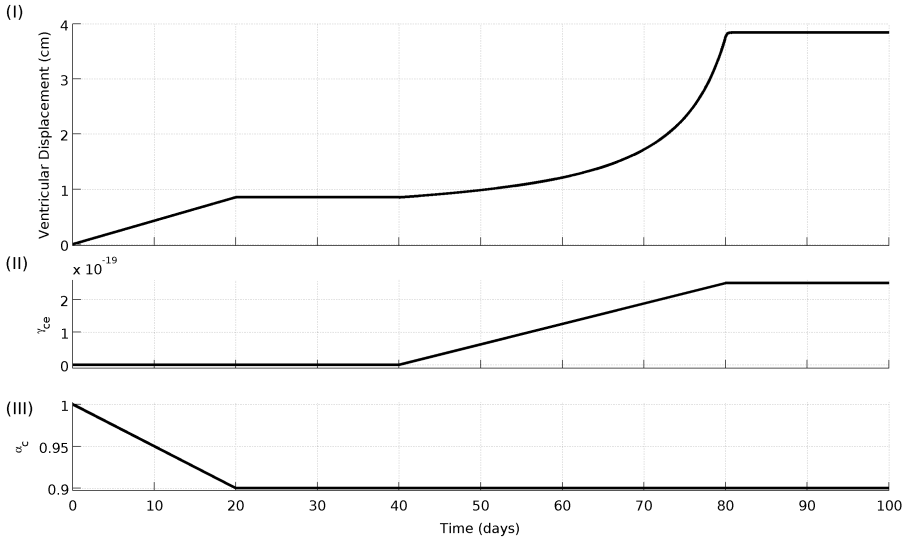

Figure 5.12: Using the MPET model we are able to interrogate the theory that NPH is a 'two-hit' disease. It is hypothesized that the patient may suffer from a form of benign infant hydrocephalus that becomes symptomatic in old age (Bradley, 2008). While it is difficult for this theory to be proved through extensive follow-up studies, it was interrogated *in silico* using the MPET model: an increased congenital compliance (by decreasing α^c over time) was assumed in the infant brain and the arteriole/capillary network was made progressively more leaky (through an increase in γ_{ce}) in old age. The infant changes produced a relatively minor increase in ventricular dilatation that was compounded by the vascular changes of old age with significant ventricular dilation in the absence of an increase in CSF pressure.

of benign infant hydrocephalus and its correlation to ultimately symptomatic NPH patients. However, using the observations made in §5.1.2.2.2, we were able to explore the Bradley hypothesis *in silico*.

By varying α^c and γ_{ce} over time, we were able to mimic a scenario not dissimilar to that used to describe NPH as a 'two-hit' disease (Figure 5.12). To simulate the initial hydrocephalus we allude to an increased congenital compliance of the arteriole/capillary network, by decreasing α^c to 0.9, that resulted in an initial displacement of the ventricles of 8-9 mm. At some time in the future we assume that the leakiness of the blood-CSF barrier increases and more fluid can flow from the arteriole/capillary network to the CSF network, γ_{ce} was increased to 2.5×10^{-19} $m^2N^{-1}s^{-1}$, and a final displacement of almost 4 cm was observed. It must be emphasized again that this was conducted with a fully un-obstructed aqueduct and the pressure recorded in the ventricles was unchanged.

The quasi-steady nature of the model meant that the time scales for the parameter changes bore no influence on the outcome (provided that the changes are made sufficiently slowly). For the same reason, the time delay between changing α^c and γ_{ce} could be one day, or 50 years, and the displacement of the ventricles would remain unchanged.

These tests show that a benign childhood hydrocephalus – introduced by increased compliance of the arteriole/capillary network through a smaller value of α^c – will give a small increase in the ventricles and cranial volume in an un-fused skull. Then, at some time in the future, a break down of the blood-CSF barrier in the arteriole/capillary network (possibly due to deep white matter ischaemia) increases the displacement of the ventricles to a clinically noticeable value and NPH results.

5.2 MPET: 1D-3D COUPLED MODEL

It has been shown in §4.2 that the introduction of patient-specific aqueduct geometry plays an important role in the development of ventriculomegaly in acute hydrocephalus. However, in chronic hydrocephalus, the aqueduct is free from obstruction and the MPET model shown in the previous section asserts that the pathophysiology of NPH may be closely tied to changes in the biophysical properties of the tissue. This section will test whether patient-specific aqueduct geometries alter these findings.

5.2.1 Methodology

Like §4.2, the capabilities of the one-dimensional model are extended through a novel coupling of the multiple-network poroelastic C++ solver with a patient-specific representation of the cerebral aqueduct. By conducting tests with patient data collected from symptomatic patients, we can investigate the relative influence of aqueduct geometry and biophysical properties on the development of NPH.

The general coupling methodology remains the same as §4.2 with additional patient-specific data obtained from four patients recruited in the John Radcliffe Hospital and through our collaborators Professor James Byrne and Dr Jaladhar Neelavalli. The raw data is extracted and converted to a computational domain,

and the CSF flow dynamics are computed using **CFD-ACE+**. However, changes were necessary in the UDS to overcome additional stiffness, inherent in the MPET model.

The findings of §5.1.2 allow us to define a set of healthy-state parameters and two additional clinically relevant parameters with which we can test the relative importance of flow geometry. Firstly, we compare the solutions of the SPET and MPET models to the case where the cerebral aqueduct of the healthy volunteer is artificially stenosed (see §4.2.2.2). In this test, we ensure that the healthy parameters from the parametric search are applicable to the coupled model. Next, we can take the three versions of the same geometry and compare the SPET results with the MPET model in a symptomatic configuration. Finally, the four symptomatic patient geometries are used to assess the influence of aqueduct geometry relative to changing individual tissue and transport properties in the MPET model.

5.2.1.1 Model Set-Up

The model set-up phase follows the same steps as those shown in §4.2. The patient-specific aqueduct geometry is created, converted to a computational mesh and prepared for parallel simulation with **CFD-ACE+**. The healthy volunteer used previously (Figure 4.8) is compared with a further four patient cases, each with suspected NPH. The case histories show the diverse range of symptoms that present in patients (with strong agreement to the observations of the condition made in §1.4.0.5):

- **Case 2:** Mid-seventies female patient scanned on July 16, 2008 (see Figure 5.13-(a)–(b)) presenting with a five year history of dementia and memory loss and a two year history of urinary incontinence and falls. Initial CT scan revealed enlarged ventricles, suggesting NPH, while the opening pressure of the lumbar puncture was 19.5 mmHg[1]. On completing an R-out study[2], the coefficient was found to be 19.1 mmHg/mL/min, which is consistent with impaired ventricular compliance. Together with the elevated opening pressure, this elevated R-out coefficient suggested that the patient may benefit from a shunting treatment.

[1] Normal CSF pressure is around 11 mmHg (Gilland et al., 1974).

[2] An R-out study is used to test the resistance to outflow of CSF from the ventricular system. The test involves measuring pressures from a lumbar puncture before and during an infusion of fluid into the system at a constant rate.

- **Case 3:** Early-seventies male patient scanned on July 30, 2008 (see Figure 5.13-(c)–(d)). Patient was referred due to poor memory, with distinct short term memory loss, and gait disturbance associated with mild bilateral limb rigidity and a shuffling gait. The result of the lumbar puncture gave an opening pressure of 8 mmHg. MRI scans reveal generalized cerebral atrophy yet no papilloedema or optic atrophy. The prominent ventricles may be due to the atrophy, however, NPH could not be ruled out. Following the initial scan, it was decided that the patient would not benefit from shunting, however, continued symptomatic deterioration lead to the patient being offered a shunt twelve months later.

- **Case 4:** Late-sixties male patient scanned on November 3, 2008 (see Figure 5.14-(a)–(b)). Following admission from a rehabilitation unit, pressure measurement during the initial lumbar puncture found an opening pressure of 6 mmHg. The patient was wheel-chair bound, and displayed no abnormal physical signs apart from a ten year history of gait disturbance. Combined with initial scans, this lead to a suspicion of NPH.

- **Case 5:** patient (see Figure 5.14-(c)–(d)) admitted with acute chronic headache, blurred vision, dizziness and nausea, and speech difficultly. An R-out study recorded an opening pressure of 10 mmHg and a finishing pressure of 50 mmHg. MRI scans revealed ventricular enlargement affecting the lateral and third ventricles with no obvious cause. CT angiogram did not find vascular abnormalities, monitoring studies did not find the ICP to be elevated, and there was flow of CSF through the aqueduct. The patient experienced subjective memory loss (although the test was considered somewhat unreliable) – although there was no reduced mobility or urinary incontinence – and 'arrested hydrocephalus' was suspected.

5.2.1.2 Simulation Set-Up

We have already seen that the coupled SPET model is a highly stiff system and the convergence of the transient **CFD-ACE+** solution is dependent on the initial conditions supplied to the flow model. Once again, the methodological approach is to compute a steady-state solution that can be used to provided a set of initial conditions for the transient solver. However, the MPET model is relatively more fragile, and

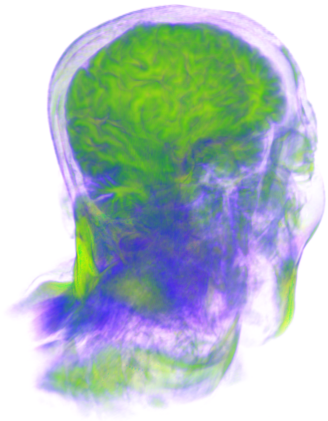

(a)

(b)

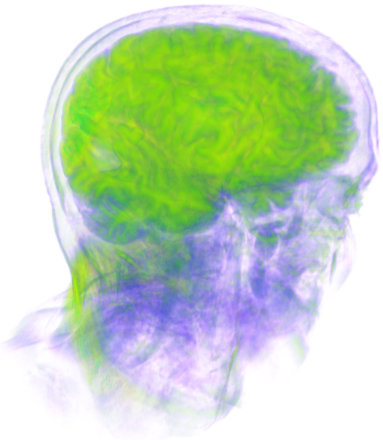

(c)

(d)

Figure 5.13: Patient-specific MRI scans: **(a)**, **(b)** Case 2, a mid-seventies female patient with history of dementia, urinary incontinence and falls; and, **(c)**, **(d)** Case 3, an early-seventies male patient with a history of short term memory loss and a shuffling gait.

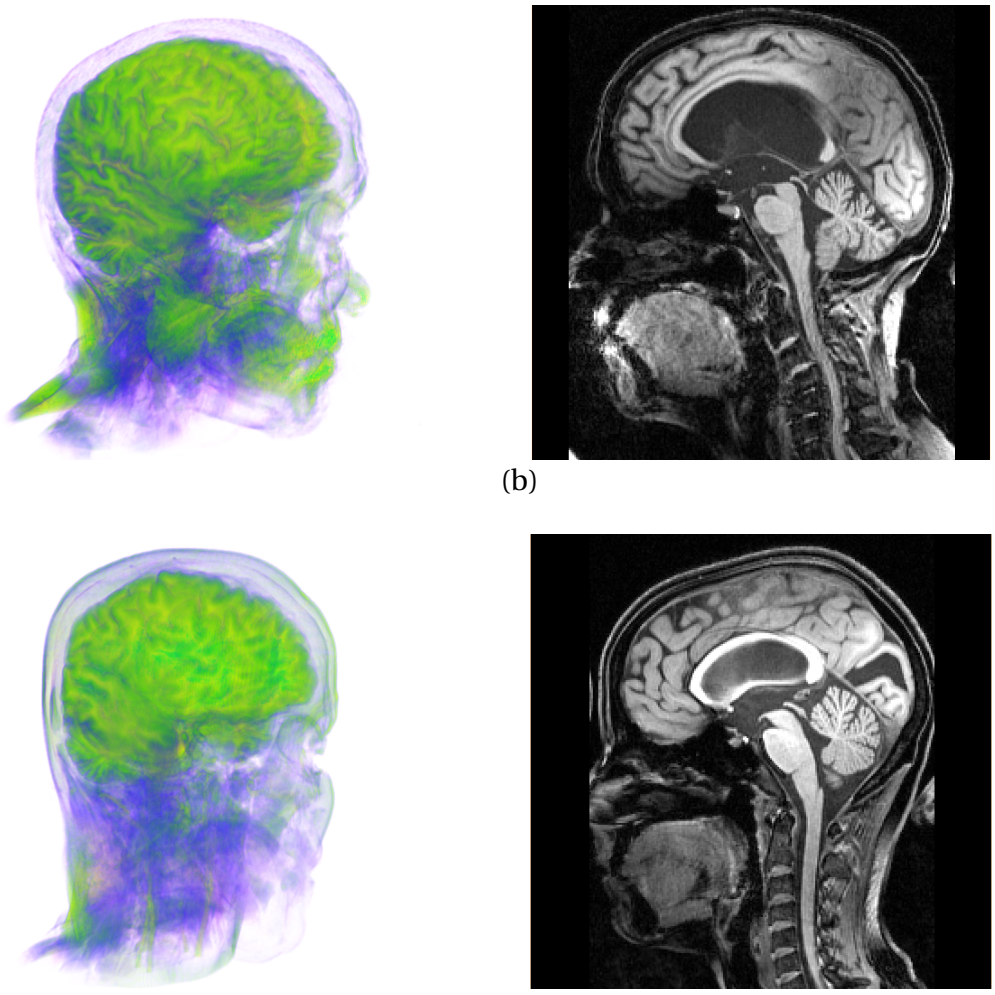

(a) (b)

(c) (d)

Figure 5.14: Patient-specific MRI scans: **(a)**, **(b)** Case 4, a late-sixties male patient with no abnormal physical signs apart from a history of gait disturbance; and, **(c)**, **(d)** Case 5, a patient presenting with acute chronic headache, blurred vision, dizziness and nausea, and speech difficultly but no gait disturbance or urinary incontinence.

several additional numerical techniques are used to maintain stability in the coupled model. Different time step sizes are used in the one- and three-dimensional solvers, under-relaxation (with a factors varying in value depending on the run being completed) is used on the inlet pressure returned by the multiple-network poroelastic C++ solver, and in the case of dynamic tissue and transport properties (to investigate NPH as a 'Two-Hit' disease) the time step size of the three-dimensional flow solver is prescribed dynamic values based on the changes in the tissue and transport parameters.

For stability of the coupled solution to be maintained, it is important to ensure that the inlet pressure received from the multiple-network poroelastic C++ solver does not oscillate artificially as the temporal iterations progress. There was a greater potential for this situation to arise when the time step size of the multiple-network poroelastic C++ solver was too large. However, the consequential decrease in time step of the **CFD-ACE+** solver increased the computational expense of the simulations beyond reasonable levels. To deal with this, different time step sizes were introduced for the one- and three-dimensional components of the coupled solver. Implementation is relatively straight-forward whereby the maximum step size of the multiple-network poroelastic C++ solver is set explicitly, the step size of the **CFD-ACE+** solver is read in to the multiple-network poroelastic C++ solver and the number of sub-iterations of the MPET model is calculated and then executed in a loop.

```
// === inner time step loop; allows for a smaller time step without
// === requiring the same from CFD-ACE
int NN;                    // the number of steps in the inner-loop
double DT;                 // the step size of the inner-loop
double dt;                 // the step size from CFD-ACE+
DT      = 1.0;             // set the maximum size
NN      = int(dt/DT)+1;    // calculate the number of steps
DT      = dt/NN;           // calculate the exact step size needed
for ( int j = 0; j < NN; j++ )
{
    // === build the A and b matrices using DT
    // === run the solver
}
```

In this implementation example, the multiple-network poroelastic C++ solver adopts an inner-loop for building and solving the **Ax** = **b** system – importantly, within this inner-loop, the same value is used for the flux of fluid through the cere-

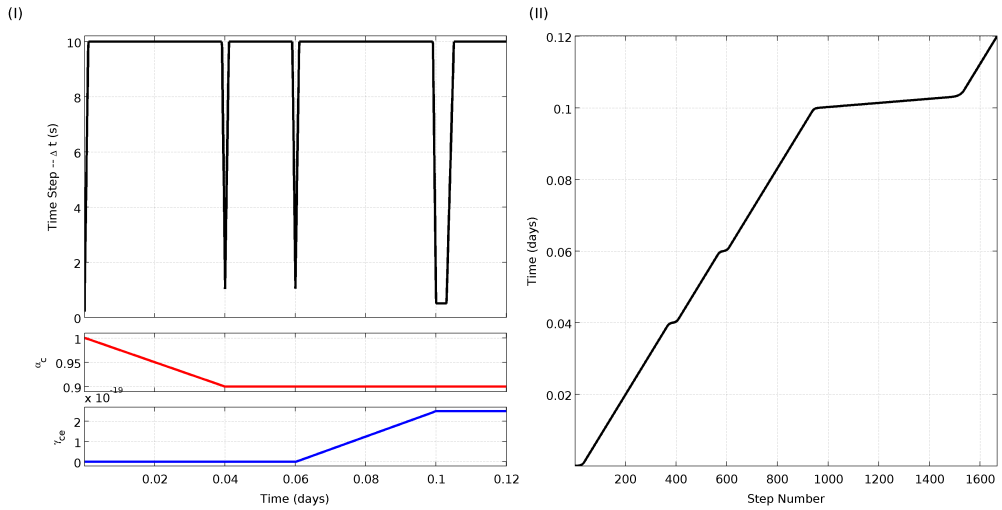

Figure 5.15: The stiffness of the coupled MPET model required a significantly smaller time step to be prescribed when the material parameters were varied with time. **(I)** shows the UDS controlled material parameters, α^c and γ_{ce}, and time step size; **(II)** shows the simulation time as a function of the iteration number.

bral aqueduct (Q_p).

The multi-time step procedure vastly improves the stability of the coupled solvers. However, the **CFD-ACE+** solver remains sensitive to the specified inlet pressure and non-linearities mean that small oscillations in this pressure soon become wild oscillations in the flow solver and the algorithm crashes. In order to overcome this challenge, extreme care must be taken to ensure that the initial flow conditions are specified from an accurate steady-state solution. Furthermore, under-relaxation is introduced to add stability to the inlet pressures returned from the multiple-network poroelastic C++ solver. Lines 163–164 in Appendix D.2 are replaced by:

```
! run the poroelastic solver
PAold    = PA * 1.0
CALL bt_solver( m, Qdot, currentTime, currentTimeStep, dtSecs, PA, PC,
    »model_name )
PA       = blend * PAold + (1-blend) * PA
```

where the value for blend is set to 0.1 (apart from the brief period mentioned in Figure 5.15).

In order to extend §5.1.2.3 to patient-specific aqueduct geometries, the time step size of the **CFD-ACE+** solver must be carefully controlled. Initial studies failed to

return results as the solver would crash if the step-size was too large when the arteriole/capillary compliance was increased (by decreasing α^c) and the arteriole/-capillary network was made progressively more leaky (through an increase in γ_{ce}). Hence, the UDS was modified to tightly control the time step size around the discrete changes in the rate of change of the tissue and transport properties (see Figure 5.15).

Like the previous coupling methodology, the step size increases from 0.1 s to 10.0 s in the first 100 seconds of the simulation, however, from 85 seconds before the ramp change in a tissue or transport parameter, the step size is decreased such that its value is 1.0 s at the ramp. In the 85 seconds that follows the start/end of the ramp, the step size is increased back to 10.0 s. However, at the conclusion of the ramp for γ_{ce}, the step size is reduced to 0.5 s, and the amount of under-relaxation is also increased to 0.5, and maintained for 170 seconds.

5.2.2 Results

The first study of chronic hydrocephalus by a four network MPET model assumed that the flow through the cerebral aqueduct could be represented by analytical Poiseuille flow. We have already shown that patient-specific aqueduct geometry plays an important role in the development of acute hydrocephalus; and now repeat the investigation using the MPET model. Firstly, the healthy configuration was used to ensure that the change in coupling methodology reproduces the same results as the SPET model; the effect of individual geometries was then explored within the context of healthy, symptomatic and transient configurations.

5.2.2.1 Confirming the Coupling Methodology

Due to the stiffness of the four-network MPET model, the coupling methodology was altered to compensate and ensure that convergence was achieved. The first investigation of the 1D-3D coupled model was thus a direct comparison of the healthy configuration with the SPET model using the patient-specific, artificially stenosed geometries in §4.2.2. The results showed that the new coupling methodology bears no influence on the ventricular displacement or CSF pressure; and furthermore, the healthy configuration found through the parametric search (with Poiseuille flow through the aqueduct) remained accurate in the coupled model (Figure 5.16).

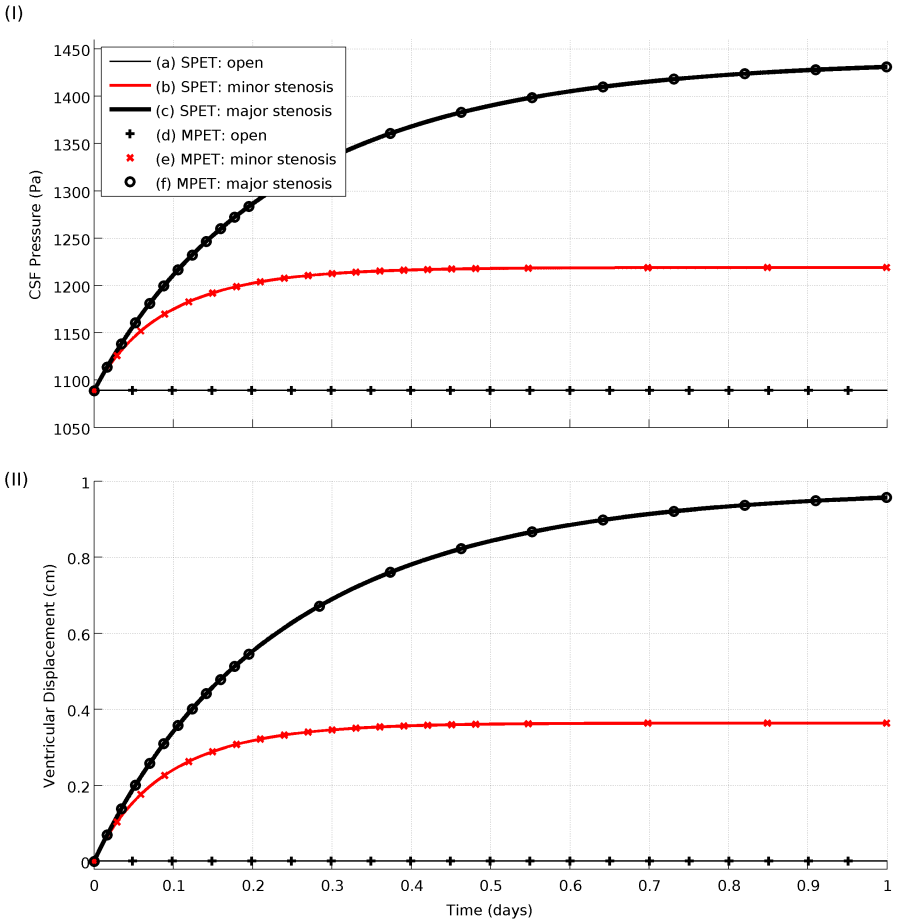

Figure 5.16: During the parametric search of §5.1.2 the new material parameters of the MPET model were found such that the model was capable of capturing the same behaviour in acute hydrocephalus as the SPET model. Here we see that this remains true when computed with patient-specific aqueduct geometry.

Following from the initial investigation, the healthy and symptomatic configurations of the MPET model were tested with the artificially occluded, patient-specific aqueducts. As expected from the previous section, the symptomatic configuration produces a much higher ventricular displacement (Figure 5.17-(I)). Yet the relative difference between the open and stenosed aqueducts (Figure 5.17-(d) and Figure 5.17-(e)–(f), respectively) was smaller as witnessed by normalizing the displacement by the initial value ($t = 0$ days) of each run (Figure 5.17-(III)).

There are two reasonable explanations for this: firstly, the simulations have not reached the steady-state due to computational expense[3]; and secondly, the intro-

[3]In order to achieve 0.4 days of simulation, each MPET model underwent more than 15,000 sim-

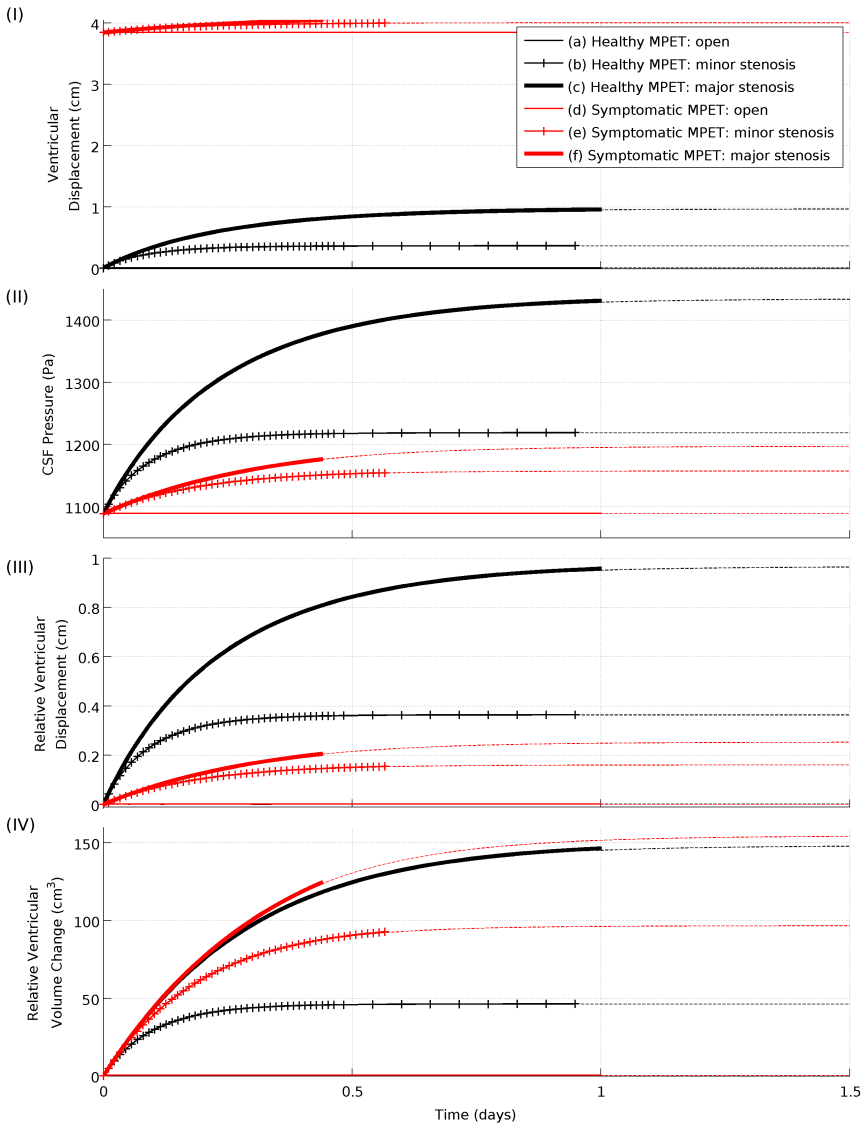

Figure 5.17: These figures represent the ventricular pressure and displacement from the MPET model in the healthy (black lines) and symptomatic configurations (red lines). The plot shows: **(I)** the raw displacement predicted by each model; **(II)** the CSF pressure in the ventricles; **(III)** the ventricular displacement normalized by adjusting the displacement at $t = 0$ days to be equal to zero; and, **(IV)** calculates the these normalized values in terms of the volume of the displaced spherical shell. It can be observed that, for a similar stenosis, the symptomatic brain experiences a smaller direct displacement, **(III)**, yet this translates to a larger volumetric displacement, **(IV)**. The dotted lines show a line fit using $f(x) = a\tanh(\frac{x^b}{c}) + d$.

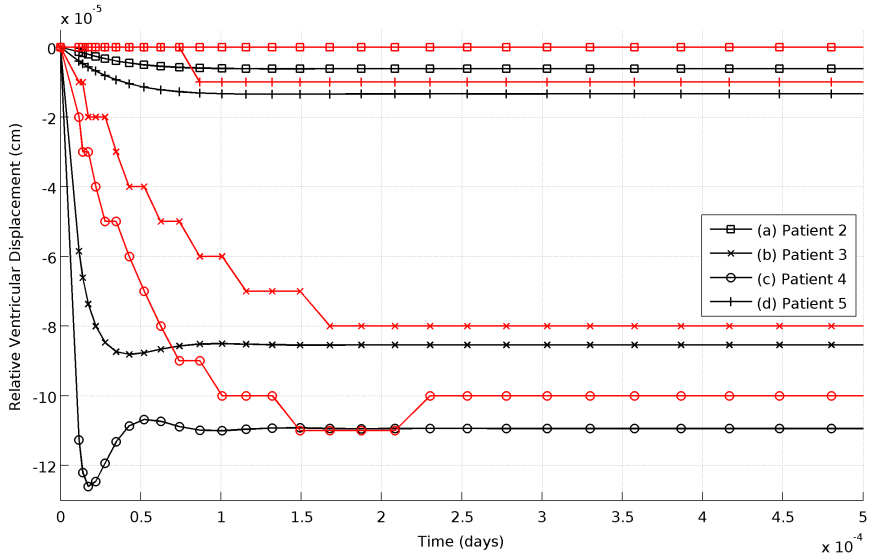

Figure 5.18: This plot focuses on the first ~ 45 seconds of computing the healthy (black lines) and symptomatic (red lines) configurations of the coupled MPET model for each of the patient geometries. The displacements shown are normalized to the initial displacement of each run and clearly show that while large differences are observed in the geometries themselves, the displacement changes only by hundreds of nanometres. It should be noted that the discrete changes in the red lines are due to truncation error in the output stage of the model.

duction of the symptomatic configuration is instantaneous and the ventricular system is already dilated, thus, a direct comparison of the displacement may yield less information than comparing the volumetric change (Figure 5.17-(IV)). While these results reveal little that is useful about the system, they do show that in the symptomatic configuration ventriculomegaly is relatively unrelated to the aqueduct geometry.

5.2.2.2 The Influence of Patient-Specific Geometry

The first set of coupled investigations showed that the MPET model is capable of reproducing the results of the SPET model and the analytic parametric study. To extend on this, each of the four symptomatic patient geometries were run with both the healthy and symptomatic configurations of the model. While each of these geometries are markedly different, interestingly, the ventricular displacement differed only by hundreds of nanometres (Figure 5.18). The flow patterns of CSF through

ulations, or more than two months of compute time on 8 cores of the `fbg-cluster`.

Patient 2	Patient 3	Patient 3	Patient 4
2.48 mms^{-1}	1.64 mms^{-1}	1.09 mms^{-1}	1.81 mms^{-1}

Table 5.4: Velocities through the patient-specific cerebral aqueducts coupled to the MPET model in the healthy configuration.

the ventricular space were distinct for each patient (see Figure 5.19) with different maximal velocities recorded (Table 5.4).

Clinically, these changes in flow are acutely important when considering surgical intervention procedures. For example, comparing the flow structure in Patient 2 and Patient 5 would inform the interventionalist of optimal shunt positioning or TV location (Figure C.4 and Figure C.5, respectively). Furthermore, each of the four patients displays varying degrees of ventriculomegaly in the MRI scans, suggesting that it is a biological change, rather than a mechanical flow change that is responsible.

5.2.2.2.1 Patient-Specific NPH as a Two-Hit Disease Section 5.1.2.3 explored the capability of the MPET model to mimic the description of NPH as a two-hit disease by varying α^c and γ_{ce} over time. Mimicking an increase in compliance of the arteriole/-capillary network (implied by decreasing α^c from 1.0 to 0.9) gave an initial displacement of the ventricles. This was further exaggerated by an increase in the leakiness of the blood-CSF barrier such that more fluid can flow from the arteriole/capillary network to the CSF network (implied by increasing γ_{ce} from 1.0×10^{-20} $\text{m}^2\text{N}^{-1}\text{s}^{-1}$ to 2.5×10^{-19} $\text{m}^2\text{N}^{-1}\text{s}^{-1}$), resulting in a displacement of almost 4 cm. For this section, the same study was conducted (albeit on a decreased time scale due to the large increase in computational requirements) on each of the four patient-specific geometries, with no change in the overall result (Figure 5.20).

While the general result did not change, it is worth noting the subtle difference between the coupled and analytic models in the case of the dynamic tissue and transport properties (Figure 5.21). Computing the coupled model is very computationally expensive, and thus the period in which the tissue and transport properties were varied was significantly reduced to a period of a few hours rather than months. In doing so, there was an apparent breach of the quasi-steady assumption resulting in a diffusion of the sharp boundaries where the tissue and transport properties stop changing (cf. $t = 0.1$ days in Figure 5.21). We can see that similar features were

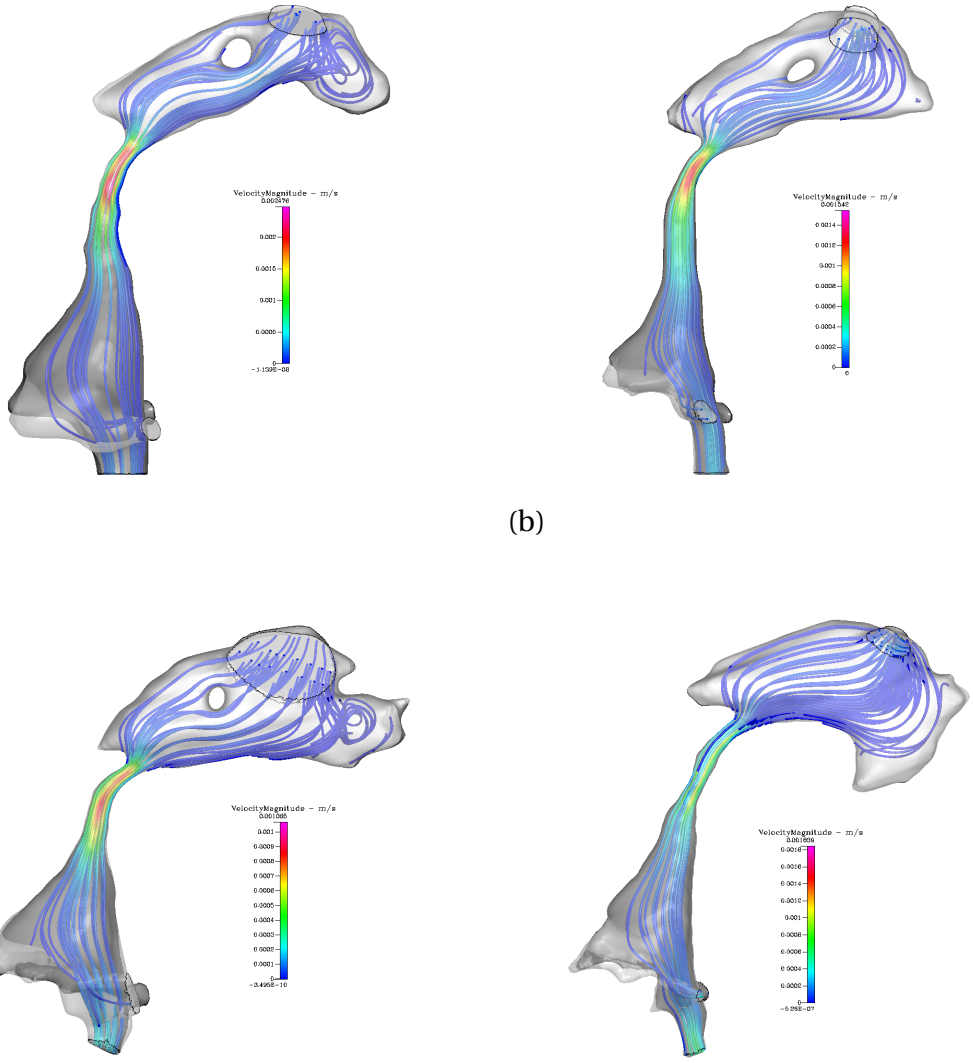

(a) (b)

(c) (d)

Figure 5.19: It is shown that patient-specific aqueduct geometry has little impact on ventriculomegaly in Figure 5.18, however, these streamline images clearly show the impact of geometry on the flow patterns. Patient 2, **(a)**, and Patient 4, **(c)**, have distinct areas of recirculation in the third ventricle, while Patient 3, **(b)**, and Patient 5, **(d)**, are relatively smooth. These patient-specific differences are likely to be of significance in the surgical intervention planning stages that are not part of the current work.

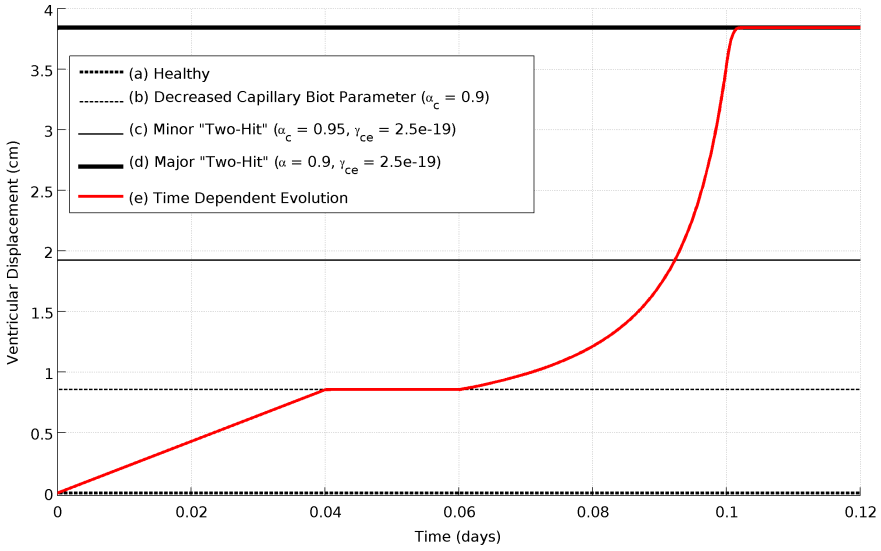

Figure 5.20: Section 5.1.2.3 explored the capability of the MPET model to mimic the description of NPH as a two-hit disease by varying α^c and γ_{ce} over time. Here, the study is repeated using patient-specific cerebral aqueduct geometries with no change in the overall result. The red line, **(e)**, represents changing the parameters α^c and γ_{ce} dynamically; with α^c changing linearly between 1.0 and 0.9 while $t = [0.00, 0.04]$ days and γ_{ce} changing linearly between 1.0×10^{-20} and 2.5×10^{-19} $m^2N^{-1}s^{-1}$ while $t = [0.06, 0.10]$ days. It should be reiterated that the actual time scale is not important as the study is quasi-steady.

present in the analytic model for the same characteristic time. However, if the analytic model is run over a period of months, or years, as was done previously these features disappear and the steady-state response remains the same.

It is clear from this study, that in the absence of a fully three-dimensional model, there is little reason to suggest that a coupled MPET model is providing a higher quality of information than a model using the Poiseuille flow assumption. This finding carries three important implications: biological changes are likely to be more significant than mechanical changes in the development of NPH; at this stage, the large computational expense of the flow solver is wasted in a 1D-3D coupled model; and, the Poiseuille flow law is likely to be sufficient while elements of the MPET model are investigated in more depth.

In concluding, there are three caveats where patient-specific geometry may be crucial; investigating the case of a fully three-dimensional model, surgical intervention planning, and a fully transient MPET model with pulsatile blood flow.

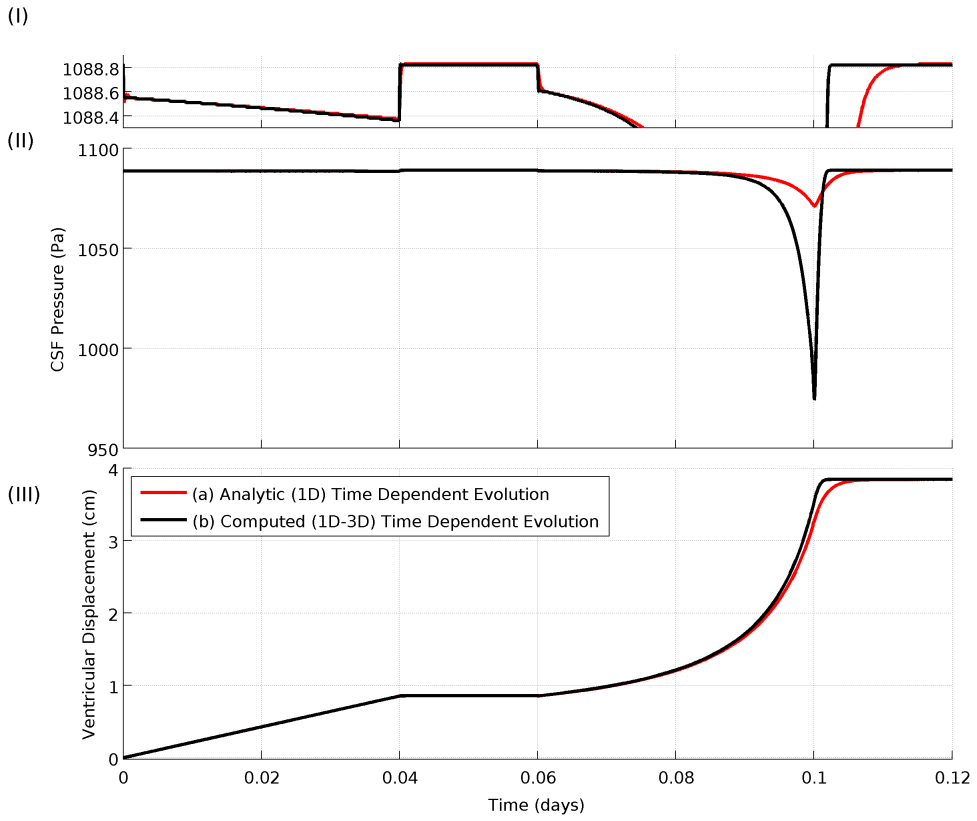

Figure 5.21: Comparing the results of the coupled simulation with the analytic MPET model. Each model arrives at the same steady-state result, however, there are slight differences in the transient response that can be attributed to the speed of changing the α^c and γ_{ce} in contradiction to the quasi-steady approximation of the system. It can be shown with the analytic model that increasing the characteristic time removes the deviations in the pressure curve seen in this image, with any influence on the steady-state response.

5.3 DISCUSSION

This chapter introduces a hypothesis test bed for NPH through the novel translation of a quadruple MPET model from geomechanics to soft tissue in the cerebral environment.

The lack of relevant experimental data meant that an extensive parametric search of the one-dimensional MPET model was conducted to find appropriate values for the various mechanical constants. Parameters related to physiological mechanisms – including a breakdown in the blood-brain and blood-CSF barriers and a changes in the mechanical properties of the cerebral vascular networks – were

identified as potential loci for physiological mechanisms for NPH. Specifically, four parameters of interest were found: Biot parameters for the arteriole/capillary (α^c) and venous (α^v) networks[4]; and, transfer coefficients of flow from the arteriole/-capillary network to the CSF space (γ_{ce}) and flow from the CSF space to the venous network (γ_{ev}).

Changing each of the four parameters in isolation showed that clinically reasonable ventriculomegaly was only possible when mimicking an increase in the compliance of the arteriole/capillary network (introduced by decreasing α^c). However, the biggest ventricular dilation came from a combination of a decreases in α^c and an increase in γ_{ce} that may, respectively, relate to increased compliance of the arteriole/capillary network and a breakdown of the blood-CSF barrier that allowed increased flow of water from the capillaries to the CSF. The displacement of the ventricle wall was observed with no associated change in the pressure of the fluid networks. It is argued by Bradley (2008) that NPH is a two stage condition and the results shown here have provided a possible explanation.

Furthermore, the initial investigations of the MPET model show little difference between conducting the simulation with analytic or patient-specific representations of the cerebral aqueduct. The latter come with significant computation expense, however, true to the assumption that NPH is more than a mechanical disruption of CSF it is shown here that biological changes to the environment may be more significant than geometrical variations. Nevertheless, importantly, the CSF flow patterns recorded in each of the patient-specific simulations remind us that individual geometries are crucially important when considering surgical intervention design.

Finally, these observations must be framed with the model assumptions in mind. The properties of the matrix and CSF network were maintained from the studies by Smillie et al. (2005) and Tully and Ventikos (2009) for two reasons: firstly, these models select values from the most widely accepted reported data; and secondly, it allowed a comparison between the single and quadruple network MPET models.

The introduction of more fluid networks added many additional assumptions due a lack of relevant experimental data. Parameters introduced, such as Biot parameters, permeabilities and transfer coefficients, have an implied 'active' property in the tissue. Similarly, we assumed that the outflow of CSF to the sagittal sinuses

[4]A reminder: in a single network poroelastic model, decreasing α corresponds to an increase in compliance of the fluid network (defined as $C = \frac{\partial V}{\partial p}$) (Sobey and Wirth, 2006).

was equal to production of water from the choroid plexus and thus implied that any accumulation in the model comes from a physiological change in the parenchyma. This was a reasonable assumption though, as one can argue that allostasis is maintained until a change is invoked and symptoms appear.

CHAPTER 6

CONCLUSIONS

It has been shown that there are several competing ideas as to the best method for modelling hydrocephalus. Of those offered, poroelastic theory has gained prominence due to its ability to provide information in both time and space. The preceding chapters have given two different poroelastic approaches to acute and chronic hydrocephalus and this chapter will offer a discussion and conclusions about the implications of these models.

Throughout the published literature, there are several challenges to the use of mathematical models in the cerebral environment. As this work is an initial step in what will be a prolonged research effort, there was no expectation or desire to address all of these challenges first up. However, assessing those challenges that were overcome is important in addressing how to move the research forward.

Hydrocephalus, chronic or acute, is simply defined by an accumulation of CSF due to a difference in its production and absorption in the absence of a noticeable increase in ventricular pressure; however, the cause of this difference is unknown (Hebb and Cusimano, 2001). For chronic hydrocephalus there are several causative mechanisms mooted in the literature; changes in brain parenchyma, vascular resistance and CSF circulation may result in decreased intra-cranial compliance and diminished cerebral blood flow (Dombrowski et al., 2009).

The multiple network poroelastic theory developed in this study has successfully investigated many of the published theories of hydrocephalus. The findings carry three important implications: biological changes are likely to be more signif-

icant than mechanical changes in the development of NPH; at this stage, the large computational expense of the flow solver is wasted in a 1D-3D coupled model; and, the Poiseuille flow law is likely to be sufficient while elements of the MPET model are investigated in more depth.

However, as with all numerical studies, results must be assessed with the primary assumptions in mind. These are: the reduction of the system to a spherical geometry; assigning material properties without consistent experimental evidence; and ignoring the role of pulsations by simplifying the system to quasi-steady.

While the spherical geometry restricts the range of quantitative results that can be provided, the model was able to capture features of the system for a qualitative assessment. Furthermore, poroelastic models have been extended into three dimensional geometries with primary costs being time of implementation and computational expense (Wirth and Sobey, 2006). With this in mind, there is no reason to believe that the MPET model presented here cannot be extended to a fully three-dimensional simulation. Likewise, the simplification to quasi-steady equations allows a thorough investigation of properties over the time scale of hydrocephalus, providing that one assumes altered pulsatility in the environment does not play a role. In order to investigate the role of pulsatility, the more general transient equations must be solved.

Uncertainties in the mechanical properties of the tissue are more difficult to overcome. Until recently, it was not possible to calculate values like the Young's modulus *in vivo*. As a result, traditional mechanical tests are carried out on excised tissue. However, it is very possible that tissue must be 'alive' and 'wetted' in order for it to behave to its true function. For example, it is likely that fluid exchange exists between the extracellular space and the capillary blood (Amiry-Moghaddam et al., 2003), yet this will not be present in excised tissue.

New studies are emerging where Magnetic Resonance Elastography (MRE) is used to calculate the shear stiffness of tissue *in vivo*, although these studies are yet to find a consistent and globally acceptable value (Sack et al., 2008; Kruse et al., 2008) and may only include the short time-scale stiffness of the tissue.

In the case of the four-network MPET model, the novelty of the system implies that experimental values for the material constants are unavailable. While this novelty is an incredible strength of the model, we must realize that experimental valida-

tion is crucial for the constants determined through the parametric search. This is a significant challenge that must be overcome if we are to consider the MPET framework (or any other numerical framework for that matter) as clinically useful for investigating diseases of the brain.

Furthermore, the MPET model assumed a linear stress-strain constitutive relationship, Equation (3.18), yet produced relatively large strains; and mechanical properties such as permeability were considered to be constant. These approximations no doubt introduced errors into the model; however, other assumptions such as a spherically symmetric geometry already implied the system was more useful providing qualitative, rather than quantitative, information. The implementation of a more complex constitutive relationship and strain-dependent permeabilities should be considered when the model is applied to patient-specific geometries.

In §2.2 a substantial list of features were listed as a suitable metric for assessing the success of the mathematical framework developed in this research. Bearing in mind the assumptions listed above (and elsewhere in this thesis) the following observations can be made:

Deformation of the ventricles and the sub-arachnoid spaces: the spherically symmetric MPET model showed real potential to replicate ventricular dilation seen in the clinic. In this research, details of the sub-arachnoid space (including the skull) were ignored according to findings from the literature; however, the general framework can be easily modified to include more definition in the boundary conditions at the periphery as further details come to light.

Elevated ICP and intra-cranial pressure waves: in the case of acute hydrocephalus, both the SPET and MPET models are capable of predicting an elevated ICP; for chronic hydrocephalus, a normal CSF pressure is maintained accordingly. Due to the quasi-steady assumption, intra-cranial pressure waves cannot be captured by the simplified model used throughout.

The temporal horns and third ventricle dilate first: by assuming a spherical geometry, the case studies presented here are unable to make a statement one way or the other about the order of dilation in the ventricles. With a fully three-dimensional MPET model, this should emerge naturally.

Hyper-dynamic CSF pulsations in the aqueduct: through the SPET investigation it was found that investigating pulsatile motion with the current model is a breach of the quasi-steady assumption. A fully transient solution using the same framework should be able to capture the pulsatile motion of the CSF.

Intra-cranial venous hypertension: the MPET model does not capture a pressure increase in the venous network. It is possible that this is due to the quasi-steady assumption, as it may be that this hypertension results from the pulsatile nature of the flow dynamics (Egnor et al., 2002).

Diminished cerebral blood flow: assumptions made in the boundary conditions at the skull (constant arterial and venous pressure) and a constant isotropic permeability of the fluid networks, preclude the blood flow from diminishing. Future work may investigate the possibility of strain dependant permeability to be included in the model.

Diminished pressure gradient between sub-arachnoid spaces and venous sinuses: once again, definition in the sub-arachnoid space is ignored in this model. As more details become known, the boundary conditions will be updated accordingly.

Malabsorption of CSF: in the acute hydrocephalus model, there is no need for a malabsorption of CSF as ventriculomegaly is the result of a radiographically identifiable obstruction to the flow. In the case of chronic hydrocephalus, the flexibility of the MPET model allows speculation over many sites of irregular CSF flow. The findings from this study suggest that a change in the fluid exchange between the cerebral capillaries and the interstitial fluid in the parenchyma may lead to the development of NPH.

Hyper-dynamic arterial pulsations in the sub-arachnoid arteries: this study is precluded from making comments on the pulsatile nature of the sub-arachnoid space due to the quasi-steady nature of the simplified models.

Selective compression of white matter and relative sparing of grey matter: due to the lack of consistent values for the elastic properties of cerebral tissue, this study assumes that white and grey matter are the same. As more data are published, this feature can be duly tested from within the current framework.

In concluding, the novelty of the MPET system is both a tremendous strength and an inherent weakness. Through extensive numerical investigations, hydrocephalus is simulated with clinically relevant ventriculomegaly produced in the absence of any visible CSF flow obstruction; yet, we are limited by the notable absence of experimental validation of the material parameters.

The importance and complexity of the brain, together with the range of unmet clinical needs that are connected with this organ, make the current research a high-priority. Cerebral diseases are recognized as pivotal in healthcare; in this study, hydrocephalus is selected for investigation due to its readily observable clinical features such as ventricular enlargement and CSF pressure, but the developed framework for cerebral water transport is promising for a wide range of diseases. We are convinced that basic understanding of fluid transport is the most promising way to address these needs meaningfully, in a clinical setting.

Finally, we hope that publishing this study will prove useful to guide experimental exploration in areas that warrant further investigation and validation.

REFERENCES

AGRE, P., NIELSEN, S., AND OTTERSEN, O. P. Towards a molecular understanding of water homeostasis in the brain. *Neuroscience*, 129(4):849–50, January 2004. ISSN 0306-4522.

AGRE, P. The aquaporin water channels. *Proceedings of the American Thoracic Society*, 3(1):5–13, January 2006. ISSN 1546-3222.

AIFANTIS, E. C. Continuum basis for diffusion in regions with multiple diffusivity. *Journal of Applied Physics*, 50(3):1334, 1979. ISSN 00218979.

AIFANTIS, E. C. On the problem of diffusion in solids. *Acta Mechanica*, 37(3-4):265–296, September 1980. ISSN 0001-5970.

AIFANTIS, E. C. AND HILL, J. M. On the theory of diffusion in media with double diffusivity i. basic mathematical results. *The Quarterly Journal of Mechanics and Applied Mathematics*, 33(1):1–21, 1980.

AMIRY-MOGHADDAM, M., OTSUKA, T., HURN, P. D., TRAYSTMAN, R. J., HAUG, F.-M., FROEHNER, S. C., ADAMS, M. E., NEELY, J. D., AGRE, P., OTTERSEN, O. P., AND BHARDWAJ, A. An alpha-syntrophin-dependent pool of AQP4 in astroglial end-feet confers bidirectional water flow between blood and brain. *Proceedings of the National Academy of Sciences of the United States of America*, 100(4):2106–11, February 2003. ISSN 0027-8424.

ANOR, T., GRIENBERG, L., MADSEN, J. R., AND KARNIADAKIS, G. E. Large-scale simulation of the human cranial arterial tree: utility in hydrocephalus. *Cerebrospinal Fluid Research*, 6(Suppl 1):S48, 2009. ISSN 1743-8454.

ASCHOFF, A., KREMER, P., HASHEMI, B., AND KUNZE, S. The scientific history of hydrocephalus and its treatment. *Neurosurgical Review*, 22(2-3):67–93; discussion 94–5, October 1999. ISSN 0344-5607.

ATESHIAN, G. A. AND WANG, H. A theoretical solution for the frictionless rolling contact of cylindrical biphasic articular cartilage layers. *Journal of Biomechanics*, 28(11):1341 – 1355, 1995. ISSN 0021-9290.

BAI, M., ELSWORTH, D., AND ROEGIERS, J.-C. Multiporosity/Multipermeability Approach to the Simulation of Naturally Fractured Reservoirs. *Water Resources Research*, 29(6):1621–1633, 1993. ISSN 0043-1397.

BAI, M., MENG, F., ELSWORTH, D., AND ABOUSLEIMAN, Y. Numerical modelling of coupled flow and deformation in fractured rock specimens. *International Journal for Numerical and Analytical Methods in Geomechanics*, 23(2):141–160, 1999.

BALÉDENT, O., GONDRY-JOUET, C., MEYER, M.-E., DE MARCO, G., LE GARS, D., HENRY-FEUGEAS, M.-C., AND IDY-PERETTI, I. Relationship between cerebrospinal fluid and blood dynamics in healthy volunteers and patients with communicating hydrocephalus. *Investigative Radiology*, 39(1):45–55, January 2004. ISSN 0020-9996.

BANAJI, M., TACHTSIDIS, I., DELPY, D., AND BAIGENT, S. A physiological model of cerebral blood flow control. *Mathematical Biosciences*, 194(2):125–73, April 2005. ISSN 0025-5564.

BATEMAN, G. A. Toward a better understanding of normal pressure hydrocephalus. *AJNR. American Journal of Neuroradiology*, 22(3):596, March 2001. ISSN 0195-6108.

BATEMAN, G. A. The pathophysiology of idiopathic normal pressure hydrocephalus: cerebral ischemia or altered venous hemodynamics? *AJNR. American Journal of Neuroradiology*, 29(1):198–203, January 2008. ISSN 1936-959X.

BATEMAN, G. A. Vascular compliance in normal pressure hydrocephalus. *AJNR. American Journal of*

Neuroradiology, 21(9):1574–85, October 2000. ISSN 0195-6108.

BATEMAN, G. A. Extending the hydrodynamic hypothesis in chronic hydrocephalus. *Neurosurgical Review*, 28(4):333–4, October 2005. ISSN 0344-5607.

BAZARIAN, J. J., MCCLUNG, J., SHAH, M. N., CHENG, Y. T., FLESHER, W., AND KRAUS, J. Mild traumatic brain injury in the United States, 1998–2000. *Brain Injury : [BI]*, 19(2):85–91, February 2005. ISSN 0269-9052.

BERGSNEIDER, M., EGNOR, M. R., JOHNSTON, M., KRANZ, D., MADSEN, J. R., MCALLISTER, J. P., STEWART, C., WALKER, M. L., AND WILLIAMS, M. A. What we don't (but should) know about hydrocephalus. *Journal of Neurosurgery*, 104(3 Suppl): 157–9, March 2006. ISSN 0022-3085.

BERING, E. A. Circulation of the cerebrospinal fluid. Demonstration of the choroid plexuses as the generator of the force for flow of fluid and ventricular enlargement. *Journal of Neurosurgery*, 19:405–13, May 1962. ISSN 0022-3085.

BERRYMAN, J. G. Extension of Poroelastic Analysis to Double-Porosity Materials: New Technique in Microgeomechanics. *Journal of Engineering Mechanics*, 128(8):840, 2002. ISSN 07339399.

BESKOS, D. AND AIFANTIS, E. On the theory of consolidation with double porosityâĂŤII. *International Journal of Engineering Science*, 24(11):1697–1716, 1986. ISSN 00207225.

BIOT, M. General theory of three-dimensional consolidation. *Journal of Applied Physics*, 12(2):155, 1941.

BIOT, M. AND WILLIS, D. The elastic coefficients of the theory of consolidation. *J. Appl. Mech*, pages 594–601, 1957.

BLUMENFELD, H. *Neuroanatomy Through Clinical Cases*. Sinauer, 2002.

BOUTAYEB, A. The double burden of communicable and non-communicable diseases in developing countries. *Transactions of the Royal Society of Tropical Medicine and Hygiene*, 100(3):191–9, 2006. ISSN 0035-9203.

BRADLEY, W. G. Normal pressure hydrocephalus: new concepts on etiology and diagnosis. *AJNR. American Journal of Neuroradiology*, 21(9):1586–90, October 2000. ISSN 0195-6108.

BRADLEY, W. G. Idiopathic normal pressure hydrocephalus: new findings and thoughts on etiology. *AJNR. American Journal of Neuroradiology*, 29(1):1–3, January 2008. ISSN 1936-959X.

BRADLEY, W. G., BAHL, G., AND ALKSNE, J. F. Idiopathic normal pressure hydrocephalus may be a two hit disease: benign external hydrocephalus in infancy followed by deep white matter ischemia in late adulthood. *Journal of Magnetic Resonance Imaging : JMRI*, 24(4):747–55, October 2006. ISSN 1053-1807.

BRADLEY, W. G., SAFAR, F. G., FURTADO, C., HURTADO, C., ORD, J., AND ALKSNE, J. F. Increased intracranial volume: a clue to the etiology of idiopathic normal-pressure hydrocephalus? *AJNR. American Journal of Neuroradiology*, 25(9):1479–84, October 2004. ISSN 0195-6108.

BRODAL, P. *The Central Nervous System: Structure and Function*. Oxford University Press, New York, 3rd editio edition, 2004.

BYRD, C. Normal pressure hydrocephalus: dementia's hidden cause. *The Nurse Practitioner*, 31(7):28–9, 31–5; quiz 36–7, July 2006. ISSN 0361-1817.

CARPENTER, M. *Core Text of Neuroanatomy*. William and Wiklins, Baltimore, 1991.

CASTEJÓN, O. J. Blood-brain barrier ultrastructural alterations in human congenital hydrocephalus and Arnold-Chiari malformation. *Folia Neuropathologica / Association of Polish Neuropathologists and Medical Research Centre, Polish Academy of Sciences*, 47(1):11–9, January 2009. ISSN 1641-4640.

CHAPMAN, D. P., WILLIAMS, S. M., STRINE, T. W., ANDA, R. F., AND MOORE, M. J. Dementia and its implications for public health. *Preventing Chronic Disease*, 3(2):A34, April 2006. ISSN 1545-1151.

CHATTERJI, S., KOWAL, P., MATHERS, C., NAIDOO, N., VERDES, E., SMITH, J. P., AND SUZMAN, R. The health of aging populations in China and India. *Health Affairs (Project Hope)*, 27(4):1052–63, 2008. ISSN 1544-5208.

CHENG, S. *The role of brain tissue mechanical properties and cerebrospinal fluid flow in the biomechanics of the normal and hydrocephalic brain*. Phd thesis, University of New South Wales, Sydney, Australia, 2006.

CHUI, H. C. Subcortical ischemic vascular dementia. *Neurologic Clinics*, 25(3):717–40, vi, 2007. ISSN 0733-8619.

CLARKE, M. J. AND MEYER, F. B. The history of mathematical modeling in hydrocephalus. *Neurosurgical Focus*, 22(4):E3, January 2007. ISSN 1092-0684.

CLATZ, O., LITRICO, S., DELINGETTE, H., PAQUIS, P., AND AYACHE, N. Dynamic model of communicating hydrocephalus for surgery simulation. *IEEE Transactions on Bio-Medical Engineering*, 54 (4):755–8, April 2007. ISSN 0018-9294.

CORKILL, R. G., GARNETT, M. R., BLAMIRE, A. M., RAJAGOPALAN, B., CADOUX-HUDSON, T. A. D., AND STYLES, P. Multi-modal MRI in normal pressure hydrocephalus identifies pre-operative haemodynamic and diffusion coefficient changes in normal appearing white matter correlating with surgical outcome. *Clinical Neurology and Neurosurgery*, 105(3):193–202, 2003. ISSN 0303-8467.

CUSHING, H. The third circulation and its channels: the cameron lecture. *Lancet, The*, 209:851, 1925. ISSN 0140-6736.

CZOSNYKA, M., CZOSNYKA, Z., MOMJIAN, S., AND PICKARD, J. D. Cerebrospinal fluid dynamics. *Physiological Measurement*, 25(5):R51–76, October 2004. ISSN 0967-3334.

DA SILVA, M. C., MICHOWICZ, S., DRAKE, J. M., CHUMAS, P. D., AND TUOR, U. I. Reduced local cerebral blood flow in periventricular white matter in experimental neonatal hydrocephalus-restoration with CSF shunting. *Journal of Cerebral Blood Flow and Metabolism : Official Journal of the International Society of Cerebral Blood Flow and Metabolism*, 15 (6):1057–65, November 1995. ISSN 0271-678X.

D'AMBROSIO, R. AND PERUCCA, E. Epilepsy after head injury. *Current Opinion in Neurology*, 17(6):731–5, 2004. ISSN 1350-7540.

DANDY, W. AND BLACKFAN, K. An experimental and clinical study of internal hydrocephalus. *Journal of the American Medical Association*, 61:2216–2217, 1913.

DANDY, W. AND BLACKFAN, K. Internal hydrocephalus, an experimental, clinical and pathological study. *American Journal of Diseases of Children*, 8:406–482, 1914.

DAUN, S. AND TJARDES, T. Modelling, analysis and calculation of cerebral hemodynamics. *Computational and Mathematical Methods in Medicine*, 8 (3):205–223, September 2007. ISSN 1748-670X.

DAVIDOFF, L. Treatment of hydrocephalus: historical review and description of a new method. *Archives of Surgery*, 18(4):1737, 1929.

DAWODU, S. T. Traumatic Brain Injury (TBI) - Definition, Epidemiology, Pathophysiology. `http://emedicine.medscape.com/article/326510-overview`, 2009.

DE DEYN, P. P., WOSTYN, P., AND AUDENAERT, K. More advanced Alzheimer's disease may be associated with a decrease in cerebrospinal fluid pressure. *Cerebrospinal Fluid Research*, 6:14, 2009. ISSN 1743-8454.

DE LA TORRE, J. Alzheimer Disease as a Vascular Disorder: Nosological Evidence. *Stroke*, 33(4):1152–1162, 2002. ISSN 00392499.

DEL BIGIO, M. R. Cellular damage and prevention in childhood hydrocephalus. *Brain Pathology (Zurich, Switzerland)*, 14(3):317–24, July 2004. ISSN 1015-6305.

DOMBROWSKI, S., CRUTCHFIELD, K., LIGON, K., BECKER, J., AND LUCIANO, M. Evidence for CSF-vascular compliance coupling in normal pressure hydrocephalus. *Cerebrospinal Fluid Research*, 6 (Suppl 1):S36, 2009. ISSN 1743-8454.

DRAKE, J. M., KULKARNI, A. V., AND KESTLE, J. Endoscopic third ventriculostomy versus ventriculoperitoneal shunt in pediatric patients: a decision analysis. *Child's Nervous System : ChNS : Official Journal of the International Society for Pediatric Neurosurgery*, 25(4):467–72, 2009. ISSN 1433-0350.

DRAPACA, C. S., TENTI, G., ROHLF, K., AND SIVALOGANATHAN, S. A Quasi-linear Viscoelastic Constitutive Equation for the Brain: Application to Hydrocephalus. *Journal of Elasticity*, 85(1):65–83, October 2006. ISSN 0374-3535.

EGNOR, M., ROSIELLO, A., AND ZHENG, L. A model of intracranial pulsations. *Pediatric Neurosurgery*, 35 (6):284–98, December 2001. ISSN 1016-2291.

EGNOR, M., ZHENG, L., ROSIELLO, A., GUTMAN, F., AND DAVIS, R. A model of pulsations in communicating hydrocephalus. *Pediatric Neurosurgery*, 36 (6):281–303, June 2002. ISSN 1016-2291.

EMAM, M., ABASHIYA, Y., CHAREUNSACK, B., SKORDOS, J., OH, J., CHOI, Y., KRALICK, F., AND NOH, H. M. A novel microdevice for the treatment of hydrocephalus: design and fabrication of an array of

microvalves and microneedles. *Microsystem Technologies*, 14(3):371–378, March 2008. ISSN 0946-7076.

CFD-ACE+ V2009.4 User Manual. ESI Group, Huntville, Alabama, 2009.

EUROCAT. EUROCAT. `http://www.bio-medical.co.uk/eurocatlive`, 2007.

FARD, P. J. M., TAJVIDI, M. R., AND GHARIBZADEH, S. High-pressure hydrocephalus: a novel analytical modeling approach. *Journal of Theoretical Biology*, 248(3):401–10, October 2007. ISSN 0022-5193.

FARRELL, D. AND BEINHOCKER, E. Next big spenders: India's middle class, 2007.

FRANCESCHINI, G. *The mechanics of human brain tissue*. Phd thesis, University of Trento, Trento, 2006.

GALLIA, G. L., RIGAMONTI, D., AND WILLIAMS, M. A. The diagnosis and treatment of idiopathic normal pressure hydrocephalus. *Nature Clinical Practice. Neurology*, 2(7):375–81, July 2006. ISSN 1745-834X.

GANGEMI, M., MAIURI, F., BUONAMASSA, S., COLELLA, G., AND DE DIVITIIS, E. Endoscopic third ventriculostomy in idiopathic normal pressure hydrocephalus. *Neurosurgery*, 55(1):129–34; discussion 134, July 2004. ISSN 0148-396X.

GEVERTZ, J. L. AND TORQUATO, S. A novel three-phase model of brain tissue microstructure. *PLoS Computational Biology*, 4(8):e1000152, January 2008. ISSN 1553-7358.

GIDEON, P., STÅ HLBERG, F., THOMSEN, C., GJERRIS, F., SØ RENSEN, P. S., AND HENRIKSEN, O. Cerebrospinal fluid flow and production in patients with normal pressure hydrocephalus studied by MRI. *Neuroradiology*, 36(3):210–5, April 1994. ISSN 0028-3940.

GILLAND, O., TOURTELLOTTE, W. W., O'TAUMA, L., AND HENDERSON, W. G. Normal cerebrospinal fluid pressure. *Journal of Neurosurgery*, 40(5):587–93, May 1974. ISSN 0022-3085.

GREITZ, D. The hydrodynamic hypothesis versus the bulk flow hypothesis. *Neurosurgical Review*, 27(4): 299–300, October 2004. ISSN 0344-5607.

GREITZ, D. Paradigm shift in hydrocephalus research in legacy of Dandy's pioneering work: rationale for third ventriculostomy in communicating hydrocephalus. *Child's Nervous System : ChNS : Official Journal of the International Society for Pediatric Neurosurgery*, 23(5):487–9, May 2007a. ISSN 0256-7040.

GREITZ, D. The bulk flow model cannot explain communicating hydrocephalus and must be replaced by a new concept. *Child's Nervous System*, 23(11): 1229–1231, September 2007b. ISSN 0256-7040.

GRINBERG, L., ANOR, T., MADSEN, J. R., YAKHOT, A., AND KARNIADAKIS, G. E. Large-scale simulation of the human arterial tree. *Clinical and Experimental Pharmacology & Physiology*, 36(2):194–205, February 2009a. ISSN 1440-1681.

GRINBERG, L., ANOR, T., CHEEVER, E., MADSEN, J. R., AND KARNIADAKIS, G. E. Simulation of the human intracranial arterial tree. *Philosophical Transactions. Series A, Mathematical, Physical, and Engineering Sciences*, 367(1896):2371–86, June 2009b. ISSN 1364-503X.

HACKETT, P. H., YARNELL, P. R., HILL, R., REYNARD, K., HEIT, J., AND MCCORMICK, J. High-altitude cerebral edema evaluated with magnetic resonance imaging: clinical correlation and pathophysiology. *JAMa : The Journal of the American Medical Association*, 280(22):1920–5, December 1998. ISSN 0098-7484.

HAKIM, S. Biomechanics of hydrocephalus. *Acta Neurológica Latinoamericana*, 1:Suppl 1:169–94, January 1971. ISSN 0001-6306.

HAKIM, S. AND ADAMS, R. D. The special clinical problem of symptomatic hydrocephalus with normal cerebrospinal fluid pressure. Observations on cerebrospinal fluid hydrodynamics. *Journal of the Neurological Sciences*, 2(4):307–27, 1965. ISSN 0022-510X.

HAKIM, S., VENEGAS, J. G., AND BURTON, J. D. The physics of the cranial cavity, hydrocephalus and normal pressure hydrocephalus: mechanical interpretation and mathematical model. *Surgical Neurology*, 5(3):187–210, March 1976. ISSN 0090-3019.

HAMLAT, A., ABDERRAHMANE, H., SID-AHMED, S., SEDDIK, S.-A., ADN, M., MAHMOUDREZA, A., ASKAR, B., BRAHIM, A., PASQUALINI, E., AND EDOUARDO, P. Idiopathic normal pressure hydrocephalus: theoretical concept of a spinal etiology. *Medical Hypotheses*, 67(1):110–4, 2006. ISSN 0306-9877.

HEBB, A. O. AND CUSIMANO, M. D. Idiopathic normal pressure hydrocephalus: a systematic review of

diagnosis and outcome. *Neurosurgery*, 49(5):1166–84; discussion 1184–6, November 2001. ISSN 0148-396X.

HOWDEN, L., GIDDINGS, D., POWER, H., AROUSSI, A., VLOEBERGHS, M., GARNETT, M., AND WALKER, D. Three-dimensional cerebrospinal fluid flow within the human ventricular system. *Computer Methods in Biomechanics and Biomedical Engineering*, 11(2):123–33, April 2008. ISSN 1025-5842.

JELLINGER, K. Neuropathological aspects of dementias resulting from abnormal blood and cerebrospinal fluid dynamics. *Acta Neurologica Belgica*, 76(2):83–102, 1976. ISSN 0300-9009.

JHA, S. Cerebral edema and its management. *MJAFI*, 59:326–331, 2003.

JOHANSON, C., MCMILLAN, P., TAVARES, R., SPANGENBERGER, A., DUNCAN, J., SILVERBERG, G., AND STOPA, E. Homeostatic capabilities of the choroid plexus epithelium in Alzheimer's disease. *Cerebrospinal Fluid Research*, 1(1):3, December 2004. ISSN 1743-8454.

KACZMAREK, M., SUBRAMANIAM, R. P., AND NEFF, S. R. The hydromechanics of hydrocephalus: steady-state solutions for cylindrical geometry. *Bulletin of Mathematical Biology*, 59(2):295–323, 1997. ISSN 0092-8240.

KIM, B.-S., JALLO, G. I., KOTHBAUER, K., AND ABBOTT, I. R. Chronic subdural hematoma as a complication of endoscopic third ventriculostomy. *Surgical Neurology*, 62(1):64–8; discussion 68, July 2004. ISSN 0090-3019.

KRUSE, S. A., ROSE, G. H., GLASER, K. J., MANDUCA, A., FELMLEE, J. P., JACK, C. R., AND EHMAN, R. L. Magnetic resonance elastography of the brain. *NeuroImage*, 39(1):231–7, January 2008. ISSN 1053-8119.

KURTCUOGLU, V. *Computational Modeling of the Cerebral Ventricular Cerebrospinal Fluid System*. Phd thesis, Swiss Federal Institute of Technology, Zurich, 2006.

KURTCUOGLU, V., POULIKAKOS, D., AND VENTIKOS, Y. Computational modeling of the mechanical behavior of the cerebrospinal fluid system. *Journal of Biomechanical Engineering*, 127(2):264–9, April 2005. ISSN 0148-0731.

LAURENCE, K. M. The Natural History of Hydrocephalus. *Postgraduate Medical Journal*, 36(421): 662–667, November 1960. ISSN 0032-5473.

LEE, J. H. M. *Numerical study of a viscoelastic model for hydrocephalus*. Phd thesis, University of Waterloo, Ontario, Canada, 2006.

LEVINE, D. N. The pathogenesis of normal pressure hydrocephalus: a theoretical analysis. *Bulletin of Mathematical Biology*, 61(5):875–916, September 1999. ISSN 0092-8240.

LEVINE, D. N. Ventricular size in pseudotumor cerebri and the theory of impaired CSF absorption. *Journal of the Neurological Sciences*, 177(2):85–94, August 2000. ISSN 0022-510X.

LEVINE, D. N. Intracranial pressure and ventricular expansion in hydrocephalus: have we been asking the wrong question? *Journal of the Neurological Sciences*, 269(1-2):1–11, June 2008. ISSN 0022-510X.

LIGGETT, J. A. AND LIU, P. L. F. The Boundary Integral Method for Porous Media Flow. *George Allen & Unwln, London*, 7, 1983.

LINNINGER, A. A., SWEETMAN, B., AND PENN, R. Normal and hydrocephalic brain dynamics: the role of reduced cerebrospinal fluid reabsorption in ventricular enlargement. *Annals of Biomedical Engineering*, 37(7):1434–47, July 2009. ISSN 1521-6047.

LINNINGER, A. A., TSAKIRIS, C., ZHU, D. C., XENOS, M., ROYCEWICZ, P., DANZIGER, Z., AND PENN, R. D. Pulsatile cerebrospinal fluid dynamics in the human brain. *IEEE Transactions on Bio-Medical Engineering*, 52(4):557–65, April 2005. ISSN 0018-9294.

LINNINGER, A. A., XENOS, M., ZHU, D. C., SOMAYAJI, M.-B. R., KONDAPALLI, S., AND PENN, R. D. Cerebrospinal fluid flow in the normal and hydrocephalic human brain. *IEEE Transactions on Bio-Medical Engineering*, 54(2):291–302, February 2007. ISSN 0018-9294.

LOTH, F., YARDIMCI, M. A., AND ALPERIN, N. Hydrodynamic modeling of cerebrospinal fluid motion within the spinal cavity. *Journal of Biomechanical Engineering*, 123(1):71–9, March 2001. ISSN 0148-0731.

LUARD, T. China's middle class revolution. `http://news.bbc.co.uk/2/hi/asia-pacific/3732914.stm`, 2004.

LUNDERVOLD, A., TAXT, T., ERSLAND, L., AND FENSTAD, A. M. Volume distribution of cerebrospinal fluid using multispectral MR imaging. *Medical Image Analysis*, 4(2):123–36, June 2000. ISSN 1361-8415.

MAAS, A. I. R., STOCCHETTI, N., AND BULLOCK, R. Moderate and severe traumatic brain injury in adults. *Lancet Neurology*, 7(8):728–41, August 2008. ISSN 1474-4422.

MADSEN, J. R., EGNOR, M., AND ZOU, R. Cerebrospinal fluid pulsatility and hydrocephalus: the fourth circulation. *Clinical Neurosurgery*, 53:48–52, January 2006. ISSN 0069-4827.

MALM, J. AND EKLUND, A. Idiopathic normal pressure hydrocephalus. *Practical Neurology*, 6(1):14–27, February 2006. ISSN 1474-7758.

MALM, J., KRISTENSEN, B., FAGERLUND, M., KOSKINEN, L. O., AND EKSTEDT, J. Cerebrospinal fluid shunt dynamics in patients with idiopathic adult hydrocephalus syndrome. *Journal of Neurology, Neurosurgery, and Psychiatry*, 58(6):715–23, June 1995. ISSN 0022-3050.

MAROULIS, H., HALMAGYI, G. M., HEARD, R., AND COOK, R. J. Sylvian aqueduct syndrome with slit ventricles in shunted hydrocephalus due to adult aqueduct stenosis. *Journal of Neurosurgery*, 109(5): 939–43, 2008. ISSN 0022-3085.

MCALLISTER, J. P. AND CHOVAN, P. Neonatal hydrocephalus. Mechanisms and consequences. *Neurosurgery Clinics of North America*, 9(1):73–93, January 1998. ISSN 1042-3680.

MCCOMB, J. G., BRADLEY, W. G., SAFAR, F. G., FURTADO, C., HURTADO, C., ORD, J., AND ALKSNE, J. F. Is a large hat size hazardous to your health? *AJNR. American Journal of Neuroradiology*, 25(9):1454–5; author reply 1455, October 2004. ISSN 0195-6108.

MILHORAT, T. H., CHOU, M. W., TRINIDAD, E. M., KULA, R. W., MANDELL, M., WOLPERT, C., AND SPEER, M. C. Chiari I malformation redefined: clinical and radiographic findings for 364 symptomatic patients. *Neurosurgery*, 44(5):1005–17, December 1999. ISSN 0148-396X.

MILLER, K., TAYLOR, Z., AND WITTEK, A. Mathematical models of brain deformation behaviour for computer-integrated neurosurgery. Technical Report February, University of Western Australia, Pert, Australia, 2006.

MITCHELL, S. A. AND VAVASIS, S. A. Quality mesh generation in three dimensions. In *SCG '92: Proceedings of the eighth annual symposium on Computational geometry*, pages 212–221, New York, NY, USA, 1992. ACM. ISBN 0-89791-517-8.

MONRO, A., CREECH, W., DONALDSON, T., CAMERON, G., ELMSLEY, P., FYFE, A., LONGMAN, T., AND MURRAY, J. *Observations on the structure and functions of the nervous system: Illustrated with tables*. printed for and sold by William Creech; and Joseph Johnson, London, 1783.

NAGASHIMA, T., TAMAKI, N., MATSUMOTO, S., HORWITZ, B., AND SEGUCHI, Y. Biomechanics of hydrocephalus: a new theoretical model. *Neurosurgery*, 21(6):898–904, December 1987. ISSN 0148-396X.

NIEDZWECKI, C. M., MARWITZ, J. H., KETCHUM, J. M., CIFU, D. X., DILLARD, C. M., AND MONASTERIO, E. A. Traumatic brain injury: a comparison of inpatient functional outcomes between children and adults. *The Journal of Head Trauma Rehabilitation*, 23(4):209–19, 2008. ISSN 1550-509X.

NINDS. Hydrocephalus Information Page. `http://www.ninds.nih.gov/disorders/hydrocephalus/detail_hydrocephalus.htm`, 2008.

NINDS. Chiari Malformation Fact Sheet. `http://www.ninds.nih.gov/disorders/chiari/detail_chiari.htm`, 2010a.

NINDS. Multi-Infarct Dementia Information Page. `http://www.ninds.nih.gov/disorders/multi_infarct_dementia/multi_infarct_dementia.htm`, 2010b.

OTAHAL, J., STEPANIK, Z., KACZMARSKA, A., MARSIK, F., BROZ, Z., AND OTAHAL, S. Simulation of cerebrospinal fluid transport. *Advances in Engineering Software*, 38(11-12):802–809, November 2007. ISSN 09659978.

OWLER, B. K. AND PICKARD, J. D. Normal pressure hydrocephalus and cerebral blood flow: a review. *Acta Neurologica Scandinavica*, 104(6):325–42, December 2001. ISSN 0001-6314.

PAPPENHEIMER, J. R. AND HEISEY, S. R. Exchange between cerebrospinal fluid and blood. *Biochemical Pharmacology*, 8(1):27 – 27, 1961. ISSN 0006-2952.

PATWARDHAN, R. V. AND NANDA, A. Implanted ventricular shunts in the United States: the billion-dollar-a-year cost of hydrocephalus treatment. *Neurosurgery*, 56(1):139–44; discussion 144–5, January 2005. ISSN 1524-4040.

PAYNE, S. J. A model of the interaction between autoregulation and neural activation in the brain. *Mathematical Biosciences*, 204(2):260–81, December 2006. ISSN 0025-5564.

PAYNE, S. J. AND TARASSENKO, L. Combined transfer function analysis and modelling of cerebral autoregulation. *Annals of Biomedical Engineering*, 34 (5):847–58, May 2006. ISSN 0090-6964.

PENN, R. D., LEE, M. C., LINNINGER, A. A., MIESEL, K., LU, S. N., AND STYLOS, L. Pressure gradients in the brain in an experimental model of hydrocephalus. *Journal of Neurosurgery*, 102(6):1069–1075, June 2005. ISSN 0022-3085.

PERSSON, E.-K., ANDERSON, S., WIKLUND, L.-M., AND UVEBRANT, P. Hydrocephalus in children born in 1999-2002: epidemiology, outcome and ophthalmological findings. *Child's Nervous System : ChNS : Official Journal of the International Society for Pediatric Neurosurgery*, 23(10):1111–8, October 2007. ISSN 0256-7040.

PETERS, R. Ageing and the brain. *Postgraduate Medical Journal*, 82(964):84–8, 2006. ISSN 1469-0756.

PINKSTON, J. B., ALEKSEEVA, N., AND GONZÁLEZ TOLEDO, E. Stroke and dementia. *Neurological Research*, 31(8):824–31, 2009. ISSN 0161-6412.

POPULATION DIVISION OF THE DEPARTMENT OF ECONOMIC AND SOCIAL AFFAIRS OF THE UNITED NATIONS. World Population Prospects: The 2006 Revision and World Urbanization Prospects: The 2005 Revision. `http://esa.un.org/unpp`, 2005.

QURESHI, A. I. AND SUAREZ, J. I. Use of hypertonic saline solutions in treatment of cerebral edema and intracranial hypertension. *Critical Care Medicine*, 28(9):3301–13, September 2000. ISSN 0090-3493.

RALEIGH, V. S. World population and health in transition. *BMJ (Clinical Research Ed.)*, 319(7215):981–4, October 1999. ISSN 0959-8138.

RANSOHOFF, J., SHULMAN, K., AND FISHMAN, R. A. Hydrocephalus: a review of etiology and treatment. *Journal of Pediatrics*, 56:399–411, March 1960. ISSN 0022-3476.

REHMAN, T., ALI, R., TAWIL, I., AND YONAS, H. Rapid progression of traumatic bifrontal contusions to transtentorial herniation: A case report. *Cases Journal*, 1(1):203, 2008. ISSN 1757-1626.

REKATE, H. L. Comments on the article by D. Greitz "Paradigm shift in hydrocephalus research in legacy of Dandy's pioneering work: rationale for third ventriculostomy in communicating hydrocephalus". *Child's Nervous System : ChNS : Official Journal of the International Society for Pediatric Neurosurgery*, 23(11):1227–8; author reply 1229–31, November 2007. ISSN 0256-7040.

REKATE, H. L. The definition and classification of hydrocephalus: a personal recommendation to stimulate debate. *Cerebrospinal Fluid Research*, 5:2, January 2008. ISSN 1743-8454.

RUBENSTEIN, E. Relationship of senescence of cerebrospinal fluid circulatory system to dementias of the aged. *Lancet*, 351(9098):283–5, January 1998. ISSN 0140-6736.

RUGE, J. AND STUBEN, K. Algebraic multigrid. *Multigrid Methods*, 3:73—-130, 1987.

SACK, I., BEIERBACH, B., HAMHABER, U., KLATT, D., AND BRAUN, J. Non-invasive measurement of brain viscoelasticity using magnetic resonance elastography. *NMR in Biomedicine*, 21(3):265–71, 2008. ISSN 0952-3480.

SADA, Y., MORIKI, T., KUWAHARA, S., YAMANE, T., AND HARA, H. Immunohistochemical study on blood-brain barrier in congenitally hydrocephalic HTX rat brain. *Zentralblatt Für Pathologie*, 140(4-5):289–98, November 1994. ISSN 0863-4106.

SATO, O. Consensus: nosographic identification. *Child's Nervous System : ChNS : Official Journal of the International Society for Pediatric Neurosurgery*, 10(3):167–71, April 1994. ISSN 0256-7040.

SEYFERT, S. AND FAULSTICH, A. Is the blood-CSF barrier altered in disease? *Acta Neurologica Scandinavica*, 108(4):252–6, October 2003. ISSN 0001-6314.

SEYFERT, S., BECHER, A., OHRING, R., AND FAULSTICH, A. The permeability of the blood-CSF barrier in hydrocephalus, polyradiculitis, and meningitis. *Journal of Neurology*, 251(3):355–6, March 2004. ISSN 0340-5354.

SILVERBERG, D. S. The effect of correction of anaemia in diabetics and non-diabetics with severe resistant congestive heart failure and chronic renal failure by subcutaneous erythropoietin and intravenous iron. *Nephrology Dialysis Transplantation*, 18(1): 141–146, January 2003. ISSN 14602385.

SILVERBERG, G. D., HEIT, G., HUHN, S., JAFFE, R. A., CHANG, S. D., BRONTE-STEWART, H., RUBENSTEIN, E., POSSIN, K., AND SAUL, T. A. The cerebrospinal fluid production rate is reduced in dementia of the Alzheimer's type. *Neurology*, 57(10):1763–6, November 2001. ISSN 0028-3878.

SILVERBERG, G., MAYO, M., SAUL, T., FELLMANN, J., AND MCGUIRE, D. Elevated cerebrospinal fluid pressure in patients with Alzheimer's disease. *Cerebrospinal Fluid Research*, 3:7, January 2006. ISSN 1743-8454.

SIVALOGANATHAN, S. Biomechanics of the brain: A theoretical and numerical study of Biot's equations of consolidation theory with deformation-dependent permeability. *International Journal of Non-Linear Mechanics*, 40(9):1149–1159, November 2005. ISSN 00207462.

SIVALOGANATHAN, S., STASTNA, M., TENTI, G., AND DRAKE, J. A viscoelastic approach to the modelling of hydrocephalus. *Applied Mathematics and Computation*, 163(3):1097–1107, April 2005. ISSN 00963003.

SMILLIE, A., SOBEY, I., AND MOLNAR, Z. A hydroelastic model of hydrocephalus. *Journal of Fluid Mechanics*, 539(-1):417, September 2005. ISSN 0022-1120.

SOBEY, I. AND WIRTH, B. Effect of non-linear permeability in a spherically symmetric model of hydrocephalus. *Mathematical Medicine and Biology : A Journal of the IMA*, 23(4):339–61, 2006. ISSN 1477-8599.

STARLING, E. H. On the Absorption of Fluids from the Connective Tissue Spaces. *The Journal of Physiology*, 19(4):312–26, May 1896. ISSN 0022-3751.

STEIN, S. C., BURNETT, M. G., AND SONNAD, S. S. Shunts in normal-pressure hydrocephalus: do we place too many or too few? *Journal of Neurosurgery*, 105(6):815–22, December 2006. ISSN 0022-3085.

STEPHENSEN, H., TISELL, M., AND WIKKELSÖ, C. There is no transmantle pressure gradient in communicating or noncommunicating hydrocephalus. *Neurosurgery*, 50(4):763–71; discussion 771–3, April 2002. ISSN 0148-396X.

STEYERBERG, E. W., MUSHKUDIANI, N., PEREL, P., BUTCHER, I., LU, J., MCHUGH, G. S., MURRAY, G. D., MARMAROU, A., ROBERTS, I., HABBEMA, J. D. F., AND MAAS, A. I. R. Predicting outcome after traumatic brain injury: development and international validation of prognostic scores based on admission characteristics. *PLoS Medicine*, 5(8):e165; discussion e165, 2008. ISSN 1549-1676.

STOQUART-ELSANKARI, S., BALÉDENT, O., GONDRY-JOUET, C., MAKKI, M., GODEFROY, O., AND MEYER, M.-E. Aging effects on cerebral blood and cerebrospinal fluid flows. *Journal of Cerebral Blood Flow and Metabolism : Official Journal of the International Society of Cerebral Blood Flow and Metabolism*, 27(9):1563–72, September 2007. ISSN 0271-678X.

STOQUART-ELSANKARI, S., LEHMANN, P., VILLETTE, A., CZOSNYKA, M., MEYER, M.-E., DERAMOND, H., AND BALÉDENT, O. A phase-contrast MRI study of physiologic cerebral venous flow. *Journal of Cerebral Blood Flow and Metabolism : Official Journal of the International Society of Cerebral Blood Flow and Metabolism*, 29(6):1208–15, June 2009. ISSN 1559-7016.

TAMAKOSHI, A., SASAKI, R., HAMAJIMA, N., AOKI, K., SUZUKI, S., YANAGAWA, H., KIKUCHI, H., AND WATANABE, K. A Nationwide Survey of Congenital Hydrocephalus in Japan âĂŤ Estimated Prevalence and Incidence. *The European Journal of Public Health*, 1(2):86–89, 1991. ISSN 1101-1262.

TANCK, E., VAN DRIEL, W. D., HAGEN, J. W., BURGER, E. H., BLANKEVOORT, L., AND HUISKES, R. Why does intermittent hydrostatic pressure enhance the mineralization process in fetal cartilage? *Journal of Biomechanics*, 32(2):153 – 161, 1999. ISSN 0021-9290.

TERZAGHI, K. *Theoretical Soil Mechanics*. John Wiley and Sons, New York, 1943.

TISELL, M., TULLBERG, M., MÅ NSSON, J.-E., FREDMAN, P., BLENNOW, K., AND WIKKELSØ, C. Differences in cerebrospinal fluid dynamics do not affect the levels of biochemical markers in ventricular CSF from patients with aqueductal stenosis and idiopathic normal pressure hydrocephalus. *European Journal of Neurology : The Official Journal of the European Federation of Neurological Societies*, 11(1):17–23, January 2004. ISSN 1351-5101.

TULI, S., ALSHAIL, E., AND DRAKE, J. Third Ventriculostomy versus Cerebrospinal Fluid Shunt as a First Procedure in Pediatric Hydrocephalus. *Pediatric Neurosurgery*, 30(1):11–15, 1999. ISSN 1423-0305.

TULLY, B. AND VENTIKOS, Y. Cerebral water transport using multiple-network poroelastic theory: Application to normal pressure hydrocephalus. *Journal of Fluid Mechanics*, In press, 2010a.

TULLY, B. AND VENTIKOS, Y. Investigating patient-specific normal pressure hydrocephalus using multiple-network poroelastic theory. *Nature Neuroscience*, Review, 2010b.

TULLY, B. AND VENTIKOS, Y. Coupling poroelasticity and CFD for cerebrospinal fluid hydrodynamics. *IEEE Transactions on Bio-Medical Engineering*, 56(6):1644–51, June 2009. ISSN 1558-2531.

URBACH, H., TSCHAMPA, H., FLACKE, S., AND THAL, D. MRI of Vascular Dementia and Differential Diagnoses. *Clinical Neuroradiology*, 17(2):88–97, June 2007. ISSN 0939-7116.

URSINO, M. AND DI GIAMMARCO, P. A mathematical model of the relationship between cerebral blood volume and intracranial pressure changes: the generation of plateau waves. *Annals of Biomedical Engineering*, 19(1):15–42, January 1991. ISSN 0090-6964.

URSINO, M. AND LODI, C. A. A simple mathematical model of the interaction between intracranial pressure and cerebral hemodynamics. *Journal of Applied Physiology (Bethesda, Md. : 1985)*, 82(4):1256–69, April 1997. ISSN 8750-7587.

VAN DOORMAAL, J. AND RAITHBY, G. Enhancements of the SIMPLE Method for Predicting Incompressible Fluid Flows. *Hear Transfer*, 7:147–163, 1984.

WANG, H. *Theory of Linear Poroelasticity with Applications to Geomechanics and Hydrogeology*. Princeton University Press, 2000.

WILLIAMS, A. J. Can a free access structure-centric community for chemists benefit drug discovery? In *ACS Meeting Philadelphia*, volume 236, 2008. ISBN 0065-7727.

WILSON, C. B. AND BERTAN, V. Interruption of the anterior choroidal artery in experimental hydrocephalus. *Archives of Neurology*, 17(6):614–9, December 1967. ISSN 0003-9942.

WILSON, D. AND PURUSHOTHAMAN, R. Dreaming with BRICs: the path to 2050. `www2.goldmansachs.com/ideas/brics/book/99-dreaming.pdf`, 2003.

WILSON, R. AND AIFANTIS, E. C. On the theory of consolidation with double porosity. *International Journal of Engineering Science*, 20(9):1009–1035, 1982. ISSN 00207225.

WINKLER, F., GSCHWENDTNER, A., THEISEN, D., PERAUD, A., AND STRAUBE, A. Reversible dementia and corresponding CSF alterations due to intraspinal lumbosacral metastasis of a prostate carcinoma. *European Journal of Neurology : The Official Journal of the European Federation of Neurological Societies*, 14(12):1400–2, December 2007. ISSN 1468-1331.

WIRTH, B. AND SOBEY, I. An axisymmetric and fully 3D poroelastic model for the evolution of hydrocephalus. *Mathematical Medicine and Biology : A Journal of the IMA*, 23(4):363–88, December 2006. ISSN 1477-8599.

WIRTH, B. AND SOBEY, I. Analytic solution during an infusion test of the linear unsteady poroelastic equations in a spherically symmetric model of the brain. *Mathematical Medicine and Biology : A Journal of the IMA*, 26(1):25–61, March 2009. ISSN 1477-8602.

WOODWORTH, G. F., MCGIRT, M. J., WILLIAMS, M. A., AND RIGAMONTI, D. Cerebrospinal fluid drainage and dynamics in the diagnosis of normal pressure hydrocephalus. *Neurosurgery*, 64(5):919–25; discussion 925–6, 2009. ISSN 1524-4040.

WOOLLAM, D. H. M. AND MILLEN, J. W. Anatomical considerations in the pathology of stenosis of the cerebral aqueduct. *Brain*, 76(1):104–12, March 1953. ISSN 0006-8950.

WORLD HEALTH ORGANIZATION. The World Health Report 1999: Making a Difference, 1999.

WOSTYN, P. Can chronic increased intracranial pressure or exposure to repetitive intermittent intracranial pressure elevations raise your risk for Alzheimer's disease? *Medical Hypotheses*, 62(6): 925–30, January 2004. ISSN 0306-9877.

WU, Y., GREEN, N., WRENSCH, M., ZHAO, S., AND GUPTA, N. Ventriculoperitoneal shunt complications in California: 1990 to 2000. *Neurosurgery*, 61 (3):557, 2007.

YANG, J. The myogenic response in isolated rat cerebrovascular arteries: smooth muscle cell model. *Medical Engineering & Physics*, 25(8):691–709, October 2003. ISSN 13504533.

ZHANG, J., WILLIAMS, M. A., AND RIGAMONTI, D. Genetics of human hydrocephalus. *Journal of Neurology*, 253(10):1255–66, October 2006. ISSN 0340-5354.

ZIENKIEWICZ, O. C. Basic formulation of static and dynamic behaviours of soil and other porous media. *Applied Mathematics and Mechanics*, 3(4):457–468, August 1982. ISSN 0253-4827.

ZIENKIEWICZ, O. C. AND BETTESS, P. Soils and other saturated media under transient dynamic conditions: General formulation and the validity of various simplifying assumptions. *Soil Mechanics-Transient and Cyclic Loads*, pages 1–16, 1982.

ZIENKIEWICZ, O. C., CHAN, A. H. C., PASTOR, M., PAUL, D. K., AND SHIOMI, T. Static and Dynamic Behaviour of Soils: A Rational Approach to Quantitative Solutions. I. Fully Saturated Problems. *Proceedings of the Royal Society of London. Series A, Mathematical and Physical Sciences (1934-1990)*, 429(1877):285–309, June 1990. ISSN 0080-4630.

ZIENKIEWICZ, O. C. AND SHIOMI, T. Dynamic behaviour of saturated porous media; The generalized Biot formulation and its numerical solution. *International Journal for Numerical and Analytical Methods in Geomechanics*, 8(1):71–96, January 1984. ISSN 0363-9061.

APPENDIX A

COMPUTATIONAL FLUID DYNAMICS

In the 1D-3D simulations, CFD is used to interrogate the flow of fluid through the cerebral aqueduct. In this work, **CFD-ACE+** is chosen as the commercial solver, however the maturity of CFD as a technology means that the results are not expected to be dependent on the choice of software.

This research extends the state-of-the-art by replacing the analytic representations to axi-symmetric, three-dimensional and patient-specific volumes. In order to do so, the poroelastic solver will be coupled to the multi-physics software **CFD-ACE+** (ESI Group, Paris, France) (cf. §4.2).

Like most solvers of its type, **CFD-ACE+** is based on the numerical solution of the equilibrium states of matter. According to Newtonian mechanics, this movement towards equilibrium is achieved through the transport of mass, energy, and momentum. An exploitable commonality in the transport phenomenon is their requirement to satisfy the conservation law for a control volume,

$$\frac{\partial \phi}{\partial t} + \nabla \cdot f\left(t, \mathrm{x}, \phi, \nabla\phi\right) = g\left(t, \mathrm{x}, \phi\right), \tag{A.1}$$

where ϕ is any conservable quantity, f represents the flux through the control volume and g is any sink or source term.

As with any complex physical system, there is a limit to the usefulness of a continuous approach and the burgeoning availability of computing power means that

discrete solutions are increasingly accurate. The computational approach for spatial and temporal physical systems is generally defined by four distinct steps:

(a) a system of (usually) partial differential equations (PDE) is discretized to an algebraic representation whose unknowns correspond to the values of each variable at a specified location in space and time.

(b) the spatial domain is discretized into individually distinct smaller volumes (each a control volume in its own right); this pre-processing step is typically referred to as mesh or grid generation.

(c) the algebraic representation is mapped to the discrete grid and solved numerically with respect to a series of initial and boundary conditions.

(d) the numerical solution is interpreted through data manipulation, visualization and processing; this step is generally referred to as post-processing.

The remainder of this chapter will outline the numerical techniques used to discretize the governing equations and numerically solve the flow of CSF through the ventricular channels. More details on the grid generation are provided in §4.2 and the general visualization of results will involve a simple combination of pressure maps and streamlines (cf. Figure 5.19).

A.0.1 Discretization of the Governing Equations

In this study, we are concerned with the numerical solution of CSF transport through the ventricular system. This low-speed, incompressible system can be suitably solved using a pressure based method, such as that provided by **CFD-ACE+**, and explained in more detail here.

A.0.1.1 Naviér-Stokes Equations

The governing equations of fluid flow are mathematical representations of the physics of the fluid based around Equation (A.1), stating that:

(a) The mass of the fluid is conserved such that there is no loss or gain in the system; and,

(b) The time rate of change of the fluid momentum equals the sum of the forces on the fluid (Newton's Second Law).

The former provides the conservation of mass equation,

$$\frac{\partial \rho}{\partial t} + \nabla \cdot (\rho \mathrm{v}) = 0, \tag{A.2}$$

where ρ is the density of the fluid and v is the velocity vector. The latter gives the well known Naviér-Stokes equations,

$$\rho \left(\frac{\partial \mathrm{v}}{\partial t} + \mathrm{v} \cdot \nabla \mathrm{v} \right) = -\nabla p + \nabla \boldsymbol{\sigma} + \mathrm{f}, \tag{A.3}$$

where p is the pressure of the fluid, $\boldsymbol{\sigma}$ is the deviatoric stress tensor and f represents the body forces per unit volume.

A.0.1.2 Finite Volume Method

Until recently, numerical analysis was dominated by three primary methods for the solution of the mathematical system:

(a) Finite differences (as explained in §4.1.1.2);

(b) Finite volume method (FVM); and,

(c) Finite element method (FEM).

For anything but the most simple geometry, finite differences is a cumbersome methodology and thus rarely used in generic flow solvers.

The remaining two methods, FEM and FVM, each have advantages and disadvantages. FEM is designed around node-based operations where system properties are approximated within the computational cell through basis functions of varying degrees of order. It is most often used for displacement-based computations (such as structural analysis); however, for complex domains, such as those found regularly in CFD, FEM requires substantial computational overhead in comparison to FVM.

The FVM is cell averaging and contains only one node per cell (at the centre, P in Figure A.1). It is typically less accurate than FEM due to the inherent smoothing, yet, this provides a conservative approach with far less computation expense and

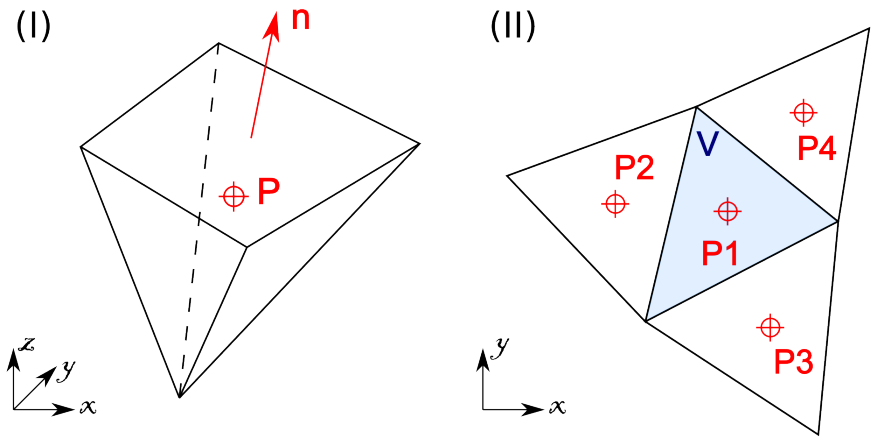

Figure A.1: **(I)** A finite volume for use with the FVM. The cell centre is designated by P and each cell surface has a normal vector $\hat{n}$. **(II)** The inter-connectedness of adjacent finite volumes (in this case a two-dimensional mesh); dependant variables and material properties averaged over the cell volume and stored at the cell centre for interpolation.

thus it is the preferred method for velocity-based computations (such as CFD). FVM makes use of Green's theorem to convert volume integrals containing a divergence term into surface integrals. These terms are subsequently evaluated as fluxes at the surface of each cell in the computational domain.

Within **CFD-ACE+**, the numerical solvers use a co-located cell-centre variable arrangement (ESI, 2009). Practically, this means that all dependant variables and material properties are stored at the cell centre, P; thus, the average value of any quantity in the control volume is given by value at the cell centre.

A.0.2 Numerical Solution of the Discretized system

The general transport equation (A.1) can be expanded and integrated over a control volume, Ω, such that,

$$\underbrace{\int_\Omega \frac{\partial \rho\phi}{\partial t} d\Omega}_{\text{transient}} + \underbrace{\int_\Omega \nabla\cdot(\rho \mathbf{v}\phi) d\Omega}_{\text{convection}} = \underbrace{\int_\Omega \nabla\cdot(\tau\nabla\phi) d\Omega}_{\text{diffusion}} + \underbrace{\int_\Omega g d\Omega}_{\text{sink/source}} . \tag{A.4}$$

A.0.2.1 The Transient Term

The transient term of Equation (A.4) is integrated using the first order Euler method,

$$\int_\Omega \frac{\partial \rho\phi}{\partial t} \mathrm{d}\Omega = \frac{\rho^k \phi^k V^k - \rho^{k-1}\phi^{k-1}V^{k-1}}{\Delta t}, \tag{A.5}$$

where k denotes the current time and $k-1$ is the previous time, and Δt is the time step. The control (cell) volume, V, may be time dependent and the second order Crank-Nicholson is available if an increased accuracy desired.

A.0.2.2 The Convection Term

The convection term is a volume integral of a divergence term, so according to Green's theorem,

$$\int_\Omega \nabla\cdot\left(\rho \mathrm{v}\phi\right)\mathrm{d}\Omega = \oint_{\partial\Omega} \rho\phi \mathrm{v}\cdot\hat{\mathrm{n}}\mathrm{dS}, \tag{A.6}$$

$$= \sum_e \left(\rho_e \phi_e v_e^n\right) A_e, \tag{A.7}$$

$$= \sum_e C_e A_e, \tag{A.8}$$

where the subscript e denotes the face of the current computational cell, A_e is the area of the face and v_e^n is the velocity normal to the face. Thus, C_e can be described as the flux through the face and its evaluation is dealt with in the discussion about pressure-volume coupling below. ϕ_e can be evaluated through a variety of interpolation methods that provide varying levels of numerical stability and accuracy.

The simplest interpolation method is that of the first-order upwind scheme. It is numerically very stable, but as the name suggests, is only first-order in accuracy. In this scheme, ϕ_e is taken to be the value of ϕ at the upstream grid point. It is provided for by cell $P1$ or $P2$ depending on the direction of flow, where cells $P1$ and $P2$ are the two cells adjacent to face e (see Figure A.1-(II)). This is represented mathematically by,

$$\phi_e^{\mathrm{UP}} = \begin{cases} \phi_{P1} \text{ if } v_e^n > 0 \\ \phi_{P2} \text{ if } v_e^n < 0 \end{cases}. \tag{A.9}$$

However, to improve the accuracy of the solver, the conventional second-order central differences scheme is applied. In this scheme, ϕ_e is found by computing a

linear weighted average of ϕ in the two cells adjacent to the face:

$$\phi_e^{\mathrm{CD}} = \gamma_e \phi_{P1} + (1-\gamma_e)\phi_{P2}, \tag{A.10}$$

where γ_e is the geometric weighting function at face e.

A well known drawback to the second-order central differences scheme, as it is presented here, is the potential introduction instabilities in the numerical solution. Furthermore, this scheme also tends to cause instabilities when used to solve the convective terms during iterative methods. Thus, **CFD-ACE+** introduces damping to the numerical scheme by blending the central differences, ϕ_e^{CD}, and upwind, ϕ_e^{UP}, schemes:

$$\phi_e = \alpha \phi_e^{\mathrm{UP}} + (1-\alpha)\phi_e^{\mathrm{CD}}, \tag{A.11}$$

where α is the blending coefficient; if $\alpha = 0$ the full central differences scheme is recovered, while $\alpha = 1$ yields the full upwind scheme.

In this work, the central differences method is employed using various blending coefficients; for stability a value of 0.3 was selected most often (as noted in §4.2.1.2).

A.0.2.2.1 Pressure-Volume Coupling Solution of the vectorial momentum equation yields the velocity field of the system. However, there is no direct specification for the pressure field in the remaining mass conservation PDE – despite its position as an important flow variable.

Many numerical techniques have been provided, however, **CFD-ACE+** makes use of the most well known algorithm the Semi-Implicit Method for Pressure-Linked Equations – Consistent (SIMPLEC) (Van Doormaal and Raithby, 1984; ESI, 2009). SIMPLEC is an extension of the original SIMPLE algorithm and is derived from the finite difference form of the momentum equation,

$$\mathrm{B}_{P1}\mathrm{v}_{P1} = \left(\sum_i \mathrm{B}_i \mathrm{v}_i + S_U\right)_{P1} - \left(\sum_e p_e A_e \hat{\mathrm{n}}_e\right)_{P1}, \tag{A.12}$$

for cell $P1$, where B is the link coefficient and S_U is the linearized source term; subscripts e and i denote each face of the cell and each adjoining cell, respectively.

SIMPLEC is an iterative solver, and as such an initial guess is required for the pressure field so that Equation (A.12) can be solved for the velocity field. If this

pressure is labelled p^*, the equation will yield the velocity field v^* that satisfies,

$$\mathrm{B}_{P1}\mathrm{v}^*_{P1} = \left(\sum_i \mathrm{B}_i \mathrm{v}^*_i + S_U\right)_{P1} - \left(\sum_e p^*_e A_e \hat{\mathrm{n}}_e\right)_{P1}, \tag{A.13}$$

yet is unlikely to satisfy continuity, so for an improved solution we can find corrections, v' and p',

$$\mathrm{v} = \mathrm{v}^* + \mathrm{v}', \tag{A.14a}$$

$$p = p^* + p'. \tag{A.14b}$$

for which an expression can be obtained by subtracting Equation (A.13) from Equation (A.12), and assuming v'_i can be approximated by v'_{P1}:

$$\mathrm{B}_{P1}\mathrm{v}'_{P1} = \frac{-1}{\mathrm{B}_{P1} - \sum_i \mathrm{B}_i}\left(\sum_e p'_e A_e \hat{\mathrm{n}}_e\right)_{P1}, \tag{A.15}$$

and that the velocity correction at the face, v'_e, is obtained by averaging the cell-centre values from adjacent cells ($P1$ and Pe),

$$\mathrm{v}'_e = \gamma_e \mathrm{v}'_{P1} + (1-\gamma_e)\mathrm{v}'_{Pe}. \tag{A.16}$$

If we now turn to the conservation of mass equation (A.2) and integrate over the cell volume,

$$\frac{\rho^k V^k - \rho^{k-1} V^{l-1}}{\Delta t} + \sum_e \rho_e \upsilon^n_e A_e = \dot{m} V^k, \tag{A.17a}$$

$$\frac{\rho^k V^k - \rho^{k-1} V^{l-1}}{\Delta t} + \sum_e C_e = \dot{m} V^k, \tag{A.17b}$$

then, if v^* and p^* are used to calculate C_e, the resulting C^*_e will not satisfy (A.17b) and again a corrective term is introduced,

$$C_e = C^*_e + C'_e. \tag{A.18}$$

The integrated mass conservation equation (A.17a) can be recast in terms of the corrective mass flux,

$$\frac{\rho'_{P1} V^k}{\Delta t} + \sum_e C'_e = S_m, \tag{A.19}$$

where $S_m = \frac{\rho^{k-1}_{P1} V^{k-1} - \rho^*_{P1} V^k}{\Delta t} + \dot{m} V^k - \sum_e C^*_e$ is the mass correction in the control volume.

With the face-normal velocity correction and the density correction expressed in terms of the pressure correction, substitutions can be made in Equation (A.19) and the pressure correction can be obtained from,

$$\mathrm{B}_{P1} p'_{P1} = \sum_i \mathrm{B}_i p'_i + S_m. \tag{A.20}$$

The SIMPLEC algorithm can be summarized by:

1. Guess an initial pressure field, p^*;
2. Obtain the velocity field, v^*, from Equation (A.13);
3. Evaluate C^* from ρ^* and v^*;
4. Evaluate the mass source, S_m;
5. Obtain the pressure correction from Equation (A.20);
6. Correct the pressure and velocity fields using Equation (A.14);
7. Solve for any other flow variables; and,
8. Iterate from Step 2 until the desired level of convergence is achieved.

A.0.2.3 The Diffusion and Source Terms

Once again, Green's theorem is applied to the volume integral of the diffusion term,

$$\int_\Omega \nabla \cdot \left(\tau \nabla \phi\right) \mathrm{d}\Omega = \oint_{\partial\Omega} \tau \nabla \phi \cdot \hat{\mathrm{n}} \mathrm{dS}, \tag{A.21}$$

$$= \sum_e \tau_e \left(\frac{\partial \phi}{\partial n}\right)_e A_e. \tag{A.22}$$

While the source term is linearized,

$$\int_\Omega S_\phi \mathrm{d}\Omega = \int_\Omega \left(S^U + S^P \phi\right) \mathrm{d}\Omega. \tag{A.23}$$

A.0.2.4 Solving the Algebraic System

With the discretization template established, the governing equations are ready to be solved. Generally, iterative solvers are computationally efficient compared with direct solvers and for this reason they are generally preferred. The two iterative solvers implemented within the **CFD-ACE+** platform are the Conjugate Gradient Squared (CGS) solver and the Algebraic Multigrid (AMG) solver (Ruge and Stuben, 1987).

The conjugate gradient methodology seeks to minimize the function,

$$f(\boldsymbol{\phi}) = \frac{1}{2}\boldsymbol{\phi}^T[\mathrm{B}]\boldsymbol{\phi} - \boldsymbol{\phi}^T\mathrm{S}, \tag{A.24}$$

where the gradient of the function is $\mathrm{B}\boldsymbol{\phi}-\mathrm{S}$ such that the minimum value returns the solution of the linear system. Theoretically, the method requires exactly N iterations (for an $N \times N$ system), however the system must symmetric and positive definite. In order to expand the applications of the conjugate gradient method, several generalizations have been made; one popular example is the bi-conjugate gradient method with its significant drawback being the necessary transpose of the system matrix.

The CGS scheme was developed without the need for this transpose to be constructed, however, AMG offers two significant advantages over the CGS solver in that:

(a) increase in solver time is dependent only on the number of unknowns in the equations; and,

(b) a faster convergence, particularly with unstructured meshes.

The basic idea of a multi-grid solution is to use a hierarchy of grids, from fine to coarse, to solve a set of equations, with each grid being particularly effective for removing errors of wavelength characteristic of the mesh spacing on that grid (ESI, 2009).

APPENDIX B

MATHEMATICAL TRANSFORMATIONS

A series of transformations useful in the derivation of the MPET system.

B.1 NABLA IN SPHERICAL COORDINATES

The standard transformations of ∇ in spherical coordinates,

$$\nabla = \frac{\partial}{\partial r}\hat{\mathrm{r}} + \frac{1}{r\sin\phi}\frac{\partial}{\partial\theta}\hat{\boldsymbol{\theta}} + \frac{1}{r}\frac{\partial}{\partial\phi}\hat{\boldsymbol{\phi}} \tag{B.1a}$$

$$\nabla\cdot\mathrm{u} = \frac{\partial u_r}{\partial r} + \frac{2}{r}u_r + \frac{1}{r\sin\phi}\frac{\partial u_\theta}{\partial\theta} + \frac{1}{r}\frac{\partial u_\phi}{\partial\phi} + \frac{\cot\phi}{r}u_\phi \tag{B.1b}$$

$$\nabla^2 = \frac{\partial^2}{\partial r^2} + \frac{2}{r}\frac{\partial}{\partial r} + \frac{1}{r^2\sin^2\phi}\frac{\partial^2}{\partial\theta^2} + \frac{\cos\phi}{r^2\sin^2\phi}\frac{\partial}{\partial\phi} + \frac{1}{r^2}\frac{\partial^2}{\partial\phi^2} \tag{B.1c}$$

$$\nabla^2\mathrm{u} = \begin{bmatrix} \frac{1}{r}\frac{\partial^2(ru_r)}{\partial r^2} + \frac{1}{r^2}\frac{\partial^2 u_r}{\partial\theta^2} + \frac{1}{r^2\sin^2\theta}\frac{\partial^2 u_r}{\partial\phi^2} + \frac{\cot\theta}{r^2}\frac{\partial u_r}{\partial\theta} - \frac{2}{r^2}\frac{\partial u_\theta}{\partial\theta} - \frac{2}{r^2\sin^2\theta}\frac{\partial u_\phi}{\partial\phi} - \frac{2}{r}u_r - \frac{\cot\theta}{r^2}u_\theta \\ \frac{1}{r}\frac{\partial^2(ru_\theta)}{\partial r^2} + \frac{1}{r^2}\frac{\partial^2 u_\theta}{\partial\theta^2} + \frac{1}{r^2\sin^2\theta}\frac{\partial^2 u_\theta}{\partial\phi^2} + \frac{\cot\theta}{r^2}\frac{\partial u_\theta}{\partial\theta} - \frac{2}{r^2}\frac{\cot\theta}{\sin\theta}\frac{\partial u_\phi}{\partial\phi} + \frac{2}{r^2}\frac{\partial u_r}{\partial r} - \frac{u_\theta}{r^2\sin^2\theta} \\ \frac{1}{r}\frac{\partial^2(ru_\phi)}{\partial r^2} + \frac{1}{r^2}\frac{\partial^2 u_\phi}{\partial\theta^2} + \frac{1}{r^2\sin^2\theta}\frac{\partial^2 u_\phi}{\partial\phi^2} + \frac{\cot\theta}{r^2}\frac{\partial u_\phi}{\partial\theta} + \frac{2}{r^2\sin\theta}\frac{\partial u_r}{\partial\phi} + \frac{2\cot\theta}{r^2\sin\theta}\frac{\partial u_\theta}{\partial\phi} - \frac{u_\phi}{r^2\sin^2\theta} \end{bmatrix}, \tag{B.1d}$$

In the context of the brain and system described in this research, the parameters can be modelled such that: $\mathrm{x} = [r,\theta,\phi]$; $\mathrm{u} = [u(r),0,0]$; $\mathrm{b} = [b_r(r),0,0]$; $p^a = p^a(r)$.

Making the substitutions with (B.1), then the following are useful:

$$\nabla^2 \mathrm{u} = \begin{bmatrix} \frac{1}{r}\frac{\partial^2(ru)}{\partial r^2} - \frac{2}{r^2}u \\ 0 \\ 0 \end{bmatrix} \qquad \frac{\partial^2(ru)}{\partial r^2} = r\frac{\partial^2 u}{\partial r^2} + 2\frac{\partial u}{\partial r}$$

$$\nabla \cdot \mathrm{u} = \frac{\partial u}{\partial r} + \frac{2}{r}u \qquad \nabla(\nabla \cdot \mathrm{u}) = \begin{bmatrix} \frac{\partial^2 u}{\partial r^2} + \frac{2}{r}\frac{\partial u}{\partial r} - \frac{2}{r^2}u \\ 0 \\ 0 \end{bmatrix}. \tag{B.2}$$

$$\nabla^2 p = \frac{\partial^2 p}{\partial r^2} + \frac{2}{r}\frac{\partial p}{\partial r} \qquad \nabla \cdot \mathrm{b} = \frac{\partial b}{\partial r} + \frac{2}{r}f$$

B.2 LINEAR STRESS-STRAIN EQUATION

B.2.1 Inverted for Stress

The generalized Hooke's law equation:

$$\epsilon_{ij} = \frac{1}{2G}\left(\sigma'_{ij} - \frac{\nu}{1+\nu}\delta_{ij}\sigma'_{kk}\right), \tag{B.3}$$

can be inverted for stress,

$$\epsilon_{kk} = \frac{1}{2G}\left[\sigma'_{kk} - \frac{\nu}{1+\nu}\delta_{kk}\sigma'_{kk}\right], \tag{B.4}$$

$$= \frac{1}{2G}\left[\sigma'_{kk} - \frac{3\nu}{1+\nu}\sigma'_{kk}\right], \tag{B.5}$$

$$= \frac{1-2\nu}{2G(1+\nu)}\sigma'_{kk}, \tag{B.6}$$

$$\sigma'_{kk} = \frac{2G(1+\nu)}{1-2\nu}\epsilon_{kk}. \tag{B.7}$$

$$\epsilon_{ij} = \frac{1}{2G}\left[\sigma'_{ij} - \frac{2G\nu}{1-2\nu}\delta_{ij}\epsilon_{kk}\right], \tag{B.8}$$

$$\sigma'_{ij} = 2G\left[\epsilon_{ij} + \frac{\nu}{1-2\nu}\delta_{ij}\epsilon_{kk}\right], \tag{B.9}$$

$$\boldsymbol{\sigma}' = 2G\left[\boldsymbol{\epsilon} + \frac{\nu}{1-2\nu}\mathrm{Tr}(\boldsymbol{\epsilon})\mathrm{I}\right]. \tag{B.10}$$

B.2.2 Stress as a Function of Displacement

Putting the linear stress-strain equation, (3.18), in terms of displacement and calculating its divergence is best done through the use of Einstein notation,

$$\boldsymbol{\sigma}' = 2G\left[\boldsymbol{\epsilon} + \frac{\nu}{1-2\nu}\mathrm{Tr}(\boldsymbol{\epsilon})\mathrm{I}\right], \tag{B.11}$$

$$\sigma'_{ij} = 2G\left[\epsilon_{ij} + \frac{\nu\varepsilon}{1-2\nu}\delta_{ij}\right], \tag{B.12}$$

$$= 2G\left[\frac{1}{2}(u_{i,j} + u_{j,i}) + \frac{\nu u_{k,k}}{1-2\nu}\delta_{ij}\right], \tag{B.13}$$

$$= Gu_{i,j} + Gu_{j,i} + \frac{2G\nu}{1-2\nu}u_{k,k}\delta_{ij}. \tag{B.14}$$

$$\sigma'_{ij,j} = Gu_{i,jj} + Gu_{j,ji} + \frac{2G\nu}{1-2\nu}u_{k,ki}, \tag{B.15}$$

$$= Gu_{i,jj} + \left(G + \frac{2G\nu}{1-2\nu}\right)u_{k,ki}, \tag{B.16}$$

$$= Gu_{i,jj} + \frac{G}{1-2\nu}u_{k,ki}, \tag{B.17}$$

$$\nabla\cdot\boldsymbol{\sigma}' = G\nabla^2\mathrm{u} + \frac{G}{1-2\nu}\nabla(\nabla\cdot\mathrm{u}). \tag{B.18}$$

APPENDIX C

OTHER USEFUL IMAGES

Various images did not appear in the final text as they interrupted the flow, they are included here for reference.

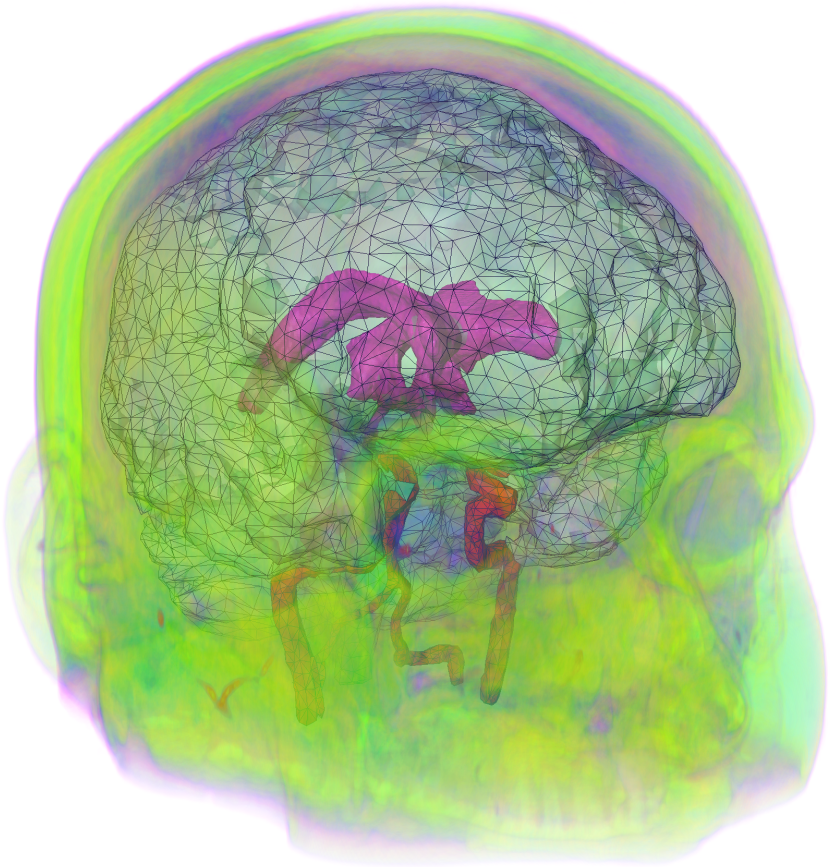

Figure C.1: Segmented brain geometry garnered from patient-specific MR imaging. The lime green area shows features such as the skull, skin and bone; the parenchyma is meshed with large triangles with an emerald green shading; the cerebral ventricles (where CSF is produced) are shaded in magenta; and the important cerebral blood vessels are segmented and shaded in red.

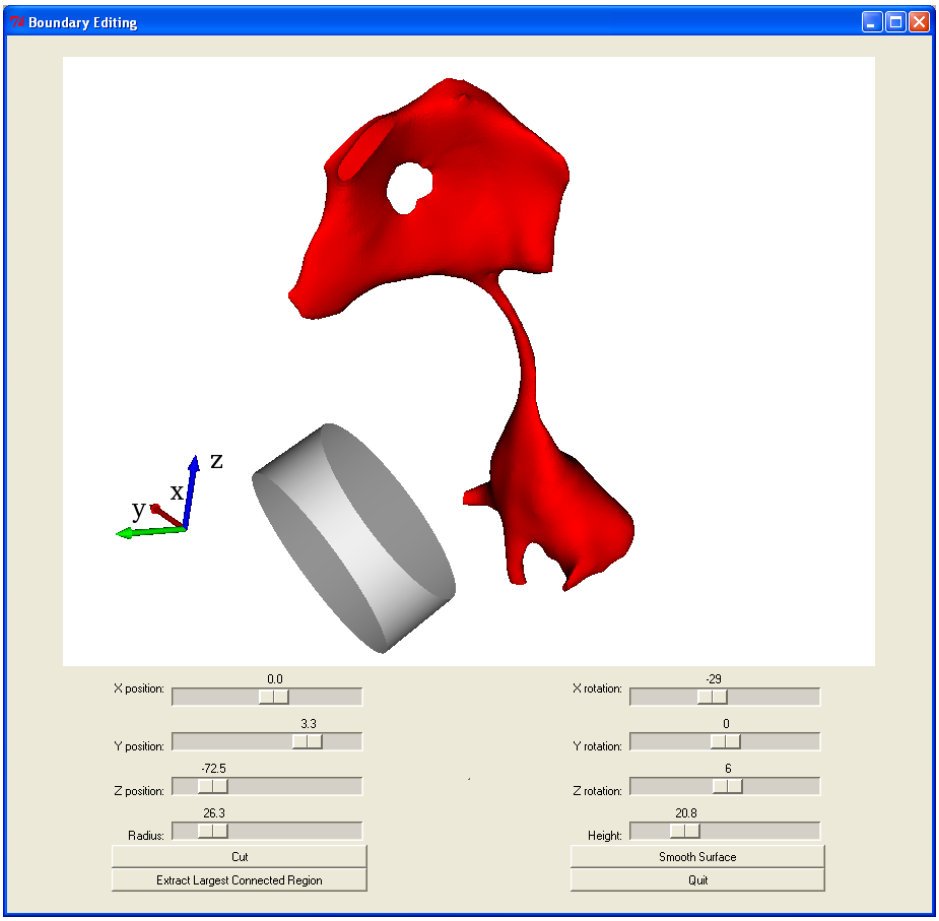

Figure C.2: The final stage of preparation of the STL surface is conducted using a `perl` script, `tcut`, that utilizes the intersection of geometric `vtk` objects with the surface to make smooth cuts for the inlet and outlet surfaces.

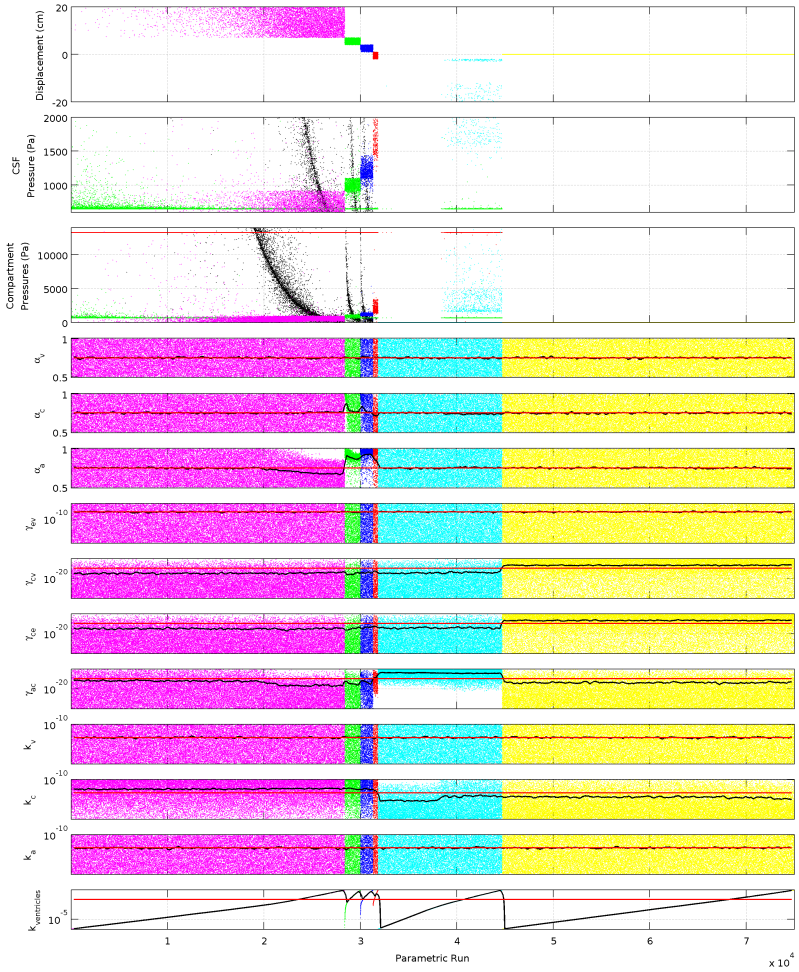

Figure C.3: A parametric investigation of the MPET model with ten unknown material properties, and a random distribution of the choroid plexus permeability. We can select an appropriate value for the permeability of the choroid plexus using the same techniques described in §5.1.1.2.2. Each of the ten material properties is assigned a random value from the respective range in Table 5.1 while the permeability is assigned a log-normal, random number in the range $\kappa_{c\rightarrow\text{ventricle}} \in [1.0\times10^{-6}, 1.0\times10^{-2}]$ m^{5}skg^{-1}. It is seen that the permeability had little effect on the ventricular displacement, but a large influence on the pressure of the arteriole/capillary network. Consequently, this plot shows the results arranged by the permeability, and and an appropriate value becomes obvious by looking at the arteriole/capillary pressure (black markers in the compartment pressure plot). Deeper analysis reveals this value to be, $\kappa_{c\rightarrow\text{ventricle}} = 6.0\times10^{-4}$ m^{5}skg^{-1}.

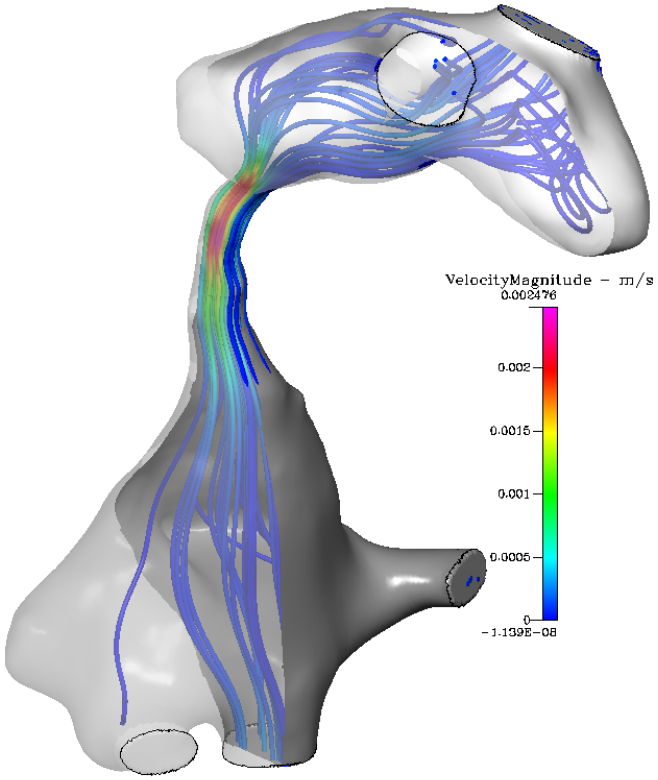

Figure C.4: An isometric view of Patient 2 in Figure 5.19-(a) clearly showing the unique flow regime through the third ventricle. These streamlines clearly show the importance of patient-specific flow information when considering surgical intervention procedures.

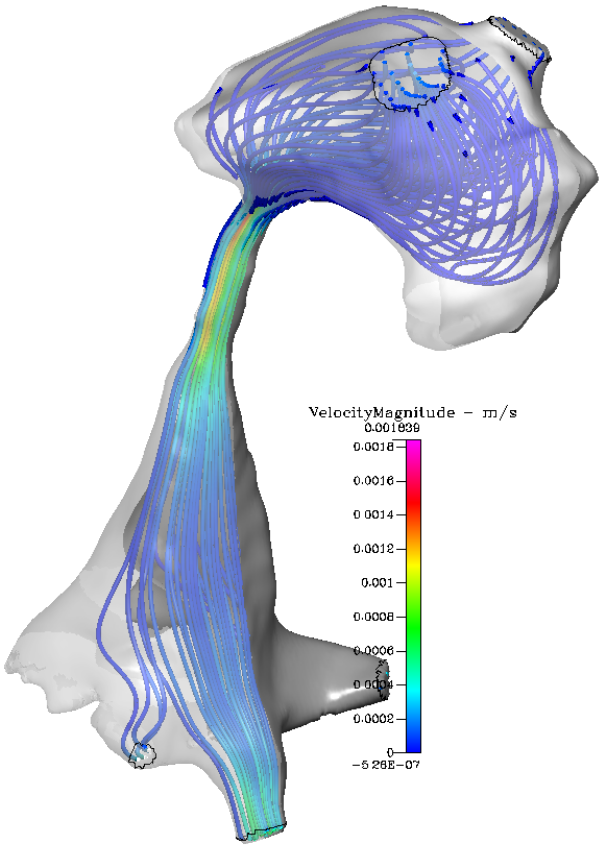

Figure C.5: An isometric view of Patient 5 in Figure 5.19-(d) shows the comparatively smooth flow through the third ventricle. These streamlines suggest that flow patterns may be of less consequence in surgical planning than in Figure C.4.

APPENDIX D

CODING SNIPPETS

For completeness, some of the interesting coding aspects are included as appendices.

D.1 SCHEME CODE FOR GAMBIT SET-UP

```
identifier name "aqueduct_MESH" new nosaveprevious
import vertexdata "verticesData.dat"
/
/ Create Ellipse 1
/
/ create edge.1
edge create center "vertex.1" major "vertex.2" onedge "vertex.3" start 0 end
    »360 ellipse
/ create edge.2
edge split "edge.1" vertex "vertex.3" connected
/ create edge.3
edge split "edge.2" vertex "vertex.4" connected
/ create edge.4
edge split "edge.3" vertex "vertex.5" connected
/
/ ... snip ...
/
/ Create long edges
/
/ create edge.45
```

```
edge create nurbs "vertex.2" "vertex.7" "vertex.12" "vertex.17" "vertex.22" "
    »vertex.27" "vertex.32" "vertex.37" "vertex.42" "vertex.47" "vertex.52"
    »interpolate
/ create edge.46
edge split "edge.45" vertex "vertex.7" connected
/
/ ... snip ...
/
/ Create Volume
/
/ create volume.1
volume create wireframe "edge.1" "edge.2" "edge.3" "edge.4" "edge.5" "edge.6"
    »"edge.7" "edge.8" "edge.45" "edge.55" "edge.65" "edge.75" real
/
/ ... snip ...
```

D.2 UDS FOR 1D-3D COUPLING

```
!***********************************************************************
 MODULE cfdrc_user
!***********************************************************************
  IMPLICIT NONE

  INTEGER, PARAMETER :: int_p  = SELECTED_INT_KIND(8)
  INTEGER, PARAMETER :: string_length = 80
  INTEGER, PARAMETER :: real_p = SELECTED_REAL_KIND(8)
  INTEGER, PARAMETER :: XDIR = 1, YDIR = 2, ZDIR = 3

  ! Utility parameters.
  REAL(real_p) , PARAMETER :: zero = 0.0d0, one = 1.0d0, two = 2.0d0, &
   &  three = 3.d0, four = 4.0d0, pi = 3.1415926535898d0

  ! declare global variables to be saved
  REAL(real_p) :: PA, PC, Qdot
  INTEGER(int_p), SAVE :: P_index, MF_index, RHO_index
  INTEGER(int_p), SAVE :: IN_index, OUT_index
  CHARACTER(len=string_length), SAVE :: model_name

 END MODULE cfdrc_user


!***********************************************************************
SUBROUTINE ubound(bc_index, var_index, face_index, xfc, yfc, zfc)
!***********************************************************************
! purpose : set boundary value of the current boundary variable.
!
! This routine is called face by face basis for each BC record. Use
```

```
! get_var_index, get_bc_index and get_active_cell to get the variable
! index, boundary index and active cell index respectively.
!
! Use set_bc() to set the value of current variable(var_index) at
! current face(face_index) along boundary(bc_index).
!-----------------------------------------------------------------------
 !DEC$ ATTRIBUTES DLLEXPORT :: ubound
 !******* DO NOT REMOVE ABOVE LINE FOR MS WINDOWS OS ************
!***********************************************************************

  ! Include required global variables declared in cfdrc_user module.
  USE cfdrc_user, ONLY : int_p, real_p, string_length
  USE cfdrc_user, ONLY : P_index, IN_index, OUT_index
  USE cfdrc_user, ONLY : PA, PC
  USE cfdrc_user_access

  !******* DO NOT REMOVE FOLLOWING LINE FOR MS WINDOWS OS ********
  IMPLICIT NONE

  ! Declaration of arguments of this subroutine.
  REAL(real_p),    INTENT(IN) :: xfc, yfc, zfc
  INTEGER(int_p), INTENT(IN) :: bc_index, var_index, face_index

  ! Declare required local variables here.
  LOGICAL :: error
  !-----------------------------------------------------------------------

  !-----------------------------------------------------------------------
  IF (IN_index .GT. 0) THEN
      IF (bc_index == IN_index .AND. var_index == P_index) THEN
        ! Set the pressure value at the inlet
        CALL set_bc(PA, error)
      ENDIF
  ENDIF
  !-----------------------------------------------------------------------

 RETURN
END SUBROUTINE ubound

!***********************************************************************
 SUBROUTINE uout(iflag)
!***********************************************************************
 ! iflag:  flag indicating calling location.
 !          1 - At the beginning of RUN.
 !          2 - At the beginning of time step
 !          3 - At the end of each iteration.
 !          4 - At the end of each time step.
 !          5 - At the end of RUN. or on "save" command.
 !-----------------------------------------------------------------------
 !DEC$ ATTRIBUTES DLLEXPORT :: uout
```

```
!******* DO NOT REMOVE ABOVE LINE FOR MS WINDOWS OS ************
!***********************************************************************

  ! Include required global variables declared in cfdrc_user module.
  USE cfdrc_user, ONLY : zero
  USE cfdrc_user, ONLY : int_p, real_p, string_length
  USE cfdrc_user, ONLY : MF_index, P_index, RHO_index
  USE cfdrc_user, ONLY : IN_index, OUT_index
  USE cfdrc_user, ONLY : PA, PC, Qdot, pi
  USE cfdrc_user, ONLY : model_name
  USE cfdrc_user_access

  !******* DO NOT REMOVE FOLLOWING LINE FOR MS WINDOWS OS ********
  IMPLICIT NONE

  ! Declaration of arguments of this subroutine.
  INTEGER(int_p), INTENT(IN) :: iflag

  ! Declare required local variables here.
  CHARACTER(len=string_length) :: token
  INTEGER(int_p) :: bc_type, n_faces, i, tmp_index
  LOGICAL :: error
  INTEGER(int_p) :: m, currentTimeStep
  REAL(real_p) :: dtSecs, currentTime, maxTime
  REAL(real_p), ALLOCATABLE, DIMENSION(:) :: tmpMF, tmpRHO
  !-----------------------------------------------------------------------
  INTEGER(int_p) :: proc_id, num_procs
  !-----------------------------------------------------------------------

  OPEN ( UNIT=99, FILE='output.log', POSITION='APPEND')
  CALL get_process_id(proc_id, error)
  m = 81

  ! 1 - At the beginning of RUN.
  IF (iflag == 1) THEN
  !-----------------------------------------------------------------------
    ! get the model constants
    CALL get_model_name(model_name,error)
    token = 'Pressure'
    CALL get_var_index(token, P_index, error)
    token = 'MASS_FLUX'
    CALL get_var_index(token, MF_index, error)
    token = 'RHO'
    CALL get_var_index(token, RHO_index, error)
    token = 'inlet'
    CALL get_bc_index(token, tmp_index, error)
    IF (.NOT. error) THEN
        IN_index = tmp_index
        ! set up the poroelastic solver
        write(99,*) "********** MODEL ::", model_name
```

```
130         Qdot = 5.795926360542450E-009
            currentTime = 0.0
            currentTimeStep = 0
            dtSecs = 1e3
            write(99,*) currentTime, proc_id, Qdot
135         CALL bt_solver( m, Qdot, currentTime, currentTimeStep, dtSecs, PA, PC,
                » model_name )
        ELSE
            IN_index = 0
        ENDIF

140     !-----------------------------------------------------------------------
    ENDIF

    ! 4 - At the end of each time step.
    IF (iflag == 4) THEN
145     !-----------------------------------------------------------------------
        Qdot = zero
        IF (IN_index .GT. 0) THEN
            ! calculate the flow rate through the inlet boundary
            CALL get_bc_info(IN_index, bc_type, n_faces, error)
150         ALLOCATE(tmpMF(n_faces))
            ALLOCATE(tmpRHO(n_faces))
            CALL get_bc(IN_index, MF_index, n_faces, tmpMF, error)
            CALL get_bc(IN_index, RHO_index, n_faces, tmpRHO, error)
            DO i = 1, n_faces
155             Qdot = Qdot + tmpMF(i)/tmpRHO(i)
            END DO
            DEALLOCATE(tmpMF)
            DEALLOCATE(tmpRHO)
            ! get the current time information
160         CALL get_time(currentTime, currentTimeStep, error)
            CALL get_time_step(dtSecs, error)
            ! run the poroelastic solver
            CALL bt_solver( m, Qdot, currentTime, currentTimeStep, dtSecs, PA, PC,
                » model_name )
            write(99,*) currentTime, proc_id, Qdot
165     ENDIF
        !-----------------------------------------------------------------------
    ENDIF

    CLOSE( UNIT=99 )
170

    RETURN
END SUBROUTINE uout

!***********************************************************************
175 SUBROUTINE udt
!***********************************************************************
 ! purpose : set the time step (dt).
```

```
!
! This routine is called every time step depending on user defined
! time step is activated through User time command in gui.
!
! Time step can be set by calling user user access routine
! 'set_time_step(dtusr,error)
!-----------------------------------------------------------------------
!DEC$ ATTRIBUTES DLLEXPORT :: udt
!******* DO NOT REMOVE ABOVE LINE FOR MS WINDOWS OS ************
!************************************************************************

 ! Include required global variables declared in cfdrc_user module.
 USE cfdrc_user, ONLY : real_p, int_p
 USE cfdrc_user, ONLY : IN_index, OUT_index
 USE cfdrc_user_access

 !******* DO NOT REMOVE FOLLOWING LINE FOR MS WINDOWS OS ********
 IMPLICIT NONE

 ! Declare required local variables here.
 REAL(real_p)    :: time, dt
 LOGICAL :: error
 INTEGER(int_p) :: ntstep
 !-----------------------------------------------------------------------

 IF (IN_index .GT. 0) THEN
     !-------------------------------------------------------------------
     CALL get_time(time, ntstep, error)
     CALL get_time_step(dt, error)
     IF (ntstep < 101) THEN
       dt = ntstep * 0.1
     ELSE
       dt = 10.0
     ENDIF
     CALL set_time_step(dt, error)
     !-------------------------------------------------------------------
 ENDIF

 RETURN
END SUBROUTINE udt
```

D.3 SUN GRID ENGINE SUBMISSION SCRIPT

```
#--------------# job-1.4.9.1.1.sge #--------------#
# Resource definitions - the following line(s) are NOT comment(s)
#$ -pe mpich 1
#$ -cwd
#$ -V
```

```
#$ -j y
#$ -o logfile.$JOB_ID

WDIR=`pwd`
MODEL_NAME="1.4.9.1.1"
HOST_FILE="$MODEL_NAME.hst"
NZONES=8
DECOMP="-sim 1 -nodecomp"

# create the hostfile for CFD-ACE
cat $PE_HOSTFILE | awk '{printf("%s\n",$1)}' > $HOST_FILE

# run CFD-ACE
cfd-ace-mpi -model $MODEL_NAME -wd $WDIR -hosts $HOST_FILE -num $NZONES
    »$DECOMP -job -nativempi
```

D.4 Parametric Search Set-Up with python

```
#!/usr/bin/python
import os
from numpy import linspace, logspace
from random import uniform
#
simFileName = "SIM_LIST.txt"
simFile = open("%s"%simFileName,"w")
#
printTrans = 0 # 0 for false, 1 for true
numRuns = 75000
for simCtr in range(1,numRuns+1):
    kA  = 10**uniform(-12, -10)
    kC  = 10**uniform(-12, -10)
    kV  = 10**uniform(-12, -10)
    #
    gAC = 10**uniform(-22, -18)
    gCE = 10**uniform(-22, -18)
    gCV = 10**uniform(-22, -18)
    gEV = 10**uniform(-13, -8)
    #
    aA  = uniform(0.5, 1.0)
    aC  = uniform(0.5, 1.0)
    aV  = uniform(0.5, 1.0)
    #
    kCE = 6e-4
    #
    baseName = "data/4-%06i"%simCtr
    simFile.write("%s %i %.4e %.4e %.4e %.4e %.4e %.4e %.4e %.4e %.4e %.4
        »e\n"%(baseName,printTrans,kA,kC,kV,gAC,gCE,gCV,gEV,aA,aC,aV,kCE))
simFile.close()
```

```
30
jobFile = open("myjob.sh","w")
jobFile.write("#!/bin/sh\n")
jobFile.write("#$ -cwd -V\n")
jobFile.write("#$ -e logFiles/error.log\n")
35 jobFile.write("#$ -o logFiles/output.log\n")
jobFile.write("TASK=$SGE_TASK_ID\n")
jobFile.write("INP=`sed ${TASK}q %s | tail -1`\n"%simFileName)
jobFile.write("./quadMPETSolver.exe $INP")
jobFile.close()
40
numCPUs = 6
numCores = numCPUs * 8
subFile = open("submit.sh","w")
subFile.write("rm -r data logFiles\n")
45 subFile.write("mkdir data logFiles\n")
if simCtr%numCores == 0:
    numJobs = int(simCtr/numCores)
else:
    numJobs = int(simCtr/numCores)+1
50 if numJobs == 1:
    subFile.write("qsub -N job1 -t 1-%i:1 myjob.sh"%(simCtr))
elif numJobs == 2:
    subFile.write("qsub -N job1 -t 1-%i:1 myjob.sh\n"%(numCores))
    subFile.write("qsub -N job2 -hold_jid job1 -t %i-%i:1 myjob.sh"%(numCores
        )+1,simCtr))
55 else:
    subFile.write("qsub -N job1 -t 1-%i:1 myjob.sh\n"%(numCores))
    for i in range(2,numJobs):
        subFile.write("qsub -N job%i -hold_jid job%i -t %i-%i:1 myjob.sh\n"%(i
            ),i-1,(i-1)*numCores+1,i*numCores))
    subFile.write("qsub -N job%i -hold_jid job%i -t %i-%i:1 myjob.sh"%(numJobs
        ),numJobs-1,(numJobs-1)*numCores+1,simCtr))
60 subFile.close()

os.system("chmod u+x *.sh")
```